Silica-Encapsulated Catalysts for Lean Methane Combustion

by

Amir Hossein Habibi

A thesis submitted in partial fulfillment of the requirements for the degree of

Doctor of Philosophy

in

CHEMICAL ENGINEERING

Department of Chemical and Materials Engineering
University of Alberta

Abstract

Due to its low cost, abundance and lower emissions compared to gasoline and diesel, there is a resurgence of interest in using natural gas as a transportation fuel. However, although the combustion of natural gas produces comparably less greenhouse gases (GHGs) and pollutants, CH_4 itself is a potent GHG and its release from natural gas vehicles' (NGVs) exhaust into the atmosphere should be avoided. The catalytic abatement of methane from exhaust emissions faces major challenges for several reasons. CH_4 has the strongest C-H bond among alkanes and is difficult to oxidize catalytically. Additionally, in the catalytic converter of a lean-burn NGV, small concentrations of CH_4 (500-1500 ppm) are to be oxidized in the presence of high concentrations of H_2O and at relatively low exhaust temperatures (below 550 °C). Pd catalysts (which have the highest CH_4 oxidation activity in lean conditions) are known to deactivate under these conditions. In an attempt to develop stable combustion catalysts, a bimetallic Pd-Pt silicon dioxide-encapsulated catalyst was designed, synthesized, and evaluated in this work. The catalyst design was aimed to benefit from the advantages of encapsulation and effects of bimetallicity.

In the first step, the effect of two synthesis procedures on the accessibility of the Pd nanoparticles after encapsulation in silica was studied. Dry catalytic combustion of CH_4 and surface area measurements were used to identify an optimal synthesis formulation for a high-loading, high-porosity monometallic Pd@SiO_2 catalyst. It was shown that the application of poly(vinylpyrrolidone) (PVP) alone as a Pd stabilizer and a potential porogen was inadvisable as it lead to non-porous catalysts. By using a suitable pore-inducing agent, Pd@mSiO_2 catalysts with high metal loading (~ 6 wt.%) and high surface area (~700 m^2g^{-1}) were synthesized. This structure was thermally stable at 550 °C and exhibited turnover frequencies similar to those of

traditional catalysts. Interestingly, 2/3 of the surface of the Pd nanoparticles was estimated to have been blocked by the shell material even in the highly porous catalysts.

To increase the catalyst activity in the presence of H_2O, bimetallic PdPt nanoparticles (7 nm in diameter) were synthesized and encapsulated in porous silica shells (60 nm in diameter) similarly to the Pd@mSiO_2 catalyst. The developed catalyst (PdPt@SiO_2), had a high metal loading (4 wt.% Pd, 7 wt.% Pt) and high surface area (600 m^2g^{-1}) and was evaluated in lean methane combustion in the presence of 5 mol% water at up to 550 °C. This structure showed a stable methane conversion during the hydrothermal ageing (HTA) test which was two- and ten-fold higher than the conversion for the impregnated Al_2O_3 and SiO_2-supported catalysts of the same metal loading, respectively. After the HTA, while the surface area and pore size distribution of the shell remained unaffected, an increase in the metal dispersion and some changes in the morphology of the PdPt nanoparticles were observed.

As a next step in the catalytic technology development, a kinetic study of methane combustion on the "aged" PdPt@SiO_2 catalyst at varying methane concentrations, temperatures and in the absence/presence of 5 mol% water was performed. The kinetic data of the dry reactions were correlated using an existing rate expression that is first order in methane and negative one order in water. Since this model failed to correlate the kinetic data in wet conditions, an alternative mechanism for wet CH_4 combustion was suggested. This mechanism was built up on the basis of previous experimental observations of the prevailing chemical state of Pd in wet feed, the ability of Pt to activate methane in oxygen-deficient atmospheres, and the inhibitory effect of water on the support-mediated oxygen exchange. To the best of our knowledge, this is the first time that the effect of support was incorporated in the wet CH_4 combustion mechanism. The resulting rate expression successfully predicted the activity of the

PdPt@SiO_2 catalyst with wet feed (5 vol.% water) in the temperature range of 550 to 750 K. Additionally, the internal mass transfer across the silica shell was studied. It was shown that for the catalysts used here, the diffusion resistance across the shell was negligibly small.

Preface

- **Chapter 1** of the thesis contains literature review related to the presented work.
- **Chapter 2** of the thesis has been published as: A. H. Habibi, R. E. Hayes, and N. Semagina, "Bringing attention to metal (un)availability in encapsulated catalysts", *Catalysis Science and Technology* 2018, **8**, 798-805. The reaction setup for methane combustion was originally designed and built by Dr. Long Wu and Dr. Robert E. Hayes. Dr. Shihong Xu performed the XPS analysis at Alberta Centre for Surface Engineering and Science (ACSES), University of Alberta. The NAA analyses were performed by Becquerel Laboratories Inc., Maxxam Analytics, Ontario. The TEM characterizations were performed by the author at Department of Oncology, Alberta Cross Cancer Institute, University of Alberta. All syntheses, reaction tests, analyses and other characterizations were performed by the author.
- **Chapter 3** of the thesis has been published as: A. H. Habibi, R. E. Hayes, and N. Semagina, "Evaluation of hydrothermal stability of encapsulated PdPt@SiO_2 catalyst for lean CH_4 combustion", *Applied Catalysis A, General.* 2018, **556**, 129-136. Dr. Shihong Xu performed XPS analysis at Alberta Centre for Surface Engineering and Science (ACSES), University of Alberta. Peng Li and Dr Jing Shen collected the HRTEM images at nanoFAB, University of Alberta. The NAA analyses were performed by Becquerel Laboratories Inc., Maxxam Analytics, Ontario. The TEM characterizations were performed by the author at Department of Oncology, Alberta Cross Cancer Institute, University of Alberta. The author performed all syntheses, reactions, analyses and other characterizations.
- **Chapter 4** of the thesis has been published as: A. H. Habibi, N. Semagina, and R. E. Hayes, "Kinetics of low-temperature methane oxidation over SiO_2-encapsulated bimetallic Pd-Pt nanoparticles" *Industrial & Engineering Chemistry Research* 2018, **57** 8160-8171. The reaction setup for methane combustion was originally designed and built by Dr. Long Wu and Dr. Robert E. Hayes. The TEM characterizations were performed by the author at Department of Oncology, Alberta Cross Cancer Institute, University of Alberta. The author performed all syntheses, reaction (ageing and kinetic) tests, analyses, and other characterizations. The MATLAB code for the nonlinear optimization and the numerical analyses were developed and implemented by the author.

This work was funded by Natural Sciences and Engineering Research Council of Canada (NSERC) and Canada Foundation for Innovation.

Dedicated to

My beloved family:

My father **Latif**,

My mother **Masoomeh**,

And my brother **Mehryar**.

Acknowledgements

Firstly, I would like to express my sincere gratitude to my supervisors. I have really enjoyed my collaboration with **Dr. Natalia Semagina and Dr. Robert E. Hayes** (from the Department of Chemical and Materials Engineering at the University of Alberta) and could not have imagined having better mentors for my PhD study.

Dr Natalia Semagina,

For her incredible support, her immense patience, and for allowing me to grow as a researcher. Her guidance helped me in every step of this journey and her positive attitude taught me how to stay motivated.

And **Dr Robert E. Hayes,**

For his patience, his enthusiasm, and for sharing his invaluable expertise. I am thankful for his priceless insights and mentorship.

I would also like to express my gratitude to:

My PhD candidacy examination committee: **Dr. Hyo-Jick Choi** (Exam Chair, Department of Chemical and Materials Engineering, University of Alberta), **Dr. Natalia Semagina** (Supervisor), **Dr. Robert E. Hayes** (Supervisor), **Dr. Ken Cadien** (Supervisory committee, Department of Chemical and Materials Engineering, University of Alberta), **Dr. Ravin Narain** (Examiner, Department of Chemical and Materials Engineering, University of Alberta) and **Dr. Hyun-Joong Chung** (Examiner, Department of Chemical and Materials Engineering, University of Alberta) for their questions, suggestions and assistance in the early stages of my research.

The committee for my PhD defense: **Dr**. **Anastasia Elias** (Exam Chair, Department of Chemical and Materials Engineering, University of Alberta), **Dr. Natalia Semagina** (Supervisor), **Dr. Robert E. Hayes** (Supervisor), **Dr. Ken Cadien** (Supervisory committee, Department of Chemical and Materials Engineering, University of Alberta), **Dr. Jingli Luo** (Examiner, Department of Chemical and Materials Engineering, University of Alberta) and **Dr.**

David Simakov (External examiner, Department of Chemical Engineering, University of Waterloo) for their valuable questions and comments on the thesis.

Dr. Jing Shen for team work and sharing her knowledge in the area of reaction engineering and also for her friendship and support.

Dr. Joe Mmbaga (Department of Chemical and Materials Engineering, Uinversity of Alberta) for his support and sharing his knowledge reggarding simulation and optimization.

Peng Li, Characterization group manager at nanoFAB**,** for collecting the HRTEM images.

Dr. Shihong Xu and **Dr. Anqiang He**, Centre for Surface Engineering and Science, University of Alberta, for performing XPS analysis. Special thanks to **Dr. Shihong Xu**, for the one-on-one advice and guidance on using CasaXPS software.

Dr. Xuejun Sun and **Pinzhang (Priscilla) Gao**, Department of Oncology, Alberta Cross Cancer Institute, University of Alberta, for the training on TEM and assistance with the TEM analysis.

My colleagues, **Dr. Allen Reule**, **Dr. Ali Mansoori**, **Dr. Hanieh Nassiri** and **Xiaoxing Wu** at Department of Chemical and Material Engineering, University of Alberta, for their friendship and support.

Dr. Nancy Zhang, **Dr. Shaofeng Yang**, **Walter Boddez**, **Les Dean**, for their continuous help with the maintenance of the lab equipment.

Lily Laser, Marion Pitchard, Kevin Heidebrecht, **Andree Koenig** and all other staff at Department of Chemical and Material Engineering, University of Alberta, for their help and support.

Table of Contents

List of Tables

List of Figures

List of Symbols

A_i	Pre-exponential factor of component *i* in the rate constant, units vary
B_i	Pre-exponential factor of component i in the adsorption constant, (mol/m^3)
C	methane concentration, (mol/m^3)
C_M	Methane concentration, (mol/m^3)
C_{M_0}	Initial Methane concentration, (mol/m^3)
C_{WP}	Weisz-Prater Number
C_1	methane concentration at the surface of the core NP, (mol/m^3)
C_2	methane concentration at the surface of silica shell, (mol/m^3)
d_p	Particle diameter, (m)
d_{pore}	Pore diameter, (m)
$d_{reactor}$	reactor diameter, (m)
D_{eff}	effective diffusion coefficient, (m^2/s)
D_K	Knudsen diffusion coefficient, (m^2/s)
D_{P}	diffusion coefficient in the pores, (m^2/s)
E_{i}	activation energy, (J/mol)
F_A	Methane flow rate, (mol/s)
h	Heat transfer coefficient ($kJ/m^2.s.K$)
k_i	Thermal conductivity of air, (W/m.K)
k_c	Mass transfer coefficient, (m/s)
k_{eff}	Effective thermal conductivity, (W/m.K)
k_i	reaction rate coefficient of component i or lumped rate coefficient, units vary
K_i	Adsorption equilibrium constant of component i, (m^3/mol)
l	reaction order with respect to water
L_{Bed}	Length of the catalytic bed, (m)
m	reaction order with respect to methane

M_W	Molecular weight (g/mol)
$M_{W\,CH_4}$	Molecular weight of methane (g/mol)
n	reaction order with respect to oxygen
n	power in the denominator of Equation 4.10
N	Order in Mears criterion formula
N	number of data points
Nu	Nusselt Number
O	objective function
Pr	Prandtl Number
r	Particle radius (m)
$-R_A$	the reaction rate in terms of metal surface area, (mol/m^2.s)
$-R_{CH_4}$	rate of the reaction, (mol/kg$_{cat}$.s)
$-R_W$	the reaction rate measured experimentally, (mol/kg$_{cat}$.s)
R_g	universal gas constant, (J/mol.K)
Re	Reynolds Number
S	support sites with oxygen vacancy
S	Surface area (m^2/g)
Sc	Schmidt Number
Sh	Sherwood Number
T	absolute temperature,(K)
T_{ref}	Reference temperature, (K)
TOF	Turnover frequency (s^{-1})
U	Superficial velocity, (m/s)
W	Catalyst mass, (g)
X	Fractional conversion
$X_{Experimental}$	methane conversion observed in the experiment
$X_{Predicted}$	methane conversion predicted by the model

Greek Letters

β	Prater Number
ΔH_i	adsorption enthalpy of component *i*, (J/mol)
$\Delta H_{reaction}$	Enthalpy of reaction, (J/mol)
ΔT_{ext}	External temperature gradient, (K)
$\Delta T_{\max}$	Maximum internal temperature rise, (K)
ε	porosity of the silica shell
ε_{bed}	Bed porosity
η	effectiveness factor
θ_i	fractional coverage of component *i*
λ	air/fuel equivalence ratio
μ	Viscosity, (Pa.s)
ν_i	Diffusion volume in Fuller equation
ρ_{Bed}	Bed density, (kg/m^3)
ρ_{Cat}	Catalyst density, (kg/m^3)
ρ_g	Gas density
ρ_M	density of the metal core, (kg/m^3)
ρ_S	density of the porous shell, (kg/m^3)
$\sum$	Sum
$\sum \nu_{air}$	Sum of the diffusion volume for air
$\sum \nu_{CH_4}$	Sum of the diffusion volume for methane
τ	tortuosity factor
ϕ_p	Particle porosity

Subscripts

Bed	Catalyst bed in the reactor
Cat	Catalyst
eff	Effective

Ext	External
G	Gas
i	Component *i*
M	Metallic core
max	Maximum
P	Particle
pore	Pore
reaction	Reaction
ref	Reference
S	Porous silica shell
WP	Weisz-Prater

List of Abbreviations

a.u.	Arbitrary Unit
ACSES	Alberta centre for surface engineering and science
AFR	Air-fuel ratio
BET	Brunauer–Emmett–Teller
BJH	Barrett-Joyner-Halenda
bhp	Brake horsepower
CH_4	Methane
CI	Compression ignition
CO	Carbon monoxide
CTAB	Cetyltrimethylammonium bromide
CTAC	Cetyltrimethylammonium chloride
DFT	Density functional theory
EDX	Energy dispersive X-ray spectroscopy
EPA	Environmental protection agency
EXAFS	Extended X-ray absorption fine structure spectroscopy
FID	Flame ionization detector
FTIR	Fourier transform infrared spectroscopy
GC	Gas chromatography

HC	Hydrocarbon
HCHO	Formaldehyde
H	Hour
HRTEM	High resolution transmission electron microscopy
LEV	Low Emission Vehicle
M	Metal
Metal@SiO_2	Silica-encapsulated metal
mi	miles
MS	Mass spectrometry
MUA	Mercaptoundecanoic Acid
MW	Molecular weight
NAA	Neutron activation analysis
$NaBH_4$	Sodium Borohydride
NGV	Natural gas fueled-vehicle
NMOG	Non-methane organic gases
NO_X	Nitrogen oxides
NP	Nanoparticle
NSERC	Natural Sciences and Engineering Research Council of Canada
PAMAM	Polymidoamine
Pd@SiO_2	Silica-encapsulated Pd, no porogen was applied in encapsulation stage
Pdm@SiO_2	Modified silica-encapsulated Pd , porogen was applied in encapsulation stage
PdPt@SiO_2	Bimetallic silica-encapsulated Pd-Pt, porogen was applied in encapsulation stage
PGM	Platinum group metal
PM	Particulate matter
PVA	Poly-(vinyl alcohol)
PVP	Poly-(vinylpyrrolidone)
S	Shell
SFTP	Supplemental Federal Test Procedure
Surf	Surface
STEM	Scanning transmission electron microscopy

TCD	Thermal conductivity detector
TEM	Transmission electron microscopy
TEOS	tetraethyl orthosilicate
TOF	Turnover frequency
TPO	Temperature programmed oxidation
TPR	Temperature programmed reduction
TTAB	Tetradecyltrimethylammonium bromide
US	United States
WHSV	Weight hourly space velocity
XPS	X-ray photoelectron spectroscopy
XRD	X-ray powder diffraction

Chapter 1

1 Introduction

1.1 Motivation: Emission control of natural gas vehicles

Natural gas is a hydrocarbon gas mixture which is primarily composed of methane (CH_4) and usually contains varying amounts of other hydrocarbons and trace amounts of N, S, and O. With a total proved worldwide reserves of over 193.9 trillion m^3, natural gas is an abundant energy source[1] that is mainly used as a fuel for heating, power generation and more recently, transportation purposes. Natural gas is considered to be an environmentally friendly clean fuel with significant advantages over other fossil fuels. Compared to gasoline and diesel fuels, natural gas has lower amounts of undesirable impurities (N and S), lower cost,[2] and has a remarkably higher octane rating.[3] Since CH_4 has the highest H/C ratio among fossil fuels, it generates the lowest amount of CO_2 per unit of produced power during combustion (54 g of CO_2 per MJ, whereas the combustion of gasoline releases 74 g CO_2/MJ).[4] Furthermore, CH_4 readily forms homogenous mixtures with air and when combusted in lean-burn conditions in a natural gas vehicle (NGV), it emits not only less CO_2 but also considerably less CO, nitrogen oxides (NO_X) and soot compared to diesel and gasoline fuels.[5] More specifically, natural gas light duty vehicles (LDV)s reduce smog-producing pollutants by 60-90% (compared to gasoline LDVs).[6] It is also believed that throughout the fuel lifecycle, NGVs emit 6 to 11 % fewer greenhouse gas (GHG) emissions than comparable gasoline vehicles.[7] Additionally, according to Argonne National Laboratory's Greenhouse Gases, Regulated Emissions, and Energy Use in Transportation (GREET) model, light-duty NGV's running on conventional and shale natural gas can reduce life-cycle greenhouse gas emissions by 11% (83% if running on renewable natural gas (biomethane)).[8]

Driven by these relative advantages and environmental regulations, NGVs are gaining worldwide popularity. With over 24 million vehicles currently in use, it is predicted that the

number of NGVs will reach a total of 30 million by 2024.[9] However, although the combustion of natural gas produces comparably less GHGs and pollutants, CH_4 itself is a potent GHG with a global warming potential (GWP) of 28–36 over 100 years.[10] Thus, even though CH_4 does not contribute to smog generation, due to its high GWP, the release of CH_4 into the atmosphere is currently a major environmental concern. In fact, according to the recent reports of the International Council on Clean Transportation, the treatment of natural gas emissions in the heavy-duty vehicles rulemaking could have critical implications for GHG emissions. Heavy duty NGVs are predicted to account for a significant proportion of the fleet, and by 2040 up to 39% of their potential climate benefits could be offset by uncontrolled methane emissions.[11]

Methane related regulations were not included in the initial automobile emissions standards of the U.S. Clean Air Act of 1970.[12,13] However, with the growing number of NGVs, more strict environmental regulations on methane emissions are emerging.[14] With the appearance of NGVs in the heavy-duty vehicle sector and potential concerns regarding CH_4 emissions, the Euro VI emission standards impose a CH_4 emission limit (0.5 g/Kwh) on "positive-ignition" vehicles (i.e., not diesels, but specifically natural gas and liquefied petroleum gas engines).[15] The most recent US emission standards for light-duty vehicles are the Tier 3 standards that follow the earlier Tier 2 (phased in from 2004 to 2009). The Tier 3 standards, which are closely aligned with California Low Emission Vehicles (LEV) III standards, were finalized on March 3, 2014 and are to be phased-in over the period from 2017 through 2025 (Table 1.1).[16] These standards require automobile manufacturers to certify their vehicles to one of the seven emission bins shown in Table 1.1. The Tier 3 standards are more stringent than the Tier 2 standards and include a number of important changes:[16]

- The fleet average limit is applicable to all vehicle categories compared to the Tier 2 regulations that allowed more relaxed fleet average emissions from heavier vehicle categories.
- The required emission durability is extended to 150,000 mi (from 120,000 mi).
- The certification bins and the fleet average standards are defined in terms of the sum of non-methane organic gases (NMOG) + NO_X emissions.
- The highest emission bin (Bin 160 (NMOG + NO_X = 160 mg/mi)) is equivalent to Tier 2 Bin 5.

Table 1.1. Tier 3 vehicle exhaust emissions standards in the USA adapted from [16]

Bin	Nonmethane-organic gases (NMOG) + NO_x, (mg/mi)	Particulate matter (PM), (mg/mi)	CO, (g/mi)	Formaldehyde (HCHO) (mg/mi)
Bin 160	160	3	4.2	4
Bin 125	125	3	2.1	4
Bin 70	70	3	1.7	4
Bin 50	50	3	1.7	4
Bin 30	30	3	1.0	4
Bin 20	20	3	1.0	4
Bin 0	0	0	0	0

Table 1.2 shows the fleet average NMOG + NO_x Supplemental Federal Test Procedure (SFTP) standards from 2018 to 2025.[16] According to the SFTP standards given in Table 1.2, by 2025, a 50% reduction in the fleet average NOMG+NO_X emissions is expected.[16] The latest US environmental regulations also affect the compression-ignition (CI) engines used in heavy-duty onroad (highway) vehicles, such as trucks and buses.[17] Table 1.3 summarizes the changes in Environmental Protection Agency (EPA) standards that apply to diesel-fueled engines, as well as to CI engines fueled by natural gas and other alternative fuels.[17] Considering these regulations, new challenges are imposed on the automotive industry to mitigate emissions by developing more efficient emission control (catalytic after treatment) systems.

The composition of the post combustion gases from an engine depends on the type of the engine, fuel and the air-fuel ratio (AFR). The exhaust stream is generally composed of air, H_2O, CO_2, CO, and NO_x. Since 1970s the allowable emissions from vehicles have been regulated by emission standards set by governments.[11] To reduce the harmful emissions and meet environmental standards, vehicles are equipped with exhaust emission control devices (catalytic converters). For over four decades, catalytic converters have been an indispensable part of any

Table 1.2. Tier 3 fleet average NMOG+NO_x SFTP standards adapted from [16]

Year	2018	2019	2020	2021	2022	2023	2024	2025
NMOG+NO_x (mg/mi)	97	90	83	77	70	63	57	50

Table 1.3. EPA emission standards for heavy-duty CI engines (g/bhp·hr), adapted from[17]

Year	CO	Hydrocarbon (HC)	$HC+NO_x$	NO_x	Particulate Matter (PM)	
					General	Urban Bus
1998	15.5	1.3	-	4.0	0.10	0.05[a]
2004	15.5	-	2.4	-	0.10	0.05
2007	15.5	0.14	-	0.20	0.01	
2015	15.5	0.14	-	0.02[b]	0.01	

[a] In-use PM standard 0.07 g/bhp·hr, [b] California optional low NO_X standards of 0.10, 0.05 or 0.02 g/bhp·hr

vehicle and have constantly been the subject of research and improvement. A typical catalytic converter is composed of metal or ceramic honeycomb monoliths coated with a thin layer of washcoat (a carrier for the catalytic materials). The washcoat is generally a high surface area material, usually γ-Al_2O_3, on which precious metals such as Pd, Pt, and Rh are dispersed. The catalysts used in catalytic converters are designed according to the type of the engine, fuel type, operating conditions, and AFR and are required to meet and exceed the emission standards.

The ratio of actual AFR to stoichiometric AFR is defined as the air/fuel equivalence ratio (λ). For any air-fuel mixture, $\lambda = 1$ represents the stoichiometric AFR. Combustion in lean-burn conditions ($\lambda > 1$) is considered to be the most efficient approach to minimize exhaust emissions from small and medium size engines.[4] Under lean-burn conditions, the presence of excess air allows for a more complete combustion at a lower temperature, thus reducing the formation of NO_x. In terms of AFR, NGVs are categorized into two groups: stoichiometric and lean-burn.[18] The emission control systems for stoichiometric NGVs operate similar to conventional auto catalyst TWCs and remove CO, HC, and NO_x. However, the emissions from lean-burn NGVs are similar to the diesel emission control technologies.[18] Heavy duty NGVs primarily operate at lean-burn conditions. The hydrocarbon composition of the exhaust of a lean-burn NGV is typically 90-95% CH_4. As stated earlier, the environmental advantages of NGVs can be offset by the emission of CH_4 in the exhaust stream. Thus, CH_4 emissions from lean-burn NGVs must be eliminated and this can be achieved by catalytic combustion of methane.

1.2 Catalytic combustion of CH_4

In the past four decades, catalytic combustion of CH_4 has been investigated as a means of mitigating fugitive CH_4 emissions and emissions from the exhaust of natural gas fuelled systems (NGVs and natural gas turbines). While thermal combustion of CH_4 occurs at high temperatures (1773 to 2273 K) which thermodynamically favor formation of nitrogen oxides (NO_x), catalytic CH_4 combustion occurs at much lower temperatures and thus generates much less environmentally harmful NO_x.[19] Also, catalytic combustion is not constrained by flammability limits,[20] and thus can be employed as a feasible emission control solution. However, catalytic combustion of CH_4 is more difficult than non-methane hydrocarbons (NMHC). CH_4 has the strongest C-H bond among alkanes (450 kJ/mol)[21] and is thus difficult to oxidize catalytically.[22] In NGV emission control, further complications are imposed by the reaction conditions of the catalytic converter of the vehicle. The exhaust of a lean-burn NGV typically contains small amounts of CH_4 (500-1000 ppmv), CO (200-700 ppmv), CO_2 (15%), large amounts of water vapor (10-15 vol.%), large excess of oxygen, SO_x (about 1 ppm) and NO_x and has a relatively low temperature (423-823 K).[23,24]

Considering the limitations on the size of the catalytic converters, catalytic abatement of methane at these temperatures is challenging and requires highly active low temperature catalysts. Another major engineering challenge is the presence of significant amounts of water vapor (10−15%) in the exhaust of lean-burn NGV engine which is known to be a major catalyst deactivation factor.[23] Thus, the main objective in the field of NGV emission control is to develop high-loading, highly stable combustion catalysts which have the highest activity at relatively low temperatures.

1.2.1 CH_4 combustion on Pd catalysts

Platinum group metals (PGMs) such as Pd, Pt, Rh, Au and transition metal oxides such as Mn, Cr, Cu, Co oxides) have been extensively studied in catalytic combustion.[22] The PGM loadings are usually reported in g/ft^3. [23] The typical PGM loading in a catalytic converter varies between 10-100 g/ft^3 for gasoline vehicles and between 100-200 g/ft^3 for diesel and NGVs.[18] In automotive emission control, designations based on monolith volume are industry standards and

are used to compare the catalyst volume and engine displacement.[23] Even though many catalysts can be used in catalytic CH_4 combustion, only those based on precious metals show sufficient activity to meet the required size of the catalytic converter for automotive applications. The maximum volume of the catalytic converter of an NGV is usually twice the engine displacement.[23] This size limitation is an important design parameter in designing catalytic converters and necessitates production of highly active high PGM loading catalysts. In a typical catalytic converter, the catalytic washcoat accounts for 12% of the volume of the catalytic monolith. The washcoat material usually has a 36% voidage. Hence, every cubic foot of the monolith contains 0.077 ft^3 (0.00218 m^3) of catalyst powder (for instance: PGM/Al_2O_3). For example, a catalyst powder with metal loadings of 1, 5 and 10 wt% PGM on alumina translates into an approximate PGM loading of 90, 450, and 950 g/ft^3 of monolith, respectively. Catalysts with low metal loading are not desirable as they give rise to unacceptably larger reactor volumes. While palladium is considered to be the most active catalyst under net oxidizing conditions (lean-burn), platinum catalysts are preferred under reducing (fuel-rich) conditions.[25,26] These metals are usually used in the form of metal nanoparticles (NPs) deposited on a high surface area support material (γ- Al_2O_3, SiO_2, ZrO_2, CeO_2, SnO_2, zeolites, and perovskites. It was initially believed that the metals are the main catalytically active sites, while the sole role of the support is to stabilize the NPs by preventing NP leaching and agglomeration. However, possible roles of the support transporting reactants to the catalytic surface and impacting the overall reactivity have also been explored.[27–30] In the operating conditions of the catalytic converter of a lean-burn NGV (in the presence of excess oxygen), Pd catalysts have the highest activity. However, in spite of their high initial activity, Pd tends to deactivate under exhaust conditions. [22,27,31–34] Deactivation of Pd catalysts has been related to several factors. Thermal[35] and water-induced [34,36]sintering of the Pd NPs, collapse of the support structure, conversion of PdO to Pd, water adsorption,[28,37] and formation of $Pd(OH)_2$,[38,39] have been reported as some of the main causes of deactivation of Pd catalysts [21,26,30]. NP sintering and water-related effects are currently two of the most significant challenges in the development of stable combustion catalysts for automotive catalytic converters.

1.2.2 Reaction mechanism and kinetics

A number of studies have supported the hypothesis that methane combustion over palladium-based catalysts occurs through a Mars van Krevelen redox-type mechanism.[40] In a Mars van Krevelen redox mechanism, the oxygen from the metal oxide catalyst is utilized in reaction, and is replenished by re-oxidation of the reduced metal oxide using oxygen from gas phase.[41] Inn 1996, Muller et al.[40] performed experiments using isotopic oxygen at temperatures from 573 to 773 K and suggested that the combustion reaction on ZrO_2-supported PdO catalysts occurred partly via a redox Mars van Krevelen mechanism but the overall conversion was affected by the interplay between the surface reaction of adsorbed reactants and the redox mechanism.[40]

Later, CH_4 oxidation at low temperatures was reported to follow a Mars–van Krevelen redox mechanism and involve the activation of CH_4 on site pairs consisting of Pd-PdO_x crystallites.[42] In these pairs, Pd acts as an oxygen vacancy and PdO_x provides the oxygen atoms.[42] CH_4 is adsorbed and dissociated on metallic Pd producing H and CH_x species; while the oxidation takes place on the adjacent PdO.[43,44] Fujimoto et al. [42] proposed this mechanism for a PdO_x/ZrO_2 catalyst. Figure 1.1 illustrates the methane dissociation on a Pd-PdO site pair.[42] This scheme, which was proposed by Fujimoto et al.[42], starts with the interaction of carbon atoms of gas phase or physisorbed CH_4 with vacant Pd sites (step 1 in Figure 1.1). In step 2, which is the C-H bond activation stage, the PdO species abstracts hydrogen atoms sequentially from the adsorbed CH_4. In step 3, surface hydroxyl groups (Pd–OH) are produced. They proposed that the initial H-abstraction stage (C-H bond activation) was the rate determining step (RDS) when OH* species

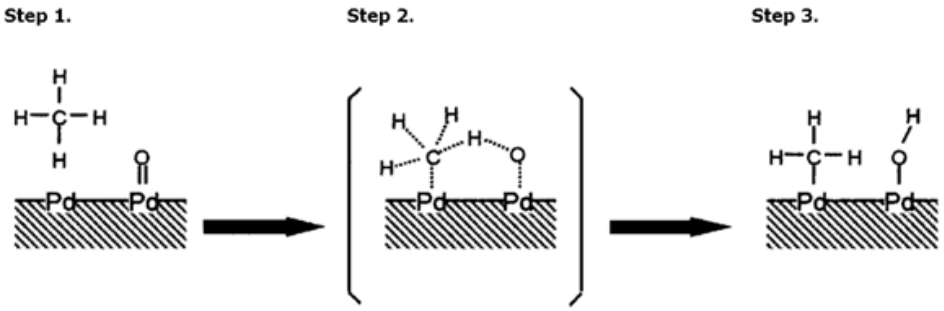

Figure 1.1.Mechanism of CH_4 dissociation on Pd/PdO site pair.[42] Reproduced with permission from.[42] Copyright © 1998, Academic Press.

were the most abundant surface intermediates (MASI).[42] A year later, Burch et al.[45] proposed that it was the decomposition of surface Pd−OH (produced from CH_4 activation and H_2O poisoning) (step 3 in Figure 1.1) that determined the rate of C−H bond activation. Ciuparu et al.[46] performed pulsed reaction experiments using labeled $^{18}O_2$ over pure Pd and Pd/ZrO_2 catalysts and confirmed the redox combustion mechanism. Since no labeled H_2O was observed they concluded that the rates of water adsorption and desorption were very slow. They reported that the produced surface hydroxyl groups inhibited the surface reoxidation and proposed an oxygen exchange mechanism (Figure 1.2). As illustrated in Figure 1.2, in this mechanism the reaction starts with the interaction between CH_4 from the gas phase and ^{16}O on the PdO surface surface.[46] After formation of OH groups and before water desorbs, the isotopic composition of the surface oxygen equilibrates with the bulk; then, due to the lower rate of hydroxyl recombination and water desorption, the oxygen vacancies on the PdO surface (produced after water desorption) are filled with transfer of $^{18}O_2$ from the bulk.[46]

The exchange of oxygen between the gas phase and the oxide support was also investigated by Schwartz et al.[27] They used continuous flow of CH_4 plus $^{16}O_2$ or $^{18}O_2$ over various combinations of isotopically labeled PdO/metal oxide catalyst (3 wt.% PdO/Al_2O_3) and showed that in the absence of CH_4 the oxygen exchange becomes significant at temperatures higher than 380°C. They concluded that the mechanism for catalytic combustion of methane over PdO/Al_2O_3 and PdO/MgO in the low temperature (below 350 °C) fuel-lean conditions includes migration and exchange of oxygen with the surface of the oxide support. They proposed that the

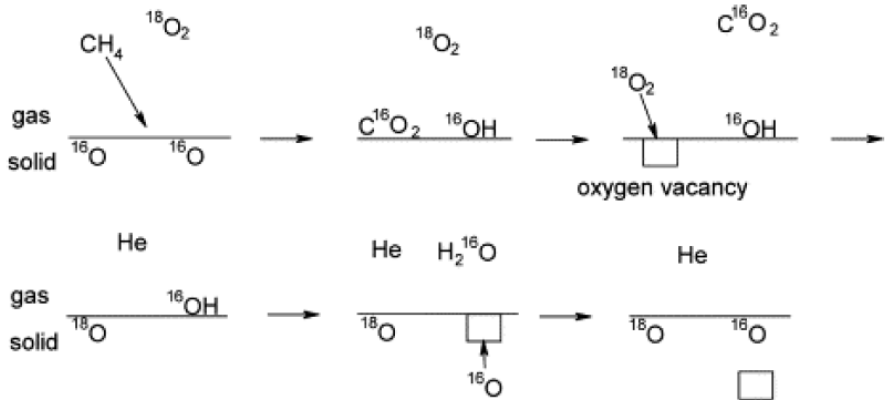

Figure 1.2. Oxygen exchange for CH_4 oxidation using labeled ($^{18}O^{16}O$) pulsed experiments.[46] Reproduced with permission from [46] Copyright © 2002, Elsevier.

oxygen bonded to Pd is used in reaction and is significantly exchanged with the support.[27] Their results were consistent with reaction mechanisms suggested by Fujimoto et al.[42] and Ciuparu et al.[21,28]:

- The RDS of CH_4 combustion in lean conditions and at low temperatures is the water desorption from the catalyst surface.[21,28,42]
- At above 450 °C the RDS is the methane activation where CH_4 decomposes to CH_3 and OH while breaking a Pd−O bond. [21,28,42]

Schwartz et al.[27] also noted that oxygen surface mobility is faster than these rate limiting steps and hence does not impact the observed combustion rate. Chin et al.[47] used kinetic and isotopic experiments and investigated the relevance of elementary kinetic steps in CH_4-O_2 reactions on Pd clusters. They proposed a reaction scheme that is based on the dissociation of both CH_4 and O_2 molecules on a Pd/Al_2O_3 catalyst surface (Figure 1.3). In this mechanism * and O* correspond to Pd-* and PdO sites. The reaction of CH_4 with O* species produces OH* and CO* species. The C-H bond activation (steps 2.1 to 2.3) is more favorable on the O*-* (an adsorbed oxygen and a vacancy site pair) than on O*-O*(two adsorbed oxygen site pair). The authors showed that the C-H bond activation and consequently the TOF is a function of the size

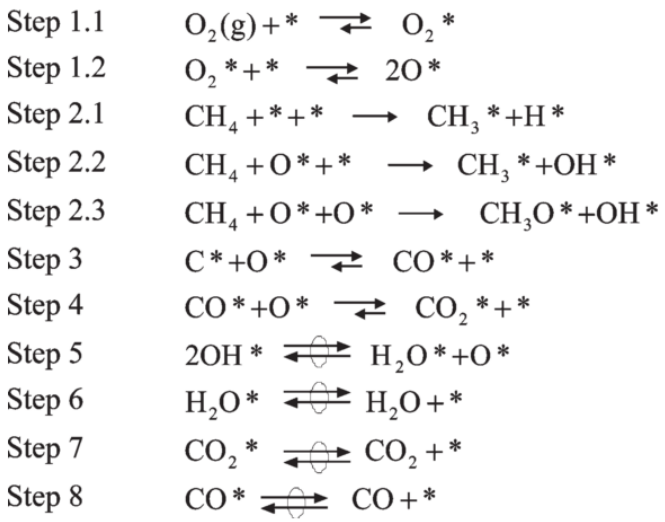

Figure 1.3. The sequence of elementary reaction steps for CH_4-O_2 reactions on supported Pd clusters. Reproduced with permission from.[47] Copyright © 2011, American Chemical Society.

of the Pd clusters and oxygen pressure.[47] At the oxygen pressure range of 0.3-1.6 kPa the small clusters are less active. The shift of C-H activation sites from O*-O* to O*-* is indicated by an increase in rate constants with decreasing O_2 pressure and occurs at a lower oxygen pressure on smaller Pd clusters. At a constant O_2 pressure larger clusters have weaker O* binding and are thus more effective for C-H bond activation than smaller clusters.

It is also agreed that the reaction mechanism also depends on the oxidation state of Pd.[48,49] Several experiments and thermodynamic calculations have shown that PdO is more active than reduced Pd.[21,48,49] The PdO (101) facet is known as the most active surface of Pd for methane combustion.[50] Chin et al.[48] performed a detailed mechanistic assessment based on isotopic and kinetic methods and investigated the potential pathways of C-H bond activation on three different surfaces: metallic Pd, Pd saturated with chemisorbed oxygen (O*) and PdO. Their observations show that C-H bond activation on metal atom pairs (*-*), oxygen atom pairs (O*-O*) and Pd cation lattice oxygen pairs (Pd^{2+}+-O^{2-}) in PdO occurs via oxidative addition, H-abstraction, and σ-bond metathesis pathways, respectively.[48,51] They proved that PdO has the lowest activation barrier among the three active species (Pd^0: 84 kJ mol^{-1},[52] O*-saturated Pd^0: 158 kJ mol^{-1},[48] and PdO: 61 kJ mol^{-1} [48]). The transition state structures of C-H bond activation over these surfaces are given in Figure 1.4-a. [48]

The authors also measured the turnover rates for CH_4−O_2 reactions over a wide range of O_2 (0.15−87 kPa) and CH_4 (0.8−4.8 kPa) pressures at 873 K and plotted the pseudo-first order rate coefficient (defined as the turnover rates divided by the CH_4 pressure (r_{CH_4}/CH_4) on Pd/Al_2O_3 (0.2 % wt Pd, 21.3 nm mean Pd cluster diameter) at differential CH_4 conversions (<1.5%)) versus oxygen pressure (Fig 1.4-b). They noted that the effect of oxygen pressure on rate constant was similar to other observations (at higher temperatures) except for the pressure at which the sharp increase occurred: at 873 K the sharp increase in rate coefficient with oxygen pressure occurred at 1.7 kPa whereas at 973 K it occurred at 35 kPa. They related this transition in the increase of rate coefficient with oxygen pressure to lower pressures at lower temperatures to the shift in the Pd−PdO phase boundary to higher oxygen chemical potentials with an increase in temperature increases, which was deemed consistent with the exothermic nature of the Pd oxidation reaction.[48]

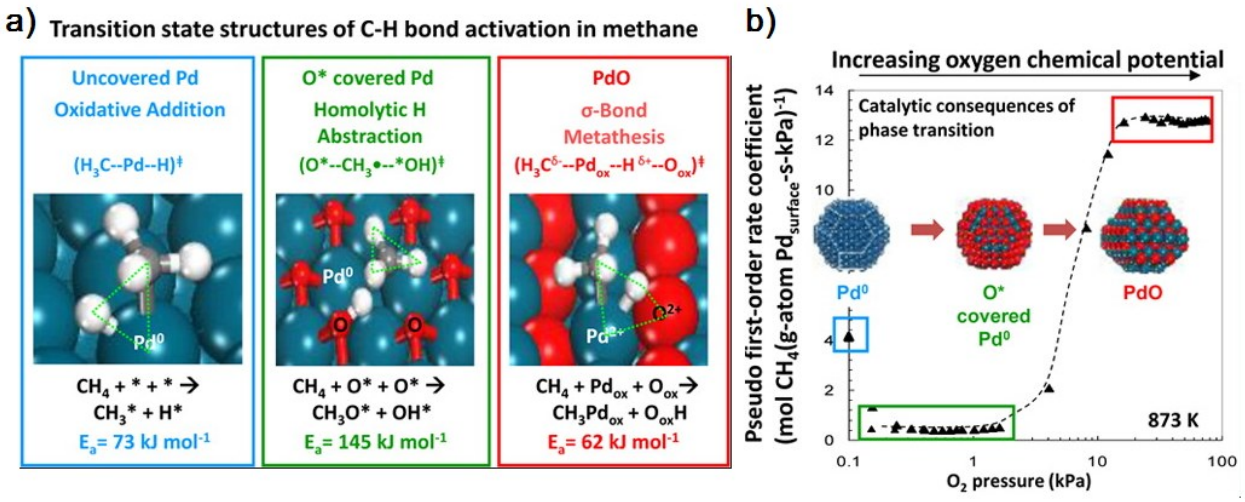

Figure 1.4. a) Transition state structures of C-H bond activation in methane. b) Reactive CH_4 collision probabilities, also the pseudo-first order rate coefficients (r_{CH_4} / CH_4) on 0.2 wt.% Pd/Al_2O_3 (21.3 nm mean Pd cluster diameter determined at the metallic state) as a function of O_2 pressure at 873 K. (0.94−3.92× 10^9 cm^3 (s mol Pd surface)$^{-1}$; 200 SiO_2/catalyst intraparticle dilution ratio; 200 and 1200 quartz/catalyst interparticle dilution ratio for O_2 pressures below and above 4 kPa, respectively).[48] Reproduced with permission from. [48] Copyright © 2011, American Chemical Society.

Kinetic models which can predict the CH_4 conversion at various reactant and product concentrations and temperatures are essential to a successful reactor (catalytic converter) design. Kinetics of methane combustion over supported PdO catalysts has been studied.[53–55] There is an extensive literature on the catalytic combustion of methane, most of which deals with Pd catalysts.[47,56–58] Langmuir–Hinshelwood,[56] Eley–Rideal,[57] and Mars–van Krevelen[47,58] mechanisms have been proposed for the combustion of methane over Pd catalysts. Several rate equations have been used to model the catalytic combustion of methane. A detailed review on the previous work in the literature on monometallic Pd, monometallic Pt, and bimetallic Pd-Pt is presented in chapter 4 of this thesis. Ideally, a kinetic model is based on the reaction mechanism in the operating conditions and reflects the real physical phenomena that occur on the catalyst surface. Although catalytic combustion of methane is widely studied, kinetic models designed specifically for the exhaust conditions of an NGV (lean conditions, 150-550 °C (423-823 K), and in the presence of water) are limited. With the more recent findings on the effect of the operating

conditions on the catalyst and reaction mechanism, it has become possible to develop more specialized kinetic models.

1.2.3 Role of the support in reaction

A heterogeneous catalyst is generally composed of active metals (usually in the form of NPs) deposited on a high surface area support material. Although the main role of the support was initially believed to be stabilization of NPs by preventing sintering and leaching, more recent studies suggest possible contribution of the support to reactant transport and to the overall reactivity.[27–30] As stated earlier a number of studies have supported that methane combustion over palladium-based catalysts occurs through a Mars van Krevelen redox-type mechanism.[40] The support is agreed to have an important effect on catalytic activity of a supported Pd catalyst. Oxygen mobility on the support has been found to be a potentially important support characteristic that affects the activity. By measuring the surface oxygen mobility using isotopic exchange experiments on supported Rh, Pt, and Pd catalysts, Descorme et al.[59] demonstrated that both the active component (metal) and the oxide support affect oxygen mobility. Later, it was shown by Ciuparu et al.[60] that depending on the temperature, oxygen from the support could have an important contribution to the methane combustion. By comparing the reaction on PdO and zirconia (ZrO_2)-supported PdO, they demonstrated that the involvement of oxygen from the support (ZrO_2) was negligible at 598 K while it was considerably higher at 698 K.[60] More interestingly, the resistance to water inhibition was shown to be greater in supports with higher oxygen mobility ($Al_2O_3 < ZrO_2 < Ce_{0.1}Zr_{0.9}O_2$).[28]

In light of conclusive observations of Schwartz et al.[27], this behavior of the support is known to be connected to the strength of water adsorption on the support. Hydroxyl accumulation (which decreases the activity by disrupting the oxygen transfer) is proven to be more acute on support materials that are intensely affected by water (such as Al_2O_3).[27] They proposed that Pd/PdO serves as a station for gas phase oxygen to dissociate, migrate to the oxide support, and exchange with oxygen from the oxide support. They also showed that the rate of this oxygen transfer depended on the type of the support and temperature.[27]

Schwartz et al.[30] later compared the inhibitory effect of the presence of water on Al_2O_3, MgO, TiO_2, and MCM-41-supported PdO catalysts. MgO-supported PdO was reported to have a

slower deactivation rate compared to Al_2O_3 and TiO_2 which was related to MgO's high oxygen mobility. However, they also observed that even though silica (the material composing MCM-41) has lower oxygen mobility than both MgO and Al_2O_3; yet, PdO/MCM-41 catalyst did not undergo severe deactivation. Hence, they noted that factors other than oxygen mobility could have been involved in decreasing the rate of catalytic deactivation.[30] Their *in situ* Fourier Transform Infrared (FTIR) transmission spectroscopy experiments at 598 K proved that during catalytic methane combustion, hydroxyl groups accumulated on the oxide support.[30] Since desorption of the water/hydroxyl groups from the support at this temperature is slow[30] and based on the previously discovered fact that oxygen from the support is actually utilized in the reaction, they proposed that the deactivation due to water occurs via accumulation of hydroxyl/water on the support which in turn impedes the catalytic combustion reaction by hindering oxygen mobility on the support.[30]

The effect of the support on reaction was also studied in the absence of water. Araya et al.[61] studied Pd/SiO_2 and Pd/ZrO_2 in dry combustion conditions and observed that even though the conversion on Pd/SiO_2 was higher, the ZrO_2-supported catalyst showed was more stable during a 40 h ageing. The lower deactivation rate of Pd/ZrO_2 was attributed to ZrO_2's high oxygen mobility.[61]

In addition to oxygen mobility, other factors such as metal-support interactions, support's acidity, and the tendency of support to encapsulate Pd can play a role in catalyst activity. For instance, according to Gannouni et al.,[62] silica-supported Pd catalysts were more active than aluminosilica-supported Pd catalysts (1% CH_4, 4% O_2 in He) since on aluminosilica, the positive effect of Al^{3+} on metal dispersion was cancelled by partial metal encapsulation.[62] Partial coverage of the surface of Pd NPs by the support was also observed to adversely affect the activity in Pd/SiO_2 catalysts. Zhu et al.[63] observed that during CH_4 combustion at 598 K, SiO_2 covered a fraction of the Pd surface. They suggested migration of silica during the combustion reaction (caused by water) or during H_2-reduction as the factors facilitating the partial encapsulation of Pd by silica.[63] The combustion activity may also be related to the support's acid strength. Yoshida et al.[64] reported a higher catalytic activity for supports (5 wt.% Pd) with moderate acid strength (Al_2O_3 and SiO_2). Higher activity of Pd on these supports was associated with higher oxidation state of Pd. On basic supports (e.g MgO), the formation of binary oxides

from PdO and the support (such as Pd/MgO_x) resulted in a lower Pd activity. More recent studies of Cargnello and coworkers[65] demonstrated the support had a limited influence on the activity of PdO. They observed that inert (SiO_2), acidic (Al_2O_3), and redox-active ($Ce_{0.8}Zr_{0.2}O_2$) supports provided similar rates, while basic (MgO) supports showed remarkably lower activity.[65] However, the activation energies were similar, suggesting that the active site or phase is likely to be similar for all four supports. They related the lower activity of Pd/MgO to two possible hypotheses: The lower activity is related to either the electronic state of the PdO phase or to strong adsorption of CO_2 on the catalytic surface. Since MgO is known to stabilize an electron-rich PdO phase where the oxide anion is strongly basic, an increased stability of the PdO phase and increased oxygen vacancy formation energy can be expected. Formation of oxygen vacancies plays a key role in the C−H bond activation on PdO which follows a Mars−van Krevelen mechanism. Thus, stabilization of the oxide ion by MgO support leads to a decrease in reaction rate. The second possibility discussed by the authors was the formation of a magnesium carbonate phase in close contact with the palladium particles. MgO is known to adsorb CO_2 to form transient magnesium carbonate species. Magnesium carbonate species may affect the surface of supported Pd particles or the metal−support interface and thus block the active sites. [65]

1.2.4 Structure sensitivity

The activity and selectivity of a catalytic reaction can depend on the particle size of the supported catalysts. This phenomenon, referred to as structure sensitivity, can be explained by the interaction between chemisorbed species and surface sites of different configuration in the metal associated with atoms in terrace, steps, and kinks.[66] Catalytic reactions can be structure-sensitive, structure-insensitive, or showing both behaviors, depending on the conditions. For many reactions, structure sensitivity stems from the higher activity of a particular surface site toward a certain reaction.[66]

Early studies reported that methane oxidation was structure sensitive. Hicks et al.[67] studied the effect of metal dispersion on the catalyst activity. They observed an increase in Pd dispersion during reaction, as Pd restructured during conversion to PdO.[67] In another study they evaluated the TOFs of alumina-supported Pd catalysts in dry methane combustion at differential conditions (CH_4 conversion below 2%) in the temperature range of 260−370°C.[68] They used the

particle dispersions obtained from hydrogen chemisorption experiments to calculate the TOFs. They reported that the reaction rate depended on Pd dispersion which was related with metal loading. While large Pd particles (2.3% Pd loading and 10% dispersion) showed a TOF of 3.3 s^{-1}, the TOF for small Pd particles (0.2% Pd loading and 84% dispersion) was 0.02 s^{-1}.[68] They suggested that the high dispersion, low-loading samples consisted of a Pd phase that strongly interacted with the support, hence stabilized PdO and reduced the activity. [68] Using H_2-O_2 titration and with the rate data obtained at <5% conversion, Fujimoto et al.[42] reported TOFs of 0.012 s^{-1} and 0.003 s^{-1} for ZrO_2-supported Pd catalysts with dispersions of 2.5% and 21.8%, respectively. They also noted that the reaction on small Pd particles (< 7 nm) was structure sensitive on alumina and zirconia supports.[42] Later, Lyubovski et al.[69] reported the oxidation reaction on metallic Pd to be structure sensitive with apparent activity increasing as Pd particles restructured into large low-index-plane crystals with lower overall surface area.

However, some opposing observations were also reported. The change in the TOF of PdO crystallites in the range of 2-110 nm was reported by Ribeiro et al. [70] (1994) to be only from 2×10-2 s^{-1} to 8×10^{-2} s^{-1}. Zhu et al.[49] compared the TOFs for Pd (111), Pd (100), and Pd (110) and showed that regardless of the surface structure, the reaction rate is only dependent on the oxygen-oxygen interaction. In 2006, Roth et al.[71] prepared Pd/Al_2O_3 catalysts with a wide range of mean particle sizes (2-30 nm, determined by H_2 chemisorption) and studied them in complete methane oxidation. As given in Figure 1.5, they observed a linear increase in TOF with increasing particle size for Pd particles smaller than 12 nm. However, for particles larger than 12 nm, the reaction was not dependent on Pd dispersion.

In 2010, Castellazzi et al.[72] reported that the TOF of 1 wt.%, 2wt.%, and 4wt.%Pd Pd/Al_2O_3 catalysts as 5.6×10^{-3}, 1.7×10^{-2}, and 3.5×10^{-2} s^{-1}, respectively. The 1 wt.% Pd catalyst showed a higher dispersion of PdO. They claimed that the TOF is mostly dependent on the Pd-support interaction rather on the PdO particle size.[72]

In a more recent study Cargnello and coworkers[65] studied the effect of the Pd particle size and the support on the activity of uniform palladium nanocrystals. They confirmed that PdO was the most active phase. Also, their normalized rate measurements on four different supports (Al_2O3, SiO_2, MgO, and CZ80) indicated a mild size dependence for Pd-catalyzed combustion for all supports (Figure 1.6).[65] Their observation proved that it was not the smallest particles that

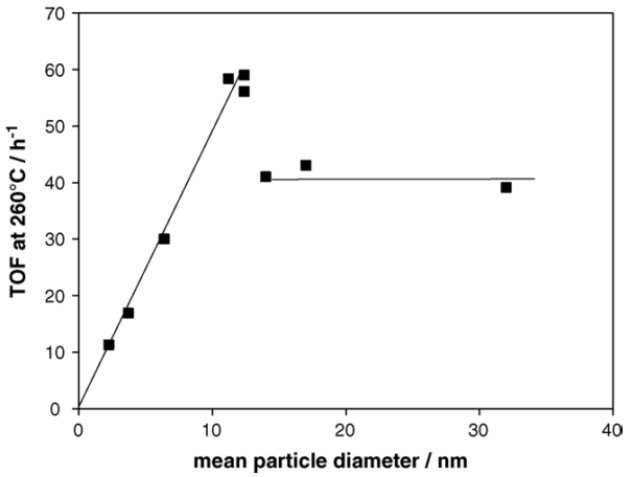

Figure 1.5. TOF or activity per surface Pd metal atom mol CO_2/(surface Pd atom h) at 260°C of Pd/Al_2O_3 catalysts vs. mean particle diameter.[71] Reproduced with permission from. [71] Copyright © 2005, Elsevier.

delivered the highest rates; instead, on all four supports, particles of intermediate particle size around 4−5 nm were the most active. (Figure 1.6-a). The apparent acivation energies were similar (about 80−100) kJ mol^{-1} across all sizes and supports (Figure 1.6-b), suggesting that the RDS for the reaction in all these catalysts were similar, likely the C−H activation on the Pd/PdO

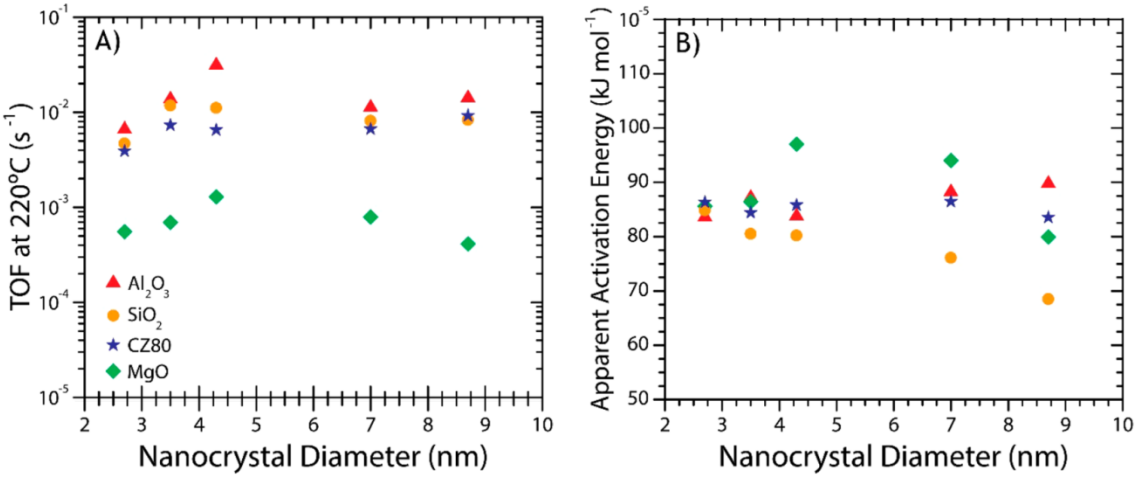

Figure 1.6. a) TOF at 220 °C and b) apparent activation energy for all support Pd nanocrystals as a function of size as calculated from Arrhenius fits. Rates were measured under the following conditions: 1% CH_4,4% O_2 in Ar at 175000 mL.g_{cat}^{-1}.h^{-1}. [65] Reproduced with permission from.[65] Copyright © 2017, American Chemical Society.

surface.[65] They related the mild dependence of reaction rate on size to variations in the surface crystal structure. The study conluded that the oxidation state did not change with partcile size and thus was not a factor in causing the observed structure sensitivity. Their EXAFS anlaysis proved the bond lengths for the Pd−O, second-shell Pd−Pd, and third-shell Pd−Pd did not vary with particle size for Al_2O_3-supported catalysts, confirming that the strain effects did not contribute to the structure sensitivity. The authors also proposed the following as the potential reasons for the observed mild structure sensitivity: oxidation state of the Pd phase, strain effects on the Pd active phase, the proportion of different sites, the relative proportion of PdO (101) to PdO (100) facets, and chemisorption effects. Based on these observations they suggested that the previous contrasting reports of structure sensitivity of Pd may have also been a result of a combination of factors, including varying proportions of sites and facets.[65]

1.2.5 Deactivation of Pd catalysts

As stated in the previous sections, deactivation of Pd catalysts is a major issue in development of catalytic CH_4 emission control systems. Several factors including thermal sintering,[35] water-induced sintering [34,36] water adsorption,[28,37] and formation of $Pd(OH)_2$,[38,39] have been reported in the literature as the main causes of deactivation of Pd catalysts. This section presents an introduction on water-related effects (including sintering) which are currently the main challenges in developing stable combustion catalysts. Since the presence of water vapor is known to exacerbate thermal NP sintering, the thermal and hydrothermal sintering of NPs will be discussed together.

1.2.5.1 Negative effects of water on combustion catalysts

The exhaust gases of a lean-burn NGV contain large amounts of water vapor (up to 10%). Water is also a reaction product produced in the catalytic converter during the catalytic combustion. The presence of water in the exhaust stream of an NGV, imposes additional challenges on designing stable combustion catalysts as water contributes to catalyst deactivation and reaction inhibition.[23,34,73,74] Water is also known to change the reaction mechanism and thus the kinetic behavior of the catalyst.[28] The negative effects of water can depend upon several factors including the catalyst formulation, methods of preparation, support material, reaction

temperature, history of exposure to reaction/ageing, and water concentration. Negative effects of water on catalytic methane combustion can be divided into two principal categories:

a) Reaction inhibition due to water adsorption and formation of $Pd(OH)_2$

b) water-assisted sintering

The inhibition effect of water is known to depend on temperature. While the inhibitory effect of water is believed to be reversible and decrease with temperature at lower temperatures,[23] the water-induced sintering of Pd catalysts at above 773 K is shown to be irreversible.[34,36]

Earlier studies agreed that in the low temperature regime (<723 K), the inhibitory effect of water was related to the water poisoning of the catalyst surface by formation of $Pd(OH)_2$.[26,39,75,76] This effect is reported to be negligible at high temperatures (T>773 K) and stronger at lower temperatures. It was shown by Burch et al.[26] that the inhibitory effect of water was significant only up to about 723 K. This temperature is specifically important because at T<723 K, water is also shown to bind more strongly to the catalytic surface (compared to the other reaction product i.e. CO_2) and to desorb from the surface at a slower rate.[37] At 723 K, the desorption delay between CO_2 and water is proven to start to disappear and desorption of water and CO_2 from the surface occur at about equal rates.[37] Although earlier studies suggested the formation of inactive $Pd(OH)_2$ to be the main deactivating factor, as it will be discussed in this section, more recent studies relate this partially reversible deactivation effect to accumulation of hydroxyl groups on the support and its interference with the oxygen transfer. The inhibitory effect of water on alumina and zirconia-supported Pd catalysts was found to be stronger at lower temperatures.[28] As a result, Ciuparu et al.[28] concluded that depending on the temperature, the reaction may take place through two different regimes: a) at lower temperatures (<773 K) the rate determining step (RDS) is the water desorption step and the reaction order with respect to water is about −1, and b) at T>773 K the RDS is the methane activation (reaction order with respect to water is 0).[28] It is also known that in the absence of water, the reaction order with respect to water is zero.[28] The water-related deactivation is also shown to be dependent on the support material. Kikuchi et al.[77] showed that even though for both 1.1 wt.% Pd/Al_2O_3 and 1.1 wt.% Pd/SnO_2 catalysts an increase in the concentration of water (between 1-20%) shifted the

ignition curves to higher temperatures (indicating catalyst deactivation), the deactivation of Pd/Al_2O_3 catalyst was much more significant than Pd/SnO_2. As it is indicated in Table 1.4, for all three supports, the T_{30} (temperature at which 30% CH_4 conversion occurs) increases with an increase in water concentration. However, the deactivation due to water is much more severe on the alumina-supported catalyst.

As discussed in the previous sections, water inhibition is greater in supports with higher oxygen mobility.[28] Schwartz et al. showed that since desorption of the water/hydroxyl groups from the support at 598 was slow and suggested that the accumulation of hydroxyl/water on the support reduced the combustion activity by hindering oxygen mobility on the support.[30]

The negative impact of water on reaction is also related to the effect that water has on oxidation state of Pd. The difference between the catalytic performance of Pd in the presence and absence of water can be explained by the oxidation (and chemical) state of Pd during the reaction. The oxidation state of Pd is known to be a critical factor in defining the catalytic behavior and also reaction mechanism. Many experiments and thermodynamic calculations have shown that PdO is more active than the reduced Pd.[21,48,49] The PdO (101) facet was reported as the most active surface of Pd for methane combustion.[50] It is also important to understand how the oxidation state of Pd can vary in the presence and absence of water in both monometallic and

Table 1.4. T_{30} for CH_4 oxidation over Pd supported on different supports.[a] [77] Reproduced with permission from[77]. Copyright © 2002, Elsevier.

Catalyst	Pd/Al_2O_3	Pd/SnO_2	Pd/Al_2O_3-NiO
Added water (vol. %)		T_{30} (°C)	
0	345	290	372
1	400	315	372
5	430	335	420
10	460	360	425
20	510	365	445

[a] metal loading for all three catalysts 1.1 wt.%, constant GHSV of 48000 h^{-1} , composition of the dry feed (1%CH_4/20% O_2 in N_2).

bimetallic catalysts. Recent *in situ* XAS analyses of Nassiri et al.[78] have revealed that for a monometallic Pd catalyst, the oxidation state of Pd during lean CH_4 combustion is affected by the presence of water. In dry lean methane combustion, Pd^0 is readily oxidized to PdO (473-823 K) and is the prevailing oxidation state; however, in wet conditions, oxidation to the more active oxide state (PdO) is gradual and occurs only at high temperatures. In a bimetallic Pd-Pt, and in the presence of water (473-773 K) the metallic Pd^0 and Pt^0 were reported to be the prevailing surface species.[78,79]

1.2.5.2 Thermal and hydrothermal sintering of NPs

A major challenge in using metal NPs as catalysts is their stability issue. NPs have high surface energies and, without sufficient surface passivation, tend to grow into larger particles. This phenomenon, referred to as NP sintering, results in a loss of active surface area available for reaction. Two mechanisms are generally accepted to be responsible for NP sintering: Ostwald ripening and particle coalescence. Both processes are driven by the reduction of total surface energy. During Ostwald ripening, atoms are leached from small particles and transport onto larger particles. Particle coalescence occurs through migration and merging of entire particles.[80] The sintering rate is dependent on the NP size and is much lower for smaller NPs.[80] In NPs smaller than 3 nm, Ostwald ripening is the most prominent sintering mechanism, whereas for larger particles (3-10 nm) may sinter through both mechanisms. The NP sintering is also suggested to depend on the metallic state, metal-support interactions, and the presence/absence of water. Pd in its metallic state is known to have a higher vapor pressure than its oxide (PdO) and thus, has a higher Ostwald ripening rate.[81] For supported Pt catalysts, a stronger metal-support interaction was shown to result in a higher O electron density and yield smaller Pt crystallites.[82]

More importantly, NP sintering is exacerbated in the presence of water. Water is known to affect the thermal stability of metals (Pt, Rh and Pd) through sintering mechanisms[81,83,84] As stated earlier, at higher temperatures (T>773) the deactivation effects of water are irreversible.[34,36] Water-assisted sintering is known to occur at T>773 K. For example, it is shown that on a Pd/SiO_2 catalyst, the presence of H_2O leads to formation of silanol (Si-OH) groups, favoring the migration and coalescence of Pd,[85] whereas in the absence of water, Ostwald

ripening is the main sintering mechanism. The activity of Pd catalysts is known to decrease irreversibly during hydrothermal ageing (HTA) at high temperatures.[34] In fact, the extent of catalyst deactivation during ageing in the presence of water (HTA) is much larger than thermal ageing (in the absence of water). Escandon et al. [34] observed a reaction T_{50} of 648, 723, and >823 K for the fresh (oxidized), aged in the air, and hydrothermally aged Pd/ZrO_2-Ce catalysts, respectively. Sintering of Pd NPs was reported to be the main reason for deactivation of Pd/Al_2O_3 catalysts after a 200 h exposure to 10% H_2O/N_2 at 1173 K.[36]

1.2.6 Bimetallic Pd-Pt catalysts in combustion

It is known that bimetallicity provides synergistic effects and improves catalytic performance in a variety of applications. Addition of a second metal to the active metal has been investigated as a feasible way of preventing metal sintering. The sintering of the bimetallic NPs can be mitigated by the nature of the added component, such as high melting point.[86] Addition of Pt to Pd has been shown to improve the stability of Pd catalysts in wet CH_4 combustion.[33,87,88] While Pd is considered to have the highest activity under net oxidizing (lean) conditions, platinum catalysts are generally preferred under reducing (fuel-rich) conditions.[25,26] In lean combustion conditions, monometallic Pt is not active [89] and also has less resistance against sintering than Pd. However, in a supported bimetallic Pd-Pt catalyst, Pd stabilizes Pt through strong interactions between PdO and the support.[54] Bimetallic Pd-Pt catalysts are usually less active than monometallic Pd [90,91] simply because they contain less Pd. This lower activity has also been attributed to the presence of smaller amounts of PdO as a result of alloy formation between Pd and Pt [90] and the transformation of PdO to metallic Pd.[92]

Nomura et al.[93] showed that addition of Pt to Pd reduced the inhibition effect of water on palladium catalysts. They related the higher resistance of Pd-Pt to water to a synergistic effect between Pt and Pd.[93] Narui et al.[33] reported that the higher PdO dispersion on PdO-Pt/α-Al_2O_3 catalyst (27%) compared to PdO/α-Al_2O_3 (14%) resulted in higher initial activity and higher stability of the bimetallic catalyst. After a 6 h exposure to the reaction feed stream at 350 °C, the particle size of the monometallic catalyst increased from 8 to 11 nm, while the growth in the particle size of PdO-Pt/α-Al_2O_3 was not significant.[33]

Yamamoto et al.[94] compared the performance of Pt-Rh/Al_2O_3 (conventional three-way catalyst), Pd/Al_2O_3,Pt/Al_2O_3, and Pd-Pt/Al_2O_3 catalysts in wet methane combustion (catalyst inlet temperature of 658 K, GHSV= 40,000^{-1}, feed composition: 2000 ppm of CH_4, 10.5% of O_2(wet basis), and 10% of H_2O). They observed that the Pd-Pt/Al_2O_3 catalyst (Pt:10 g/L, Pd: 15 g/L) exhibited higher and longer lasting CH_4 oxidation activity than Pt-Rh/ Al_2O_3, Pt/Al_2O_3, and Pd/Al_2O_3 catalysts. Their XRD analyses showed that the crystallite growth with time for both Pd (111) and PdO (101) was faster on monometallic Pd/Al_2O_3 compared to the bimetallic Pd (10 g/L)-Pt (10 g/L)/Al_2O_3 catalyst (Figure 1.7).[94]

Persson et al. [95] studied the effect of adding eight co-metals (Co, Rh, Ir, Ni, Pt, Cu, Ag, and Au) to Pd (at a 1:1 ratio on a molar basis) on dry catalytic methane combustion. The catalysts were prepared using incipient wetness and the combustion tests were performed on a gas feed containing 1.5 vol % CH_4 in air at a gas hourly space velocity (GHSV) of 250,000 h^{-1}. They concluded that a catalyst containing both Pd and Pt (Pd-Pt/Al_2O_3) was the most promising, as it had a high activity that did not decline with time. Pd-Ag was also a promising candidate, but

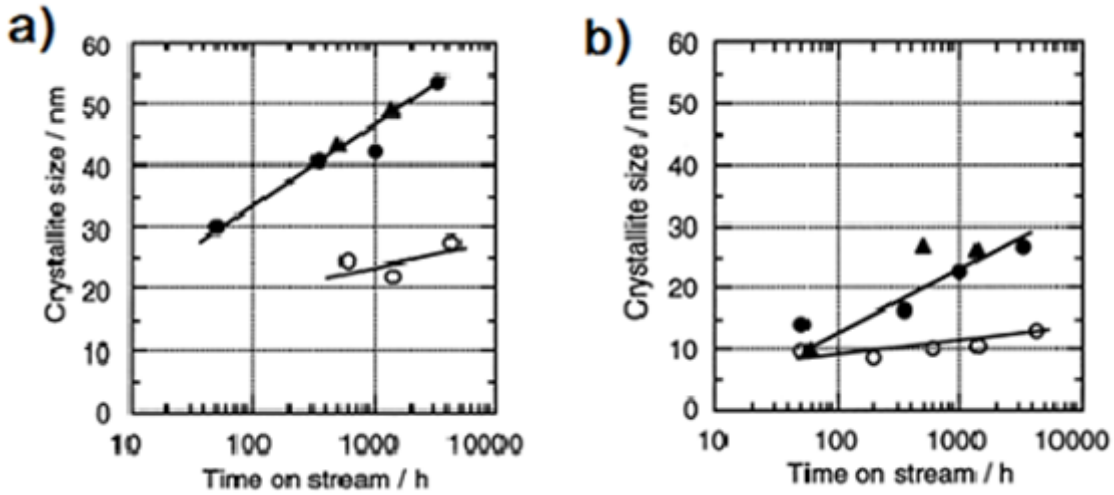

Figure 1.7. a) Growth of Pd crystallite sizes calculated from Pd(111) reflection as a function of time on stream for various catalysts. (○) Pt 10 g/L-Pd 10g/L/alumina, (▲) Pd (10g/L)/alumina, (●)Pd 50 g/L/alumina. b) Growth of Pd crystallite sizes calculated from PdO(101) reflection as a function of time on stream for various catalysts. (○) Pt 10 g/L-Pd 10g/L/alumina, (▲) Pd (10g/L)/alumina, (●)Pd 50 g/L/alumina.[94] Reproduced with permission from.[94] Copyright © 1998, Elsevier.

its activity was slightly lower. In PdCo and PdNi, the co-metals formed spinel structures with the Al_2O_3 support, and for this reason, their presence did not affect the performance of palladium. The co-metals in PdRh, PdIr, PdCu, and PdAg formed separate particles consisting of the corresponding metal oxide. In PdPt and PdAu, the co-metals formed alloys with palladium and both catalysts showed a stable activity.[95] Later, they examined Pd-Pt bimetallic catalysts supported on five different support materials (Al_2O_3, ZrO_2, ceria-stabilised ZrO_2, yttria-stabilised ZrO_2 and $LaMnAl_{11}O_{19}$) and observed that all Pd–Pt catalysts (molar ratio of 2:1 Pd:Pt) independent of the support, have considerably more stable methane conversion (in dry conditions) than the monometallic palladium catalyst.[90] The *in situ* XRD spectra of PdPt–Al_2O_3 (molar ratio of 2:1 Pd:Pt) showed that the fresh catalyst produces a large peak in the Pd–Pt position (111) and also a PdO peak (101) (Figure 1.8).[90] PdO was not detected at 300 °C and 400 °C. However, the PdO peak reappeared at 500 °C and 600 °C. At above 700 °C no PdO was detected which was consistent with the activity loss at high temperatures. [90] The study also noted that even though monometallic Pd catalyst shows a higher activity compared to Pd-Pt catalyst in transient activity tests, at steady-state conditions (when temperature was kept constant) the methane conversion of the monometallic Pd drops significantly with time.[90] Based on high temperature *in situ* XRD results, they suggested that this drop in activity was not attributable to decomposition of PdO into its metallic form (Pd). Interestingly, during operation at steady state,

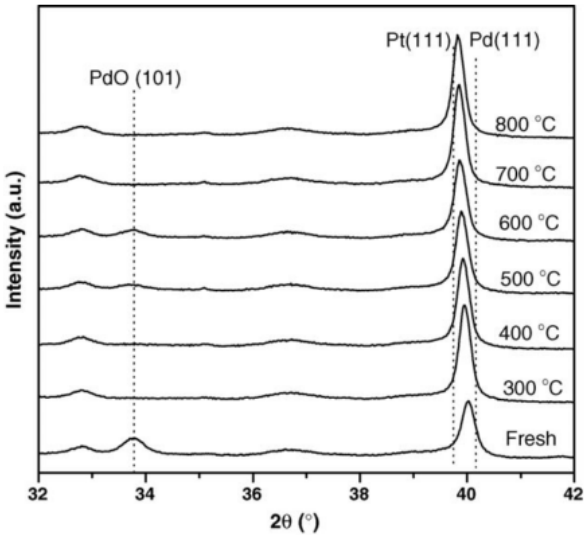

Figure 1.8. High-temperature *in situ* XRD profiles of PdPt-Al_2O_3 during heating. Reproduced with permission from [90]. Copyright © 2006, Elsevier

all bimetallic Pd-Pt catalysts (supported on Al_2O_3, ZrO_2, ceria-stabilised ZrO_2, yttria-stabilised ZrO_2 and $LaMnAl_{11}O_{19}$) were significantly more stable compared to the monometallic Pd.[90]

Ozawa et al.[96] investigated the effects of the addition of Pt to PdO/Al_2O_3 on catalyst deactivation (dry conditions, 1.0 vol.% CH_4/air). After the catalyst was heated to 1073 K (at the rate of $10Kmin^{-1}$), the deactivation test was performed at 1073 K for 10 h. They observed that the initial combustion rate for the PdO/Al_2O_3 catalyst dropped with the addition of a small amount of Pt but increased with increasing of the Pt amount. Thy related the decrease in the combustion activity at the initial stage to the particle growth of PdO while calcining up to 1073K with the addition of a small amount of Pt in the catalyst preparation. The study concluded that the addition of Pt prolongs the lifetime of the PdO/Al_2O_3 catalyst by decreasing the initial activity. They concluded that this behavior was due not to the transformation of PdO to Pd–Pt but to the prevention of the growth of PdO and Pd–Pt particles during the reaction.[96]

The amount of added Pt is also known to affect the catalytic performance. Persson et al.[91] studied the catalytic oxidation of methane (1.5 vol% CH_4 in air GHSV= 250,000 h^{-1}) over six catalysts with different Pd:Pt molar ratios. All bimetallic catalysts had a loading of 470 μmol metal/g catalyst powder. They observed that an alloy between Pd and Pt was formed in close contact with the PdO phase (except for the Pt-rich catalyst, where no PdO was observed). Adding small amounts of Pt to Pd, improved the activity. However, higher amounts of Pt were required for stabilizing the methane conversion. The Pd-Pt bimetallic catalysts with Pd:Pt ratios of 2:1 and 1:1 were the most stable while the Pt-rich catalyst showed a very poor activity.[91]

The effect of adding Pt to Pt on the resistance of Pd to water has also been studied. Pieck et al.[97] observed that after thermal treatment at 600 °C for 4 h in wet air (60 cm^3min^{-1} air flow with 0.356 cm^3h^{-1} water) the T_{50} of the bimetallic Pd-Pt/Al_2O_3 catalyst (0.4% Pt-0.8%) was about 50°C lower than that of monometallic Pd.[97] Lapisardi et al.[87] studied the catalytic combustion of methane over bimetallic Pd-Pt catalysts at low temperature under lean conditions (2000 vol. ppm CH_4 and 5 vol.% O_2 (He balance), GHSV=20,000 h^{-1}, for experiments under wet conditions 10 vol.% water was added). The catalysts were prepared using successive impregnation (2 wt.% metal loading and varying compositions in Pt and Pd). They showed that in the absence of water added to the feed, the methane conversion over Pd-rich bimetallic catalysts (Pt/Pt+Pd molar ratios less than 0.3) was the same as that of the monometallic Pd/Al_2O_3

catalyst. However, under wet conditions, these bimetallic catalysts exhibited an improved performance compared to Pd/Al_2O_3. While the increase in T_{50} of the Pd/Al_2O_3 upon addition of 10% water was from 320 °C to 425 °C, the increase in T_{50} for the bimetallic catalyst ($Pd_{0.93}Pt_{0.07}/Al_2O_3$) was from 320 °C to 400 °C. This effect was maintained during mild steam ageing (10 vol.% H_2O, 600 °C for 22 h). They concluded that the partial substitution of Pd with Pt on Al_2O_3-supported Pd catalysts leads to an improved performance in catalytic oxidation of methane under lean-burn conditions, especially in the presence of large amounts of water vapor. This effect was maintained even after mild steam ageing and was associated by the authors to interactions between Pd and Pt. This was confirmed by temperature programmed oxidation (TPO) experiments indicating that addition of Pt affected the formation and decomposition of PdO.[87] Abbasi et al.[88] studied commercial Pt and Pd-Pt (4:1 ratio) catalysts in dry and wet CH_4 combustion and observed that both catalysts permanently lost a large portion of their activity as a result of exposure to 5 vol.% water. When addition of water stopped, the Pt–Pd catalyst recovered some but not all of its initial activity. However, the activity loss of the Pt catalyst was mostly permanent.[88]

Recently, Nassiri et al.[98] evaluated the effect of the Pd:Pt ratio (0.3 wt.% with Pd:Pt ratios ranging from 5:1, to 1:5) on the stability of $Pd\text{-}Pt/\gamma\text{-}Al_2O_3$ catalyst during and after 40-hour *in situ* hydrothermal ageing at 400-550 °C (feed stream containing 4000 ppm CH_4, O_2-to-CH_4 molar ratio of 50, and 5% water vapor). The catalysts were prepared via simultaneous reduction of metal precursors using a colloidal synthesis via alcohol reduction in the presence of a stabilizer PVP (producing "alloys") and also through a hydrogen-sacrificial method (producing core-shell NPs). The stability of Pd, Pt and Pd-Pt catalysts (with the same Pd loading) are given in Figure 1.9. The monometallic Pt catalyst was reported to be the least active. The low activity of Pt in lean combustion conditions is well established and is attributed to Pt sites being blocked by oxygen [60]. Although active at the beginning, the monometallic Pd catalyst deactivated quickly and after 25 hours of time-on-stream showed a conversion of < 10%. More interestingly, the performance of the bimetallic catalysts depended on the Pd-to-Pt ratio. While Pd-rich catalysts showed significantly higher activity than monometallic Pd, they deactivated similarly to the monometallic Pd. The catalysts with a higher Pd content deactivated faster (Figures 1.9-a and c).

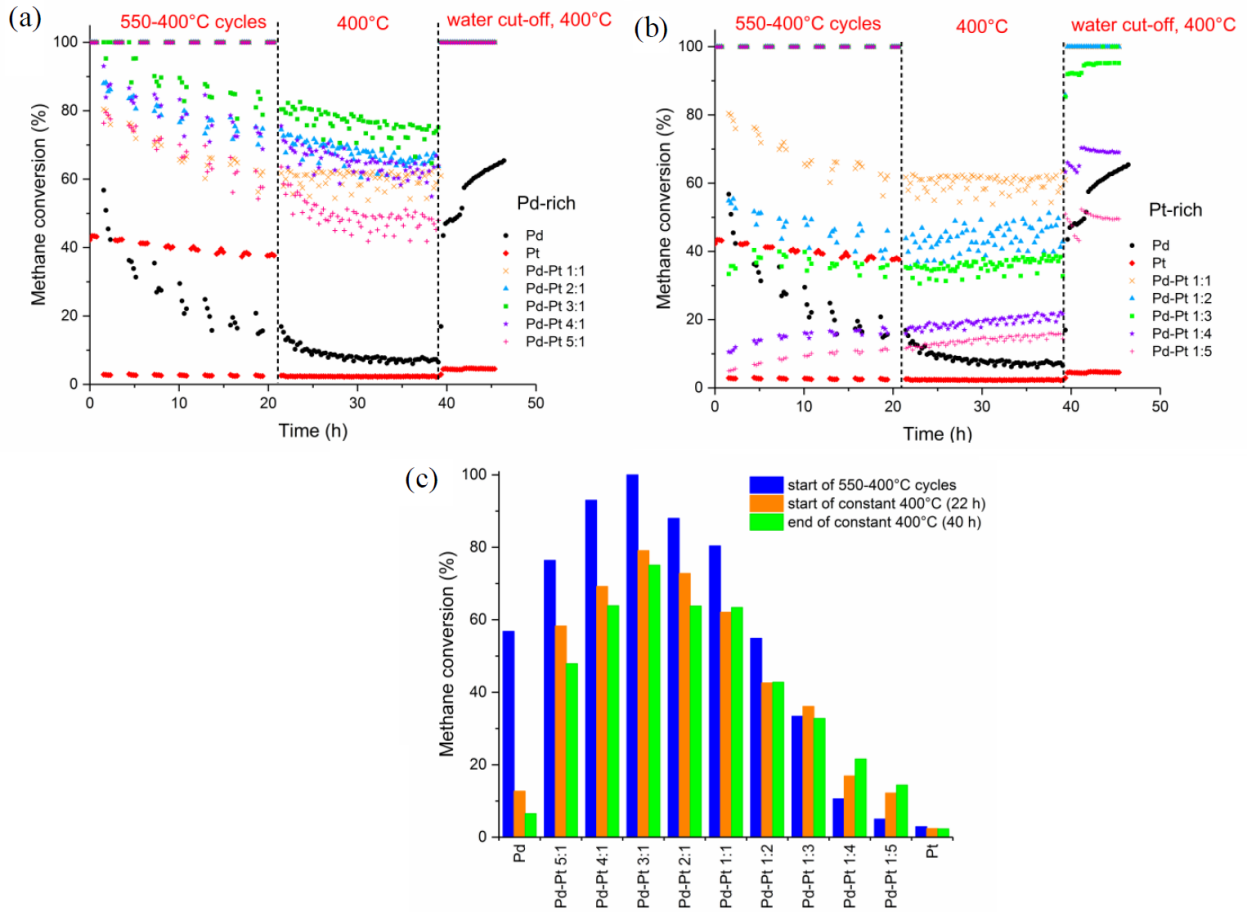

Figure 1.9. Hydrothermal ageing tests. Pd and Pd-Pt catalyst amounts correspond to the same Pd loading in the reactor (1.2 mg). Pt catalyst loading corresponds to 1.2 mg of Pt.[98] Reproduced with permission from.[98] Copyright © 2018 Elsevier.

Even though Pt-rich catalysts (Figs. 1-9-b and 1.9-c) had lower initial activities, their activity was maintained (and even improved) during the HTA. The authors concluded that Pd-Pt ratios of 1:1 to 4:1 were optimal from the viewpoint of activity; however the 1:1 ratio was the most stable formulation (Figure 1.9-c).[98] The increase in stability at 400 °C was also observed at ratios higher than 1:1, but at lower activity levels. The effect was reported not to be affected by the particle size but by the ratio of Pd:Pt. The authors observed significant structural changes in Pd core–Pt shell nanoparticles as these NPs progressively transformed into alloyed structures, and their catalytic performance approached those of the alloyed NPs. More importantly, platinum was reported to vaporize significantly under wet feed conditions. The ratio of Pd:Pt was concluded to be more influential than the method of preparation.[98]

1.3 Synthesis of combustion catalysts

As stated previously, a heterogeneous catalyst is generally composed of an active phase deposited on a support material. Commonly, the active phase is the metal NPs and the support is a high-surface area oxide. In automotive emission control systems, Pd, Pt and Rh are some of the most frequently used metal particles [99] and Al_2O_3 is a widely used support. A variety of industrial applications prefer the catalytically active metals to be small in size as smaller particles have higher surface-to-volume ratios. Traditionally, catalyst preparation is done via impregnation of a salt or an organometallic precursor on the support, followed by a calcination or reduction step.[100] However, this method of catalyst preparation, though very common, leads to generation of particles with a wide variation in size, shape and morphology. Since the particle size and morphology strongly affect the ultimate catalytic performance,[101–103] such heterogeneity in the physical status of the final particles is highly undesirable as it creates difficulties for designing catalysts with a specific activity/stability.

A more controlled preparation of NPs with desired size, shape and structures has been made possible with the recent progresses in the field of nanotechnology and colloidal chemistry.[104] In addition to surface-to-volume ratio, the size of NPs also affects the distribution of surface atoms. The fraction of atoms present on the edges and corners is larger in smaller particles.[105] It is also believed that only certain atomic distributions and particle size may favor a desired reaction pathway. Clearly, for many catalytic applications, a synthesis procedure that leads to a monodispersed NP distribution will be desired as it can lead to a more predictable overall catalytic performance. Traditional methods such as impregnation are incapable of providing this level of control over NP size and generate polydispersed catalysts. To maximize the usefulness of nanodimensional materials in catalysis, more reliable synthesis methods are needed that can generate well-defined nanoparticles with a high degree of monodispersity. Colloidal synthesis is a promising alternative and is discussed in the following section.

1.3.1 Colloidal synthesis and chemical reduction of metal salt precursors

Preparation of colloidal metal NPs can be classified into two general methods: [106]

- "top-down methods" in which bulk metals are divided using physical methods

- "bottom-up methods" which start from atoms and grow particles by utilizing solution-phase colloidal chemistry[106]

The top-down methods can produce a large quantity of nanocrystals. However, it is difficult to achieve uniform NPs using top-down methods. In contrast, the colloidal chemical synthesis methods offer more control on NP uniformness and size distribution.[106] The colloidal chemical synthesis methods can be divided into three main categories: chemical reduction of metal salt precursors, electrochemical synthesis, and controlled decomposition of organometallic compounds and metal-surfactant complexes.[106] The chemical reduction of metal salt precursors is the main preparation method used in this thesis and is introduced in the following.

In the chemical reduction of metal salt precursors, the metal precursor salt is reduced using a reducing agent in the presence of a stabilizing agent (Equation 1.1).

$$x\,\mathrm{M}^{n+} + nxe^{-} + \text{stabilizer} \rightarrow \mathrm{M}^{0}n(cluster) \qquad 1.1$$

Various reducing agents such as sodium, hydrogen, alcohols, hydrazine and boronhydrides, and stabilizing agents (eg. ligands, polymers or surfactants) have been used in NP synthesis. The role of the stabilizing agents is to prevent agglomeration. First reports on this approach date back to 1857, in which Faraday prepared a colloidal gold NPs by reduction of $HAuCl_4$ with phosphorus.[107] Turkevich and co-workers[108] were the first to report a reproducible synthesis, by preparing stable uniform gold NPs (13-nm) by using sodium citrate as both reductant and stabilizer. This method, often also referred to as wet chemical reduction, follows the stepwise formation of NPs based on nucleation, growth and agglomeration (proposed by Turkeveich et al.[108]) and has become the most common method for synthesis of NPs. Due to the application of NP stabilizers in this method, it offers the distinctive advantages of better control over NP size and morphology and also higher NP stability.[109] The surface energy of NPs is higher than their lattice energy thus NPs thermodynamically unstable. Consequently, they need to be kinetically stabilized and in colloidal methods this is typically achieved using a protective stabilizer. The presence of stabilizing agents in the colloidal solution, is known to prevent the NP agglomeration and growth and generate stable metal particles of specific size and morphology. The stabilization is normally provided by electrostatic forces, steric forces, or a combination of the two (electrosteric protection). The strength and nature of the interaction between the stabilizer and

the NP controls the long-term stability of the NPs. The most common stabilizers include ligands, surfactants, polymers and dendrimers which are discussed here.

1.3.1.1 Organic ligands

Addition of an organic ligand that typically contains a heteroelement bearing an accessible lone pair is one of the most common ways of stabilizing Pd NPs. The heteroatom binds strongly to the surface of the metal and the organic chain of the ligand prevents agglomeration. Pd-stabilization via sulfur-based,[110] phosphorous-based,[107] nitrogen-based [111] and carbon-based[112] ligands has been reported in the literature.

1.3.1.2 Surfactants

Using salts/surfactants is a common NP stabilization route. The presence of surfactant prevents the irreversible NP agglomeration through a combination of electrostatic and steric forces.[113] It is believed that metal NPs strongly adsorb a layer of anions to their surface, which in turn are surrounded by a layer of countercations to retain electroneutrality (Figure 1.10).[114] The concentration of the surfactant plays a key role in obtaining monodisperse NPs.[115] It is possible

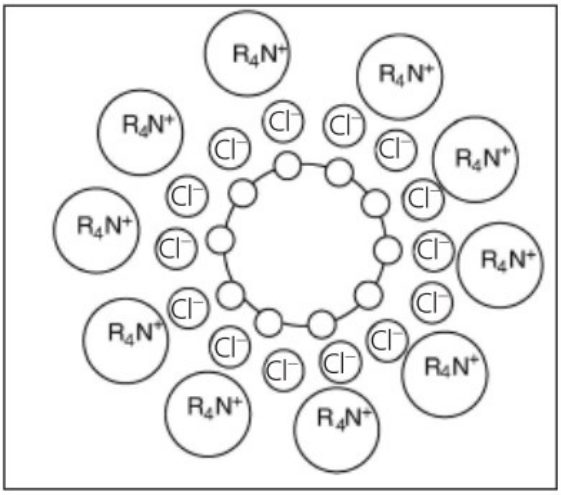

Figure 1.10. Electrosteric stabilisation of a nanoparticle by a surfactant. [114] Reproduced with permission from[114]. Copyright © 2007, American Chemical Society

to prepare surfactant-stabilized NPs dispersed in both organic and aqueous media by changing the cationic component of the surfactant. Tetra- N-alkylammonium halide salts (such as cetyltrimethylammonium bromide (CTAB)) are commonly used for this purpose while other similar materials (such as imidazolium-based ionic liquids)[116–118] have also been used.

1.3.1.3 Steric Stabilization

Metal NPs can be stabilized by incorporation in an organic matrix (either a polymer or a pre-organized dendritic structure). In this case, NP agglomeration is prevented by the steric bulk of these materials.[119,120] Due to their relatively low cost and solubility in a range of solvents, polymers such as poly(N-vinyl-2-pyrrolidone) (PVP) and poly(vinyl alcohol) (PVA) are widely in NP stabilization. For clusters smaller than 7 nm, PVP molecules act as electron donors that cap on the surface atoms of the metallic clusters via their C=O and C−N functional groups;[121,122] whereas for NPs larger than 25 nm in size, the charge transfer is from metal to side chain (CH_2) of PVP.[123] A common procedure in colloidal synthesis, is to stabilize the NPs using polymers and reduce them (Figure 1.11) using an alcohol usually ethylene glycol.[124,125] (hence this method is also referred to as the "polyol" method). An advantage of using an alcohol as a reducing agent

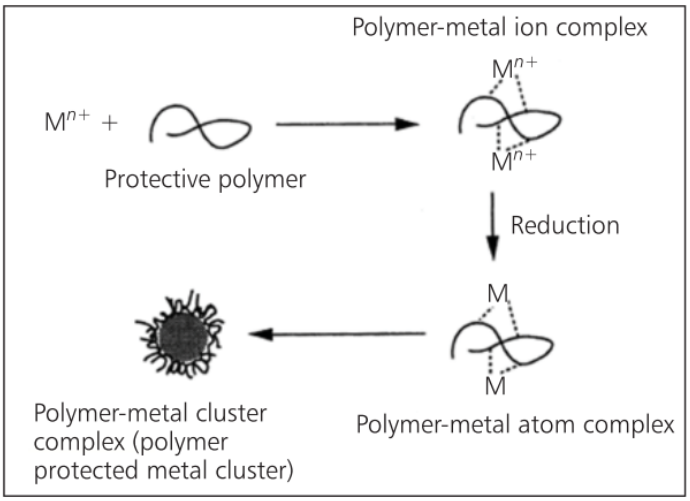

Figure 1.11. Schematic representation of the reduction process of metal salts in the presence of a stabilizing polymer[125]. Reproduced with permission from[125]. Copyright © 1998, Royal Society of Chemistry.

is that the byproducts of reduction are simple organic compounds, unlike the residues of other reducing agents such as borane derivatives[126] (e.g. $NaBH_4$). Additionally, the alcohol acts as both solvent and reducing agent. The type and concentration of the alcohol used strongly affects the NP size. As a general rule, higher boiling point alcohols produce smaller NPs. For example, the Pd NPs reduced using different alcohols were in the order of 1-propanol<ethanol<methanol.[127] However, other factors such as type and concentration of the stabilizer and the concentration of the alcohol also affect the particle size and morphology.

1.3.1.4 Dendrimers

Dendrimers are macromolecules that unlike polymers have a perfectly defined structure on the molecular level. The dendrimer-templating technique was originally developed by Scott et al.[128] Dendrimers have internal cavities that act as molecular boxes and can trap and stabilize metal NPs. Poly(amidoamine) (PAMAM) and poly(propylene imine) (PPI) families are two of the most extensively studied dendrimers.[129,130]

1.3.2 Encapsulation of metal NPs in silica

As discussed in the previous section, colloidal synthesis is a robust technique in preparation of stable NPs. However, metal NPs are generally deposited on a catalyst support (such as metal oxides, zeolites, carbon, etc) to form heterogeneous catalysts. Although it is theoretically possible to design the size and shape of the NPs to enhance the exposure of certain high-energy facets, corners, and edges, in practice, NPs may rapidly grow toward lower-energy shapes leading to a significant loss in activity. This is particularly an issue for demanding reactions (high pressure or high temperatures). As a result, during or after high-temperature reactions, the size, shape and composition of NPs can be different from the initial design of the catalyst. Many catalytic processes, including CH_4 combustion are performed at high temperatures. Although colloidal synthesis can provide stable monodisperse solutions of metal NPs, it is obvious that the stabilization effects provided by the surfactant/polymer (in the solution form) will be lost after deposition (which requires drying and is generally followed by high temperature calcination). Thus, even though colloidal synthesis provides a remarkable control in NP synthesis and leads to monodisperse NPs of desired size and morphology, after deposition,

metal NPs sitting on the support surface are still prone to agglomeration and sintering. Also, the sintering issue is more emphasized at high metal loading catalysts in which a larger number of particles exist per unit area. Most industrial applications require or prefer high metal loading catalysts, as a high loading catalyst will translate into a smaller reactor volume. This applies especially to catalytic converters of NGVs which are limited in terms of maximum allowable size.

Hence challenges still remain, in enhancing the NP stability during catalytic reactions and ensuring that the active NPs maintain their chemical and structural stability during exposure to high temperatures or severe reaction conditions. Preventing NP sintering during the reaction is critical to the production of stable catalysts. As a solution to NP sintering, in the past two decades, encapsulation of metal NPs in an oxide shell has attracted considerable attention. The resulting core–shell structure (core@shell) which is composed of metal NPs in the core in an oxide shell, has important implications in catalysis.[131,132] In these structures, the outer shell immobilizes the catalytically active NP and, by functioning as a physical barrier, prevents the sintering of the core NPs during exposure to high temperatures. Since the metal NPs and the oxide shells can be prepared separately and in independent synthesis conditions, it is possible to design and adjust the core and the shell properties independently. The independent adjustability and functionality of the core and the shell makes core@shell structures a versatile system with great potential for applications in catalysis, drug delivery, biosensors, etc.

In the field of catalysis, metal NPs (such as Pd, Pt, Au, Zr, Ti, Fe and Ni) of various diameters and morphologies, have been successfully encapsulated in oxide shells (e.g. SiO_2, TiO_2 and CeO_2) of different size, structure and porosity. Several thermally stable core@shell catalysts have been successfully prepared and the high thermal stability of oxide-encapsulated metal NPs (often denoted as metal@Oxide) has been established.[132] Among the shell materials SiO_2 is one of the most straight-forward ones to synthesize and M@SiO_2 structures have been extensively studied. Encapsulation of NPs in silica is generally based on a Stöber [133] reaction. Stöber reaction is a sol-gel process (developed in 1968) in which silica particles of uniform size are generated by means of hydrolysis (Equation 1.2) of alkyl silicates and subsequent condensation (Equation 1.3) of silicic acid in an alcoholic solution. Ammonia is usually used as a morphological catalyst.[133] In a typical synthesis, a silica precursor, often tetraethyl orthosilicate

($Si(OEt)_4$, TEOS) is hydrolyzed in an alcohol (typically methanol or ethanol) in the presence of ammonia as a catalyst.[133,134]

$$Si(OC_2H_5)_4 + 4H_2O \xrightarrow{NH_3} Si(OH)_4 + 4C_2H_5OH \quad 1.2$$

The reaction between the silica precursor and water produces ethanol and a mixture of ethoxysilanols (such as $Si(OEt)_3OH$, $Si(OEt)_2(OH)_2$, and even $Si(OH)_4$) which then condense with either the silica precursor (TEOS) or another silanol with loss of alcohol or water [134]

$$Si(OH)_4 \xrightarrow{NH_3} SiO_2 + 2H_2O \quad 1.3$$

Further hydrolysis of the exthoxy (CH_3CH_2O-) groups and condensation reactions result in a cross-linking and form the SiO_2 network. The Stöber reaction is a one-step process and the hydrolysis and condensation reactions occur in one reactor.[133] Monodisperse colloidal silica spheres 10 to 500 nm can be prepared using this method. [133,134] Since early 2000s, there has been an increasing interest in coating colloidal particles with silica and a variety of coating procedures were developed. In one of the fundamental works, in 1996, Liz-Marzan et al.[135] used a two-step synthesis method to coat citrate stabilized gold particles with SiO_2. In this approach, first a silane coupling agent was added as a primer to gold NPs to form a thin layer of SiO_2. The particles were then transferred into an alcohol for further growth using Stöber method. This method was especially useful for particles that could not be directly coated by a Stöber-based technique. In 2003, Graf et al.[136] developed a general method of coating metal NPs with SiO_2 using the amphiphilic polymer poly(vinylpyrrolidone) PVP. This work introduced a general one-step encapsulation scheme and showed that by adsorbing PVP on the colloidal surface, metal NPs could be directly coated with SiO_2. Since its introduction this procedure has been used to encapsulate numerous colloidal systems and has become a standard method of NP encapsulation. In the past decade synthesis of SiO_2 encapsulated metals ($M@SiO_2$) prepared based on the method developed by Graf et al. [136] and involving various ligands, surfactants and polymers have been reported. A general three-step procedure is common the literature: 1) Colloidal synthesis of metal NPs usually using colloidal reduction in an aqueous/organic medium, 2) formation of SiO_2 shells around the metal NPs using Graf et al.'s [136] sol-gel method, and 3) removal of the organics or templates by calcination leading to final $M@SiO_2$.

Li et al.[137] coated PVP-stabilized Pd NPs and prepared Pd@SiO_2 catalysts with a Brunauer–Emmett–Teller (BET) surface area of 104 m^2g^{-1}. Using tetradecyltrimethylammonum bromide (TTAB) as a capping agent, Joo et al.[132] synthesized Pt@SiO_2 particles with high thermal stability and evaluated them in ethylene hydrogenation and CO oxidation. Krier et al.[138] reported the 1,3-butadiene hydrogenation on 4 nm Pt@SiO_2, Pd@SiO_2, and Rh@SiO_2 Core-Shell Catalysts. Thermal stability of the Pd@SiO_2 structures synthesized by Hu et al.[139] is demonstrated in Figure 1.12. As the TEM images in Figure 1.12 show, it is clear that the physical barrier due to the presence of the shell has effectively prevented sintering of the Pd NPs.

For most catalytic applications, in addition to parameters such as shell diameter, size distribution, stability of the core, and metal loading, an M@SiO_2 structure would also have to be sufficiently porous to allow for mass transfer of reactants to the metal sites. Even though M@SiO_2 structures are known to be sinter-resistant, the accessibility of the active catalyst sites after encapsulation and the added diffusion limitation are some of the current concerns in designing industrial catalysts.

The existing practices to make "porous" SiO_2 shells can be divided into two groups: template/porogen-based methods [132,137,138,140–146] and etching based-methods.[147,148] The former employ surfactants, polymers or ligands as a molecular template or porogen during the sol-gel

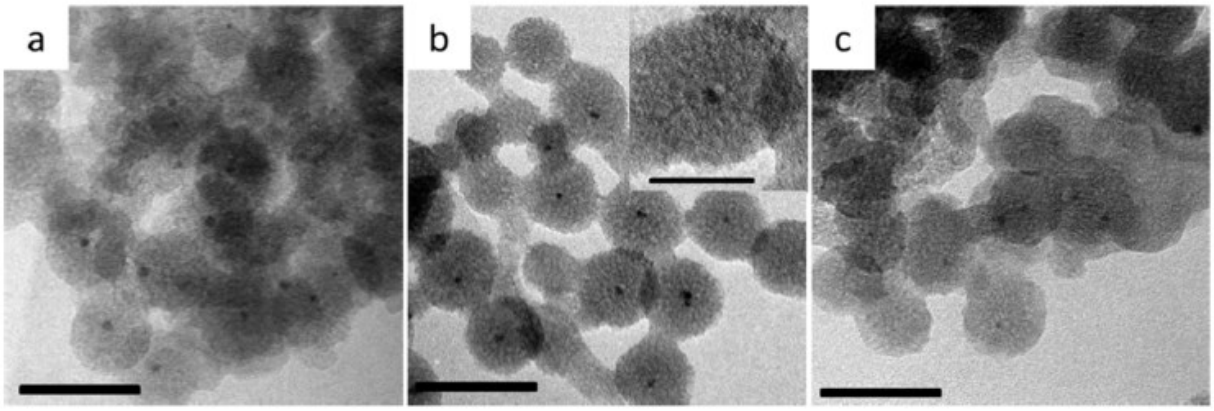

Figure 1.12. TEM images of Pd@SiO_2 a) after 400 °C calcination and 500 °C H_2-reduction; b) after 500 °C calcination and 500 °C H_2-reduction and c) after 600 °C calcination and 500 °C H_2-reduction. Scale bars 50 nm. Reproduced with permission from[139]. Copyright © 2013, American Chemical Society

step which later generates hollow pores inside the oxide during calcination. PVP[137,149,150], hexadecyltrimethylammonium bromide (CTAB),[151–153] Cetyltrimethylammonium chloride (CTAC),[154] mercaptoundecanoic acid (MUA),[155] Igepal CO560,[156] and PS-b-PVP-b-PEO triblock copolymer[157] are some of the commonly used surfactants/polymers for the purpose of NP encapsulation. The etching-based methods apply an additional step of chemical etching to increase porosity.

Although an extensive literature on catalytic application of Metal@SiO_2 structures prepared using various methods have been reported, a detailed study of the effects of the stabilizers/porogens on the ultimate characteristics of the catalysts seems to be lacking. Additionally, to the best of our knowledge the presence or absence of additional mass transfer limitations due to encapsulation has not been investigated in the literature.

1.3.2.1 Silica encapsulated catalysts in CH_4 combustion

Pi et al.[158] prepared a series of encapsulated Pd catalysts (Pd@SiO_2, Pd@CeO_2, and Pd@ZrO_2) supported on Si-modified Al_2O_3 (all with a loading of 1 wt.%) and studied their performance in lean methane combustion under dry and wet conditions. To test the catalytic activity, they used 60 mg of catalyst at a weight hourly space velocity (WHSV) of 50000 $mLg^{-1}h^{-1}$ (feed stream composition: CH_4 (1 vol%), O_2 (20 vol%), H_2O (0 or 10 vol%), and N_2 (balance gas)). They observed a combustion activity order of Pd@ZrO_2<Pd@SiO_2 < Pd@CeO_2 under dry conditions (Figure 1.13.a).. However, in the presence of water vapor, Pd@SiO_2 had the highest catalytic activity among the three catalysts (Figure 1.13.b). They also investigated the effect of water vapor on the stability of the Pd@SiO_2/Si-Al_2O_3 using isothermal continuous experiments under dry and wet conditions. As shown in Figure 1.13.c, for a time-on-stream of 12 h, the methane conversion is stable in dry conditions at 400 °C and 500 °C. However, in the presence of 10% water (GHSV=50000 $mLg^{-1}h^{-1}$, feed stream 1% CH_4, 20% O_2, and 10% H_2O, N_2 as balance gas) the conversion decreased from 100% to 85.2% after 5h at 500 °C, and even more significantly, from 67.5% to 22.1 % over 4h at 400 °C (Figure 1.13.c). The larger loss in the catalytic activity at 400 °C compared to that at 500 °C was associated with the larger inhibitory effect of water vapor at 400 °C.[158] This observation is consistent with the findings of Schwartz and coworkers [27] which suggested that the accumulation of hydroxyl/water on the support was

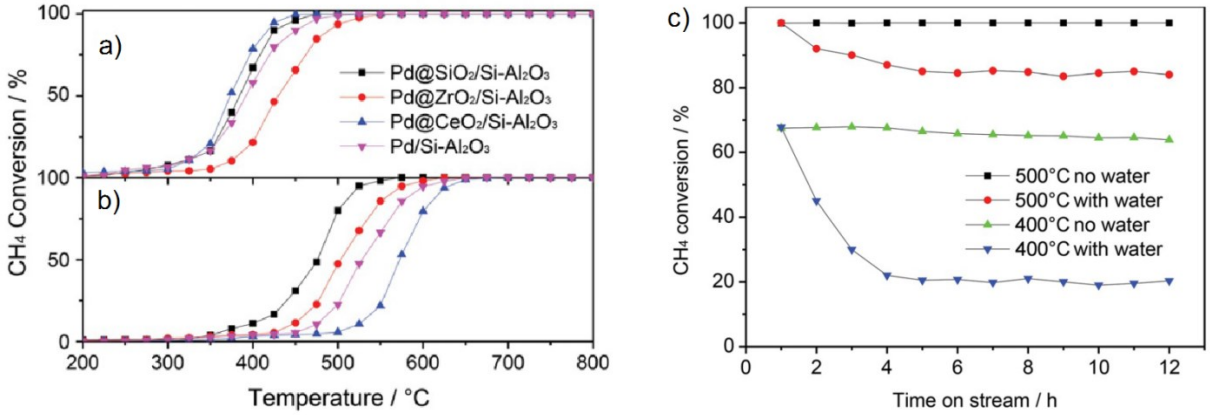

Figure 1.13. a) CH_4 combustion as a function of reaction temperature in the absence of water, b) CH_4 combustion as a function of reaction temperature in the presence of water vapor (10%). c) CH_4 conversion profiles for$Pd@SiO_2/Si\text{-}Al_2O_3$ as a function of time on stream. Reaction conditions for a, b and c: catalyst 60 mg, GHSV= 50000 $mLg^{-1}h^{-1}$, feed stream: 1% CH_4, 20% O_2, and 10%H_2O (if present), N_2 as balance gas.[158] Reproduced with permission from.[158] Copyright © 2016 John Wiley and Sons

significant at temperatures below 450 ^oC.

1.4 Lessons from the literature review

The first learning from the literature is that Pd catalysts are known to have the highest activity for methane combustion under lean conditions. However, due to NP sintering and complications caused by the presence of water, they quickly lose their initial activity. NP sintering is more severe in high metal loading catalysts and, also, is exacerbated in the presence of water. Thus, catalysts designed for a catalytic converter of a lean-burn NGV are required to be

- stable at high temperatures (up to 550 °C)
- active at a low (relative to three-way catalysts) temperatures (300-500 °C)
- high in metal-loading: to comply with the size limitations of the catalytic converters of NGV
- active in the presence of 5-10% water

The second main learning is that, as discussed in this introduction, the sintering of the NPs can be effectively prevented by encapsulating them in an oxide shell such as silica. However, even though M@SiO_2 structures have thermal resistance, the accessibility of the active catalyst sites after encapsulation, the added diffusion limitation, the potential interaction of the shell material with the active phase, and stability of the encapsulated system under reaction conditions are still some of the current concerns in designing M@SiO_2 structures for NGV emission control systems.

Lastly, it is known that addition of Pt as a co-metal and at a ratio of 1:1 improves the thermal stability of Pd. The bimetallic Pd-Pt is also known to have a higher stability in the presence of water; however, Pt's effect on the stability of Pd at temperatures < 450 °C where water inhibition effects are the most pronounced, is more than just to prevent metal sintering. Recent *in situ* EXAFS analyses have proven how the presence of Pt sites adjacent to Pt sites affects the metallic state of the active species in the presence of water and affects the reaction.

Based on these learnings from the literature, to address the current challenges in developing stable catalysts for emission control systems of NGVs, the following catalyst design seems relevant:

A bimetallic Pd-Pt catalyst encapsulated in silica shells (PdPt@SiO_2) which has:

- bimetallic cores of Pd-Pt alloys with a Pd:Pt ratio of 1:1, and a uniform particle size of around 8 nm.
- Silica shells of maximum porosity to allow for the diffusion of reactants
- Highest possible metal loading, thus multiple cores in each shell, without agglomeration of the core NPs

To the best of our knowledge, neither synthesis nor performance evaluation of such a structure in CH_4 combustion has been previously reported.

1.5 Thesis objective

Since NP sintering and inhibitory effects of water are the two most important challenges in development of emission control catalysts for NGV applications, the objectives of this thesis were formed as follows:

- To engineer a catalytic structure which is capable of addressing the most important deactivation issues in the field of CH_4 catalytic combustion.
- To realize the designed catalytic structure through a tailored linkage between colloidal synthesis methods (which provide stable core NPs) and Sol-Gel based methods (to create porous shells).
- To synthesize high loading, high porosity monometallic catalyst ($Pd@SiO_2$)
- To study the accessibility of the active sites after encapsulation in silica by using dry CH_4 combustion as a model reaction
- To identify or develop a synthesis route that ensures the availability of the active sites after encapsulation
- To identify the fraction of the surface atoms which may be inevitably inaccessible after encapsulation (due to being blocked at the Metal/SiO_2 interface)
- To synthesize high-loading and high-porosity bimetallic $PdPt@SiO_2$ structures using the learnings from synthesis of the monometallic catalyst ($Pd@SiO_2$),
- To study the performance $PdPt@SiO_2$ catalyst in wet lean methane combustion
- To gain insights on the effect of hydrothermal ageing on the stability of the $PdPt@SiO_2$ catalyst

- To develop a kinetic model to predict the conversion of the aged PdPt@SiO_2 at various CH_4 concentrations, and in the absence/presence of water

1.6 Approach of the thesis

To achieve the objectives of the thesis, a series of synthesis experiments, combustion and HTA experiments, kinetic experiments and nonlinear optimization were performed.

- **Chapter 1** of the thesis (the Introduction) provides a review on motivation, catalytic combustion of CH_4, reaction mechanisms, deactivation of Pd catalysts, bimetallic Pd-Pt catalysts, colloidal synthesis and encapsulation of NPs.
- **Chapter 2** of the thesis provides a detailed review on encapsulation methods, and categorizes them into three main groups. Then, by comparing two mainstream methods of encapsulation and investigating the impact of the presence/absence of a porogen on the final catalytic structure, assesses the availability of the active sites from the viewpoint of shell porosity (i.e., reactant diffusion) and catalytic activity. This chapter uses lean methane combustion as a reaction model, intentionally in dry conditions to avoid the potential complications caused by the presence of water. Chapter 2 discusses that even though PVP has been used as both a stabilizer and a porogen in many studies, relying on PVP alone for encapsulation purposes is not advisable. Also, as a first in literature, this chapter presents an investigation on the fraction of metal surface area which becomes blocked by the shell material (even in the highly porous catalysts).
- **Chapter 3** of this thesis, as a first in literature, introduces a structure composed of PdPt NPs encapsulated in porous silica shells (PdPt@SiO_2) as a promising catalyst for NGV applications. This chapter provides a highly reproducible synthesis formulation for high-loading PdPt@SiO_2 catalysts and evaluates the performance of PdPt@SiO_2 in wet lean methane combustion. The hydrothermal stability of the bimetallic PdPt@SiO_2 is compared to two impregnated catalysts of the same metal loading supported on γ-Al_2O_3 and SiO_2. The effect of HTA on the core NPs and on the silica shells are investigated.
- **Chapter 4** of this thesis presents a kinetic study of lean methane combustion on bimetallic Pd-Pt@SiO_2 (1:1 molar ratio) catalysts at varying CH_4 concentrations,

temperatures and in the absence/presence of added water. The kinetic behavior of the bimetallic catalyst is correlated in dry and wet conditions using an existing rate expression that is first order in methane and negative one order in water. It is shown that the predictions of the model are acceptable only under dry conditions. To improve the predictions in wet conditions, an alternative model is suggested based on the previous experimental observations in the literature. The corresponding rate expression successfully predicts the activity of the silica encapsulated Pd-Pt catalyst in the presence of water in the temperature range of 550 to 750 K. In addition, for the first time in the literature, the diffusion equation across a porous silica shell is solved and the role of internal mass transfer limitations across metal@SiO_2 systems is elucidated.

- **Chapter 5** of the thesis presents the conclusions of this study along with its fundamental contributions to science and recommendations for future work.
- The appendices include:
  - Appendix A provides the Supplementary information for Chapter 2.
  - Appendix B presents the Supplementary information for Chapter 4.
  - Appendix C provides supporting calculations regarding internal/external heat and mass transfer limitations, and TOF
  - Appendix D provides the calculations of the PGM loading of a catalytic converter washcoated with PdPt@SiO_2
  - Appendix E presents the MATLAB codes related to the kinetic modeling

1.7 References

1. U.S. Government. The World Factbook, Central Intelligence Agency. https://www.cia.gov/library/publications/the-world-factbook/geos/xx.html, 2017, (last accessed December 2017).

2. US Department of Energy. Energy Efficiency and Renewable Enrgy, Publications. https://www.afdc.energy.gov/uploads/publication/alternative_fuel_price_report_jan_2018.pdf. 2018, (last accessed May 2018)

3. E. Genchi, G. and Pipitone, *SAE Int. J. Fuels Lubr.*, 2014, **7**, 1041–1049.

4. M. L. Poulton, *Fuel Efficient Car Technology*, Computational Mechanics Publications, Southampton, UK., 1997.

5. B. Liu, R. E. Hayes, M. D. Checkel, M. Zheng and E. Mirosh, *Chem. Eng. Sci.*, 2001, **56**, 2641–2658.

6. Center for Transportation Research Energy Systems Division, Argonne National Laboratory available at https://www.afdc.energy.gov/pdfs/anl_esd_10-4.pdf, 2010, (last accessed May 2018)

7. US Department of Energy, Energy Efficiency and Renewable Energy, Alternative Fuels Data Center, Fuels and Vehicles, Natural Gas, Natural Gas Vehicle Emissions, https://www.afdc.energy.gov/vehicles/natural_gas_emissions.html., 2018, (last accessed May 2018)

8. US Department of Energy, Energy Efficiency and Renewable Energy, Alternative Fuels Data Center, Fuels and Vehicles, Natural Gas, Natural Gas Benefits and Considerations, https://www.afdc.energy.gov/fuels/natural_gas_benefits.html., 2018, (last accessed May 2018)

9. Natural Gas Vehicle Knowledge Base. http://www.iangv.org/, NGV Global. 2018, (last accessed May 2018)

10. United States Environmental Protection Agency, Understanding Global Warming Potentials. https://www.epa.gov/ghgemissions/understanding-global-warming-potentials, 2017, (last accessed December 2017).

11. The International Council on Clean Transportation, Publications, White Paper. Assessment of Heavy-Duty Natural Gas Vehicle Emissions: Implications and Policy Recommendations, https://www.theicct.org/sites/default/files/publications/ICCT_NG-HDV-emissions-assessmnt_20150730.pdf, 2015, (last accsessed May 2010)

12. R. J. Farrauto, *Science*, 2012, **337**, 659–660.

13. U.S. Environmental Protection Agency, Summary of the Clean Air Act, 42 U.S.C. 7401 et seq. (1970). https://www.epa.gov/laws-regulations/summary-clean-air-act, 2017, (last accessed December 2017).

14. U. S. Environmental Protection Agency, New Source Performance Standards and Permitting Requirements, Final Rules. https://www.epa.gov/controlling-air-pollution-oil-and-natural-gas-industry/new-source-performance-standards-and, 2017, (last accessed December 2017).

15. The International Council on Clean Transportation, Publications, Briefing, A technical summary of Euro 6/VI vehicle emission standards, https://www.theicct.org/sites/default/files/publications/ICCT_Euro6-VI_briefing_jun2016.pdf., 2016, (last accsessed May 2010)

16. Dieselnet Emissions Standards, United States: Cars and Light-Duty Trucks: Tier 3 Introduction, https://www.dieselnet.com/standards/us/ld_t3.php#ftp., 2018, (last accessed May 2018)

17. Dieselnet Emissions Standards, United States: Heavy-Duty Onroad Engines, https://www.dieselnet.com/standards/us/hd.php., 2018, (last accessed May 2018).

18. S. T. G. Ronald M. Heck, Robert J. Farrauto, *Catalytic Air Pollution Control: Commercial Technology*, John Wiley & Sons, New Jersey, 3rd edn., 2016.

19. R. Lanza, S. G. Jaras and P. Canu, *Appl. Catal. A.*, 2007, **325**, 57–67.

20. L. D. Pfefferle and W. C. Pfefferle, *Catal. Rev. Sci. Eng.*, 1987, **29**, 219–267.

21. D. Ciuparu, M. R. Lyubovsky, E. Altman, L. D. Pfefferle and A. Datye, *Catal. Rev.*, 2002, **44**, 593–649.

22. T. V. Choudhary, S. Banerjee and V. R. Choudhary, *Appl. Catal. A.*, 2002, **234**, 1–23.

23. P. Gélin and M. Primet, *Appl. Catal. B*, 2002, **39**, 1–37.

24. T. Ando, Y. Isobe, D. Sunohara, Y. Daisho and J. Kusaka, *JSAE Rev.*, 2003, **24**, 33–40.

25. R. Burch, P. K. Loader and F. J. Urbano, *Catal. Today*, 1996, **27**, 243–248.

26. R. Burch, F. J. Urbano and P. K. Loader, *Appl. Catal. A.*, 1995, **123**, 173–184.

27. W. R. Schwartz and L. D. Pfefferle, *J. Phys. Chem. C*, 2012, **116**, 8571–8578.

28. D. Ciuparu and L. Pfefferle, *Appl. Catal. A*, 2001, **209**, 415–428.

29. D. Ciuparu, F. Bozon-verduraz and L. Pfefferle, *J. Phys, Chem. B,* 2002, **106**, 3434–3442.

30. W. R. Schwartz, D. Ciuparu and L. D. Pfefferle, *J. Phys. Chem. C*, 2012, **116**, 8587–8593.

31. A. Ersson, H. Kušar, R. Carroni, T. Griffin and S. Järås, *Catal. Today*, 2003, **83**, 265–277.

32. K. Persson, A. Ersson, A. M. Carrera, J. Jayasuriya, R. Fakhrai, T. Fransson and S. Järås, *Catal. Today*, 2005, **100**, 479–483.

33. K. Narui, H. Yata, K. Furuta, A. Nishida, Y. Kohtoku and T. Matsuzaki, *Appl. Catal. A*, 1999, **179**, 165–173.

34. L. S. Escandón, D. Niño, E. Díaz, S. Ordóñez and F. V. Díez, *Catal. Commun.*, 2008, **9**, 2291–2296.

35. H. Arai and M. Machida, *Catal. Today*, 1991, **10**, 81–94.

36. Q. Xu, K. C. Kharas, B. J. Croley and A. K. Datye, *ChemCatChem*, 2011, **3**, 1004–1014.

37. D. Ciuparu, N. Katsikis and L. Pfefferle, *Appl. Catal. A*, 2001, **216**, 209–215.

38. C. F. Cullis, T. G. Nevell and D. L. Trimm, *J. Chem. Soc., Faraday Trans.*, 1972, **68**, 1406–1412.

39. R. Burch, *Catal. Today*, 1997, **35**, 27–36.

40. C. A. Muller, M. Maciejewski, R. A. Koeppel, R. Tschan and A. Baiker, *J. Phys Chem,* 1996, **100**, 20006–20014.

41. P. Mars and D. W. van Krevelen, *Chem. Eng. Sci.*, 1954, **3**, 41–59.

42. K.-I. Fujimoto, F. H. Ribeiro, M. Avalos-Borja and E. Iglesia, *J. Catal.*, 1998, **179**, 431–442.

43. G. Centi, *J. Mol. Catal. A.*, 2001, **173**, 287–312.

44. J. N. Carstens, S. C. Su and A. T. Bell, *J. Catal.*, 1998, **176**, 136–142.

45. R. Burch, D. J. Crittle and M. J. Hayes, *Catal. Today.*, 1999, **47**, 229–234.

46. D. Ciuparu and L. Pfefferle, *Catal. Today.*, 2002, **77**, 167–179.

47. Y. C. Chin and E. Iglesia, *J. Phys. Chem. C,* 2011, **115**, 17845–17855.

48. Y. H. Chin, C. Buda, M. Neurock and E. Iglesia, *J. Am. Chem. Soc.*, 2013, **135**, 15425–15442.

49. G. Zhu, J. Han, D. Y. Zemlyanov and F. H. Ribeiro, *J. Am. Chem. Soc.*, 2004, **126**, 9896–9897.

50. N. M. Martin, M. Van Den Bossche, A. Hellman, H. Grönbeck, C. Hakanoglu, J. Gustafson, S. Blomberg, N. Johansson, Z. Liu, S. Axnanda, J. F. Weaver and E. Lundgren, *ACS Catal.*, 2014, **4**, 3330–3334.

51. Y. H. C. Chin, M. García-Diéguez and E. Iglesia, *J. Phys. Chem. C*, 2016, **120**, 1446–1460.

52. A. Yamaguchi and E. Iglesia, *J. Catal.*, 2010, **274**, 52–63.

53. T. R. Baldwin and R. Burch, *Appl. Catal.*, 1990, **66**, 337–358.

54. C. F. Cullis and B. M. Willatt, *J. Catal.*, 1983, **83**, 267–285.

55. R. E. Hayes, S. T. Kolaczkowski, P. K. C. Li and S. Awdry, *Chem. Eng. Sci.*, 2001, **56**, 4815–4835.

56. G. Groppi, *Catal. Today*, 2003, **77**, 335–346.

57. S. Seimanides and M. Stoukides, *J. Catal.*, 1986, **98**, 540–549.

58. P. Hurtado, S. Ordóñez, H. Sastre and F. V. Diez, *Appl. Catal. B,* 2004, **51**, 229–238.

59. C. Descorme and D. Duprez, *Appl. Catal. A.*, 2000, **202**, 231–241.

60. D. Ciuparu, R. Altman and L. Pfefferle, *J. Catal.*, 2001, **203**, 64–74.

61. P. Araya, S. Guerrero, J. Robertson and F. J. Gracia, *Appl. Catal. A*, 2005, **283**, 225–233.

62. A. Gannouni, B. Albela, M. .Said Zina and L. Bonneviot, *Appl. Catal. A*, 2013, **464–465**, 116–127.

63. G. Zhu, K. I. Fujimoto, D. Y. Zemlyanov, A. K. Datye and F. H. Ribeiro, *J. Catal.*, 2004, **225**, 170–178.

64. H. Yoshida, T. Nakajima, Y. Yazawa and T. Hattori, *Appl. Catal. B*, 2007, **71**, 70–79.

65. J. J. Willis, A. Gallo, D. Sokaras, H. Aljama, S. H. Nowak, E. D. Goodman, L. Wu, C. J. Tassone, T. F. Jaramillo, F. Abild-pedersen and M. Cargnello, *ACS Catal.,* 2017, **7**, 7810–7821.

66. G. A. Somorjai and J. Carrazza, *Ind. Eng. Chem. Fundam.*, 1986, **25**, 63–69.

67. R.F. Hicks, H. Qi, M. L. Young and R. G. Lee, *J. Catal.*, 1990, **122**, 295–306.

68. R. F. Hicks, H. H. Qi, M. L. Young and R. G. Lee, *J. Catal.*, 1990, **122**, 280–294.

69. M. Lyubovsky, L. Pfefferle, A. Datye, J. Bravo and T. Nelson, *J. Catal.*, 1999, **187**, 275–284.

70. F.H. Ribeiro, M. Chow and R. A. Dallabetta, *J. Catal.*, 1994, **146**, 537–544.

71. D. Roth, P. Gélin, A. Kaddouri, E. Garbowski, M. Primet and E. Tena, *Catal. Today*, 2006, **112**, 134–138.

72. P. Castellazzi, G. Groppi, P. Forzatti, A. Baylet, P. Marécot and D. Duprez, *Catal. Today.*, 2010, **155**, 18–26.

73. K. Persson, L. D. Pfefferle, W. Schwartz, A. Ersson and S. G. Järås, *Appl. Catal. B*, 2007, **74**, 242–250.

74. R. Gholami, M. Alyani and K. Smith, *Catalysts*, 2015, **5**, 561–594.

75. D. Gao, S. Wang, C. Zhang, Z. Yuan and S. Wang, *Chin. J. Catal.*, 2008, **29**, 1221–1225.

76. D. Roth, P. Gélin, M. Primet and E. Tena, *Appl. Catal. A.,* 2000, **203**, 37–45.

77. R. Kikuchi, S. Maeda, K. Sasaki, S. Wennerström and K. Eguchi, *Appl. Catal. A*, 2002, **232**, 23–28.

78. H. Nassiri, K.-E. Lee, Y. Hu, R. E. Hayes, R. W. J. Scott and N. Semagina, *J. Catal.*, 2017, **352**, 649–656.

79. H. Nassiri, K. E. Lee, Y. Hu, R. E. Hayes, R. W. J. Scott and N. Semagina, *ChemPhysChem*, 2017, **18**, 238–244.

80. T. W. Hansen, A. T. DeLaRiva, S. R. Challa and A. K. Datye, *Acc. Chem. Res.*, 2013, **46**, 1720 – 1730.

81. J. J. Barbier and D. Duprez, *Appl. Catal. B*, 1994, **4**, 105–140.

82. Y. Nagai, T. Hirabayashi, K. Dohmae, N. Takagi, T. Minami, H. Shinjoh and S. Matsumoto, *J. Catal.,* 2006, **242**, 103–109.

83. S. Kang, S. Han, S. Nam, I. Nam, B. Cho, C. Kim and S. Oh, *Top. Catal.*, 2013, **56**, 298–305.

84. H. Shinjoh, *Catal. Surv. Asia*, 2009, **13**, 184 – 190.

85. R. Lamber, N. Jaeger and G. Schulz-Ekloff, *J. Catal.*, 1990, **123**, 285–297.

86. A. Cao, R. Lu and G. Veser, *Phys. Chem. Chem. Phys.*, 2010, **12**, 13499–13510.

87. G. Lapisardi, L. Urfels, P.Gelin, M. Primet, A. Kaddouri, E. Garbowski, S. Toppi and E. Tena, *Catal. Today*, 2006, **117**, 564–568.

88. R. Abbasi, L. Wu, S. E. Wanke and R. E. Hayes, *Chem. Eng. Res. Des.*, 2012, **90**, 1930–1942.

89. E. Becker, P. Carlsson, H. Grönbeck and M. Skoglundh, *J. Catal.*, 2007, **252**, 11–17.

90. K. Persson, A. Ersson, S. Colussi, A. Trovarelli and S. G. Jaras, *Appl. Catal. B*, 2006, **66**, 175–185.

91. K. Persson, A. Ersson, K. Jansson, J. L. G. Fierro and S. G. Järås, *J. Catal.*, 2006, **243**, 14–24.

92. W. J. Kuper, M. Blaauw, F. V. Berg and G. H. Graaf, *Catal. Today*, 1999, **47**, 377–389.

93. K. Nomura, K. Noro, Y. Nakamura, Y.Yazawa, H.Yoshida, A. Satsuma and T. Hattori, *Catal. Lett.*, 1998, **53**, 167–169.

94. H. Yamamoto and H. Uchida, *Catal. Today*, 1998, **45**, 147–151.

95. K. Persson, A. Ersson, K. Jansson, N. Iverlund and S. Järås, *J. Catal.*, 2005, **231**, 139–150.

96. Y. Ozawa, Y. Tochihara, A. Watanabe, M. Nagai and S. Omi, *Appl. Catal. A*, 2004, **259**, 1–7.

97. C. L. Pieck, C. R. Vera, E. M. Peirotti and J. C. Yori, *Appl. Catal. A*, 2002, **226**, 281–291.

98. H. Nassiri, R. E. Hayes and N. Semagina, *Chem. Eng. Sci.* 2018, **186,** 44-51.

99. E. S. J. Lox and B. H. Engler, *Handbook of Heterogeneous Catalysis*, Volume 4*,* Wiley-VCH, Weinheim, 1997.

100. F. Pinna, 1998, *Catal. Today*, 1998, **41**, 129–137.

101. G. A. Somorjai, H. Frei and J. Y. Park, *J. Am. Chem. Soc.*, 2009, **131**, 16589 – 16605.

102. F. Zaera, *J. Phys. Chem. Lett.*, 2010, **1**, 621 – 627.

103. F. Zaera, *Acc. Chem. Res.*, 2009, **42**, 1152 – 1160.

104. K. S. N. H. Bonnemann, in *Metal Nanoclusters in Catalysis and Materials Science: The Issue of Size Control*, ed. N. T. B. Corain, G. Schmid, Elsevier B.V., Amsterdam, 2008,

105. R. van Hardeveld and F. Hartog, *Surf. Sci.*, 1969, **15**, 189–230.

106. C.-J. Jia and F. Schüth, *Phys. Chem. Chem. Phys.*, 2011, **13**, 2457-2487

107. M. Faraday, *Phil. Trans. Roy. Soc.*, 1857, **147**, 145-181.

108. J. Turkevich, P. C. Stevenson and and J. Hillier, *Discuss. Faraday Soc.,* 1951, **11**, 55–75.

109. N. Semagina and L. Kiwi Minsker, *Catal. Rev.*, 2009, **51**, 147–217.

110. S. S.-Y. Lee, M. Yamada and M. Miyake, *Sci. Technol. Adv. Mater.*, 2005, **6**, 420-426.

111. V. Mazumder and S. Sun, *J. Am. Chem. Soc.*, 2009, **131**, 4588-4589.

112. W. Chen, J. R. Davies, D. Ghosh, M. C. Tong, J. P. K. And and S. Chen, *Chem. Mater.*, 2005, **18**, 5253-5259.

113. H. Ishizuka, T. Tano, K. Torigoe, K. Esumi and K. Meguro, *Colloids Surf.*, 1992, **63**, 337-340.

114. D. Astruc, *Inorg. Chem.*, 2007, **46**, 1884-1894.

115. E. Coronado, A. Ribera, J. García-Martínez, N. Linares, L. M. Liz-Marzan, *J. Mater. Chem.,* 2008, **18**, 5682-5688

116. P. Migowski and J. Dupont, *Chem. Eur. J*, 2007, **13**, 32-39.

117. R. Venkatesan, M. H. G. Prechtl, J. D. Scholten, R. P. Pezzi, G. Machado and J. Dupont, *J. Mater. Chem.,* 2011, **21**, 3030-3036.

118. A. S. Pensado and A. A. H. Pádua, *Angew. Chem. Int. Ed.*, 2011, **50**, 8683-8687

119. J. S. Bradley and V. G. ed. G. Schmid, *'The Chemistry of Transition Metal Colloids', in: 'Clusters and Colloids: From Theory to Applications'*, Wiley-VCH Verlag GmbH, Weinheim, 1994.

120. B. Corain, K. Jerabek, P. Centomo and P. Canton, *Angew. Chem. Int. Ed.,* 2004, **43**, 959-962

121. J. Xian, Q. Hua, Z. Jiang, Y. Ma and W. Huang, *Langmuir*, 2012, **28**, 6736–6741.

122. Y. Borodko, S. M. Humphrey, T. D. Tilley, H. Frei and G. A. Somorjai, *J. Phys. Chem. C*, 2007, **111**, 6288–6295.

123. L. Qiu, F. Liu, L. Zhao, W. Yang and J. Yao, *Langmuir*, 2006, **22**, 4480–4482.

124. H. Bönnemann and R. M. Richards, *Eur. J. Inorg. Chem.,* 2001, **2001**, 2455-2480

125. N. Toshima and T. Yonezawa, *New J. Chem*., 1998, **22**, 1179-1201

126. B. Thiébaut, *Platin. Met. Rev.,* 2004, **48**, 62-63

127. T. Teranishi and M. Miyake, *Chem. Mater.*, 1998, **10**, 594–600.

128. R.W.J. Scott, O. M. Wilson and R. M. Crooks, *J. Phys. Chem. B.*, 2005, **109**, 692–704.

129. L. Balogh and D. A. Tomalia, *J. Am. Chem. Soc.,* 1998, **120**, 7355-7356.

130. L. K. Yeung and R. M. Crooks, *Nano Lett.*, 2001, **1**, 14-17.

131. G. A. Somorjai and R. M. Rioux, *Catal. Today*, 2005, **100**, 201–215.

132. S. H. Joo, J. Y. Park, C.-K. Tsung, Y. Yamada, P. Yang and G. A. Somorjai, *Nat Mater*, 2009, **8**, 126–131.

133. W. Stöber, A. Fink and E. Bohn, *J. Colloid Interface Sci.*, 1968, **26**, 62–69.

134. A. Van Blaaderen, J. Van Geest and A. Vrij, *J. Colloid Interface Sci.*, 1992, **154**, 481–501.

135. L. M. Liz-Marzan, M. Giersig and P. Mulvaney, *Langmuir*, 1996, **12**, 4329–4335.

136. C. Graf, D. L. J. Vossen, A. Imhouf and A. van Blaaderen, *Langmuir*, 2003, **19**, 6693–6700.

137. K. T. Li, M. H. Hsu and I. Wang, *Catal. Commun*., 2008, **9**, 2257–2260.

138. J. M. Krier, W. D. Michalak, X. Cai, L. Carl, K. Komvopoulos and G. A. Somorjai, *Nano Lett.*, 2015, **15**, 39–44.

139. Y. Hu, K. Tao, C. Wu, C. Zhou, H. Yin and S. Zhou, *J. Phys. Chem. C,* 2013, **117**, 8974–8982.

140. D.-S. Bae, K.-S. Han and J. H. Adair, *J. Mater. Chem.*, 2002, **12**, 3117–3120.

141. J. C. Park, J. U. Bang, J. Lee, C. H. Ko and H. Song, *J. Mater. Chem.*, 2010, **20**, 1239–1246.

142. K. An, Q. Zhang, S. Alayoglu, N. Musselwhite, J. Y. Shin, and G. A. Somorjai, *Nano Lett.,* 2014, **14**, 4907–4912.

143. S. B. Yoon, J. Y. Kim, J. H. Kim, Y. J. Park, K. R. Yoon, S. K. Park and J. S. Yu, *J. Mater. Chem.*, 2007, **17**, 1758-1761.

144. M. Seo, S. Kim, D. Lee, H. Eun and K. Lee, *Appl. Catal., A*, 2016, **511**, 87–94.

145. S. Kim, D. W. Lee, K. Y. Lee, and E. A. Cho, *Catal. Lett.,* 2014, **144**, 905–911.

146. S. Soulé, J. Allouche, J.-C. Dupin and H. Martinez, *Microporous Mesoporous Mater.,* 2013, **171**, 72–77.

147. I. Lee, Q. Zhang, J. Ge, Y. Yin and F. Zaera, *Nano Res.*, 2011, **4**, 115–123.

148. Q. Zhang, I. Lee, J. Ge, F. Zaera and Y. Yin, *Adv. Funct. Mater.*, 2010, **20**, 2201–2214.

149. H. Yang, Y. Chong, X. Li, H. Ge, W. Fan and J. Wang, *J. Mater. Chem.,* 2012, **22**, 9069–9076.

150. L. Li, S. He, Y. Song, J. Zhao, W. Ji and C.-T. Au, *J. Catal.,* 2012, **288**, 54–64.

151. L. Wang, J. Shi, Y. Zhu, Q. He, H. Xing, J. Zhou, F. Chen and Y. Chen, *Langmuir*, 2012, **28**, 4920–4925.

152. M. C. Chao, H. P. Lin, C. Y. Mou, B. W. Cheng and C. F. Cheng, *Catal. Today*, 2004, **97**, 81–87.

153. R. I. Nooney, D. Thirunavukkarasu, Y. Chen, R. Josephs and A. E. Ostafin, *Langmuir,* 2003, **19**, 7628–7637.

154. J. Yang, D. Shen, Y. Wei, W. Li, F. Zhang, B. Kong, S. Zhang, W. Teng, J. Fan, W. Zhang, S. Dou and D. Zhao, *Nano Res.,* 2015, **8**, 2503–2514.

155. V. Sudheeshkumar, A. Shivare and R. W. J. Scott, *Catal. Sci. Technol.,* 2017, **7**, 272–280.

156. A. J. Forman, J. N. Park, W. Tang, Y. S. Hu, G. D. Stucky and E. W. McFarland, *ChemCatChem,* 2010**, 2**, 1318–1324.

157. B. P. Bastakoti, Y. Li, N. Miyamoto, N. M. Sanchez-Ballester, H. Abe, J. Ye, P. Srinivasu and Y. Yamauchi, *Chem. Commun.,* 2014, **50**, 9101–9104.

158. D. Pi, W. Z. Li, Q. Z. Lin, Q. F. Huang, H. Q. Hu and C. Y. Shao, *Energy Technol.,* 2016, **4**, 943–949.

Chapter 2

2 Bringing attention to metal (un)availability in encapsulated catalysts[1]

2.1 Introduction

One of the major challenges in the field of heterogeneous supported metal catalysts is to maintain the chemical and structural stability of active nanoparticles (NPs). As a solution to this instability issue, encapsulation of metal NPs in metal oxides and particularly in silicon dioxide (SiO_2) has attracted considerable attention. Theoretically, a SiO_2 shell can function as a physical barrier against aggregation and protect the metal NP core from sintering at high temperatures. The Stöber reaction,[1] which involves amine-catalyzed hydrolysis and condensation of a silicon alkoxide, is the basis of most SiO_2 encapsulation methods. In the past decade, SiO_2 encapsulated metals ($M@SiO_2$) prepared using various synthesis schemes involving ligands, surfactants and polymers have been reported. In one of the earliest works, in 1996 Liz-Marzan et al. coated citrate stabilized gold particles with SiO_2 using a two-step synthesis method.[2] First, a silane coupling agent was added as a primer to gold NPs where it formed a thin layer of SiO_2. The particles were then transferred into an alcoholic solution for further growth using the Stöber method. This method was especially useful for particles that could not be directly coated by a

[1] Chapter 2 of this thesis has been published as: A. H. Habibi, R. E. Hayes, and N. Semagina, "Bringing attention to metal (un)availability in encapsulated catalysts", *Catalysis Science and Technology*, 2018, **8**, 798-805. The reaction setup for methane combustion was originally designed and built by Dr. Long Wu and Dr. Robert E. Hayes. Dr. Shihong Xu performed the XPS analysis at Alberta Centre for Surface Engineering and Science (ACSES), University of Alberta. The NAA analyses were performed by Becquerel Laboratories Inc., Maxxam Analytics, Ontario. All syntheses, reactions, analyses and other characterizations were performed by the author. This paper was reprinted with permission from Ref.[73]

Stöber-based technique. As an improvement to this two-step encapsulation method, in 2003 Graf et al. introduced a revolutionary method of coating metal NPs with SiO_2 using the amphiphilic polymer poly(vinylpyrrolidone) (PVP).[3] They showed that by adsorbing PVP onto various colloids, metal NPs could be directly transferred into an ammonia/ethanol mixture where smooth and homogeneous silica coatings could be grown by the addition of a silicon precursor. PVP is already a widely used stabilizer in colloidal synthesis; however, Graf et al. discovered its coupling effect in the direct encapsulation of metal NPs in silica. Since then a general three-step procedure of encapsulating metal NPs in SiO_2 has prevailed: 1) synthesis of metal NPs usually using colloidal reduction in an aqueous/organic medium, 2) formation of SiO_2 shells around the metal NPs using Stöber-based sol–gel chemistry, and 3) removal of the organics or templates by calcination leading to a final M@SiO_2 structure. For most catalytic applications, in addition to having parameters such as a specific shell thickness, a uniform size distribution, stability of the core, and a (preferably high) metal loading, an M@SiO_2 structure would also have to be sufficiently porous to permit satisfactory mass transfer of reactants to the metal sites. In fact, an M@SiO_2 catalyst cannot find any practical application in heterogeneous catalysis unless its core NPs are sufficiently accessible to the reactant molecules. Hence, the porosity of the SiO_2 shells is a key characteristic of these encapsulated materials. In general, the existing practices to make "porous" SiO_2 shells can be divided into two groups: template/porogen- based methods[4–18] and etching based-methods.[19,20] The former employ surfactants, polymers or ligands as a molecular template or porogen during the sol–gel step; the porogen later generates hollow pores inside the oxide during calcination. The latter apply a chemical etching step subsequent to encapsulation.[20] In a further classification, the template-based methods reported in the literature can be divided into three general classes: a) Methods in which the NP-stabilizer (such as PVP) also serves as a pore-inducing agent;[13–15,21–23] b) Methods that use a single surfactant as a stabilizer and porogen leading to high surface area porous structures;[9,17,24,25] c) Methods that use both a NP-stabilizer during colloidal synthesis and a porogen during the Stöber stage.[16] Although numerous catalytic applications of materials prepared using all these three methods have been reported (Table A. 1),[9,10,13,15–17,20–54] it is important to realize the effects of the presence of these stabilizers/porogens on the characteristics of the final catalysts and adjust the existing synthesis procedures for specific applications. For example, for a reproducible encapsulation of NPs after colloidal synthesis, it is critical to separate the NPs from the parent solution (usually containing excess

amounts of alcohol) without sacrificing some metals during separation. The efficiency of this transfer step will highly depend on the nature and concentration of the stabilizing agent used in colloidal synthesis and also on the available separation equipment. Using high concentrations of stabilizer at this step to promote the eventual porosity is not recommended as high stabilizer concentrations will disrupt the separation step by over-stabilizing the NPs in the colloidal solution. Also, the morphology of the oxide shell depends on the polymers and/or surfactants involved in the encapsulation step. Realizing that both the alcohol reduction step and the Stöber step generally employ specific concentrations of these surfactants/polymers, it seems necessary to differentiate between the functions of these agents and how they affect the core and shell morphology of the final catalysts. An overview of the literature (Table A. 1) shows that relying on one single polymer/surfactant as both a stabilizing agent and a porogen (as in methods (a) and (b)) may restrict the properties of the resulting catalyst. Most of the structures prepared using PVP-alone (class (a)) exhibit a relatively small surface area (normally less than 100 $m^2\ g^{-1}$). Surface area calculations based on assuming spherical shells 50 to 200 nm in diameter estimate the external surface area of the silica shell to be as high as 170 $m^2\ g^{-1}$. Hence, a reported surface area of below 200 $m^2\ g^{-1}$ (as in most of class (a) materials) may simply be the external surface area of the silica particles. The structures prepared using class (b) methods may suffer from low dispersion of the core NPs especially at high metal concentrations since the electrostatic repulsion is highly sensitive to the bulk ionic strength and diminishes significantly at high concentrations.[55] While a variety of encapsulated catalysts were reported, a systematic comparison of the catalytic activity of the structures prepared with and without a porogen seems to be lacking. Acknowledging the distinction between the roles of the stabilizing agents and porogens can help one link the existing colloidal synthesis techniques to the Stöber-based methods without losing precious metals during synthesis or compromising on the dispersion (of the core NPs) or porosity (of the oxide shells). Thus, the objective of the current work is to compare two mainstream methods of encapsulation and investigate the impact of the presence/absence of a porogen in addition to a widely used stabilizer (PVP) on the final catalytic structure. By assessing the active site availability from the viewpoint of shell porosity (i.e., reactant diffusion) and catalytic activity, this work answers the following questions:

■ Is it advisable to rely on PVP as both a stabilizer and a porogen to obtain porous structures?

■ Is it enough to create a high porosity silica encapsulated catalyst?

For this purpose, two different synthesis schemes (classes (a) and (c)) with regard to the application of the porogen were investigated. It is shown that even though sinter-resistant encapsulated Pd structures can be readily made using both routes, only one method actually leads to sufficiently porous structures that are active in catalysis. Additionally, introducing the porogen and the stabilizer at different stages of the synthesis enables us to integrate a well-established alcohol reduction method with the Stöber method while inducing a high template-oriented porosity in the oxide shells. Since the variation in shell thickness of the class (a) materials (prepared using PVP-alone) was also reported in the preparation of encapsulated catalysts,[21] we also included this investigation in our work for a complete comparison.

Encapsulated Pd@SiO_2 structures are chosen as a model system, since Pd is a widely employed catalytically active metal which was already reported in some studies[14,48,52,56] and is known for its low sintering resistance. The model test reaction is methane combustion, which requires high temperatures (here, up to 550 °C) and thus benefits from the use of stabilized nanoparticles. CH_4 is a potent greenhouse gas and its emission from gas turbines, coal mines and natural gas vehicles into the atmosphere must be avoided.[57] As will be seen, a proper design of the nanoshell morphology is required for catalysts with high porosity and catalytic activity. We also show that although the nanoparticles are efficiently stabilized, the majority of their outermost atoms are blocked by the encapsulating shell material, even in the highly porous structures.

2.2 Experimental

2.2.1 Materials

Palladium(II) chloride solution ($PdCl_2$, 5% w/v, Acros), poly-(vinylpyrrolidone) (PVP) (MW: 40,000, Sigma–Aldrich), reagent alcohol (ethanol, 95 vol.%, Fisher Scientific), ammonium hydroxide solution (ACS reagent, 28.0-30.0% NH_3 basis, Sigma-Aldrich), tetraethylorthosilicate (TEOS, reagent grade, 98%, Sigma-Aldrich),

cetyltrimethylammonium bromide (CTAB, Sigma) and acetone (99.7%, Fisher Scientific) were used as received. MilliQ water was used throughout the work.

2.2.2 Synthesis of Pd nanoparticles

Pd nanoparticles were prepared by alcohol reduction of PVP-stabilized Pd ions to metallic Pd according to Teranishi et al.[58] with some modifications. At room temperature, 100 μmol $PdCl_2$ and PVP (1 mmol, PVP-to-Pd molar ratio = 10/1) were dissolved in a mixture of 50 mL DI water and 34 mL of ethanol in a 250 mL flask. The mixture temperature was increased from room temperature to the reflux point. The solution was heated and stirred under reflux for 2 h. At the end of the reaction the colour of the solution changed from orange to black indicating that all of the ionic Pd(II) was converted to metallic Pd. After cooling to room temperature, the solution (about 82 mL) was transferred to a 500 mL flask and about 220 mL acetone was added to the mixture. After mixing for 5 minutes the solution was centrifuged at 7500 rpm for 12 minutes. Complete separation of the PVP-stabilized Pd from the solution (water, ethanol, acetone) was achieved in this step. The resulting precipitate (100 μmol of PVP-stabilized Pd nanoparticles) was redispersed in 40 mL of ethanol using ultrasonication for 10 minutes.

2.2.3 Encapsulation of Pd NPs

2.2.3.1 Pd@SiO_2 (no porogen addition).

A Stöber-based method was adapted from earlier works[15,22] and modified to encapsulate Pd nanoparticles from the previous step with SiO_2 shells. The molar ratio of reagents (ethanol:water:ammonia:TEOS) to Pd was adjusted for a high metal loading (5–7%) and uniformness of the final powder. The concentration of TEOS applied in the syntheses was between 120–190 mol m^{-3}; higher or lower concentrations were found to give rise to a metal free SiO_2 layer or an uncoated black metal layer on top, respectively. The reaction time and ammonia concentration were held constant while optimizing the concentration of the SiO_2 precursor (TEOS) for the desired shell thickness. In a typical synthesis, 3.6 mL water and 1 mL of 28% ammonium hydroxide were added to the

solution of Pd NPs (100 μmol Pd in 40 mL ethanol from previous step). The mixture was sonicated for 10 minutes followed by 10 minute magnetic stirring. Depending on the desired shell thickness, a specific amount of TEOS was added (Table 2.1). The solution was stirred at room temperature for 150 minutes. A change in the opacity of the solution at the end of the Stöber process indicated the successful formation of SiO_2 shells. A Stöber reaction yield of 63% was obtained. The Pd@SiO_2 particles were collected and separated from the solution using centrifugation at 7500 rpm for 12 minutes and the supernatant was discarded. The precipitate was washed two times by dispersing in 30 mL of ethanol using sonication for 5 minutes followed by centrifugation at 7500 rpm. Finally, the Pd@SiO_2 particles were dried at 60 °C for 2 h followed by calcination at 550 °C for 16 h.

2.2.3.2 Pd@mSiO_2 (with a porogen addition).

The encapsulation of the Pd@mSiO2 (m: modified) catalysts (Pdm1, Pdm2 and Pdm3) was carried out using a technique employed by ref. [16] and [45] which is similar to the preparation of the Pd@SiO_2 structures with one difference: after addition of ammonia and water to the solution of NPs (100 μmol Pd in 40 mL ethanol), a specific amount of CTAB was also added as a porogen (Table 2.1)

2.2.4 Characterization

PVP-stabilized Pd nanoparticles, Pd@SiO_2, and Pd@mSiO_2 structures were characterized by transmission electron microscopy (TEM) at 200 kV using a JEOL 2100 transmission electron microscope (Cell Imaging Facility, University of Alberta). The mean diameter and standard deviation of nanoparticles were calculated by counting more than 200 particles from TEM images using ImageJ software. The actual loadings of the final catalysts (after calcination) were determined by neutron activation analysis (NAA) at Becquerel Laboratories (Maxxam Company, Ontario). Samples were irradiated for 20 min in the Cd shielded, epithermal site of the reactor core. Palladium was counted for 15 min after 24 h decay using an Aptec CS13-A31C gamma detector. The BET surface area and adsorption isotherms of the catalysts were determined at 77.3 K by volumetric measurements using a surface area

Table 2.1. Characteristics of the encapsulated catalysts

Catalyst series	$Pd@SiO_2$ (no porogen)			$Pd@mSiO_2$ (with porogen)		
Catalyst [a]	Pd1	Pd2	Pd3	Pdm1	Pdm2	Pdm3
PVP/Pd[b] during alcohol reduction	10	10	10	10	10	10
CTAB for Stöber synthesis (mmol)	0	0	0	1.37	2.74	4.12
TEOS for Stöber synthesis (mmol)	5.59	6.71	8.95	5.59	5.59	5.59
TEOS/Pd[b]	56	67	90	56	56	56
TEOS/PVP[b]	5.59	6.71	8.95	56	56	56
TEOS/CTAB[b]	-	-	-	4.08	2.04	1.35
Pd NP size from TEM (nm)[c]	8.0± 1.0	8.0± 1.0	8.0± 1.0	8.0± 1.0	8.0± 1.0	8.0± 1.0
SiO_2 shell diameter (nm)[c]	70-90	80-100	90-120	70-90	70-90	70-90
Pd loading (wt%)[c]	7.07	6.33	4.30	5.48	5.50	5.53
Surface Pd concentration (wt%) from XPS[c]	0.06	0.06	0.05	0.11	0.23	0.24
BET surface area ($m^2\ g^{-1}$ catalyst)[c]	70	62	51	610	695	764
Total pore volume ($mL\ g^{-1}$)[c]	0.195	0.176	0.167	0.347	0.387	0.403

[a] During the Stöber stage 100 μmol of PVP-protected Pd, 40 ml of ethanol, 3.6 mL of water, 1 mL of 28–30% ammonium hydroxide and a constant reaction time of 2.5 h were used in all of the syntheses. [b] Molar ratio. [c] For the calcined catalysts.

analyzer (Quantachrome, Autosorb iQ). Prior to analyses, 30 to 100 mg of sample was degassed for 3 to 4 h at 350 °C under vacuum with a backfill gas of helium to remove any moisture or volatiles within the existing pores of the material. The specific surface area was calculated using the BET method, the pore size distribution was obtained using the desorption branch of the BJH model, and the total pore volumes were obtained from the adsorbed quantity at a relative pressure of 0.990. CO chemisorption analyses were performed by dosing with a 3% CO/He gas mixture at room temperature using an AutoChem 2920HP instrument equipped with a quartz U-tube reactor and a thermal conductivity detector (TCD). Prior to analysis, the calcined catalysts were reduced in a flow of 10% H_2/Ar (25 $mL\ min^{-1}$) at 350 °C for 1 h. Three independent measurements of CO adsorption on pure silica showed that its contribution is in the range of 1–

6% from the quantities adsorbed on Pd, thus, it can be considered negligible. The X-ray photoelectron spectroscopy (XPS) measurements were carried out using an Axis-165 X-ray photoelectron spectrometer (Kratos Analytical). A monochromatic Al Kα source (hν = 1486.6 eV) at a power of 168 W was used. The survey spectra were collected with an analyzer pass-energy of 160 eV and a step of 0.4 eV. The high resolution spectra were obtained at a pass-energy of 20 eV with a step of 0.1 eV. During the data acquisition, charge neutralization was used to compensate sample charging. The binding energies were referenced to C1s (284.8 eV) and the signals were fitted by mixed Lorentzian–Gaussian curves using Casa XPS software.

2.2.5 Methane oxidation reaction

Catalytic oxidation of methane over the developed catalysts was investigated according to the previous study published by Abbasi et al.[59] The calcined catalysts (550 °C, 16 h in air) with a total Pd loading of 1.2 mg were packed into a 20″ long tubular reactor with an inner diameter of 3/8″. Layers of quartz wool were used at both ends of the catalyst bed to hold the catalyst in place. The reactor was then placed inside a furnace equipped with a temperature controller. Two thermocouples were used to measure the temperature at each end of the catalyst bed. Gases (10% CH_4/N_2 and extra dry air) were purchased from Praxair. The flow rates of the feed gases were controlled by mass flow controllers (Matheson and MKS). The feed consisted of a gas mixture of 10 vol% CH_4 in N_2 (8.5 ml min^{-1}, standard temperature and pressure (STP)) and air (extra-dry, 205 mL min^{-1}, STP) for a CH_4 concentration of approximately 4000 ppm in the feed. The corresponding gas hourly space velocities (GHSV) were between 586000– 592000 L STP per h per kg Cat. The GHSVs were calculated using the total feed flow rate (214 mL min^{-1}, STP) and the mass of the catalysts used in the reactor (about 22 mg). Methane oxidation was carried out at a constant pressure of 27 psig (287.5 kPa). Ignition and extinction curves were obtained by increasing the reaction temperature stepwise from 200 to 550 °C (50 °C for each step with a ramping rate of 5 °C min^{-1}). During methane combustion, the temperature at each stage was held constant for 30 min in ignition–extinction tests. Post combustion gas stream from the reactor was analyzed every 15 min using an online Agilent HP-7890-A gas chromatograph equipped with a thermal conductivity detector (TCD) and a flame ionization detector (FID) in series. The absence of heat and mass transfer calculations were conducted similar to Nassiri et

al.[60] Using the methane conversion and kinetic parameters at 360 °C for the reactions with porous Pd@mSiO$_2$ catalysts, the presence of intrinsic kinetic conditions under isothermal reactor operation was confirmed. The Mears criterion for external mass transfer limitation (MTL) was found to be 10−9 (no external MTL existed if the value was below 0.15).[61] The Weisz-Prater criterion for internal MTL was found to be 10^{-6} which confirmed the absence of internal MTL. The absence of an external temperature gradient was confirmed by Mears correlation (10^{-13}, which is below the maximum limit of 0.15 for a negligible gradient).[61] The maximum internal temperature rise was calculated to be 0.05 K, assuming an activation energy of 92 kJ mol^{-1} [62] and a constant heat of combustion of 890 kJ mol^{-1}. Calculations also confirmed that plug flow assumptions with no wall effects or axial dispersion applied.

2.3 Results and discussions

2.3.1 Creating porous capsules

The core–shell structures were designed to have an average Pd core diameter of about 8 nm and an average oxide shell diameter of about 90 nm because Pd NPs are reported to have the highest methane combustion turnover frequencies at a particle size of 8–10 nm[63] and the particle size of the powders used in the catalytic converter washcoats are typically below 100 nm.[64] Pd nanoparticles were synthesized using a polymer-protected alcohol reduction method[58] which is well-known for its excellent control over the particle size. Figure 2.1 depicts TEM images of as-synthesized nanoparticles, as well as encapsulated catalysts prepared with and without the use of a porogen (CTAB) before and after calcination at 550 °C. Once encapsulation in SiO_2 shells was completed, the size or shape of the core Pd NPs was not affected after exposure to high temperature. However, even though no sintering was observed, the core Pd NPs encapsulated in the absence of a porogen appeared to follow a chain-like form inside the shells whereas the NPs encapsulated in the presence of CTAB were encapsulated with greater distance from each other (Figure 2.1) because CTAB can provide additional stabilization of Pd nanoparticles.[65] Preparation of core–shell particles with single metal cores inside each shell is typically reported in the literature.[8,17] However, considering the targeted shell size in this work, multi-core Pd@SiO_2 structures (and thus relatively higher concentrations of Pd NPs in the encapsulation

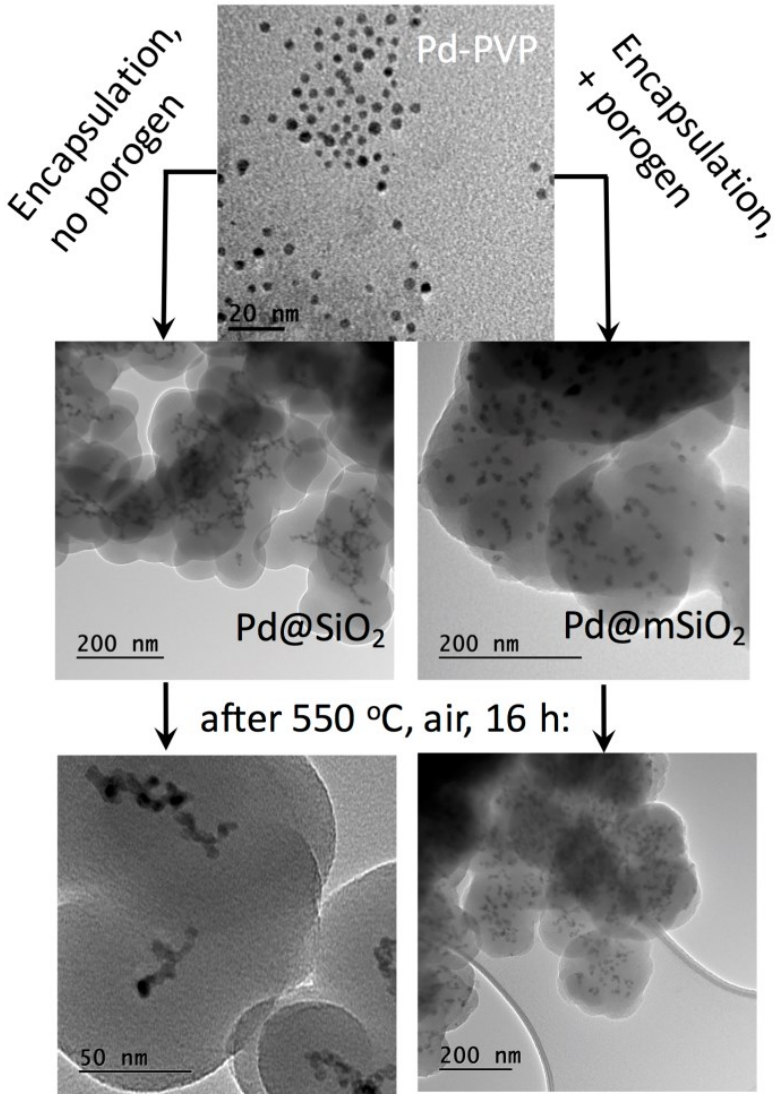

Figure 2.1. TEM images of as-synthesized metal nanoparticles and encapsulated catalysts: Pd1 (right) and Pdm1 (left).

step) were preferred as they would eventually give rise to high metal loadings and smaller reactor (catalytic converter) volumes.

During the Stöber process, the concentration of the silica precursor (TEOS) was adjusted to control the shell thickness and the final metal loading. The TEOS/Pd ratio also had to be adjusted to obtain a uniform powder with no uncoated metallic Pd layer or excess SiO_2 layer in the final catalyst. For the concentrations used in this work, the suitable TEOS/Pd ratio was found to be between 5.6 and 9.0 (molar basis). The average core size and shell diameter of the

catalysts, as measured by TEM, are presented in Table 2.1. As was anticipated, lower TEOS concentrations yielded smaller shell diameters (Pd1 vs. Pd3). Addition of CTAB before encapsulation resulted in the dramatic increase in porosity from ~70 m^2 g^{-1} for Pd@SiO_2 materials to ~700 m^2 g^{-1} for Pd@mSiO_2, as seen from Table 2.1 and Figure 2.2. The latter areas are among the highest reported in the literature (Table A. 1). We found that there is an upper limit of CTAB concentration beyond which the surfactant starts to interfere with the encapsulation step leaving some metal NPs uncoated which will have to be discarded during precipitation. It is known that CTAB can also serve both as a nanoparticle stabilizing agent and the porogen, as shown by Chen et al.[38] for Au@SiO_2 catalysts, but using one single surfactant as the stabilizing agent and the porogen can limit the possible combinations of core@shell size and morphology. Also, the electrostatic repulsion provided by CTAB diminishes at high metal concentrations and results in a lower dispersion of the core NPs. At the metal/TEOS ranges used in this work, the addition of CTAB to a solution of CTAB-protected Pd NPs reduced by sodium borohydride resulted in porous Pd@mSiO_2 structures with agglomerated metal cores. Even though they were porous, this group of catalysts showed an activity of less than 20% and is not presented here. A representative TEM image of this group of catalysts is given in Figure A.1. In the Pd@mSiO_2 series, addition of the stabilizing agent and the porogen at two distinct stages of the synthesis allowed for independent concentrations of PVP and CTAB to be used serving the following two goals: a) stable Pd NPs of the desired size, morphology and concentration were

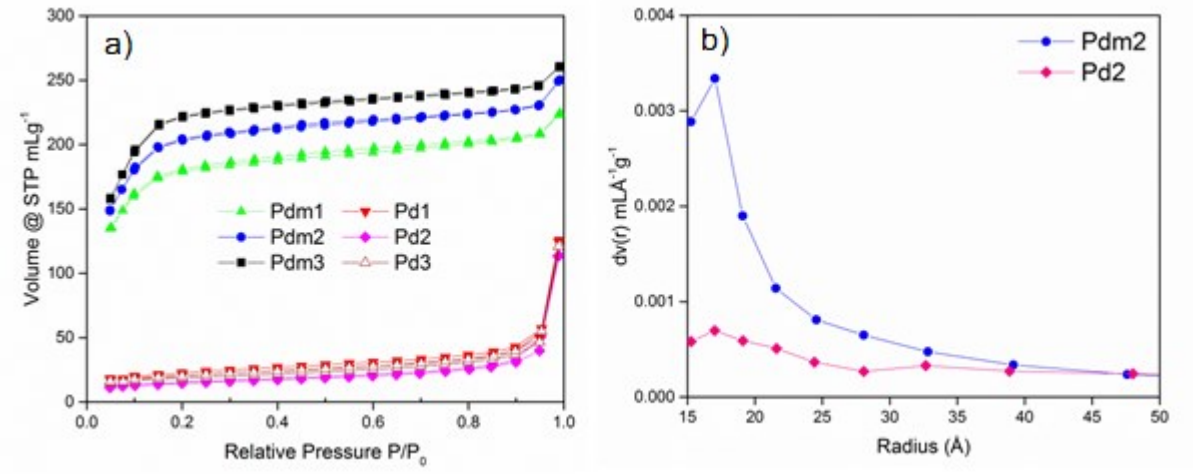

Figure 2.2. a) Nitrogen adsorption isotherms and b) pore size distribution of the calcined catalysts

prepared and separated completely from the alcoholic solution and b) a desired concentration of CTAB could be added independently during the Stöber step for creating maximum porosity. The prepared catalysts had relatively high Pd loadings of 4.3 to 7 wt%, as determined by NAA in the final calcined materials, which are among the highest reported in the literature (see references in Table A.1). High metal loading catalysts are more desirable in industrial applications as they can eventually result in a smaller reactor (or catalytic converter) volume. The Pd concentration in the top 3–10 nm catalyst surface layer, as probed by XPS, is in the range of only 0.05–0.2 wt% (Table 2.1), confirming that practically no Pd is present on the outer surface of the synthesized capsules. The high reproducibility of the syntheses and metal loadings were confirmed by duplicate batches, which was possible due to the optimized TEOS/ metal ratio and reaction time and controlled addition of the stabilizer and the porogen.

2.3.2 The effect of capsule porosity on catalysis

The activity of the encapsulated catalysts was assessed in lean methane combustion at the temperature interval be- tween 200 and 550 °C. The ignition curves (Figure 2.3) show that Pd@SiO_2 (no porogen) catalysts exhibited a limited maximum conversion of 28% at 550 °C regardless of the shell thickness. As evidenced by TEM results (Figure 2.1), the Pd NPs of any of the catalysts tested in combustion had not experienced any sintering during 16 h calcination at 550 °C. So, the low activity of the Pd@SiO_2 series was mainly due to the non-porous nature of the SiO_2 shells (which was also proved by N_2 adsorption). Moreover, even though reducing the TEOS/PVP ratio in the Pd@SiO_2 series reduced the shell thickness, comparison of the adsorption isotherms (Figure 2.2) and activity of the Pd1, Pd2 and Pd3 samples (Figure 2.3) showed that thinner shells would not improve the metal-site accessibility when the oxide shell was intrinsically non-porous. The ignition curves of the Pd@mSiO_2 series show how application of a porogen at the Stöber stage improved the site accessibility and hence the activity. Also, at the concentration ranges applied in this work, an increase in the CTAB concentration increased the surface area of the Pd@mSiO_2 series (Table 2.1); however, the effect on the catalytic activity was insignificant (Figure 2.3). Using CTAB concentrations higher than those reported in Table 2.1 would interfere with the Stöber reaction and lead to losing precious metals during encapsulation without any improvement in the catalyst activity. The ignition curves are similar to

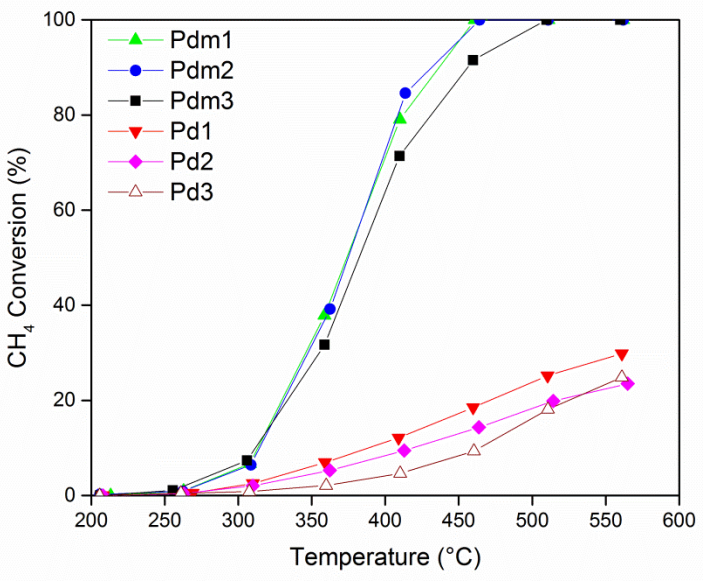

Figure 2.3. Ignition curves in methane combustion. In all the tests, a catalyst amount corresponding to 1.2 mg of Pd was loaded in the reactor.

those reported in the literature for Pd-catalyzed dry lean methane combustion. For example, an earlier study performed under the same reaction conditions and the same Pd loading in the reactor (1.2 mg)[66] for a Pd/Al_2O_3 catalyst prepared by impregnation of alumina with Pd nanoparticles also showed about 50% methane conversion at 350 °C and 95% conversion at 400 °C which are within 10–20% variation from the current work. However, in the previous work, the total mass of catalyst was 22 times higher than the amount of the encapsulated $Pd@mSiO_2$ catalyst used here. This again shows the advantage of the use of high-loading encapsulated catalysts to ensure lower reactor (catalytic converter) volumes. The Pd metal dispersion in the Pdm1 catalyst was found by CO chemisorption to be 5%, which was used to calculate the turnover frequency (TOF) at 310 °C and under differential conditions (Figure 2.3), which is 0.1 s^{-1}. For Pd particle sizes of 8–12 nm, the literature reports values of 0.04–0.08 $^{s-1}$,[62,67] and values as high as 0.26 $^{s-1}$ [68] (the TOF values were recalculated using an activation energy of 85 kJ mol^{-1}).[62] Thus, the accessible Pd active sites behave similarly to the known conventional catalysts.

2.3.3 "Is it enough to create high porosity in the encapsulated catalysts?"– No.

As was shown in the previous section, the Pd@mSiO_2 series catalysts possessed enough porosity to ensure an efficient mass transfer of reactants to active sites. Recalling that the silica shell (even though porous) is built around Pd nanoparticles, it is questionable if the shell's material actually physically blocks Pd atoms on the outermost surface layer of the nanoparticles. In addition, the migration of oxidized silicon in oxidative wet atmospheres is known to occur at temperatures as low as 200 °C.[69] Pd atoms, in turn, can incorporate into the silica support via oxygen vacancies.[70] The existing literature on silica-encapsulated catalysts indicates this possibility. For example, Pi et al.[56] reported 2 nm encapsulated Pd particles, as seen by TEM, but CO chemisorption revealed only 16% metal dispersion vs. 50% expected for this size. We also performed CO chemisorption on the porous Pdm1 catalyst which showed a CO consumption of 28 mmol CO per mol Pd. Assuming a 0.6 CO/surface Pd stoichiometry,[71] the metal dispersion is only 5%. The TEM images (Figure 2.1) show 8 nm particles that should possess a dispersion of 15%.[72] This indicates that the silica shell (or migrated silica species) blocks 2/3 of the Pd surface atoms. Thus, the steric protection of Pd particles from agglomeration comes at a cost of losing some of its active sites, even if a sufficient porous structure in the shell had been created.

2.4 Conclusions

Encapsulation of Pd NPs in SiO_2 shells effectively prevents the high temperature sintering of the metal cores. Adjustments to the known synthesis conditions helped make high loading encapsulated catalysts that were both thermally resistant and sufficiently porous. Application of PVP alone for encapsulation purposes is inadvisable since the resulting structure will be practically a non-porous powder. Addition of the stabilizing polymer and the pore-inducing agent at two different stages of the synthesis allowed for control over the size of the core NPs and creating maximum shell porosity without losing any precious metals during synthesis. When no porogen was applied, forming thinner shells did not improve the catalyst activity because the non-porous nature of the shells would still hinder the mass transfer regardless of the shell thickness. Although both non-porous and porous SiO_2 encapsulated

catalysts resisted high temperature sintering and maintained the original Pd particle size, only the porous catalysts were capable of reaching full methane combustion conversion at temperatures similar to those of impregnated catalysts. However, there is a trade-off between the particle stabilization and blockage of metal core active sites with the shell material (which was found to be as large as 67% of the Pd surface sites), even when a sufficient porosity for reactant mass transfer was achieved. Further fine-tuning of the pore size is recommended for applications with larger diffusing molecules.

Conflicts of interest

There are no conflicts to declare.

Acknowledgements

Financial support from NSERC (Strategic grant STPGP 478979-15) and CFI (Leaders' Opportunity Fund, grant 24766) is appreciated. The porosity analysis, XPS and TEM work were performed at the nanoFAB (University of Alberta).

2.5 References

1. W. Stöber, A. Fink and E. Bohn, *J. Colloid Interface Sci.*, 1968, **26**,62–69.
2. L. M. Liz-marzan, M. Giersig and P. Mulvaney, *Langmuir*, 1996, **12**, 4329–4335.
3. C. Graf, D. L. J. Vossen, A. Imhouf and A. van Blaaderen, *Langmuir*, 2003, **19**, 6693–6700.
4. T. Li, J. Moon, A. A. Morrone, J. J. Mecholsk y, D. R. Talham and J. H. Adair, *Langmuir*, 1999, **15**, 4328–4334.
5. D. S. Bae, K.-S. Han and J. H. Adair, *J. Mater. Chem.,* 2002, **12**, 3117–3120.
6. J. C. Park, J. U. Bang, J. Lee, C. H. Ko and H. Song, *J. Mater. Chem.,* 2010, **20**, 1239–1246.
7. R. K. Sharma, M. Yadav, R. Gaur, Y. Monga and A. Adholeya, *Catal. Sci. Technol.,* 2015, **5**, 2728–2740.
8. J. M. Krier, W. D. Michalak, X. Cai, L. Carl, K. Komvopoulos and G. A. Somorjai, *Nano Lett.,* 2015, **15**, 39–44.
9. S. H. Joo, J. Y. Park, C.-K. Tsung, Y. Yamada, P. Yang and G. A. Somorjai, Nat. Mater., 2009, **8**, 126–131.

10. K. An, Q. Zhang, S. Alayoglu, N. Musselwhite, J. Y. Shin and G. A. Somorjai, *Nano Lett.*, 2014, **14**, 4907–4912.
11. H. Liu, K. Tao, C. Xiong and S. Zhou, *Catal. Sci. Technol*., 2015, **5**, 405–414.
12. S. B. Yoon, J. Y. Kim, J. H. Kim, Y. J. Park, K. R. Yoon, S. K. Park and J. S. Yu, *J. Mater. Chem.*, 2007, **17**, 1758-1761.
13. K. T. Li, M. H. Hsu and I. Wang, *Catal. Commun*., 2008, **9**, 2257–2260.
14. M. Seo, S. Kim, D. Lee, H. Eun and K. Lee, *Appl. Catal., A*, 2016, **511**, 87–94.
15. S. Kim, D. W. Lee, K. Y. Lee and E. A. Cho, *Catal. Lett.*, 2014, **144**, 905–911.
16. S. Soulé, J. Allouche, J.-C. Dupin and H. Martinez, *Microporous Mesoporous Mater.,* 2013, **171**,72–77.
17. Y. Hu, K. Tao, C. Wu, C. Zhou, H. Yin and S. Zhou, *J. Phys. Chem. C,* 2013, **117**, 8974–8982.
18. R. L. Oliveira, T. Nijholt, M. Shakeri, P. E. de Jongh, R. J. M. Klein Gebbink and K. P. de Jongh, *Catal. Sci. Technol*., 2016, **6**, 5124–5133.
19. I. Lee, Q. Zhang, J. Ge, Y. Yin and F. Zaera, *Nano Res*., 2011, **4**, 115–123.
20. Q. Zhang, I. Lee, J. Ge, F. Zaera and Y. Yin, *Adv. Funct. Mater*., 2010, **20**, 2201–2214.
21. L. Li, S. He, Y. Song, J. Zhao, W. Ji and C.-T. Au, *J. Catal.,* 2012, **288**, 54–64.
22. J. G. Oh and H. Kim, *Curr. Appl. Phys.,* 2013, **13**, 130–136.
23. L. F. Zhang, M. Li, T.-Z. Ren, X. Liu and Z.-Y. Yuan, *Int. J. Hydrogen Energy*, 2015, **40**, 2648–2656.
24. C. Zhang, Y. Zhou, Y. Zhang, Z. Zhang, Y. Xu and Q. Wang, *Powder Technol.,* 2015, **284**, 387–395.
25. R. I. Nooney, D. Thirunavukkarasu, Y. Chen, R. Josephs and A. E. Ostafin, *Langmuir,* 2003, **19**, 7628–7637.
26. M. C. Chao, H. P. Lin, C. Y. Mou, B. W. Cheng and C. F. Cheng, *Catal. Today*, 2004, **97**, 81–87.
27. Q. Zhang, T. Zhang, J. Ge and Y. Yin, *Nano Lett*., 2008, **8**, 2867–2871.
28. A. J. Forman, J. N. Park, W. Tang, Y. S. Hu, G. D. Stucky and E. W. McFarland, *ChemCatChem,* 2010**, 2**, 1318–1324.
29. Y. Wang, A. V. Biradar, C. T. Duncan and T. Asefa, J. Mater. Chem., 2010, **20**, 7834–7841.

30. J. C. Park, H. J. Lee, J. Y. Kim, K. H. Park and H. Song, *J. Phys. Chem. C,* 2010, **114**, 6381–6388.

31. Y. Wang, A. V. Biradar and T. Asefa, *ChemSusChem,* 2012, **5**, 132–139.

32. L. Wang, J. Shi, Y. Zhu, Q. He, H. Xing, J. Zhou, F. Chen and Y. Chen, *Langmuir*, 2012, **28**, 4920–4925.

33. H. Yang, Y. Chong, X. Li, H. Ge, W. Fan and J. Wang, *J. Mater. Chem.,* 2012, **22**, 9069–9076.

34. S. He, Z. Fei, L. Li, B. Sun, X. Feng and W. Ji, *Chin. J. Catal.,* 2013, **34**, 2098–2109.

35. C. Xiao, R. V. Maligal-Ganesh, T. Li, Z. Qi, Z. Guo, K. T. Brashler, S. Goes, X. Li, T. W. Goh, R. E. Winans and W. Huang*, ChemSusChem*, 2013, **6**, 1915–1922.

36. L. Tan, X. Wu, D. Chen, H. Liu, X. Meng and F. Tang, *J. Mater. Chem. A,* 2013, **1**, 10382–10388.

37. Y. Y. Xu, J. Ma, Y. Y. Xu, L. L. Xu, L. L. Xu, H. H. Li and H. H. Li, *RSC Adv.,* 2013, **3**, 851–858.

38. J. Chen, R. Zhang, L. Han, B. Tu and D. Zhao, *Nano Res.,* 2013, **6**, 871–879.

39. T. Wu, W. Cai, P. Zhang, X. Song and L. Gao, *RSC Adv*., 2013, **3**, 23976–23979.

40. J. Xu, Y. Deng, X. Zhang, Y. Luo, W. Mao, X. Yang, L. Ouyang, P. Tian and Y. Han, *ACS Catal.,* 2014, **4**, 4106–4115.

41. A. Samanta, B. B. Dhar and R. N. Devi, *New J. Chem.,* 2012, **36**, 2625–2629.

42. B. P. Bastakoti, Y. Li, N. Miyamoto, N. M. Sanchez-Ballester, H. Abe, J. Ye, P. Srinivasu and Y. Yamauchi, *Chem. Commun.,* 2014, **50**, 9101–9104.

43. J. G. Li, C. Y. Tsai and S.-W. Kuo, *RSC Adv*., 2015, **5**, 42798–42807.

44. H. Liu, H. Yu, C. Xiong and S. Zhou, *RSC Adv*., 2015, **5**, 20238–20247.

45. Y. Zhang, S. Xiang, Y. Zhou, Y. Xu, Z. Zhang, X. Sheng, Q. Wang and C. Zhang, *RSC Adv.*, 2015, **5**, 48187–48193.

46. J. Yang, D. Shen, Y. Wei, W. Li, F. Zhang, B. Kong, S. Zhang, W. Teng, J. Fan, W. Zhang, S. Dou and D. Zhao, *Nano Res.,* 2015, **8**, 2503–2514.

47. Z. Wang, X. Yang, J. Yang, Y. Jiang and N. He, *Anal. Chim. Acta,* 2015, **862**, 53–63

48. X. J. Lin, A. Z. Zhong, Y. B. Sun, X. Zhang, W. G. Song, R. W. Lu, A. M. Cao and L.-J. Wan, *Chem. Commun.,* 2015, **51**, 7482–7485.

49. S. Mondal, A. Samanta, B. B. Dhar and R. N. Devi, *Catal. Today*, 2015, **251**, 114–120.

50. J. Martins, N. Batail, S. Silva, S. Rafik-Clement, A. Chaumonnot, D. Uzio, T. S. Nguyen and L. Piccolo, *Appl. Catal., A*, 2015, **504**, 504–508.

51. D. Shen, L. Chen, J. Yang, R. Zhang, Y. Wei, X. Li, W. Li, Z. Sun, H. Zhu, A. M. Abdullah, A. Al-Enizi, A. A. Elzatahry, F. Zhang and D. Zhao, *ACS Appl. Mater. Interfaces,* 2015, **7**, 17450–17459.

52. J. Ying, H. Peng, X. Xu, R. Wang, F. Yu, Q. Sun, W. Liu, Z. Gao and X. Wang, *Catal. Sci. Technol.,* 2016, **6**, 5405–5414.

53. M. Seo, S. Kim, H. E. Jeong, D. W. Lee and K. Y. Lee, *J. Mol. Catal*. *A: Chem*., 2016, **413**,1–6.

54. V. Sudheeshkumar, A. Shivare and R. W. J. Scott, *Catal. Sci. Technol.,* 2017, **7**, 272–280.

55. L.-K. Chau and H.-T. Chang, *From Bioimaging to Biosensors*, CRC press, New York, 2013.

56. D. Pi, W. Z. Li, Q. Z. Lin, Q. F. Huang, H. Q. Hu and C. Y. Shao, *Energy Technol.,* 2016, **4**, 943–949.

57. R. E. Hayes, *Chem. Eng. Sci.,* 2004, **59**, 4073–4080.

58. T. Teranishi and M. Miyake, *Chem. Mater.,* 1998, **10**, 594–600.

59. R. Abbasi, L. Wu, S. E. Wanke and R. E. Hayes, *Chem. Eng. Res. Des*., 2012, **90**, 1930–1942.

60. H. Nassiri, K.-E. Lee, Y. Hu, R. E. Hayes, R. W. J. Scott and N. Semagina, *J. Catal.,* 2017, **352**, 649–656.

61. H. Scott Fogler, *Elements of Chemical Reaction Engineering*, 5th edn, Prentice Hall, Kendaville, IN, 2016.

62. F. H. Ribiero, M. Chow and R. A. Dalla Betta, *J. Catal.,* 1993, **146**, 537–544.

63. T. V. Choudhary, S. Banerjee and V. R. Choudhary, *Appl. Catal., A*, 2002, **234**, 1–23.

64. G. Ertl, H. Knözinger, F. Schüth and J. Weitkamp, *Handbook of Heterogeneous Catalysis*, Volume 5, 2nd edn., Wiley-VCH, Weinheim, 2008.

65. G. Berhault, M. Bausach, L. Bisson, L. Becerra, C. Thomazeau and D. Uzio, *J. Phys. Chem. C,* 2007, **111**, 5915–5925.

66. H. Nassiri, K. E. Lee, Y. Hu, R. E. Hayes, R. W. J. Scott and N. Semagina, *ChemPhysChem*, 2017, **18**, 238–244.

67. D. Roth, P. Gélin, A. Kaddouri, E. Garbowski, M. Primet and E. Tena, *Catal. Today,* 2006, **112**, 134–138.

68. Y. Chin and D. E. Resasco, *J. Catal*, 1999, **14**, 1–39.

69. C. R. F. Lund and J. A. Dumesic, *J. Catal.,* 1981, **72**, 21–30.

70. W. Juszczyk and Z. Karpiński, *J. Catal*., 1989, **117**, 519–532.

71. I. Yuranov, L. Kiwi-Minsker and A. Renken, *Appl. Catal., B,* 2003, **43**, 217–227.

72. J. Shen and N. Semagina, *ChemCatChem,* 2016, **8**, 2565–2571.

73. A. H. Habibi, R. E. Hayes, and N. Semagina, *Catal. Sci. Technol.,* 2018, **8**, 798-805.

Chapter 3

3 Evaluation of hydrothermal stability of encapsulated PdPt@SiO_2 catalyst for lean CH_4 combustion[2]

3.1 Introduction

Composed primarily of methane, natural gas is an abundant energy source with a total proved worldwide reserve of over 193.9 trillionm^3.[1] Since methane has the lowest carbon to hydrogen ratio among all hydrocarbon fuels it generates the lowest amount of CO_2 per unit of produced energy during combustion. Methane also readily forms homogenous air-fuel mixtures and lean-burn combustion of methane in natural gas fueled vehicles (NGVs) typically emits not only less CO_2, but also considerably less CO, nitrogen oxides (NO_x) and soot compared to diesel engines.[2] All these environmental benefits combined with its low cost make methane an attractive fuel for the purposes of energy production. However, although methane does not contribute to tropospheric ozone production[3] or smog-generation, it is a potent greenhouse gas with a global warming potential (GWP) of 28–36 over 100 years[4] thus the environmental benefits of burning methane can be offset by an unacceptable level of methane emission in the exhaust of NGVs. The initial automobile emissions standards written into the U.S. Clean Air Act of 1970, did not include methane in the list of pollutants covered by such regulations;[5,6] however, today it has been realized that methane emissions must be eliminated from the combustion gases and more strict environmental regulations on methane are emerging.[7] As a means to reduce CH_4

[2] Chapter 3 of the thesis has been published as: A. H. Habibi, R. E. Hayes, and N. Semagina, "Evaluation of hydrothermal stability of encapsulated PdPt@SiO_2 catalyst for lean CH_4 combustion", *Applied Catalysis A, General,* 2018, **556**, 129-136. Dr. Shihong Xu performed XPS analysis at Alberta Centre for Surface Engineering and Science (ACSES), University of Alberta. Peng Li and Dr Jing Shen collected the HRTEM images at nanoFAB. The NAA analyses were performed by Becquerel Laboratories Inc., Maxxam Analytics, Ontario. The author performed all syntheses, reactions, analyses and other characterizations. This paper was reprinted with permission from Ref [66].

emissions, catalytic combustion of methane on transition metals has been extensively studied.[8-12] However, the catalytic removal of methane from exhaust emissions is still a major challenge for automakers for several reasons. Having a relatively strong C—H bond (450 kJ/mol),[13] methane is the most difficult alkane to oxidize catalytically. Also, in the catalytic converter of an NGV low concentrations of methane (400–1500 ppmv) must be oxidized in the presence of high concentrations of water (10–15 vol.%) and CO_2 (15 vol.%) at relatively low exhaust gas temperatures (450–550 °C).[14] Oxide supported Pd catalysts, which are known to have the highest activity for CH_4 oxidation are widely used in catalytic methane abatement systems.[3,13,15-17] However, these catalysts have a poor stability and tend to deactivate severely during operation.[16,18-20] Several mechanisms have been discussed in the literature as the causes of this deactivation. Thermal sintering of the Pd nanoparticles (NPs), collapse of the support structure, conversion of PdO to Pd, and water-related effects have been reported as some of the main deactivation reasons of Pd catalysts.[11,13,21] NP sintering can occur through Ostwald ripening and/or particle migration and is more pronounced in highly loaded catalysts. Thermal and water-induced sintering of the Pd NPs leads to NPs agglomeration and thus decreases the available specific surface area for the reaction. Water-induced sintering is reported to occur at above 500 °C;[22,23] however thermal sintering of Pd occurs at lower temperatures as well.[24] The effects of the presence of water vapor on the activity of Pd catalysts have been studied extensively. The inhibition effect of water is reported to be temperature dependent and the reaction order with respect to water concentration was shown to vary from −1 at 300 °C to 0 at 500 °C.[25] In the low temperature regime (T < 450 °C) water poisoning of the catalyst surface due to the formation of $Pd(OH)_2$ is one of the main deactivation causes.[26-28] It was also shown that water inhibition was significant up to about 450 °C.[21] This was also reported to be consistent with the fact that the accumulation of water on the catalyst surface and its delayed desorption were more significant up to 450 °C. At temperatures above 450 °C water and CO_2 desorb at similar rates and the accumulation is no longer occurring. Schwartz et al.[16] proposed that accumulation of hydroxyl/water on the support impedes the catalytic combustion at temperatures below 450 °C by hindering the oxygen mobility on the support.

To improve the stability of the Pd catalysts, several methods have been investigated and reported in the literature. Addition of platinum to Pd has been shown in several studies to improve the stability of the Pd catalysts considerably.[20,29,30] Ersson et al.[18] showed that the

activity loss caused by the presence of water vapor was irreversible for Pd/Al_2O_3 catalysts, whereas the bimetallic Pd-Pt catalysts were inhibited by water to a lower degree and could recover the activity when water vapor was removed. Also, it was shown by Ozawa et al.[29] that the addition of Pt improves the catalyst stability by preventing the growth of PdO and Pd-Pt particles during methane combustion at high temperatures (800 °C). Recently, Nassiri et al.[31] associated the improved activity of the Pd-Pt catalysts compared to monometallic Pd with a lack of oxygen on the surface in wet combustion conditions, which allowed Pt-catalyzed methane activation. Also, a molar Pd/Pt ratio of 1 was reported by Nassiri et al.[32] to show the most stable performance during hydrothermal ageing in wet methane combustion. Thus, in the current study Pd-Pt bimetallic nanoparticles with a 1:1M ratio were selected as an active phase for the wet lean-burn methane combustion study.

During the past decade, the encapsulation of metal NPs in various oxides (NPs@Oxide structures) has been investigated as a means of protecting NPs from sintering. The presence of the oxide shell immobilizes the metal NPs and has been shown to prevent sintering of the NPs at high temperatures.[33-35] Among the various reported shell materials, silica is one of the most researched and relatively straight- forward ones to prepare (as compared to CeO_2 for instance [36]), making it a promising candidate for industrially-viable encapsulation purposes. $Pd@SiO_2$ catalysts have been synthesized and tested in various catalytic applications.[35,37,38] Pi et al. recently investigated the catalytic combustion of methane over $Pd@SiO_2$ in dry/ wet conditions. Encapsulation of Pd in SiO_2 was shown to be effective in preventing sintering of the Pd NPs.[33,40] Using dry methane combustion as a model reaction, we recently investigated the effect of the synthesis conditions on the porosity and accessibility of the Pd sites encapsulated in silica ($Pd@SiO_2$).[41]

The effect of metal-support interactions on the stability of the silica-supported Pd (Pd/SiO_2) catalysts in methane combustion has been investigated in several studies. In 1990, Burch et al.[9] reported a higher activation rate in the combustion environment as well as a higher sintering of the PdO sites on Pd/SiO_2 compared to the Pd/Al_2O_3 catalysts. They associated this behavior of the Pd/SiO_2 catalyst to its more rapid reconstruction during combustion. Stability of silica in the presence of water is known to be compromised at high temperatures. At temperatures above 700 °C reaction of silica with water vapor and formation of ($Si(OH)_4$)

hydroxides becomes feasible [42-45] resulting in a poor stability. Formation of silanol (—Si—OH) groups in the presence of water was suggested by Lamber et al.[46] to favor the migration and coalescence of Pd NPs. Recently, Gholami et al.[45] studied the role of the SiO_2 in the deactivation of Pd/SiO_2 catalysts. They observed that silica desorbs physisorbed and chemisorbed water at about 97 and 397 °C, respectively. They associated the higher degree of catalyst deactivation and water-inhibition of the Pd/SiO_2 during hydrothermal ageing to the migration of silica and occlusion of PdO.[45] This observation was also in accordance with previous studies.[47] Since the operating temperatures at the catalytic converter of a NGV operating at lean burn conditions are below 550 °C, the negative effect of silanol groups is less likely to be a major concern.

Since encapsulation of metal NPs in silica shells effectively prevents NP sintering [34,41,48-50] and bimetallic PdPt nanoparticles (1:1) are known to be more active and stable during hydrothermal ageing than Pd,[20,29,30,32] a structure composed of PdPt NPs encapsulated in porous silica shells could presumably be a promising methane combustion catalyst. To the best of our knowledge, the performance of the silica-encapsulated bimetallic PdPt ($PdPt@SiO_2$) catalysts in wet methane combustion has not been reported. Thus, the objective of this study was to assess the hydrothermal stability of a bimetallic Pd-Pt encapsulated catalyst in lean-burn methane combustion. The performance of the encapsulated catalyst is compared to two impregnated catalysts of the same metal loading. γ-Al_2O3 and SiO_2 were selected as the support materials of the reference catalysts since Al_2O_3 is one of the most widely used support materials in catalytic combustion and SiO_2 is the material composing the shells of the encapsulated catalyst. The silica-encapsulated catalyst, silica-supported catalyst, and alumina-supported catalyst are hereafter referred to as $PdPt@SiO_2$, $PdPt/SiO_2$ and $PdPt/Al_2O_3$, respectively.

3.2 Experimental

3.2.1 Chemicals and materials

Palladium (II) chloride solution ($PdCl_2$, 5% w/v, Acros), hexachloroplatinic acid solution (H_2PtCl_6, 8 wt.% in H_2O, Sigma) poly-(vinylpyrrolidone) (PVP) (MW: 40,000, Sigma–Aldrich), reagent alcohol (ethanol, 95 vol.%, Fisher Scientific), reagent grade methanol (Laboratory≥99.6%, Sigma), ammonium hydroxide solution (ACS reagent, 28.0–30.0% NH_3

basis, Sigma-Aldrich), tetraethylorthosilicate (TEOS, reagent grade, 98%, Sigma-Aldrich), cetyltrimethylammonium bromide (CTAB, Sigma), acetone (99.7%, Fisher Scientific), silica (mesoporous, particle size: 1 μm, and pore size: 4 nm, Sigma–Aldrich) and aluminum oxide (∼150 mesh, pore size: 58 Å, Sigma) were used as received. Milli-Q water (18.2MΩcm) was used throughout the work.

3.2.2 Synthesis of the catalysts

3.2.2.1 Synthesis of the PdPt nanoparticles

Bimetallic nanoparticles (1:1M Pd:Pt) were prepared by simultaneous alcohol reduction[51] of PVP-stabilized Pd and Pt ions. At room temperature, 100 μmol of $PdCl_2$, 100 μmol of H_2PtCl_6 and 0.6 g PVP were dissolved in 50mL of Milli-Q water in a 250mL single-neck round bottom flask and were mixed for 10 min. Then 50mL of methanol was added. The mixture temperature was increased from room temperature to the reflux point. The solution was heated under reflux and stirring for 2 h. After cooling to room temperature, 250mL of acetone was added to the mixture. After mixing for 5 min the solution was centrifuged at 8000 rpm for 12 min. The supernatant was discarded and a complete separation of the PVP-stabilized bimetallic NPs from the solution was achieved. The resulting PVP-stabilized PdPt nanoparticles (100 μmol of each metal) were redispersed in 40mL of ethanol using ultrasonication for 10 min.

3.2.2.2 Encapsulation of PdPt NPs

High metal loading catalysts with as high metallic surface area aspossible are more desirable in most industrial applications especially in NGV's catalytic converter as they eventually result in a smaller reactor or catalytic converter volume. Therefore, the synthesis method applied in this work was designed to produce the highest equimolar metal loading possible-without losing any uncoated metal NP or forming agglomerates in the core during the Stöber stage of the synthesis. In the chemical system used in our synthesis, a concentration of 2.5 mmol/L of each of the metals was found to be the highest permissible metal concentration in the Stöber stage- subsequently leading to catalysts with final Pd and Pt loadings of 4.205 and 6.98 wt.%, respectively.

The PVP-stabilized PdPt NPs prepared in the previous step were coated by silica shells according to a Stöber-based encapsulation method adapted from.[52] In a typical synthesis, 3.6mL of water, 1mL of 28% ammonium hydroxide, and 2 g of CTAB were added to the PVP-stabilized PdPt nanoparticles from the previous step (a solution of 100 μmol of each metal in 40mL of ethanol). The solution was sonicated for 10 min followed by a 15 min magnetic stirring. Then 5.59 mmol of TEOS was added and the solution was mixed under magnetic stirring for 2.5 h. The molar ratio of the reagents (ethanol: water: ammonia: TEOS) to metals was adjusted for the highest metal loading, high shell porosity and uniformness of the final powder. The mixture was sonicated for 10 min followed by a 10-min magnetic stirring. The PdPt@SiO_2 particles were collected and separated from the solution using centrifugation at 8000 rpm for 12 min and the supernatant which contained no metal or SiO_2 particles was discarded. The precipitate was washed two times by dispersion in 30mL of ethanol using sonication for 5 min followed by centrifugation at 7500 rpm. Finally, the PdPt@SiO_2 particles were dried at 60 °C for 2 h followed by calcination under static air at 550 °C for 16 h.

3.2.2.3 Synthesis of the impregnated catalysts (PdPt/SiO_2 and PdPt/Al_2O_3)

The PdPt/SiO_2 and PdPt/Al_2O_3 catalysts were prepared using an incipient wetness impregnation method to achieve the same metals loadings as in the encapsulated PdPt@SiO_2 catalyst. A solution of specific amounts of palladium (II) chloride and hexachloroplatinic acid was impregnated onto the silica and alumina support (precalcined at 550 °C for 4 h). The catalysts were dried overnight at room temperature and were subsequently calcined under air at 550 °C for 16 h.

3.2.3 Characterization

Transmission electron microscopy (TEM) of the PVP-stabilized nanoparticles and PdPt@SiO_2 (during different steps of synthesis and after HTA) was performed at 200 kV on a JEOL 2100 transmission electron microscope at Cell Imaging Facility of the University of Alberta. ImageJ software was used to measure the particle size and standard deviation of the samples. The measurements were done by counting 200 particles from the TEM images.

Neutron activation analysis (NAA) was used to measure the actual loading on the catalysts after calcination. During the NAA which was performed at Becquerel laboratories (Maxxam Company, Ontario) the samples were irradiated for 20 min in the Cd shielded, epithermal site of the reactor core. They were counted for 30 min each on an Aptec CS11-A31C gamma detector approximately 12 h after irradiation.

Nitrogen physisorption at 77.3 K by volumetric measurements using a surface area analyzer (Quantachrome, Autosorb iQ) was used to measure the surface area and adsorption isotherms of the catalysts. Prior to adsorption analyses, 60–90mg of sample was degassed for 3.5 h at 350 °C under vacuum with a He backfill to remove any moisture or volatiles within the pores of the material. The BET model was used to determine the surface area of the catalysts from the N_2 adsorption isotherms at a relative pressure range of P/P0=0.02 to 0.025. Specific surface area was calculated using the BET method, the pore size distribution was derived from Barrett-Joyner-Halenda (BJH) model, and the total pore volumes were obtained from the adsorbed quantity at a relative pressure (P/P0=0.995).

Kratos Axis 165 X-ray photoelectron spectrometer with a Mono Al Kα source (hν=1486.6 eV) (operated at 15mA and 14 kV) was used to perform the X-ray photoelectron spectroscopy (XPS) measurements. The survey spectra were collected with analyzer pass energy of 160 eV and a step of 0.4 eV; the high resolution spectra were scanned with a pass energy of 20 eV and a step of 0.1 eV. During the acquisition of the spectrum, charge neutralization was applied to compensate the insulating problem of the sample. Mixed Lorentzian–Gaussian curves and Casa XPS software was used to fit the XPS signals. All binding energies are reported after calibration for C1s peak to match 284.8 eV.

CO pulse chemisorption was performed by injecting 3%CO/He gas at room temperature with an AutoChem 2950HP (Micromeritics, U.S.A.) instrument equipped with a quartz U-tube reactor and a thermal conductivity detector (TCD). Prior to the analyses, the calcined samples (~30 mg) were reduced in a flow of 10% H_2/Ar (25 mL/min) at 350 °C for 1 h. The reduction temperature was based on the temperature-programmed reduction profiles, as reported in Section 3.3. Then, the catalysts were purged with argon at 550 °C for 30 min and then cooled to ambient temperature under inert atmosphere. The dispersions were calculated assuming 1:1 CO:surface

metal stoichiometry. The CO up- take of the pure silica and alumina were also measured and subtracted from the CO uptakes of the catalysts.

Temperature programmed reduction (TPR) experiments of the catalysts were performed using the same AutoChem 2950 HP instrument (Micromeritics, U.S.A.). 0.1 g of catalyst was loaded in a quartz reactor. Prior to the analysis, the catalysts were calcined at 550 °C for 2 h in a flow of 10%O2/He (20 ml/min). Temperature was increased from room temperature to 900 °C with a ramping rate of 10 °C/min in a flow of 10% H2/Ar (10 ml/min). TCD signal was inverted, so a positive peak means hydrogen consumption; and a negative peak means hydrogen evolution.

The S/TEM/EDX (energy-dispersive X-ray) analysis was performed on a JEOL JEM-ARM200cF S/TEM, which was equipped with a cold Field-Emission Gun and a probe Cs corrector. EDX maps were acquired with a Silicon Drift EDX detector at an acceleration voltage of 200 kV.

3.2.4 Catalytic tests and hydrothermal ageing

Dry and wet methane combustion in lean conditions was investigated in a similar manner reported by [17]. After calcination at 550 °C for 16 h in static air, 100mg of catalyst (4.205 wt.% Pd and 6.98 wt.% Pt) was packed into a 20-in. long tubular reactor made of 316 stainless steel with an inner diameter of 3/8 in. To hold the catalyst bed in place, both ends of it were packed with quartz wool. A furnace equipped with a temperature controller was used to heat the reactor. The internal reaction temperatures (before and after the catalytic bed) were measured by two K-type thermocouples inserted into the reactor. The temperature difference between these two internal thermocouples was below 2 °C and the average of the two was reported as the reaction temperature. The feed gases (10% CH_4/N_2 and extra dry compressed air) were purchased from Praxair. All of the reported gas flow rates are based on standard temperature and pressure (STP) conditions (0 °C and 1 atm). Mass flow controllers (Matheson and MKS) were used to control the gas flow rates. Methane (10% balanced in nitrogen, 8.5 mL/min) and air (extra-dry, 205 mL/min STP) were pre-mixed and fed into the reactor. The concentration of CH_4 in the gas mixture was about 4000 ppm. The corresponding gas hourly space velocity (GHSV) was calculated to be 133,800 LSTP/(h kgcat). Methane oxidation was carried out at a constant

pressure of 30 psig (2.87 bar). During wet combustion and HTA, liquid water was injected from a syringe pump at a controlled rate to give 5 vol.% water vapor in the feed stream. The reactor feed line was heated to vaporize the water. The exit gas from the reactor passed through a cold trap to remove water vapor, and was then analyzed using an online Agilent HP-7890-A gas chromatograph (GC) equipped with a series thermal conductivity detector (TCD) and flame ionization detector (FID). The ignition and extinction (IE) curves were obtained by increasing and decreasing the reaction temperature stepwise between 200–550 °C (50 °C for each step at a heating rate of 5 °C/ min). At each step the temperature was held constant for 30 min and two samples from the product stream were analyzed by the GC. The IE curves were plotted using the average conversion calculated from these two measurements. Two dry and two wet IEs were performed. The average of the two wet IEs was used as the IE of the fresh catalyst.

To investigate the catalyst stability the reaction was followed by a 50-h HTA test using the exact feed gas conditions of the wet combustion experiment (total flow rate of 223 mL/min, methane concentration of 4000 ppm and 5 mol% water). During the HTA the reaction temperature was increased to 550 °C (5 °C/min ramping rate) and then was decreased to 385 °C. The reaction temperature was held constant for 1 h at each of these steps and the 550–385 °C temperature cycling was repeated 8 times (taking approximately 25 h). After this temperature cycling, the catalyst was aged at a constant temperature of 385 °C for another 18 h. Finally, two ignition-extinction tests in wet conditions were performed to check the catalytic activity after 50 h of hydrothermal aging and the average of the two was used as the IE after HTA. To ensure reproducibility, this experiment (IE before HTA, HTA and IE after HTA) was repeated using 100mg of fresh catalyst and the averaged conversion of the two experiments (less than 8% difference at each temperature) were reported.

The absence of heat and mass transfer calculations were done in a manner similar to[31]. Methane conversion and kinetic parameters at 360 °C were used to confirm the presence of intrinsic reaction conditions under isothermal reaction conditions. The Mears criterion for external mass transfer limitation (MTL) was found to be 10^{-11} (no external MTL existed if the value was below 0.15).[53] The Knudsen diffusivity and Weisz–Prater criterion for internal MTL were found to be 10^{-6} and 10^{-7}, respectively. An internal effectiveness factor of 0.97 was calculated and the internal MTL was negligible.[54] The absence of an external temperature

gradient was confirmed by Mears correlation (value of 10^{-14}, which was below the maximum limit of 0.15 for a negligible gradient).[53] The maximum internal temperature rise was calculated, by using β, to be10^{-4} K, assuming an activation energy of 72.6 kJ/mol[17] and constant heat of combustion of 890 kJ/mol. Calculations also confirmed that plug flow conditions with no wall effects or axial dispersion applied. To verify the physical integrity of the catalysts after exposure to hydrothermal ageing, an accelerated hydrothermal ageing was performed. During the accelerated HTA the catalyst was held at a constant temperature of 550 °C in the wet combustion environment (4000 ppmv methane, 5 mol% water, total flow rate of 223 mL/min) for 170 h. The TEM images, CO chemisorption capacity and N_2 physisorption results of this aged catalyst are compared to the fresh catalysts in the results section.

3.3 Results and discussions

3.3.1 Methane combustion

During the hydrothermal ageing tests, the reactor temperature was increased to 550 °C and then reduced to 385 °C (with a hold time of 1 h at each step). The upper temperature bound (550 °C) was selected based on the highest temperature of a lean-burn NGV's catalytic converter; the lower temperature bound (385 °C) would help study the stability since water inhibition effects are profound at temperatures below 450 °C.[9] The ignition-extinction (IE) curves before and after the HTA are presented in Figure 3.1a. Figure 3.1b presents the conversion vs time on stream during the HTA. As shown in Figure 3.1, the PdPt@SiO_2 catalyst provided significantly higher conversions than the impregnated silica- and alumina-supported catalysts of the same metal loading. During the HTA test, the encapsulated catalyst was able to deliver full conversion at 550 °C and the highest conversion among the three studied catalysts at 385 °C. The impregnated silica catalyst did not even reach 100% conversion at 550 °C. During cycling and at 385 °C the encapsulated catalyst lost some activity; however the activity was maintained during the rest of the HTA which is expected for the bimetallic Pd-Pt 1:1 catalysts.[32] The following sections aim at identifying the potential causes of this activity loss by investigating the various aspects of the HTA effects on the encapsulated catalyst.

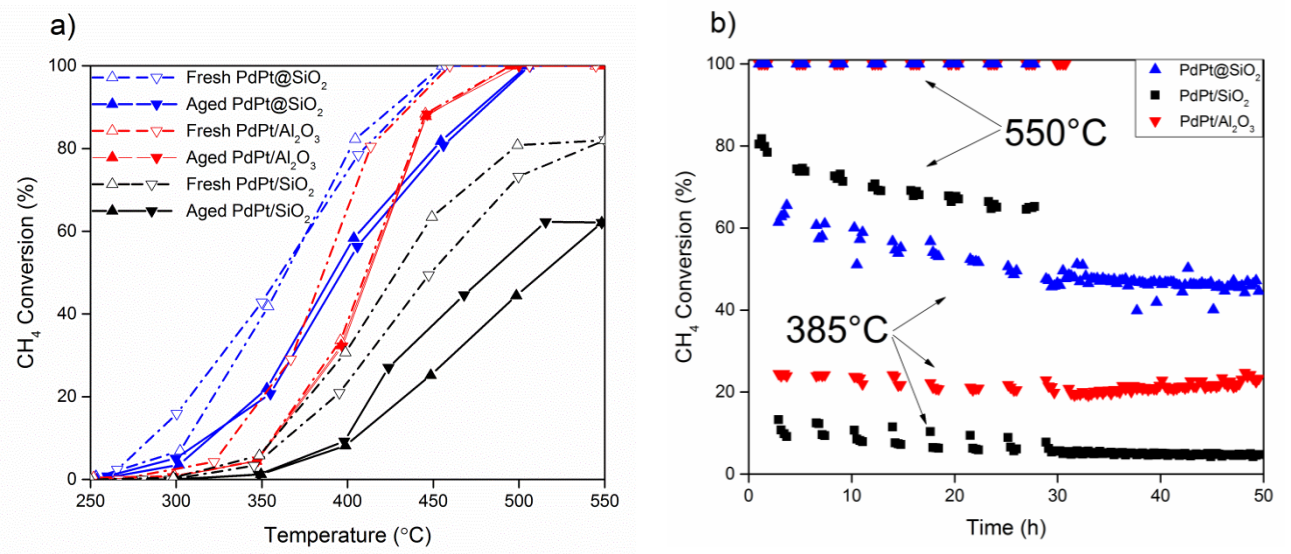

Figure 3.1. a) Iginition (pyramid symbols) and extinction (inverted pyramids) data before and after HTA; b) methane conversion vs time on stream during HTA. Reaction conditions: 100 mg catalyst (4.205 wt.% Pd, 6.98 wt.% Pt), GHSV 133800 $L_{STP}/(h \cdot kg_{cat})$, initial CH_4 concentration 4000 ppm and 5 mol% H_2O.

3.3.2 Characterization of the encapsulated and impregnated PdPt catalysts

3.3.2.1 The PdPt NPs

In the current work alcohol reduction of Pd and Pt precursors was used to prepare bimetallic PdPt NPs. During the alcohol reduction step, PVP was used to stabilize NPs with a uniform size distribution. To improve the thermal stability, the bimetallic nanoparticles were then encapsulated in porous silica shells. Previously we studied the effect of synthesis conditions on the shell porosity and activity of the silica-encapsulated Pd catalysts using dry methane combustion as the model reaction. It was shown that once PVP-stabilized NPs were created, the presence of a pore inducing agent during the Stöber reaction was crucial for the formation of a sufficiently porous silica shell.[41] Similarly, in this work the accessibility of the PdPt NPs after encapsulation in silica was ensured by the application of a pore-inducing agent (CTAB) in the Stöber stage of the synthesis. The synthesis procedure was designed to produce uniformly alloyed PdPt cores of 6–8nm in size, inside porous SiO_2 shells of 60–80nm in diameter since the Pd NPs are reported to have the highest methane combustion turnover frequencies at a particle

size of 8-10nm[55] and the powders used in the catalytic converter washcoats are typically below 100nm in size.[56]

The surface composition of the encapsulated catalysts was measured using XPS. The surface-mass percentage of the Pd and Pt atoms was found to be much smaller than the bulk metal loading measured by the NNA (Table 3.1). As the signal intensity of XPS is most sensitive to the outermost atomic layers (within 10nm from the surface) and decays exponentially with increasing depth,[57] the appearance of weak Pd and Pt peaks in the XPS spectra proved that the majority of the metal NPs were effectively coated within the silica shells.

The size and morphology of the encapsulated nanoparticles during various steps of the synthesis and after HTA were investigated using TEM (Figure 3.2). According to the TEM images, the as-synthesized PdPt nanoparticles had a mean particle size of 6.1 ± 1.0nm and 7.2 ± 1.4 nm after encapsulation in silica (Figure 3.2a, b). The particle size or morphology of the PdPt NPs after encapsulation in silica was not affected by the 16-h calcination under static air (Figure 3.2b, c). However, after the HTA test even though the core PdPt NPs did not sinter, some changes in their morphology were observed. As shown in Figure 3.2d, the HTA resulted in the

Table 3.1. Catalyst properties before and after hydrothermal ageing (HTA)

Catalyst[a]	Metal dispersion,[b] %		Surface concentration from XPS[c]		Surface area, m^2/g		Pore volume, mL/g		Pore size, nm	
	Before HTA	After HTA	wt.% Pd	wt.% Pt	Before HTA	After HTA	Before HTA	After HTA	Before HTA	After HTA
$PdPt@SiO_2$	4	9	0.3	0.5	598	592	0.49	0.47	3.4	3.4
$PdPt/SiO_2$	2	1	3.1	2.6	350	350	0.3	0.3	4	4
$PdPt/Al_2O_3$	11	6	2.9	3.4	156	156	0.274	0.274	5.8	5.8

[a] final metal loadings as determined by NAA are 4.205 wt.% Pd and 6.98 wt%. Pt; [b] determined by CO chemisorption assuming 1:1 CO:metal stoichiometry; [c] before HTA.

increased size deviation with the formation of smaller and larger NPs. These changes were not unique and were observed throughout the sample but only after the HTA. The elemental distribution of the Pd-Pt NPs after encapsulation and after HTA was investigated using EDX. The elemental mapping of the NPs after encapsulation (and before reaction) proved that the Pd and Pt atoms were present in an alloy form inside the shells (Figure 3.2e, f). However, after the HTA some segregated Pt-rich/Pd-rich NPs were observed inside the silica shells (Figure 3.2g) which were absent before the HTA (Figure 3.2f). Such a change in the morphology and local metal distribution can be related to the reconstruction of the bimetallic PdPt sites during the HTA

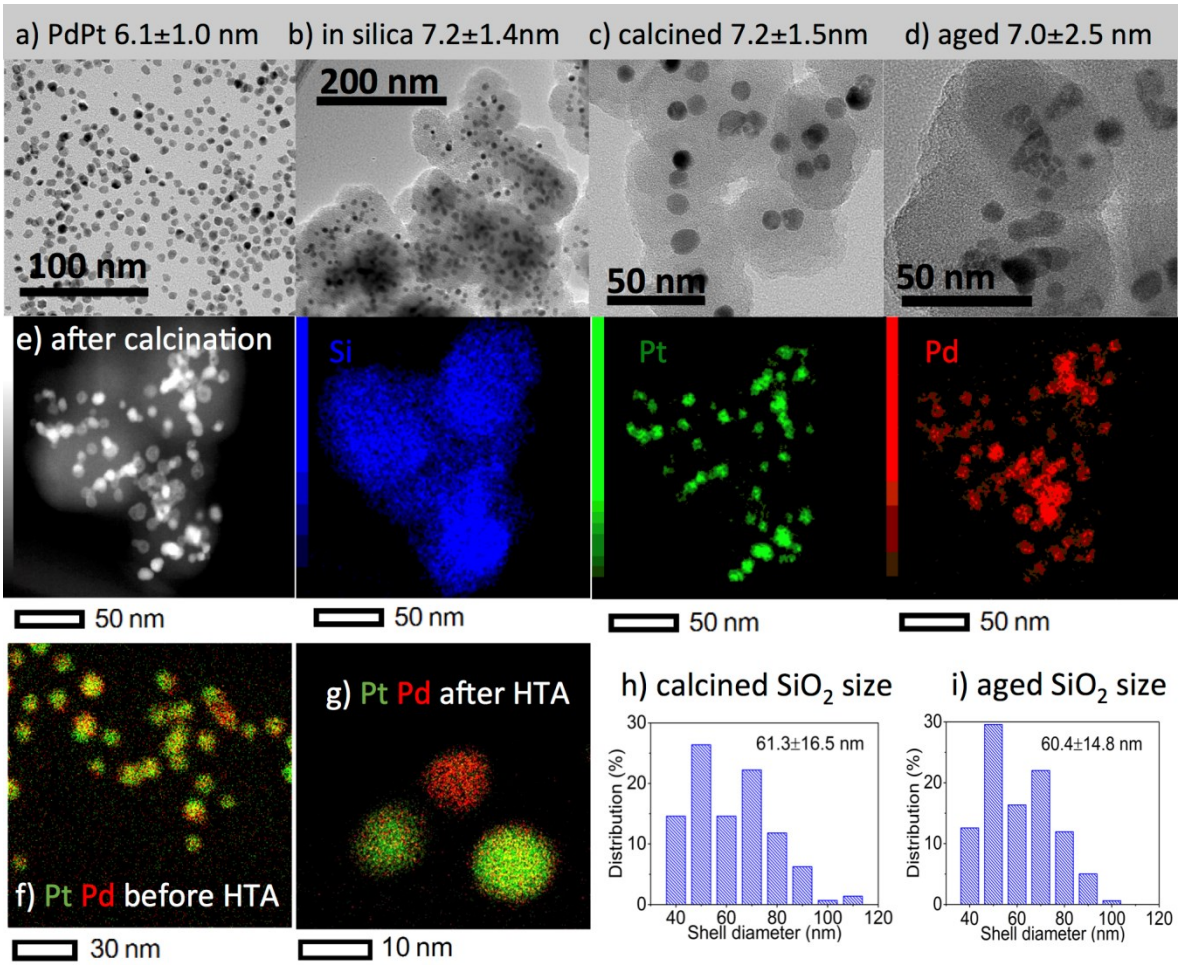

Figure 3.2. TEM images and EDX mapping analyses: a) as-synthesized PVP-protected PdPt NPs; b) PdPt@SiO_2 nanoparticles after encapsulation; c), e), f) PdPt@SiO_2 after calcination for 16 h at 550 ^oC in air; d), g) PdPt@SiO_2 after HTA; h) shell size distribution after calcination; i) shell size distribution after HTA

which is in accordance with similar observations in the literature. Redistribution of the bimetallic PdPt NPs is known to occur under hydrothermal ageing conditions via Pt oxide vaporization or PdO migration and gives rise to a surface enrichment of PdO in bimetallic catalysts.[58-61]

The TEM images of the encapsulated NPs after HTA (Figure 3.2d, g) can be compared those of the impregnated Al_2O_3 and SiO_2-supported catalysts (Figure 3.3). As shown in Figure 3.3, even though Pd and Pt on the impregnated catalysts have formed alloys and are present in close contact to each other, the nanoparticles have sintered severely during calcination and HTA and have formed large agglomerates.

The metal dispersions in the catalysts before and after the HTA were measured by CO chemisorption and are presented in Table 3.1. The impregnated catalysts lost their metallic surface area during the HTA and showed lower metal dispersions as compared to the encapsulated catalyst, which is in line with their lower catalytic activities (Figure 3.1). Between the impregnated catalysts, the NPs sintered more significantly on SiO_2 than on Al_2O_3. PdO is known to exhibit stronger metal-support interaction with Al_2O_3 as compared to SiO_2 which

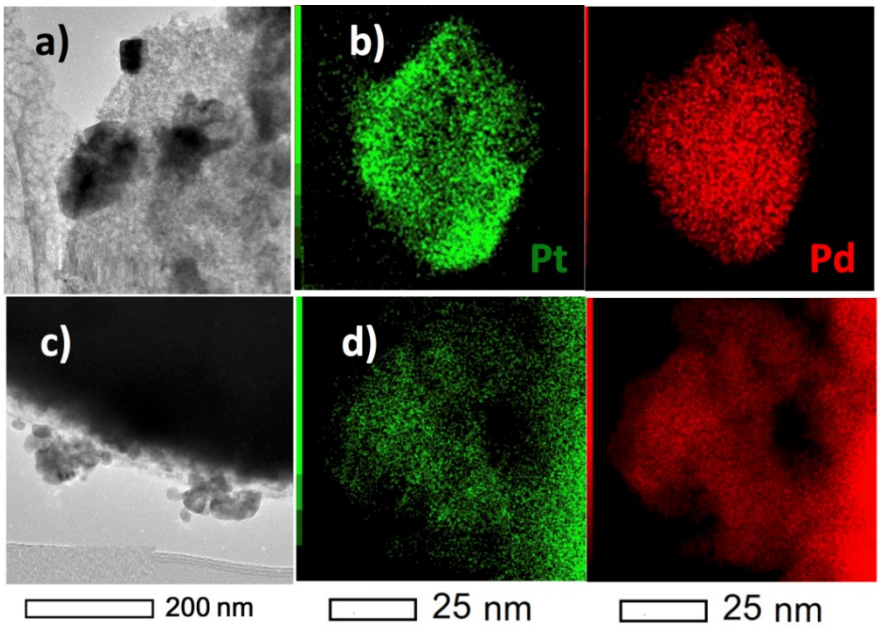

Figure 3.3. The TEM images and EDX mappings of impregnated catalysts after the HTA: a), b) $PdPt/Al_2O_3$ and c), d) $PdPt/SiO_2$.

impedes the NPs sintering.[45,62] As opposed to the impregnated catalysts, the metal dispersion in encapsulated catalyst increased after HTA, which is in line with the TEM observations on the formation of smaller NPs (Figure 3.2d). Two possible events during the HTA could have contributed to this change in the CO-chemisorption capacity. Some silica removal via formation of labile Si(OH)4 hydroxides could occur at the PdPt-silica interface and thus "clean" the surface of the metal NPs,[42-45] and/or Pt oxide vaporization and PdO migration could miniaturize some of the original nanoparticles.[58-61]

The turnover frequencies (TOFs) of the aged catalysts were calculated based on the measured post-HTA metal dispersions (Table 3.1) and conversions from the post-HTA ignition curves at differential conditions (CH_4 conversion<8%), followed by normalization to 350 °C using an activation energy of 72.6 kJ/mol.[17] The TOFs were found to be $3.1x10^{-3}$, $3.3x10^{-3}$ and $2.0x10^{-3}$ s^{-1} for the PdPt@SiO_2, PdPt/SiO_2 and PdPt/Al_2O_3, respectively. These TOF values are consistent with the TOF ranges reported for methane combustion in the presence of water vapor (10^{-4}–10^{-3} s^{-1}).[31,63,64] Remarkably, the TOFs of both silica-based catalysts are the same, indicating that the intrinsic PdPt active site performance in the PdPt@SiO_2 is not affected by the silica preparation method. The significant drop in activity for the SiO_2-impregnated catalyst as compared to the encapsulated one (Figure 3.1) is thus related only to the sintering of metal NPs in the impregnated catalyst as opposed to the stable encapsulated PdPt NPs.

The TPR profiles (Figure 3.4) also confirm that the metal-support interaction is similar for both silica-based catalysts below 400 °C reduction. In both silica catalysts some hydrogen evolution occurs below 100 °C which is typical for β-hydrides formed at lower temperatures.[65] The hydrogen consumption peaks for the encapsulated catalyst above 550 °C can be explained by Pd silicides formation,[47] which are not pronounced for the impregnated sample because of its significantly lower Pd/Si interfacial area. PdPt/Al_2O_3 catalyst showed a different reducibility behavior (hydrogen consumption for the metal NPs reduction below 100 °C, Figure 3.4) indicating the effect of metal-support interactions on the PdPt properties, which is in line with a different TOF for PdPt/Al_2O_3 catalyst ($2x10^{-3}$ s^{-1}) as compared to the both silica catalysts ($3x10^{-3}$ s^{-1}). The support is known to affect the Pd TOF in methane combustion.[64]

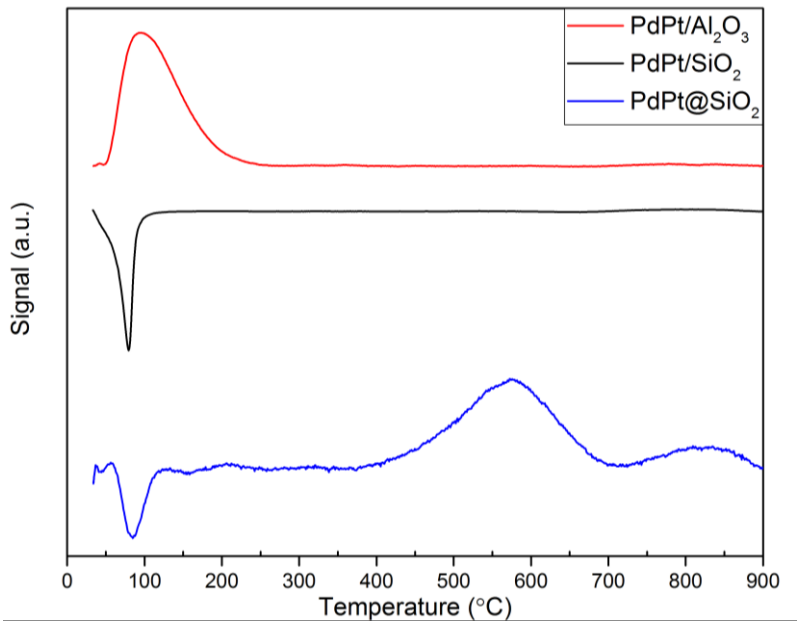

Figure 3.4. TPR profiles.

Thus, the characterization results show that at high metal loading the impregnated $PdPt/SiO_2$ catalyst shows a significantly lower activity than the $PdPt@SiO_2$ catalyst (Figure 3.1b) only due to the larger metal NPs, which were not formed in the encapsulated catalyst. The alumina support was able to stabilize the impregnated metals more efficiently than silica in $PdPt/SiO_2$ catalyst, but still not as efficient as the silica shells. The twice lower activity of the Al_2O_3-based catalyst during the HTA as compared to the $PdPt@SiO_2$ catalyst (Figure 3.1b) is connected to both the larger NP size and lower TOFs due to the strong metal-support interactions.

3.3.2.2 The silica shells: surface area, shell porosity, size and pore size distribution before and after HTA

This section addresses the question of potential silica shell deterioration during the high-temperature reaction in a wet feed. During the synthesis of $PdPt@SiO_2$, CTAB was used a pore-inducing agent to ensure high surface area and porosity of the encapsulated catalyst. The decomposition of CTAB during calcination is known to create a network of pores in the silica shells resulting in a structure with a high surface area. The change in the physical properties of the shells before and after HTA was investigated using TEM and N_2-physisorption. The TEM

images showed that the effect of HTA on the size and size distribution of the silica shells was negligible (Figure 3.2c, d, h and i). A N_2-physisorption method was used to verify the porous structure of the PdPt@SiO_2 NPs after calcination and after the HTA. The N_2-adsorption–desorption isotherms and pore size distribution of the encapsulated catalysts before and after HTA are given in Figure 3.5. No changes were observed in the N_2 adsorption characteristics of the encapsulated catalyst after the HTA. The pore size distribution of the catalysts were plotted using the desorption branch of the Barrett–Joyner–Halenda (BJH) model and indicated a median pore diameter of 3.4 nm for both fresh and aged catalyst (Figure 3.5b). The median indicated that the majority of the pores in the structure had a diameter of 3.4 nm (which is consistent with silica structures formed by using CTAB as a template).[41] The BET surface area, total pore volume, and mean pore size of the fresh and aged catalysts remained unchanged (Table 3.1). Overall, the N_2-physisorption results and TEM analyses (Figure 3.2) proved that the physical structure of the silica shell was stable after 170 h of exposure to wet lean combustion atmosphere (4000 ppm CH_4, 550 °C and 5 mol % water).

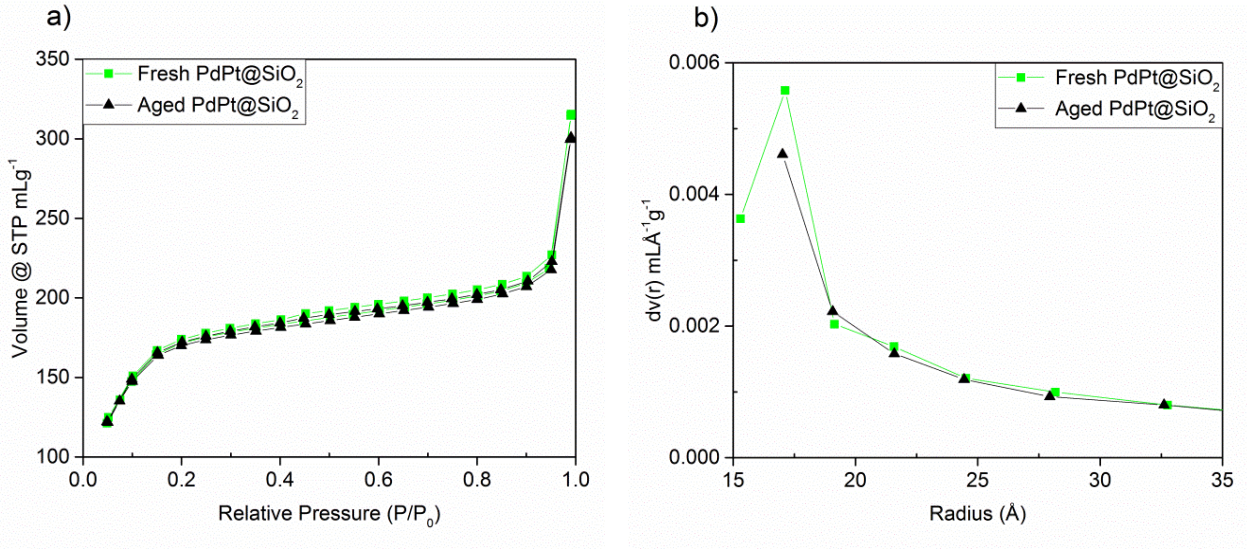

Figure 3.5. a) Nitrogen adsorption isotherms of the encapsulated catalyst and b) pore size distribution of the catalyst before and after HTA.

3.4 Conclusions

Bimetallic PdPt nanoparticles of 7 nm in size were synthesized and encapsulated in porous SiO_2 shells of 60 nm in diameter at high metal loading (4.205 wt.% Pd and 6.98 wt%. Pt). The stability of the encapsulated catalyst in the lean CH_4 combustion was investigated using a hydrothermal ageing test at temperatures up to 550 °C at 5 mol% water in the feed. No changes occurred in the silica shell morphology after 170 h of exposure to the wet lean combustion atmosphere. The aged encapsulated catalyst showed higher conversions at T < 425 °C compared to the aged impregnated $PdPt/Al_2O_3$ and $PdPt/SiO_2$ catalysts of the same metal loading due to its higher metal dispersion provided by the shells. CO chemisorption and TEM analyses also showed the dispersion increase of PdPt nanoparticles in the encapsulated catalyst during HTA, most likely due to the metal surface cleaning from silica on the Pd/Si interface[42-45] and Pt oxide vaporization and/or PdO migration.[58-61] Overall, the silica-encapsulated catalyst allowed for improved methane combustion at high GHSV and remained stable for 70 h on stream, which suggests its potential use in relatively small-size catalytic converters for methane emission control from lean combustion engines.

Acknowledgements

The study was supported by the NSERC (Strategic grant STPGP 478979-15) and CFI (Leaders' Opportunity Fund, grant 24766). This work made use of the nanoFAB facilities at the University of Alberta. We thank Dr. Jing Shen for the assistance with TEM and EDX analyses.

3.5 References

1. U.S. Government. The World Factbook, Central Intelligence Agency. https://www.cia.gov/library/publications/the-world-factbook/geos/xx.html, 2017, (accessed on 21 December 2017).

2. B. Liu, R. E. Hayes, M. D. Checkel, M. Zheng, and E. Mirosh*, Chem. Eng. Sci.,* 2001, **56**, 2641-2658.

3. J. Lampert, M. Kazi, and R. Farrauto, *Appl. Catal., B,* 1997, **14**, 211–223.

4. United States Environmental Protection Agency, Understanding Global Warming Potentials. https://www.epa.gov/ghgemissions/understanding-global-warming-potentials, 2017, (accessed on 21 December 2017).

5. U.S. Environmental Protection Agency, Summary of the Clean Air Act, 42 U.S.C. 7401 et seq. (1970). https://www.epa.gov/laws-regulations/summary-clean-air-act, 2017, (accessed on 21 December 2017).

6. R.J. Farrauto*, Science,* 2012, **337**, 659–660.

7. U. S. Environmental Protection Agency, New Source Performance Standards and Permitting Requirements, Final Rules. https://www.epa.gov/controlling-air-pollution-oil-and-natural-gas-industry/new-source-performance-standards-and, 2017, (accessed on 21 December 2017).

8. K.-I. Fujimoto, F.H. Ribeiro, M. Avalos-Borja, and E. Iglesia, *J. Catal*., 1998, **179**, 431–442.

9. T.R. Baldwin, and R. Burch, *Appl. Catal.,* 1990, **66**, 359–381.

10. A.P. Wong, E.A. Kyriakidou, T.J. Toops, and J.R. Regalbuto, *Catal. Today,* 2016, **267**, 145–156.

11. W. R. Schwartz, D. Ciuparu, and L. D. Pfefferle, *J. Phys. Chem. C,* 2012, **116**, 8587–8593.

12. C. Shao, W. Li, Q. Lin, Q. Huang, and D. Pi, *Energy Technol.,* 2017, **5**, 604–610.

13. D. Ciuparu, M. R. Lyubovsky, E. Altman, L. D. Pfefferle, and A. Datye, *Catal. Rev.,* 2002, **44**, 593–649.

14. A. Winkler, P. Dimopoulos, R. Hauert, C. Bach, and M. Aguirre, *Appl. Catal. B*, 2008, **841**, 62–169.

15. R. J. Farrauto, M. C. Hobson, T. Kennelly, and E. M. Waterman, *Appl. Catal. A*, 1992, **81**, 227–237.

16. W. R. Schwartz, and L. D. Pfefferle, *J. Phys. Chem. C*, 2012, **116**, 8571–8578.

17. R. Abbasi, L. Wu, S. E. Wanke, and R. E. Hayes, *Chem. Eng. Res. Des*., 2012, **90**, 1930–

1942.

18. A. Ersson, H. Kušar, R. Carroni, T. Griffin, and S. Järås, *Catal. Today*, 2003, **83**, 265–277.

19. K. Persson, A. Ersson, A. M. Carrera, J. Jayasuriya, R. Fakhrai, T. Fransson, and S. Järås, *Catal. Today*, 2005, **100**, 479–483.

20. K. Narui, H. Yata, K. Furuta, A. Nishida, Y. Kohtoku, and T. Matsuzaki, *Appl. Catal. A,* 1999, **179**, 165–173.

21. R. Burch, F.J. Urbano, and P.K. Loader, *Appl. Catal. A,* 1995, **123**, 173–184.

22. L.S. Escandón, D. Niño, E. Díaz, S. Ordóñez, and F. V. Díez, *Catal. Commun.*, 2008, **9**, 2291–2296.

23. Q. Xu, K. C. Kharas, B. J. Croley, and A. K. Datye*, ChemCatChem*, 2011, **3**, 1004 – 1014.

24. H. Arai, and M. Machida, *Catal. Today*, 1991, **10**, 81–94.

25. D. Ciuparu, and L. Pfefferle, *Appl. Catal. A,* 2001, **209**, 415–428.

26. D. Gao, S. Wang, C. Zhang, Z. Yuan, and S. Wang, Chin. *J. Catal.,* 2008, **29**, 1221–1225.

27. F. H. Ribeiro, M. Chow, and R. A. Dalla Betta, *J. Catal.,* 1994, **146**, 537–544.

28. R. Burch, Catal. Today, 1997, **35**, 27–36.

29. Y. Ozawa, Y. Tochihara, A. Watanabe, M. Nagai, and S. Omi, *Appl. Catal. A*, 2004, **259**, 1–7.

30. K. Persson, A. Ersson, S. Colussi, A. Trovarelli, and S.G. Jaras, *Appl. Catal. B,* 2006, **66**, 175–185.

31. H. Nassiri, K.-E. Lee, Y. Hu, R. E. Hayes, R. W. J. Scott, and N. Semagina, *J. Catal.,* 2017, **352**, 649–656.

33. H. Nassiri, R. E. Hayes and N. Semagina, *Chem. Eng. Sci.* 2018, **186,** 44-51.

33. Y. Hu, K. Tao, C. Wu, C. Zhou, H. Yin, and S. Zhou, *J. Phys. Chem. C,* 2013, **117**, 8974-8982.

34. S. H. Joo, J. Y. Park, C. K. Tsung, Y. Yamada, P. Yang, and G. A. Somorjai, *Nat. Mater.,* 2009, **8**, 126–131.

35. S. Kim, D. W. Lee, K. Y. Lee, and E. A. Cho, *Catal. Lett.,* 2014, **144**, 905–911.

36. M. Cargnello, D. Jaén, C. H. Garrido, K. Bakhmutsky, T. Montini, C. Gamez, R. Gorte, and P. Fornasiero, *Science,* 2012, **337**, 713-717.

37. J. M. Krier, W. D. Michalak, X. Cai, L. Carl, K. Komvopoulos, and G.A. Somorjai, *Nano Lett.,* 2015, **15**, 39−44.

38. Y. Wang, J. Liu, P. Wang, C. J. Werth, and T. J. Strathmann, *ACS Catal.,* 2014, **4**, 3551–3559.

39. D. Pi, W. Z. Li, Q. Z. Lin, Q. F. Huang, H. Q. Hu, and C. Y. Shao, *Energy Technol.,* 2016, **4**, 943–949.

40. M. Kim, S. Lee, K. Kim, D. Shin, H. Kim, and H. Song, *Chem. Commun.* 2014, **50**, 14938–14941.

41. A. H. Habibi, R. E. Hayes, and N. Semagina, *Catal. Sci. Technol.,* 2018, **8**, 798-805.

42. E. J. Opila, N. S. Jacobson, D. L. Myers, and E. H. Copland, *JOM,* 2006, **58**, 22-28.

43. N. S. Jacobson, E. J. Opila, D. L. Myers, and E.H. Copland, *J. Chem. Thermodyn*., 2005, **37**, 1130–1137.

44. R. Gholami, M. Alyani, and K. Smith, *Catalysts,* 2015, **5**, 561-594.

45. R. Gholami, and K. J. Smith, *Appl. Catal. B,* 2015, **168–169**, 156–163.

46. R. Lamber, N. Jaeger, and G. Schulz-Ekloff, *J. Catal.,* 1990, **123**, 285–297.

47. G. Zhu, K. I. Fujimoto, D. Y. Zemlyanov, A. K. Datye, and F. H. Ribeiro*, J. Catal.,* 2004, **225**, 170–178.

48. A. S. Reddy, H. Y. Jeong, K. Qadir, J. Y. Yun, and J. Y. Park, 18th Int. Conf. Compos. Mater., Jeju Island, South Korea, 2011, pp. 21–26 p. 1-6.

49. S. Soulé, J. Allouche, J. C. Dupin, and H. Martinez, *Microporous Mesoporous Mater.,* 2013, **171**, 72–77.

50. K. An, Q. Zhang, S. Alayoglu, N. Musselwhite, J. Y. Shin, and G. A. Somorjai, *Nano Lett.,* 2014, **14**, 4907–4912.

51. R. S. Miner, S. Namba, and J. Turkevich, *Stud. Surf. Sci., Catal.,* 1981, **7**, 160-172.

52. J. G. Oh, and H. Kim, *Curr. Appl. Phys.,* 2013, **13**, 130–136.

53. H. Scott Fogler, *Elements of Chemical Reaction Engineering,* 5th edn, Prentice Hall, Kendaville, IN, 2016.

54. M. A. Vannice, *Kinetics of Catalytic Reactions*, Springer, New York, 2005.

55. T. V. Choudhary, S. Banerjee, and V. R. Choudhary, *Appl. Catal. A,* 2002, **234**, 1–23.

56. G. Ertl, H. Knözinger, F. Schüth, and J. Weitkamp, *Handbook of Heterogeneous Catalysis,* Volume 5, 2nd edn., Wiley-VCH, Weinheim, 2008.

57. J. T. Wolan, and G. B. Hoflund, *J. Vac. Sci. Technol., A,* 1998, **16**, 3414–3419.

58. J. L. Aluha, G. Pattrick, and E. Van Der Lingen, *Top. Catal.,* 2009, **52**, 1977–1982.

59. J. H. Sinfelt*, Acc. Chem. Res.,* 1977, **10**, 15–20.

60. A. Morlang, U. Neuhausen, K. V. Klementiev, F. W. Schütze, G. Miehe, H. Fuess, and E. S. Lox, *Appl. Catal. B*, 2005, **60**, 191–199.

61. P. F. Skoda, M. F, Astier, and G. M, Pajonk, M, *React. Kinet. Catal. Lett.,* 1995, **55**, 101-110.

62. X. Chen, Y. Cheng, C. Yup, J. W. Schwank, and R. W. McCabe, *Appl. Catal. B*, 2015, **163**, 499–509.

63. E. D. Goodman, S. Dai, A. C. Yang, C. J. Wrasman, A. Gallo, S. R. Bare, A. S. Hoffman, T. F. Jaramillo, G. W. Graham, X. Pan, and M. Cargnello, *ACS Catal.,* 2017, **7**, 4372–4380.

64. J. J. Willis, A. Gallo, D. Sokaras, H. Aljama, S. H. Nowak, E. D. Goodman, L. Wu, C. J. Tassone, T. F. Jaramillo, F. Abild-pedersen, and M. Cargnello, *ACS Catal.* 2017, **7**, 7810–

7821.

65. R. M. Navarro, B. Pawelec, J. M. Trejo, R. Mariscal, and J. L. G. Fierro, *J. Catal.,* 2000, **189**, 184–194.

66. A. H. Habibi, R. E. Hayes, and N. Semagina, *Appl. Catal. A*. 2018, **556***,* 129-136.

Chapter 4

4 Kinetics of low-temperature methane oxidation over SiO_2-encapsulated bimetallic Pd-Pt nanoparticles[3]

4.1 Introduction

Increasingly strict environmental laws regarding the emissions from the automotive sector, especially limits on the emission of carbon dioxide and particulates, have resulted in a resurgence of interest in the use of natural gas vehicles (NGVs). Much of the interest centres on heavy duty vehicles, which typically use compression ignition engines (usually powered by diesel fuel) which run in the lean mode, that is, with an excess of oxygen. Natural gas is an abundant and low cost energy source,[1] and when combusted in lean-burn conditions emits less CO_2, CO and NO_X compared to standard diesel engines.[2] However, even though it produces the lowest amount of CO_2 per unit of produced energy, methane has a global warming potential (GWP) of 28-36 times that of CO_2 over 100 years.[3] As reflected in recent environmental regulations,[4] such a strong GWP necessitates elimination of methane from the exhaust systems.

In the past three decades catalytic combustion has been extensively investigated in methane emission control as it allows for complete oxidation of CH_4 without concurrent

[3] Chapter 4 of the thesis has been published as: A. H. Habibi, N. Semagina, and R. E. Hayes, "Kinetics of low-temperature methane oxidation over SiO_2-encapsulated bimetallic Pd-Pt nanoparticles" *Industrial & Engineering Chemistry Research,* 2018, **57**, 8160-8171. The reaction setup for methane combustion was originally designed and built by Dr. Long Wu and Dr. Robert E. Hayes. The author performed all syntheses, reactions, analyses, and other characterizations. The MATLAB code for the nonlinear optimization and the numerical analyses were developed and implemented by the author. This paper was reprinted with permission from Ref [80]. Copyright © 2018, ACS

formation of high levels of NO_X and also is not constrained by flammability limits.[5] However, the conditions present in the exhaust of a lean-burn NGV pose a major challenge for the catalytic removal of CH_4. In a catalytic converter for a lean-burn NGV, low concentrations of methane (400–1500 ppm) must be oxidized in the presence of high concentrations of water (5-15 vol.%) and at relatively low exhaust gas temperatures (350–550 °C).

Although many catalysts can be used for the catalytic combustion of methane, only those based on precious metals show enough activity to give the required size of catalytic converter for automotive applications. Thus, Pd and Pt catalysts are among the most studied metal catalysts used in methane combustion. These metals are deposited on a high surface area support material. It was initially believed that the metals are the primary catalytically active sites, while the role of the support is only to stabilize the metal particles by preventing leaching and agglomeration. However, possible roles of the support in transporting reactants to the catalytic surface and affecting the overall reactivity have also been explored.[6-9]

Palladium catalysts are considered to have the highest activity under net oxidizing conditions, whereas platinum catalysts are generally preferred under reducing conditions.[10,11] However, Pd catalysts are prone to deactivation at high temperatures,[6,12-14] which limits their application. Water adsorption,[7,15] formation of $Pd(OH)_2$,[16,17] thermal sintering[18] and water-induced sintering[19,20] are reported to be the main causes of deactivation of Pd catalysts. Sintering of the metal particles can occur through Ostwald ripening and/or particle migration leading to a severe loss in the surface area available for reaction. It has been shown that addition of Pt to Pd can improve the catalyst stability in CH_4 combustion in the presence of water.[13,14,21-23] This improved stability is often attributed to the suppression of particle growth in the bimetallic system,[14] and depends strongly on the ratio of the Pd to Pt in the catalyst. In fact, depending on the Pd:Pt ratio, preparation method, and the support type, addition of Pt to Pd can improve or impair methane conversion.[22,24-27] Persson et al.[23] suggested that addition of Pt increased the catalyst activity by improving the dissociation of CH_4 and O_2, and Pd:Pt ratios of 2:1 and 1:1 have been reported to be the most stable. In another study, addition of Pt to Pd was reported to reduce the intrinsic lean CH_4 combustion activity by shifting the onset of PdO to Pd transformation to lower temperatures in the range of 1120–1220 K.[28] Note that this observation is related to dry combustion (no water in the feed) at a temperature range that is not relevant to

the exhaust conditions of lean-burn natural gas engines. Nassiri et al.[29] attributed the improved activity of the Pd−Pt catalysts in wet combustion to a lack of oxygen on the surface, which allowed for Pt-catalyzed methane activation.

As another solution to sintering, encapsulation of metal nanoparticles (NP) in a silicon dioxide (SiO_2) shell has received attention over the past two decades. It has been shown that immobilization of the metal NPs inside SiO_2 effectively prevents the NP sintering.[30-36] Encapsulation of NPs in SiO_2 can be done with various methods, most of which are based on a Stöber synthesis.[30] However, the accessibility and availability of the active catalyst sites after encapsulation and the added diffusion limitation due to the presence of the oxide shell are concerns in designing industrial catalysts. By comparing the effect of two different synthesis methods on the porosity and metal accessibility of SiO_2-encapsulated Pd (Pd@SiO_2) catalysts, it was recently shown that, although both methods led to thermally stable Pd NPs, only the catalyst encapsulated in the presence of a pore inducing agent was active in dry CH_4 combustion.[37] Clearly, an encapsulating shell must have sufficient porosity to allow access to the active metal NP. Furthermore, diffusion limitation across the shell thickness is also of concern. To the best of our knowledge, mass transfer studies across a porous silica shell have not been reported.

Kinetic models are crucial for a successful reactor design. Ideally, a kinetic model is based on the reaction mechanism and considers the phenomena that occur on the catalyst surface. Langmuir–Hinshelwood,[38] Eley–Rideal,[39] and Mars–van Krevelen[40,41] mechanisms have been proposed for the combustion of methane over Pd catalysts under various reaction conditions.

While methane combustion on monometallic Pd and Pt has been studied extensively, far less research has been dedicated to bimetallic Pd-Pt catalysts. Additionally, considering the more recent experimental and computational observations regarding wet CH_4 combustion on bimetallic Pd-Pt catalysts, a need for updated kinetic models and rate expressions that take into account the plausible surface phenomena has emerged. Even though some models have been used in the past to predict both wet and dry combustion conversions, the observed differences in the chemical state of Pd during the reaction in the presence and absence of water[29] reinforce the idea that the rate expressions might be different for wet and dry conditions.

This work presents a kinetic study of lean methane combustion on bimetallic Pd-Pt@SiO_2 catalysts in the presence and absence of added water (5 vol.%). To improve the kinetic predictions in the presence of water, a new model based on earlier experimental observations is suggested. The corresponding rate equation provides accurate predictions in the range of (550-750 K) for the wet data. In addition, for the first time in the literature, the diffusion equation across a porous silica shell is solved here and the role of internal mass transfer limitations across metal@SiO_2 systems is elucidated.

4.2 Experimental and modeling procedures

4.2.1 Catalyst preparation

The bimetallic Pd-Pt@SiO_2 catalyst was prepared and characterized using the synthesis and characterization procedures explained in detail previously.[42] The final catalyst was composed of bimetallic Pd-Pt nanoparticles of 9 nm in diameter encapsulated in porous silica shells of 70 nm in outside diameter. After the synthesis, the catalyst was calcined in static air at 550 °C for 16 h. To simulate the long term ageing in real exhaust conditions, prior to performing kinetic experiments, the catalyst was hydrothermally aged at 550 °C under a wet combustion environment (4000 ppmv CH_4, 5 vol.% water, total flow rate of 223 mL/min) for 170 h. The physical properties of the "aged" catalyst are given in Table 4.1.[42]

Table 4.1. The physical properties of the aged PdPt@SiO_2 catalyst

Catalyst	Pd wt.%	Pt wt.%	Metal dispersion, %	Surface area, m^2/g	Pore volume, mL/g	Pore diameter, nm	Core diameter, nm	SiO_2 shell diameter, nm
aged Pd-Pt@SiO_2	4.21	6.98	9	592	0.47	3.4	9	70

We make a few further comments about the catalyst structure. The measured surface area of the silica shells can be used in conjunction with the measured mean pore diameter to calculate the approximate shell porosity. Assuming that the non-porous silica would be amorphous with a density of 2200 kg/m^3, we can use the parallel pore model to estimate the shell porosity at 52.5%. TEM analysis of the catalyst particles reveals that on average there were multiple cores in a shell. Using the data in Table 4.1, and the calculated shell porosity, we can estimate that there were on average about 3.7 cores in each porous shell. The calculations are shown in the supplementary information (Appendix B).

4.2.2 Kinetic experiments

The catalytic combustion experiments on the aged catalyst were performed under lean conditions in the presence or absence of water in the feed gas similar to our previous work.[42] A catalyst mass of 96 mg (4.21 wt.% Pd and 6.98 wt.% Pt) was packed into a 51 cm long micro-catalytic fixed bed reactor tube, which had an inner diameter of 9.2 mm. Layers of quartz wool were used at each end of the catalytic bed to contain the catalyst particles within the reactor. The reactor tube was placed inside of a tubular furnace equipped with a PID temperature controller. The temperature at each end of the catalytic bed was measured using K-type thermocouples that were inserted into the reactor and touched the ends of the bed. The difference in the temperature readings of these two thermocouples was less than 1 °C and their average is reported here as the reaction temperature. The gases used in the reaction, a mixture of methane and nitrogen (10 % CH_4/N_2) and extra dry compressed air, were purchased from Praxair. The flow rate of the feed gases was controlled by mass flow controllers (Matheson and MKS). All of the reported gas flow rates are based on STP conditions (0 °C and 1 atm). The feed consisted of a gas mixture of 10 vol % CH_4 in N_2 (2.2 -11.2 ml min^{-1} depending on the desired initial CH_4 concentration) and air (extra-dry, 205 mL min^{-1}). During the hydrothermal ageing and in wet combustion experiments, water was injected at a controlled rate into the reactor feed line using a syringe pump to give 5% by volume. The feed line was heated to vaporize the water. The post combustion gas stream was passed through a cold trap to remove water vapour, and then analyzed using an online Agilent HP-7890-A gas chromatograph equipped with a thermal conductivity detector (TCD) and a flame ionization detector (FID) in series.

The conversion data were obtained on the aged catalyst at various inlet concentrations of CH_4 in the presence or absence of 5 vol.% water vapour in the feed gas by performing steady-state ignition tests at a constant pressure of 287.5 kPa. The inlet CH_4 concentrations varied from 1000 to 5000 ppmv and were tested in the following order: 1000, 5000, 2000, 4000, 3000 ppmv of CH_4. Each ignition curve was obtained at a constant inlet CH_4 concentration by increasing the reaction temperature stepwise from 250 to 450 °C (25 °C for each step at a ramping rate of 10 °C min^{-1}). The temperature was held constant at each stage for 5 minutes. After the ignition test the reactor was cooled to 220 °C at a rate of 10 °C min^{-1} without methane and water in the feed, and then the next ignition test (at a different inlet CH_4 concentration in the absence or presence of water) was performed. The first set of ignition tests was performed at five inlet CH_4 concentrations in dry conditions, and then at the same five initial concentrations in wet conditions. To verify the reproducibility of the obtained data and to minimize the experimental error, a second set of dry and wet ignition tests was performed at the previous initial CH_4 concentrations in the same test order used in the first set of experiments. The conversion data of both sets of runs were directly used in the optimization.

4.2.3 Reactor model and optimization

The kinetic parameters in the proposed models were determined using a nonlinear optimization routine coupled to an integral model for the reactor. In this analysis the steady-state mole balance in the ideal packed bed plug flow reactor with no pressure drop was solved to predict the conversion data that were then compared to the experimental results. The insignificance of the wall effects and axial dispersion effects on the plug flow assumption was verified using the criteria from the literature.[43,44] The Mears criterion was calculated similar to previous work[42] and showed that the external mass transfer limitations (MTL) and external temperature gradients were negligible.

The nonlinear optimization problem was solved using MATLAB with the Pattern Search algorithm. The objective function, O, was defined using the fractional conversion X as:

$$O = \frac{1}{N}\sum_{i=1}^{N}\left(X_{\text{Predicted}} - X_{\text{Experimental}}\right)^2 \qquad 4.1$$

Rate and adsorption equilibrium constants were expressed in terms of an Arrhenius and a van't Hoff's expressions, respectively, assuming constant heats of adsorption:

$$k_i = A_i \exp\left(\frac{-E_i}{R_g T}\right) \quad 4.2$$

$$K_i = B_i \exp\left(\frac{\Delta H_i}{R_g T}\right) \quad 4.3$$

The data at dry and wet conditions were optimized separately. The conversion data for all of the concentrations and temperatures (the experimental conversions ranging from approximately 8–80%) from both sets of the experimental runs were used in each optimization.

4.3 Results and discussions

4.3.1 Kinetic study: experimental results

The ignition results of the aged Pd-Pt@SiO_2 from two sets of experimental runs for an initial CH_4 concentration of 4000 ppm in the presence and absence of 5% added H_2O are presented in Figure 4.1. As indicated in Figure 4.1, the obtained experimental points were highly

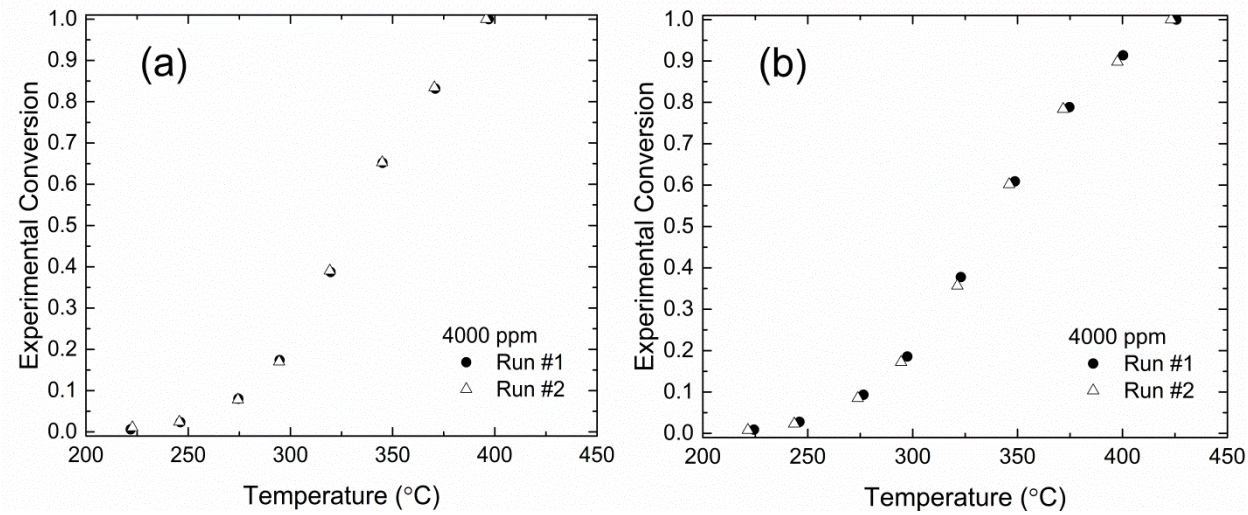

Figure 4.1. Reproduciblity of the experimental data obtained at an initial CH_4 concentration of 4000 ppm a) dry feed, and b) 5 mol % H_2O added to the feed.

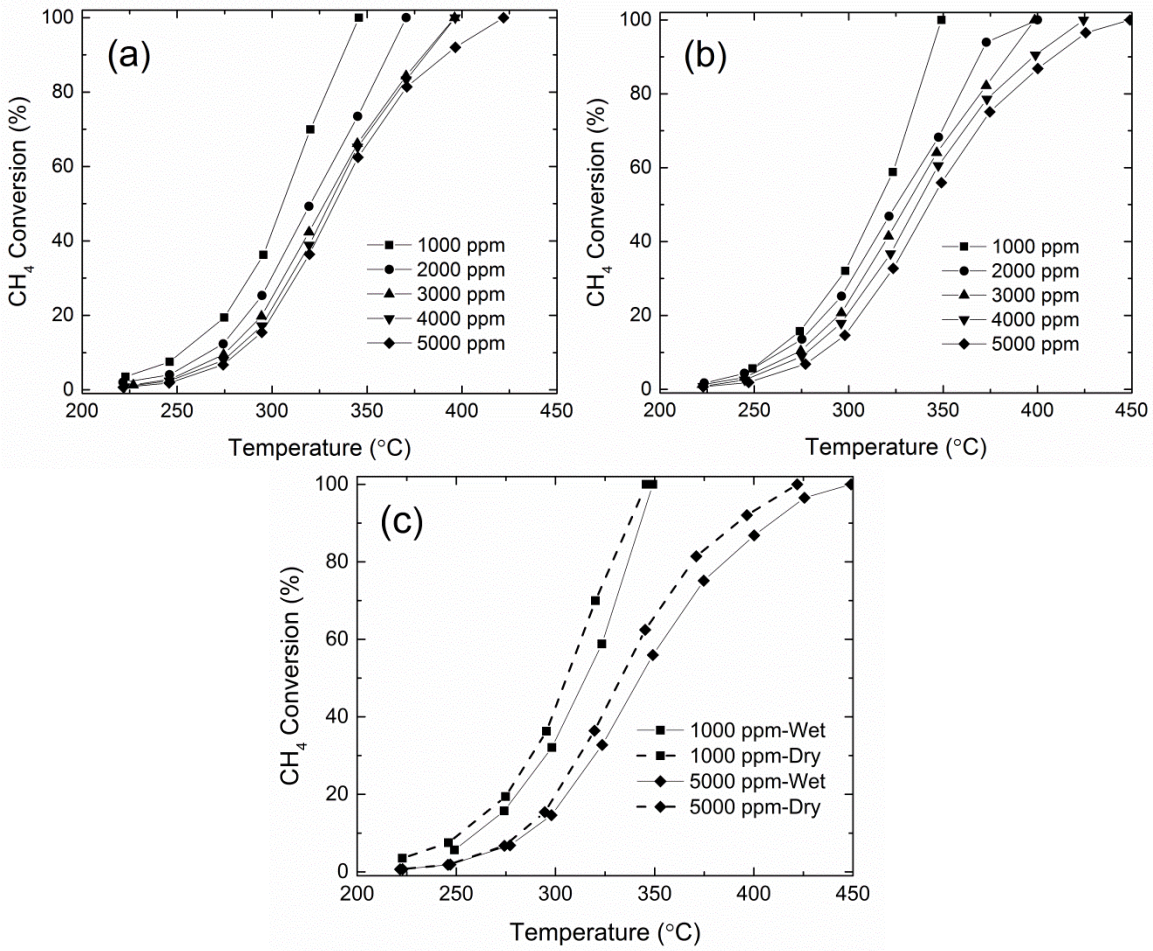

Figure 4.2. Ignition curves (average of the two experimental runs) at various initial CH_4 concentrations. a) dry feed, b) 5 mol % H_2O in feed and c) summary of the effect of water and initial concentration on the ignition curves.

reproducible at this concentration. The reproducibility of the experimental points at other initial CH_4 concentrations (1000, 2000, 3000, and 5000 ppm) is shown in Figure B.1 (for dry conditions) and Figure B.2 (for wet conditions). Since the difference between the two experimental runs were negligibly small (Figures 4.1, B.1 and B.2), for a better presentation of the results, the ignition curves were plotted using the average of the two experimental runs (Figure 4.2). Figures 4.2a and 4.2b, present the ignition curves at different methane concentrations in dry and wet conditions, respectively Figure 4.2c summarizes the effect of initial CH_4 concentration and the effect of added water. For the sake of clarity only two concentrations are included in Figure 4.2c. Figure 4.2 shows that at a given temperature in both dry and wet conditions, the conversion decreases as the inlet CH_4 concentration increases. Also,

as expected,[24,45] the conversion at a constant CH_4 concentration and temperature is lower when 5% water is added to the feed stream. In the latter case, the 50% conversion point is about 5 °C higher, and the 100 % conversion point is about 25 °C higher.

4.3.2 Kinetic modeling

4.3.2.1 Previous work on monometallic Pd and Pt catalysts

There is an extensive literature on the catalytic combustion of methane, most of which deals with Pd catalysts.[38-41] The oxidation state of Pd is an important factor in the catalytic behaviour. Many experiments and thermodynamic calculations have shown that PdO is more active than reduced Pd.[46-48] The reaction mechanism is also agreed to depend on the oxidation state of Pd.[46,47] In a detailed mechanistic assessment Chin et al.[46] studied the potential pathways of C-H bond activation on metallic Pd, Pd surfaces saturated with chemisorbed oxygen (O*) and PdO. They proposed that C-H bond activation on metal atom pairs (*-*), oxygen atom pairs (O*-O*) and Pd cation lattice oxygen pairs (Pd^{2+}+-O^{2-}) in PdO occurred via oxidative addition, H-abstraction, and σ-bond metathesis pathways, respectively.[46,49] PdO was proven to have the lowest activation barrier among the three active species (Pd^0: 84 kJ mol^{-1},[50] O*-saturated Pd^0: 158 kJ mol^{-1},[46] and PdO: 61 kJ mol^{-1} [46]). First principle investigations of Van Den Bossche et al.[51] also suggest that, depending on the temperature, dry methane oxidation on PdO (101) facet (which is the most active surface of Pd for methane combustion[52]) occurs through two routes: in the low temperature region (500-630 K) the reaction involves an early insertion of oxygen in carbonaceous species and C−H breakage by reaction with OH groups. At high temperatures (900−1000 K) the OH-coverage is low, favoring C−H bond breakage through reaction with lattice oxygen atoms. They also pointed out that at low temperatures water adsorbed on under-coordinated Pd-sites and that the dissociative adsorption of methane was the sole rate determining step (RDS) only at high temperatures.[51] Using microcalorimetry, Xin et al.[53] showed that dry CH_4 combustion on PdO is pseudo first order with respect to the methane concentration. They showed that over the range of 560-800 K, the reaction rate is determined by the dissociative adsorption of CH_4 on the PdO surface which accounts for the effects of surface oxygen coverage and the intrinsic rate of dissociative CH_4 adsorption on a vacant Pd site

surrounded by PdO.[53] Specchia et al.[54] investigated several rate models and concluded that dry methane combustion on $PdO/Ce_xZr_{1-x}O_2$ catalyst occurred through a Mars–van Krevelen mechanism which was based on a reduction and reoxidation step by non-dissociative oxygen, taking into account the dissociation rate of the adsorbed molecular oxygen. Recent *in situ* X-ray absorption spectroscopy (XAS) observations have shown that in dry combustion conditions (473-773 K), monometallic Pd exists in the PdO form.[55] Wet combustion on monometallic Pd was reported to be independent of oxygen and CO_2 concentrations and have an order of 1 and -1 with respect to CH_4 and water.[56,57]

In situ XAS have shown that Pd^0 is readily oxidized in lean dry combustion (473-823 K);[29] however, oxidation to a PdO state is gradual in wet combustion and occurs with an increase in temperature.[29] The RDS of wet combustion on monometallic Pd at temperatures below 723 K was suggested to be the water desorption from the catalyst surface[7] while it is typically the methane activation step at higher temperatures.[57]

Models consistent with these mechanistic observations have been proposed. In the absence of water inhibition terms, a classical power law was proposed in early works,[38,58,59] that is:

$$\left(-R_{CH_4}\right) = k\left[CH_4\right]^m\left[O_2\right]^n \tag{4.4}$$

where typically *m* is near unity and *n* is near zero in most examples.[58,59] Water is known to have a strong inhibition effect on Pd catalysts, so a corresponding term should be included as:[60,61]

$$\left(-R_{CH_4}\right) = k\left[CH_4\right]^m\left[O_2\right]^n\left[H_2O\right]^l \tag{4.5}$$

The power on water concentration, *l*, is often close to negative one.[60,61] For large concentrations of water, the concentration would be essentially constant, and Equation 4.5 would collapse to the form of Equation 4.4. Mechanistically based models (usually following Mars-van Krevelen and Langmuir-Hinshelwood approaches) have also have been proposed. In an early kinetic study, Mezaki and Watson[62] compared a large number of models and proposed that the RDS could be the surface reaction between gaseous methane and adsorbed oxygen. Using a Mars-van Krevelen mechanism, Golodets [63] developed the equation for methane oxidation:

$$\left(-R_{CH_4}\right) = \frac{k_1\left[CH_4\right]}{1+k_2\left\{\left[CH_4\right]/\left[O_2\right]\right\}} \tag{4.6}$$

This model can be extended to include water inhibition effects [63,64] to give:

$$\left(-R_{CH_4}\right) = \frac{k_1\left[CH_4\right]}{1+k_2\left\{\left[CH_4\right]/\left[O_2\right]\right\}+K_3\left[H_2O\right]} \qquad 4.7$$

If adsorbed water is the most abundant surface intermediate (MASI), this model simplifies to:

$$\left(-R_{CH_4}\right) = \frac{k_1\left[CH_4\right]}{1+K_3\left[H_2O\right]} \text{ (hereafter referred to as Model 1)} \qquad 4.8$$

Hayes et al.[56] used a model of the form of Equation 4.8 (hereafter referred to as Model 1) with values of k_3 adapted from Mezaki and Watson[62] to correlate data for the catalytic combustion of methane over a Pd catalyst both with and without water added to the feed. They found a good agreement with experimental results, and confirmed that the water produced in the combustion reaction must be included in the rate model. Later, by assuming methane oxidation to be the RDS and a Langmiur isotherm for adsorbed water, Kikuchi et al.[65] used the same rate expression to model wet methane combustion on an alumina-supported PdO catalyst. It should be noted that the experiments in these two studies covered a large temperature interval (473-873 K).

More recent DFT-based postulations of Qi et al.[66] proposed a sequence of elementary reactions to be relevant in dry CH_4 combustion on a Pd catalyst which assumed the dissociation of CH_4 on matched pair sites to be the RDS. The proposed rate equation in the special case of OH* species being the MASI is simplified into Equation 4.5 with m=1, n=0, and l=-1.

Kinetic and modelling studies on Pt catalysts have also been reported.[24,67-69] Unlike PdO, for Pt catalysts the metallic state is active in methane activation.[10,70,71] Also, Pt is known for its low activity in lean methane combustion.[10,70] The sticking coefficient of oxygen on Pt is 15 times higher than that for methane[72] thus in lean conditions Pt is severely blocked by oxygen and becomes unavailable for methane dissociation.[73] In the presence of high concentrations of oxygen, water inhibition on Pt is shown to be negligible even at high H_2O concentrations [66] and the reaction is reported to be first order with respect to CH_4 and zeroth order with respect to water and oxygen.[24,67] Hence, the generally accepted rate equation for a monometallic Pt catalyst has the form [24,67,74]

$$\left(-R_{CH_4}\right) = k\left[CH_4\right] \qquad 4.9$$

Considering methane reacting from gas phase and the initial H-abstraction step by chemisorbed oxygen on Pt to be the RDS, Qi et al.[66] developed a rate equation that in the special case of O* being the MASI, simplifies to Equation 4.9.

4.3.2.2 Previous work on bimetallic Pd-Pt catalysts

Kinetic studies on bimetallic Pd–Pt systems are less prevalent than for either monometallic Pd or Pd. As discussed above, the chemical state of the catalyst is a fundamental element in determining the reaction mechanism. Martin et al.[75] observed that in Pd−Pt/Al_2O_3 structures under oxidizing conditions, Pd segregates to the shell and forms PdO. In a detailed DFT-based and experimental study of lean-burn methane conversion in a dry feed (conversions <10%), Qi et al.[66] classified the studied Pd-Pt catalysts with various metal ratios as "Pd-like" and "Pt-like" surfaces. The mechanism on "Pd-like" catalysts includes methane dissociation of pair sites of unsaturated metal and adjacent oxygen as an RDS, while on "Pt-like" catalysts methane reacts from a gas phase with initial H abstraction by chemisorbed oxygen being the RDS. A rate expression in the form of Equation 4.5 was used to model the kinetic data. The reaction orders with respect to water on $Pd_{0.75}Pt_{0.25}$, $Pd_{0.5}Pt_{0.5}$ and $Pd_{0.25}Pt_{0.75}$ were -1.05, -0.98 and -0.79, respectively.[66] Their mechanism is consistent with Pt being poisoned by oxygen in the dry feed and thus being unavailable for methane activation.[29]

Abbasi et al.[24] used an empirical rate equation to model combustion data on a commercial bimetallic Pd-Pt catalyst with and without water added to the feed. Their model had the form:

$$\left(-R_{CH_4}\right) = \frac{k_1\left[CH_4\right]}{\left(1+K_2\left[CH_4\right]+K_3\left[H_2O\right]\right)^n} \qquad 4.10$$

They reported that K_2 was essentially zero, and that n had a value of 1, thus their model was equivalent to Equation 4.8. Note that this catalyst was Pt rich, with four times the Pt as Pd on a mass basis. Their finding of an n value of 1 is consistent with the earlier work of Hayes et al.[56] and others [60,61] who observed that the power with respect water is about -1 for Pd and Pd-Pt catalysts. Recent *in situ* XAS analyses in the dry and wet feed indicated that for a bimetallic Pd-Pt catalyst and in the presence of water (473-773 K) the metallic Pd^0 and Pt^0 were the prevailing

catalytic species [29,55] with gradual oxidation of Pd to PdO as temperature increased from 473 to 773 K [29,55] but no kinetic modelling or model derivation was performed.

4.3.2.3 Kinetic modeling results (this work) Model 1 (Equation 4.8)

The ignition curves shown in Figure 4.2 demonstrate that the fractional conversion decreases with an increase in inlet methane concentration, everything else being equal. This result is consistent with those observed by Hayes et al.[56] for monometallic Pd and Abbasi et al.[24] for a bimetallic Pd-Pt catalyst. Furthermore, the fact that this behavior was observed with both wet and dry runs indicates that the effect of water produced in the reaction is significant. In both of the earlier investigations, Model 1 was able to correlate data for both dry and wet feed, therefore testing this model was a logical first step. As stated earlier, the conversion data of the two sets of experiments were directly used in the modelling, and the wet and dry data were optimized separately. The results from the best fit parameters are shown in Figure 4.3. Figure 4.3a shows the parity plot that compares the experimental and predicted conversions obtained from Model 1 for the dry data, along with the plus and minus 10 % error lines. Figure 4.3b shows the same for the wet data. Considering Figure 4.3, we see that for the experiments conducted with dry feed there is a good correlation between the experimental and predicted values, with a

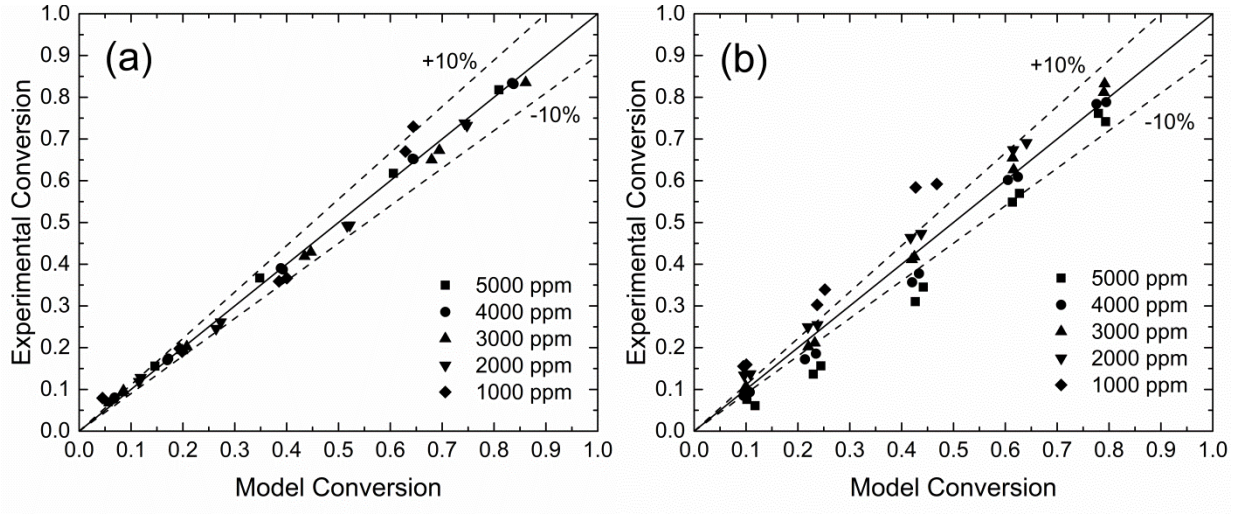

Figure 4.3. Comparison of the experimental and model conversions using Model 1 for (a) dry feed and (b) with 5 mol % H_2O added to the feed.

maximum deviation between the two being less than or equal to 10 %. However, it is clear that the results with the wet feed are not acceptable. Although some of the predictions are within 10% of the experimental values, the trends shown in Figure 4.3b are not consistent with the experiments. The model predictions do not show a significant effect of inlet concentration of methane; that is, all of the model predictions at a given reactor temperature are the same, regardless of the inlet methane concentration. It is an interesting result, and one that is different from the two cited works that addressed Pd-Pt catalysts with a different metal loading and metal ratio on the supports other than silica.[24,56] We conclude, therefore, that while Model 1 is suitable for the case of dry feed, it is not acceptable with large excess of water present. The parameters for the dry feed case are:

$$\left(-R_{CH_4}\right) = \frac{44{,}594\exp\left(\frac{-28{,}853}{R_g T}\right)[CH_4]}{1 + 2.51\times10^{-7}\exp\left(\frac{131{,}592}{R_g T}\right)[H_2O]} \quad \frac{\text{mol}}{\text{kg}_{\text{catalyst}}\text{s}} \qquad 4.11$$

The concentrations have units of mol/m^3. The light-off curve at an initial CH_4 concentration of 4000 ppm (dry conditions) produced using Equation 4.11 along with the experimental points are presented in Figure 4.4. Similar plots for other initial CH_4 concentrations (1000, 2000, 3000, and 5000 ppm) are given in Figure B.1.

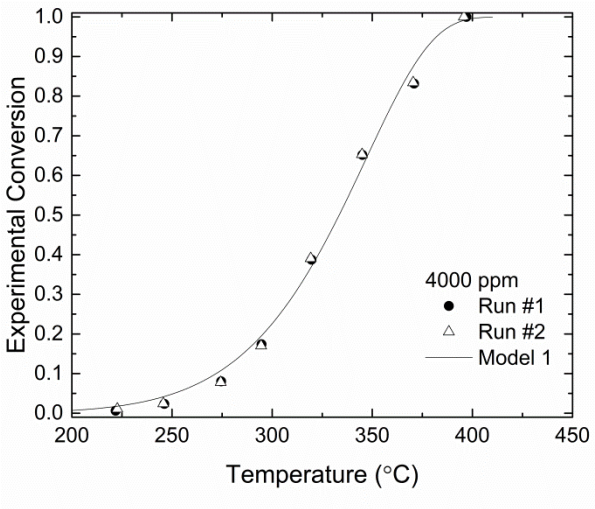

Figure 4.4. The predicted ignition curve produced by Model 1 and the experimental points. Reaction in dry conditions and at an initial CH_4 concentration of 4000 ppm.

4.3.2.4 Kinetic modeling results (this work) Model 2 for the wet feed

To develop a rate expression capable of producing more accurate predictions for a bimetallic Pd-Pt catalyst for the wet feed, it is necessary to understand the effect of the presence of water on active sites, especially given that water is also produced as a combustion product and is present in the reacting system even in the case of dry feed. In this respect, we would like to refine the definition of "dry" and "wet" conditions for the catalytic methane combustion and base our classification not on the presence or absence of added water to the feed, but on the effect of water on the oxygen availability to active sites. Our recent *in situ* XAS experimental study of originally reduced Pd in methane combustion without and with added water (5%, same as in the current work) revealed that in the "dry" feed metallic Pd was fully oxidized already at 200 °C and maintained its oxidized form up to 500 °C, when full conversion was achieved.[29] However, when water was added, Pd remained in its metallic form at 200 °C and gradually oxidized with temperature rise up to 500 °C. Thermodynamic analysis showed that this is only possible if there is a deficiency of oxygen available to active sites.[29] Our *in situ* XAS findings [29] are in agreement with earlier works of L. Pfefferle's group[6] which provided evidence that water inhibits the migration of oxygen on the support and its exchange between the support and PdO. Thus, when no water is added in the studied "dry" feed, there is enough oxygen in the vicinity of the active sites, but in the "wet" feed (5% water), there is a significant surface oxygen deficit. At present, there are no experimental *in situ* XAS data to provide a clear guidance on the dependence of oxygen availability on water concentration and temperature.

Considering the PdPt system, in the dry feed, Pt is blocked by oxygen, because the sticking coefficient of oxygen on Pt is 15 times higher than that for methane.[72] In the lack of oxygen, Pt sites are free for methane activation[10,70,71,76], and as we showed earlier,[29,77] the PdPt system is significantly more active than Pd and Pt alone in the wet feed, but less active than PdO in the dry feed. The water presence, thus, affects the contribution of Pt and Pd/PdO to methane activation via its temperature-dependent effect on oxygen mobility and oxygen exchange.

Based on these experimental studies by L. Pfefferle's, Burch's and our group, we suggest that a universal model for PdPt-catalyzed methane combustion should include PdO active sites as the most active for methane activation and metallic Pt active sites. Although metallic Pd is

known for methane activation, in the presence of low amounts of chemisorbed oxygen (without PdO formation), its methane activation capability is significantly suppressed (the activation barrier for methane activation on Pd^0, O*-saturated Pd^0 and PdO is 84 kJ mol^{-1},[50] 158 kJ mol^{-1},[46] and 61 kJ mol^{-1} [46], respectively). PdO is the dominant species in our defined "dry" feed (in the excess of local surface oxygen). In the wet feed, at the local oxygen deficit, metallic Pd and Pt sites prevail but metallic Pd alone was significantly less active than the PdPt combination[29,55,77] indicating the dominant contribution of Pt active sites for methane activation in the lack of oxygen.

Oxygen activation for combustion occurs on palladium active sites. PdO is formed in the excess of oxygen in the dry feed, while chemisorbed oxygen is prevalent at low oxygen concentration without PdO formation.[46] The activated oxygen species exchange with the lattice oxygen on the support[6] which is suppressed at high oxygen concentration and at low temperatures. The interplay between all these active sites for methane and oxygen activation strongly depends on the water concentration and temperature. Although we suggest this universal mechanism to cover all ranges of temperatures and water concentrations, we advocate against a universal model because of a large number of adjustable parameters (temperature-dependent rate constants and adsorption constants for the multiple active sites and parallel activation modes and the RDS dependence on the reaction conditions). In addition, the practical applications of "dry" and "wet" feed conditions are different and simple models for each of these cases are preferable both from the application and statistically-sound mechanistic viewpoints.

Thus, below we propose a simplified mechanism, based on the above considerations [8,29,46,55], that is valid for T<723 K (where water inhibition effects are significant[11]). For the model development, we assume the existence of two types of active sites: 1) Pd sites for activating oxygen and 2) Pt sites for activating CH_4. The surface reaction between the adsorbed CH_4 and active oxygen (O*) is assumed to be the RDS with the following H-abstraction steps being kinetically insignificant.[57] The origin of the active O* here is defined as established by Pffefrele and colleagues:[6,8] Pd dissociates gas-phase O_2 and delivers it to the support (S). The presence of water suppresses the oxygen availability[29] via hydroxylation of the catalyst surface as shown by ref [6] and [9], which agrees with our earlier *in situ* XAS analyses.[29] Metallic Pd with chemisorbed oxygen is unable to activate methane due to a very high activation energy (as calculated by Chin

et al.[46]), however, its presence is essential for the reaction to deliver the activated O* to the support surface. When lattice O from the support is consumed, O can diffuse from the support bulk only for supports with high O mobility such as ZrO_2 at higher temperature.[8] For Al_2O_3 and SiO_2, the oxygen vacancy on the support (S) surface should be replenished from the gas phase via dissociative chemisorption on metallic Pd followed by the oxygen exchange:

$$2\ Pd + O_{2\ (gas)} \leftrightarrow 2PdO \qquad 4.12$$

$$PdO + S \leftrightarrow Pd + SO \qquad 4.13$$

Water also adsorbs on the support impeding oxygen mobility and exchange as shown by [6,7,9,15] :

$$SO + H_2O \leftrightarrow SO{\bullet}H_2O \qquad 4.14$$

Pt sites activate methane:

$$Pt + CH_4 \leftrightarrow Pt{\bullet}CH_4 \qquad 4.15$$

The RDS is suggested as a first hydrogen abstraction from methane. Equation 4.16 shows a cumulative reaction of several elementary steps where further hydrogen abstractions are kinetically irrelevant:

$$Pt{\bullet}CH_4 + SO \rightarrow CO_2{\bullet}Pt + SO{\bullet}H_2O \qquad 4.16$$

The catalytic cycle is closed with the fast and equilibrated CO_2 desorption:

$$CO_2{\bullet}Pt \leftrightarrow CO_2 + Pt \qquad 4.17$$

Rate of the RDS (Equation 4.16) is:

$$\left(-R_{CH_4}\right) = k\,\theta_{CH_4}\theta_{SO} \qquad 4.18$$

Because Pd is affected by water, methane is only adsorbed on Pt:

$$\theta_{CH_4} = K_{CH_4}\left[CH_4\right]\theta_{Pt} \qquad 4.19$$

$$\theta_{CH_4} + \theta_{Pt} + \theta_{CO_2} = 1 \qquad 4.20$$

CO_2 coverage is assumed to be negligible, hence:

$$\theta_{Pt} = \frac{1}{\left(1 + K_{CH_4}\left[CH_4\right]\right)} \qquad 4.21$$

The support surface balance is:

$$\theta_{SO} + \theta_{SO\bullet H_2O} + \theta_S = 1 \tag{4.22}$$

At temperatures below 450 °C the surface is hydroxylated,[9] therefore:

$$\theta_S \approx 0 \tag{4.23}$$

$$\theta_{SO\bullet H_2O} = K_{H_2O}\theta_{SO}[H_2O] \tag{4.24}$$

$$\theta_{SO} = \frac{1}{K_{H_2O}[H_2O]} \tag{4.25}$$

The reaction rate is then written as:

$$\left(-R_{CH_4}\right) = \frac{k K_{CH_4}[CH_4]}{\left(1 + K_{CH_4}[CH_4]\right) K_{H_2O}[H_2O]} \tag{4.26}$$

Lumping the constants gives the final result:

$$\left(-R_{CH_4}\right) = \frac{k'[CH_4]}{\left(1 + K_{CH_4}[CH_4]\right)[H_2O]} \tag{4.27}$$

This model is referred to as Model 2. The parity plots for Model 2 for both dry and wet feeds are given in Figure 4.5. It is clear that the model does not fit for the dry feed case (Figure 4.5a), but its predictions for the wet kinetic data are reasonable (Figure 4.5b), and it captures the trend of decreasing conversion with increased feed methane concentration. We note that this rate expression was specifically developed for, and is meant to be used in, lean CH_4 combustion on a bimetallic PdPt catalyst in the presence of excess of water. The model with the optimized parameters for the wet feed case is given below (Equation 4.28). Note that the nominator terms are lumped parameters. The methane adsorption term is not neglected, (unlike the case of Model 1), because of different involved active sites (Pt for Model 2 and PdO for Model 1). The calculated enthalpy of adsorption of methane on Pt (83.59kJ/mol) is consistent with a calorimetric study that reported the heats between 60 and 150 kJ/mol depending on methane coverage.[78]

$$\left(-R_{CH_4}\right) = \frac{150\exp\left(\frac{-36,251}{R_g T}\right)[CH_4]}{\left(1 + 3.33\times10^{-7}\exp\left(\frac{83,591}{R_g T}\right)[CH_4]\right)[H_2O]} \quad \frac{\text{mol}}{\text{kg}_{\text{catalyst}}\text{s}} \tag{4.28}$$

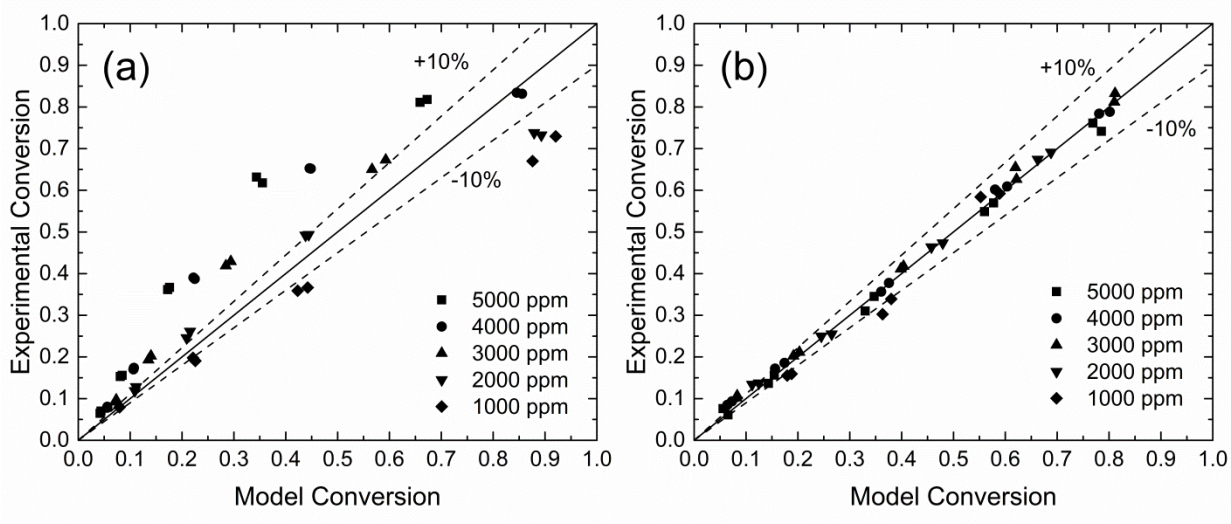

Figure 4.5. Comparison of the experimental and model conversions using Model 2 for (a) dry feed and (b) with 5 mol% water added to the feed.

The ignition curve at an initial CH_4 concentration of 4000 ppm (wet conditions) produced using Equation 4.28 along with the experimental points are presented in Figure 4.6. Plots for other initial CH_4 concentrations (1000, 2000, 3000, and 5000 ppm) are given in Figure B.2.

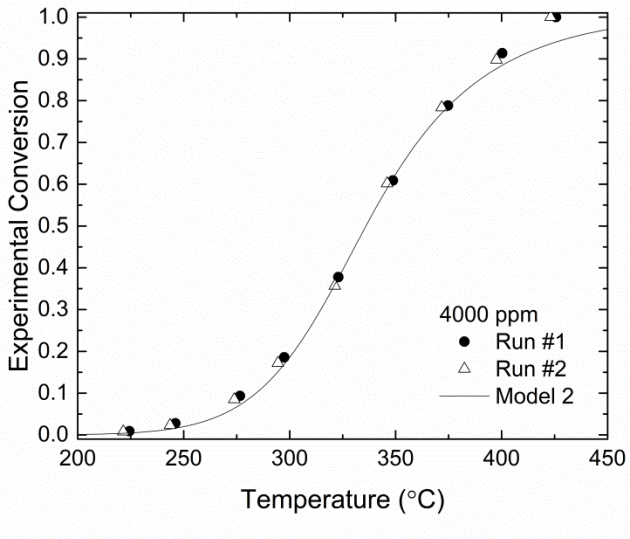

Figure 4.6. The predicted ignition curve produced by Model 2 and the experimental points. Reaction in the presence of 5 mol% H_2O and at an initial CH_4 concentration of 4000 ppm.

4.3.3 Diffusion in the porous shells

It is evident that the porous shell must have a sufficient porosity to allow access to the active metal nanoparticle, as shown previously.[37] The porosity determines the fraction of the metal surface that is exposed to the diffusing reactants. In the following calculations, the equations for an apparent effectiveness factor are developed, and the possible influence of diffusion across the shell on the results given here is determined. To develop the calculations for the real case would be fairly complex, because as noted earlier we have multiple cores in the shell. Therefore we will use a simplified analysis, but one that represents the worst case scenario.

We will consider the case of a single metal nanoparticle surrounded by a porous silica shell. Assume that the metal nanoparticles form a sphere of radius r_1, surrounded by a shell with outside radius r_2. Assume further that the particle and shell are symmetrical such that a one dimensional analysis can be performed. Using the classical approach which assumes diffusion across the entire area, the mole balance in 1D is:

$$\frac{1}{r^2}\frac{d}{dr}\left(r^2 D_{\text{eff}}\frac{dC}{dr}\right) = 0 \qquad 4.29$$

D_{eff} is the effective diffusion coefficient based on the total cross sectional area of the shell. The boundary conditions are then:

$$\text{at} \quad r = r_1 \qquad D_{\text{eff}}\frac{dC}{dr} = \varepsilon\left(-R_A(C_1)\right) \qquad 4.30$$

$$\text{at} \quad r = r_2 \qquad C = C_2 \qquad 4.31$$

In Equation 4.30, $\left(-R_A(C_1)\right)$ is the rate expressed in terms of the surface metal and is evaluated at the interface concentration, C_1, and ε is the shell porosity. Note that $\varepsilon\left(-R_A(C_1)\right)$ thus represents the maximum possible rate for a given particle of a specified shell porosity. For a narrow pore size distribution the effective diffusivity can be found using the parallel pore model of Wheeler.[79]

$$D_{\text{eff}} = \frac{\varepsilon}{\tau}D_{\text{P}} \qquad 4.32$$

τ is the tortuosity factor. The diffusion coefficient in the pores, D_P, is essentially equal to the Knudsen diffusion coefficient for the small pores in the shell:

$$D_K = 97 r_p \sqrt{\frac{T}{M}} \tag{4.33}$$

Solution of Equation 4.29 subject to the boundary conditions gives an equation for the concentration profile in the shell:

$$C = C_2 + \left(\frac{1}{r_2} - \frac{1}{r}\right)\frac{r_1^2 \varepsilon\left(-R_A(C_1)\right)}{D_{\text{eff}}} \tag{4.34}$$

It follows that the concentration at r_1 is given by:

$$C_1 = C_2 + \left(\frac{1}{r_2} - \frac{1}{r_1}\right)\frac{r_1^2 \varepsilon\left(-R_A(C_1)\right)}{D_{\text{eff}}} \tag{4.35}$$

It is clear from this relationship that for a very thin shell, such that $r_1 \approx r_2$, then the two concentrations will be close. It further follows that, as the shell radius increases, there is a maximum concentration difference that will occur, given by:

$$\left(C_2 - C_1\right)_{\max} = \frac{r_1 \varepsilon\left(-R_A(C_1)\right)}{D_{\text{eff}}} \tag{4.36}$$

It is clear from our experiments that the highest reaction rate occurs in the absence of water, and thus we can use the rate expression obtained with the dry feed to determine the maximum effect of diffusion resistance. Furthermore, let us consider the extreme case with zero water concentration, which gives the maximum theoretical rate. Thus let the rate be approximated by:

$$\left(-R_{\text{CH}_4}\right) \approx k[\text{CH}_4] \tag{4.37}$$

The methane concentration in Equation 4.37 corresponds to C_1 in Equation 4.35, which can then be written, after substitution, as:

$$C_1 = \frac{C_2}{1 + \left(\frac{1}{r_1} - \frac{1}{r_2}\right)\frac{r_1^2 \varepsilon k}{D_{\text{eff}}}} \tag{4.38}$$

The effectiveness factor is defined as the ratio of the observed rate to the rate evaluated at the external surface concentration:

$$\eta = \frac{1}{1 + \left(\frac{1}{r_1} - \frac{1}{r_2}\right)\frac{r_1^2 \varepsilon k}{D_{\text{eff}}}} \tag{4.39}$$

When the shell is thin, that is $r_1 \approx r_2$, then it is evident that the effectiveness factor will be close to one. As the shell thickness increases, then the influence of r_2 rapidly decreases, and it is clear that the importance of diffusion depends on the value of:

$$\frac{r_1 \varepsilon k}{D_{\text{eff}}} \tag{4.40}$$

The minimum value for the effectiveness factor occurs when this value is very large. Incorporating the definition of effective diffusion coefficient from Equation 4.32 then gives the lower asymptotic limit for the effectiveness factor as:

$$\eta_{\text{min}} = \frac{D_{\text{eff}}}{r_1 \varepsilon k} = \frac{D_K}{r_1 \tau k} \tag{4.41}$$

The minimum value of the effectiveness factor does not depend on the shell thickness or porosity. It is also clear from Equation 4.39 that for a small nanoparticle core, the rate constant must be many orders of magnitude larger than the diffusion coefficient for there to be a strong influence of diffusion resistance. We now re-write Equation 4.39 in the following explicit form, in terms of a real and apparent rate constant:

$$\frac{1}{\eta k} = \frac{1}{k_{\text{apparent}}} = \frac{1}{k} + \left(\frac{1}{r_1} - \frac{1}{r_2}\right)\frac{r_1^2 \varepsilon}{D_{\text{eff}}} \tag{4.42}$$

or:

$$\frac{1}{k} = \frac{1}{k_{\text{apparent}}} - \left(\frac{1}{r_1} - \frac{1}{r_2}\right)\frac{r_1^2 \varepsilon}{D_{\text{eff}}} \tag{4.43}$$

To determine the real rate constant from the actual one requires the conversion of the apparent rate constant, which is based on the total particle mass, to the value based on the total

nanoparticle external surface area. We define $(-R_A)$ as the reaction rate in terms of metal surface area, in mol/(m^2s). The reaction rate that is measured experimentally is denoted $(-R_W)$ and has units of mol/(kg_{cat}s), where the mass of catalyst refers to both nanoparticle and shell. For a fraction of exposed metal nanoparticle equal to the shell porosity, the two rates are related by:

$$\varepsilon(-R_A) = \frac{(-R_W)}{3}\left[r_1 \rho_M + \left(\frac{(r_2)^3 - (r_1)^3}{(r_1)^2} \right) \rho_S \right] \tag{4.44}$$

where ρ_S and ρ_M are the densities of the porous shell and the metal core with values of:

$$\rho_M = 16,715 \ \frac{\text{kg}}{\text{m}^3} \qquad \rho_S = 1045 \ \frac{\text{kg}}{\text{m}^3} \tag{4.45}$$

the rate expression for dry feed becomes:

$$\varepsilon(-R_A) = \frac{33.94 \exp\left(\frac{-28,853}{R_g T} \right)[\text{CH}_4]}{1 + 2.51\times10^{-7} \exp\left(\frac{131,592}{R_g T} \right)[\text{H}_2\text{O}]} \ \frac{\text{mol}}{\text{m}^2\text{s}} \tag{4.46}$$

The maximum temperature for the experiments was 700 K. We use this temperature to calculate the maximum deviation of the apparent rate constant from the real rate constant. With a mean pore diameter of 3.4 nm, the Knudsen diffusion coefficient at 700 K for methane is 1.09×10^{-6} m^2/s. Taking the tortuosity factor as 2, and substituting into Equation 4.43 gives

$$\frac{1}{k} = \frac{1}{0.2385} - \left(\frac{1}{4.5\times10^{-9}} - \frac{1}{35\times10^{-9}} \right) \frac{\left(4.5\times10^{-9}\right)^2 2}{1.09\times10^{-6}} = \frac{1}{0.2385} \tag{4.47}$$

It is clear that the effectiveness factor is unity. Note that all rates observed in this set of experiments would be lower than the maximum case used for this calculation, and therefore we can conclude that none of the experiments was influenced by diffusion resistance across the shell. We note again that the effectiveness factor does not depend on the porosity; however, as we showed before,[37] the shell must have sufficient porosity to allow for the reactants to have access to the active sites on the surface of the nanoparticle.

4.4 Washcoat loading

Ultimately the test of the practicality of a new catalyst for a catalytic converter is that it has sufficient activity to give a small volume converter. One measure is the loading of PGM in the washcoat. Although it is not really the scope of this work to develop a washcoated monolith, we offer some ballpark estimates. The standard measure of PGM loading in an automotive catalytic converter is grams of PGM per cubic foot of monolith. As a rough estimate, a typical converter of cell density 400 CPSI is comprised of about 12% by volume washcoat. For the sake of illustration, we assume that the final washcoat has a porosity of 36%, thus a cubic foot of monolith contains 0.077 ft^3 of catalyst. Thus, assuming that the entire washcoat was composed of catalyst, the PGM loading would be about 285 g/ft^3. Typical PGM loadings for current commercial NGV exhaust systems are of the order of 100 – 200 g/ft^3, thus we are able to achieve higher loadings than existing catalysts and have a sinter free environment.

4.5 Conclusions

A kinetic study of methane combustion on silica encapsulated bimetallic Pd-Pt catalyst has been presented. Two rate equations were necessary to describe the kinetics, one for the case of dry feed and for the case of wet feed, when water suppresses the availability of oxygen to active sites and shifts methane activation from PdO (in the dry feed) to Pt (in the wet feed) active sites. The rate equation for dry feed (Model 1) was based on one previously published, whilst the one for wet feed is new (Model 2), and is based on a proposed mechanism that applies when a large excess of water is present. For the kinetic modelling, methane concentrations and temperatures were varied for 0 and 5 vol.% water in the feed. Care should be taken when extrapolating the models to other water concentrations, because the water concentration affects the oxidation state of Pd and availability of Pt for methane activation, which is also temperature-dependent. To the best of our knowledge, this is the first study to develop a model for PdPt-catalyzed methane combustion including the water and support effects, and it can pave the way to future adjustments and discussions. Mass transfer calculations in the silica shell indicate that mass transfer resistance through the shell was negligible.

Acknowledgements

Funding for this work was provided by the Natural Science and Engineering Research Council of Canada (Strategic grant STPGP 478979-15).

4.6 References

1. U.S. Government. The World Factbook, Central Intelligence Agency. https://www.cia.gov/library/publications/the-world-factbook/geos/xx.html, 2018, (accessed on 20 March 2018).

2. B. Liu, R. E. Hayes, M. D. Checkel, M. Zheng and E. Mirosh, *Chem. Eng. Sci.*, 2001, **56**, 2641–2658.

3. United States Environmental Protection Agency, Understanding Global Warming Potentials. https://www.epa.gov/ghgemissions/understanding-global-warming-potentials, 2018, (accessed on 20 March 2018).

4. U. S. Environmental Protection Agency, New Source Performance Standards and Permitting Requirements, Final Rules. https://www.epa.gov/controlling-air-pollution-oil-and-natural-gas-industry/new-source-performance-standards-and, 2016, (accessed on 20 March 2018).

5. L. D. Pfefferle and W. C. Pfefferle, *Catal. Rev. Sci. Eng.*, 1987, **29**, 219–267.

6. W. R. Schwartz and L. D. Pfefferle, *J. Phys. Chem. C*, 2012, **116**, 8571–8578.

7. D. Ciuparu and L. Pfefferle, *Appl. Catal. A.*, 2001, **209**, 415–428.

8. D. Ciuparu, F. Bozon-verduraz and L. Pfefferle, *J. Phys, Chem. B*, 2002, **106,** 3434–3442.

9. W. R. Schwartz, D. Ciuparu and L. D. Pfefferle, *J. Phys. Chem. C*, 2012, **116**, 8587–8593.

10. R. Burch, P. K. Loader and F. J. Urbano, *Catal. Today*, 1996, **27**, 243–248.

11. R. Burch, F. J. Urbano and P. K. Loader, *Appl. Catal. A*, 1995, **123**, 173–184.

12. A. Ersson, H. Kušar, R. Carroni, T. Griffin and S. Järås, *Catal. Today*, 2003, **83**, 265–277.

13. K. Persson, A. Ersson, A. M. Carrera, J. Jayasuriya, R. Fakhrai, T. Fransson and S. Järås, *Catal. Today*, 2005, **100**, 479–483.

14. K. Narui, H. Yata, K. Furuta, A. Nishida, Y. Kohtoku and T. Matsuzaki, *Appl. Catal. A*, 1999, **179**, 165–173.

15. D. Ciuparu, N. Katsikis and L. Pfefferle, *Appl. Catal. A.* 2001, **216**, 209–215.

16. C. F. Cullis, T. G. Nevell and D. L. Trimm, *J. Chem. Soc., Faraday Trans.* 1971, **1**, 1406–1412.

17. R. Burch, *Catal. Today*, 1997, **35**, 27–36.

18. H. Arai and M. Machida, *Catal. Today*, 1991, **10**, 81–94.

19. L. S. Escandón, D. Niño, E. Díaz, S. Ordóñez and F. V. Díez, *Catal. Commun.*, 2008, **9**, 2291–2296.

20. Q. Xu, K. C. Kharas, B. J. Croley and A. K. Datye, *ChemCatChem*, 2011, **3**, 1004–1014.

21. K. Persson, A. Ersson, S. Colussi, A. Trovarelli and S. G. Jaras, *Appl. Catal. B,* 2006, **66**, 175–185.

22. Y. Ozawa, Y. Tochihara, A. Watanabe, M. Nagai and S. Omi, *Appl. Catal. A*, 2004, **259**, 1–7.

23. K. Persson, A. Ersson, K. Jansson, J. L. G. Fierro and S. G. Järås, *J. Catal.*, 2006, **243**, 14–24.

24. R. Abbasi, L. Wu, S. E. Wanke and R. E. Hayes, *Chem. Eng. Res. Des.*, 2012, **90**, 1930–1942.

25. G. Lapisardi, L. Urfels, P.Gelin, M. Primet, A. Kaddouri, E. Garbowski, S. Toppi and E. Tena, *Catal. Today* , 2006, **117**, 564–568.

26. C. Micheaud, P. Marecot, G. M and Barbier J, *Appl. Catal. A, Gen.*, 1998, **171**, 229–239.

27. Y. Deng and T. G. Nevell, *Catal. Today,* 1999, **47**, 279–286.

28. R. Strobel, J. Grunwaldt, A. Camenzind, S. E. Pratsinis and A. Baiker, *Catal. Letters*, 2005, **104**, 9–16.

29. H. Nassiri, K.-E. Lee, Y. Hu, R. E. Hayes, R. W. J. Scott and N. Semagina, *J. Catal.*, 2017, **352**, 649–656.

30. W. Stöber, A. Fink and E. Bohn, *J. Colloid Interface Sci.*, 1968, **26**, 62–69.

31. C. Graf, D. L. J. Vossen, A. Imhof and A. van Blaaderen, *Langmuir*, 2003, **19**, 6693–6700.

32. S. H. Joo, J. Y. Park, C.-K. Tsung, Y. Yamada, P. Yang and G. A. Somorjai, *Nat Mater*, 2009, **8**, 126–131.

33. J. M. Krier, W. D. Michalak, X. Cai, L. Carl, K. Komvopoulos and G. A. Somorjai, *Nano Lett.*, 2015, **15**, 39–44.

34. I. Lee, Q. Zhang, J. Ge, Y. Yin and F. Zaera, *Nano Res.*, 2011, **4**, 115–123.

35. Q. Zhang, I. Lee, J. Ge, F. Zaera and Y. Yin, *Adv. Funct. Mater.*, 2010, **20**, 2201–2214.

36. G. Prieto and F. Schüth, *J. Catal.*, 2015, **328**, 59–71.

37. A. H. Habibi, R. E. Hayes and N. Semagina, *Catal. Sci. Technol.*, 2018, **8**, 798–805.

38. G. Groppi, *Catal. Today*, 2003, **77**, 335–346.

39. S. Seimanides and M. Stoukides, *J. Catal.*, 1986, **98**, 540–549.

40. P. Hurtado, S. Ordóñez, H. Sastre and F. V. Diez, *Appl. Catal. B.,*2004, **51**, 229–238.

41. Y. C. Chin and E. Iglesia, *J. Phys. Chem. C ,* 2011, **115**, 17845–17855.

42. A. H. Habibi, R. E. Hayes and N. Semagina, *Appl. Catal. A*. 2018, **556***,* 129-136

43. O. Levenspiel, *Chemical Reaction Engineering: An Introduction to the Design of Chemical Reactors*; Wiley: New York, 1998.

44. D. E. Mears, Tests for Transport Limitations in Experimental Catalytic Reactors. *Ind. Eng.*

Chem. Process Des. Dev. **1971**, *10*, 541-547

45. R. Gholami, M. Alyani and K. Smith, *Catalysts*, 2015, **5**, 561–594.

46. Y. H. Chin, C. Buda, M. Neurock and E. Iglesia, *J. Am. Chem. Soc.*, 2013, **135**, 15425–15442.

47. G. Zhu, J. Han, D. Y. Zemlyanov and F. H. Ribeiro, *J. Am. Chem. Soc.*, 2004, **126**, 9896–9897.

48. D. Ciuparu, M. R. Lyubovsky, E. Altman, L. D. Pfefferle and A. Datye, *Catal. Rev.*, 2002, **44**, 593–649.

49. Y. H. C. Chin, M. García-Diéguez and E. Iglesia, *J. Phys. Chem. C*, 2016, **120**, 1446–1460.

50. A. Yamaguchi and E. Iglesia, *J. Catal.*, 2010, **274**, 52–63.

51. M. Van Den Bossche and H. Grönbeck, *J. Am. Chem. Soc.*, 2015, **137**, 12035–12044.

52. N. M. Martin, M. Van Den Bossche, A. Hellman, H. Grönbeck, C. Hakanoglu, J. Gustafson, S. Blomberg, N. Johansson, Z. Liu, S. Axnanda, J. F. Weaver and E. Lundgren, *ACS Catal.*, 2014, **4**, 3330–3334.

53. Y. Xin, S. Lieb, H. Wang and C. K. Law, *J. Phys. Chem. C*, 2013, **117**, 19499–19507.

54. S. Specchia, F. Conti and V. Specchia, *Ind. Eng. Chem. Res.*, 2010, **49**, 11101–11111.

55. H. Nassiri, K. E. Lee, Y. Hu, R. E. Hayes, R. W. J. Scott and N. Semagina, *ChemPhysChem*, 2017, **18**, 238–244.

56. R. E. Hayes, S. T. Kolaczkowski, P. K. C. Li and S. Awdry, *Chem. Eng. Sci.*, 2001, **56**, 4815–4835.

57. K.-I. Fujimoto, F. H. Ribeiro, M. Avalos-Borja and E. Iglesia, *J. Catal.*, 1998, **179**, 431–442.

58. T. R. Baldwin and R. Burch, *Appl. Catal.*, 1990, **66**, 337–358.

59. K. Otto, *Langmuir*, 1989, **5**, 1369 – 1374.

60. J. C. van Giezen, *The Catalytic Combustion of Methane. Ph.D. Thesis, University Utrecht*; Netherlands, **1997**.

61. F.H. Ribeiro, M. Chow and R. A. Dalla betta, *J. Catal.*, 1994, **146**, 537–544.

62. R. Mezaki and C. C. Watson, *I&EC Process Des. Dev.*, 1966, **5**, 62–65.

63. G. I. Golodets, *Stud. Surf. Sci. Catal.*, 1983, **15**, 126–150.

64. L. Van De Beld, M. P. G. Bijl, A. Reinders, B. Van Der Wert and K. R. Westerterp, *Chem. Eng. Sci.*, 1994, **49**, 4361–4373.

65. R. Kikuchi, S. Maeda, K. Sasaki, S. Wennerström and K. Eguchi, *Appl. Catal. A*, 2002, **232**, 23–28.

66. W. Qi, J. Ran, R. Wang, X. Du, J. Shi and J. Niu, *RSC Adv.*, 2016, **6**, 109834–109845.

67. M. Boşomoiu, G. Bozga and G. Soare, *Rev. Roum. Chim.*, 2008, **53**, 1105–1115.

68. O. Deutschmann, F. Behrendt and J. Warnatz, *Catal. Today*, 1998, **46**, 155–163.

69. O. Deutschmann, R. Schmidt, F. Behrendt and J. Warnatz, *Proc. Combust. Inst.*, 1996, **26**, 1747–1754.

70. P. Gélin and M. Primet, *Appl. Catal. B.*, 2002, **39**, 1–37.

71. R. Burch and P. K. Loader, *Appl. Catal. B.,* 1994, **5**, 149–164.

72. E. Becker, P. Carlsson, H. Grönbeck and M. Skoglundh, *J. Catal.* 2007, **252**, 11–17.

73. D. Ciuparu, R. Altman and L. Pfefferle, *J. Catal.*, 2001, **203**, 64-74.

74. H. W. J. P. Neomagus, G. Saracco, H. F. W. Wessel and G. F. Versteeg, *Chem. Eng. J.*, 2000, **77**, 165–177.

75. N. M. Martin, J. Nilsson, M. Skoglundh, E. C. Adams, X. Wang, P. Velin, G. Smedler, A. Raj, D. Thompsett, H. H. Brongersma, T. Grehl, G. Agostini, O. Mathon, S. Carlson, K. Norén, F. J. Martinez-Casado, Z. Matej, O. Balmes and P.-A. Carlsson, *J. Phys. Chem. C*, 2016, **120**, 28009–28020.

76. P. Castellazzi, G. Groppi and P. Forzatti, *Applied Catal. B*, 2010, **95**, 303–311.

77. H. Nassiri, R. E. Hayes and N. Semagina, *Chem. Eng. Sci.* 2018, **186,** 44-51.

78. S. Pálfi, W. Lisowski, M. Smutek and S. Černý, *J. Catal.*, 1984, **88**, 300–312.

79. A. Wheeler, *Catalysis P. H. Emmett, Ed.,*; Reinhold: New York, 1955.

80. A. H. Habibi, N. Semagina, and R. E. Hayes. *Ind. Eng. Chem. Res.* 2018, **57**, 8160−8171.

Chapter 5

5 Conclusions, contribution and recommendations

5.1 Conclusions

This thesis reports development of a sinter-resistant bimetallic Pd-Pt catalyst for lean CH_4 combustion in the presence of water. It is concluded that when sufficient porosity is ensured, core@shell structures can offer great advantages in the field of catalytic applications due to their high thermal stability. The effect of the synthesis procedure on the porosity of the shell and accessibility of the metallic sites after encapsulation was studied. Monometallic Pd@SiO_2 and Pd@mSiO_2 catalysts were prepared and tested in dry lean methane combustion. It is shown that even though silica shells can be readily synthesized by using PVP as a stabilizer and without addition of a porogen, the resulting catalyst will not be porous enough to be employed in the combustion reaction. Porous shells are only produced when an additional surfactant is applied during the encapsulation stage (Stöber reaction) of the synthesis. Since the properties of the NPs prepared using colloidal methods depend on the nature of the stabilizer used during this step, and the properties of the silica shells depend on the nature of the additional surfactant, encapsulation of various morphologies of NPs in various shells becomes possible. Addition of stabilizer and porogen in two different steps of the synthesis allows for an independent preparation of metal NPs and silica shells: metal NPs of the desired size and shape can be synthesized using colloidal reduction and then, can be encapsulated using a specific porogen to obtain shells of desired properties (e.g. porosity).

It is also noted the synthesis procedure used here allows for preparation of high-loading encapsulated catalysts without agglomeration of the core NPs. This was achieved by application of the stabilizaer and porogen at two different steps of thes synthesis and is especially important in designing catalysts for catalytic converters of NGVs where high-loading catalysts are required. Conventional synthesis methods are usually limited in metal loading since sintering of the NPs becomes more severe in high metal loading catalysts. It was concluded that

encapsulation in silica, when proper synthesis chemistry is applied, can produce high metal loading catalysts while effectively preventing NP sintering.

Since monometallic Pd is known to lose its activity in wet combustion conditions, the catalyst designed for the wet conditions was a bimetallic PdPt encapsulated in porous silica shells (PdPt@SiO_2). The bimetallic catalyst was developed similarly to the Pd@mSiO_2 catalyst and had similar properties (high metal loading and high surface area). The performance of the bimetallic catalyst in the absence and presence of water, during hydrothermal ageing, and after hydrothermal ageing was compared to two supported catalysts of the same metal loading prepared using impregnation (PdPt/SiO_2 and PdPt/Al_2O_3). The PdPt@SiO_2 catalyst showed a remarkable resistance to sintering during hydrothermal ageing (5 mol.% water, up to 550 °C). No noticeable change in the size or morphology of the silica shells was observed after 170 h of exposure to the wet lean combustion atmosphere. After the HTA test, the PdPt@SiO_2 catalyst showed higher conversions at T<425 °C compared to the aged impregnated PdPt/Al_2O_3 and PdPt/SiO_2 catalysts of the same metal loading due to its higher metal dispersion provided by its resistance to sintering. It was observed via CO chemisorption and TEM analyses that the dispersion of the PdPt nanoparticles in the encapsulated catalyst increased during the HTA, most likely due to some silica being cleaned off the metal surface at the Pd-Si interface and vaporization of Pt oxide and/or PdO migration. Overall, the bimetallic silica-encapsulated catalyst (PdPt@SiO_2) allowed for improved methane combustion at high GHSVs and remained stable for over 70 h of time on stream, making it a suitable candidate to be used in in relatively small-size catalytic converters for mitigation of CH_4 from lean combustion engines.

The kinetics of lean CH_4 combustion over the bimetallic catalyst designed, developed and hydrothermally aged according to the previous steps, was studied over a range of CH_4 concentration (1000-5000 ppm), at the temperature range of 550-750 K and in the presence and absence of 5.0 mol.% water. The presence of water decreased the combustion activity at all initial CH_4 concentrations. The ignition curves demonstrated that the fractional conversion decreases with an increase in inlet CH_4 concentration. Since this behavior was observed in both dry and wet conditions, it is concluded that the effect of water produced during the reaction is significant. The dry kinetic data were satisfactorily fitted using an existing rate equation from the literature. However, this model could not provide acceptable predictions in wet conditions. To

improve the kinetic predictions in the presence of 5.0 mol% water, a new kinetic model based on the most recent discussions in the literature was proposed. The proposed model is theoretically valid for T<723 K (where water inhibition effects are significant) and assumes the existence of two types of active sites: 1) Pd sites for activating oxygen and 2) Pt sites for activating CH_4. The surface reaction between the adsorbed CH_4 and active oxygen (O*) is assumed to be the RDS with the following H-abstraction steps being kinetically insignificant. In this mechanism Pd dissociates the gas-phase O_2 and delivers it to the support. Metallic Pd with chemisorbed oxygen is unable to active methane due to the very activation energy, but its presence is essential for the reaction to deliver the activated O* to the support surface. The rate equation developed based on this mechanism, was able to provide satosifcatry predictions of the conversion data under wet conditions. It was concluded that two rate equations were necessary for describing the combustion kinetics, one for the case of dry feed and one for the case of wet feed. Finally, solving the mass transfer equation for the encapsulated catalyst indicated that the mass transfer resistance through the silica shell was negligible.

5.2 Contribution of the work

5.2.1 Contribution to applied science

To achieve the objectives of the research, a new catalytic structure was designed, synthesized, and evaluated in lean methane combustion. From a practical point of view, the properties of the bimetallic catalyst prepared in this work (metal loading, NP size, porosity, resistance to sintering, and stability in the presence of water) provide a practical solution to the most current challenges in development of CH_4 emission control catalysts for the catalytic converters of lean-burn NGVs. The formulation used in this work, was optimized to produce a highly reliable synthesis method for high-loading, high porosity bimetallic catalysts. Both *the concepts* (NP size, encapsulation, bimetallic effects, porosity, and high metal-loading with no sintering) and *the methods* (colloidal reduction, and Sol-Gel encapsulation) discussed in this work, pave the way for addressing the current challenges in the field of catalytic CH_4 abatement. Thus, the practical objectives of the research were achieved and the ideas and formulations provided in this work, with/out some alterations can be anticipated to find a role in addressing

the needs of the industry. It is believed that employment of the catalysts developed here in catalytic converters can help automobile manufacturers in meeting their emission control targets. Another practical contribution of this work to the methane combustion literature would be the introduction of a new reaction mechanism and its corresponding rate equation. For the first time in literature, the role of oxygen from the support, the effect of water, and the metallic state of the Pd and Pt in bimetallic catalysts were incorportated in the development of the kinetic model for lean CH_4 combustion in the presence of water. To the best of our knowledge this model was introduced here for the first time and opens the door for further discussions in the catalytic combustion community.

5.2.2 Contribution to fundamental science

The first funadamental contribution of this work to science would be emphasizing the importance of understanding the role of each component in the synthesis of core@shell nanostructures by demonstrating how an independent addition of stabilizers and porogens at two different stages of the synthesis (colloidal reduction and encapsulation) can be used to tailor the properties of the core NPs and the shell nanostructures. Such independence, highlighted in this work, adds a great versatility to core@shell nanostructures as it allows for core NPs of desired size and morphology to be created using a desired method (in this case colloidal methods), and then to be encapsulated in oxide shells of desired composition and physical texture.

Secondly, by presenting a critical classification on the existing encapsulation formulations, this work reveals that even though silica shells can be prepared by using PVP during the synthesis, the ultimate catalyst synthesized using this approach may not have the sufficient porosity required for catalytic purposes. Thus, it was concluded here that the N_2 adsorption behavior and surface area of the encapsulated nanostructures are of great significane in desiging encapsulated catatlysts. Even though some encapsulated catalysts with a surface area less than 150-200 m^2/g have been used in some reactions and have shown an activity of some level, it was proven in this work that the core NPs in the these structures were actually inaccessible to reactant molecules due to the nonporous nature of the as-prepared silica shells. Also, after ensuring that the silica shells were “sufficiently porous”, by comparing the number of atoms available for CO chemisorption after encapsulation to the CO chemisorption capacity of

the corresponding non-encapsulated Pd NPs, a quantitative estimate of the fraction of surface atoms that became inaccessible after encapsulation was offered. This inevitable inaccessibility, which occured even in highly porous materials (surface area of 600 m^2/g), was attributed to the blockage of the NP surface by the shell right at the metal/silica interface. Thus, ulitmately, as a first in the literature, this work offered a detailed discussion and a critical view on

- the existing encapsulation formulations
- metal unavailability in the encapsulated structures
- the effect of porogens on the accessibility of catalytic sites after encapsulation

Lastly, this study demonstrates that the kinetic models should be developed based on experimentally-relevant assumptions and for the narrow operating window of their application. Since the reaction mechanisms are defined by the operating conditions (temperature range and concentration of the reactants and potentially present poisons), reliable kinetic models can only be developed by considering the prevailing active species on the surface and relevant mechanisms in the goverining reaction conditions. To the best of our knowledge it was the first time that two different kinetic models (one for wet conditions and one for dry conditions) were being used for predicting the kinetic behavior of a combustion catalyst.

5.3 Recommendations and future work

5.3.1 Synthesis of bimetallic PdPt catalysts encapsulated in hollow structures and other oxides such as ZrO_2

In this study, it was discovered that even when the silica shells are porous, up to 2/3 of the surface atoms of the encapsulated core are unavailable for reaction. Development of a practical synthesis method leading to hollow silica shells around PdPt NPs is recommended since such a structure may have a greater exposed surface area. Also, encapsulation of bimetallic PdPt NPs in other oxides such as ZrO_2 (zirconia) can be recommended. Encapsulation in ZrO_2 can allow for zirconia's enhanced oxygen transfer properties to be utilized in the combustion reaction. Another interesting encapsulated structure would be a Metal@hollow-ZrO_2 since in such a structure, the surface blockage in the interfacial surface between the core NPs and shell material would be minimal and a greater thermal stability (for the shell) can be expected.

5.3.2 Kinetic modeling for a wider range of H_2O concentrations

In this study the reactor model was applied to the experimental data obtained on a $PdPt@SiO_2$ catalyst (4.2 wt.% Pd 7 wt.% Pt) for lean CH_4 combustion at a varying CH_4 concentration (1000 ppm to 5000 ppm) in the presence and absence of a constant H_2O concentration (5 mol%). It is recommended that the kinetic studies performed here be extended to a varying H_2O concentrations (0 -15 mol%) as this parameter can vary under real conditions.

5.3.3 Preparing of washcoat material and performing catalytic tests in more realistic conditions

In this work, the performance of the bimetallic $PdPt@SiO_2$ catalyst was assessed in a laboratory scale fixed-bed reactor under plug flow condition. It is recommended that the performance and stability of the catalyst be investigated in an actual prototype catalytic converter. Thus, the next step would be to washcoat the catalyst on a honeycomb monolith structure and perform the catalytic tests on the monolith. The aging protocols are also recommended to be changed to portray various operation conditions of the real engine exhaust gas conditions such as cold start, hot start, acceleration, and steady state so more realistic predictions of the catalytic performance can be derived. Additionally, it is recommended that the feed stream be a an actual mixture of gases coming from the exhaust of a heavy duty lean-burn NGV, rather than just water vapor, methane and air.

5.3.4 Scale-up of the synthesis

The synthesis procedure used in this work can produce a few grams of catalyst per every batch. The scale-up of the synthesis procedure by designing an efficient high through-put process can be recommended. A synthesis method that requires the least amount of solvents or recycles the solvents, and/or modifies or bypasses the centrifugation step, can lead to a feasible process for large scale production of encapsulated catalysts.

Bibliography

A. Cao, R. Lu and G. Veser, *Phys. Chem. Chem. Phys.*, 2010, **12**, 13499–13510.

A. Ersson, H. Kušar, R. Carroni, T. Griffin and S. Järås, *Catal. Today*, 2003, **83**, 265–277.

A. Gannouni, B. Albela, M. .Said Zina and L. Bonneviot, *Appl. Catal. A*, 2013, **464**–**465**, 116–127.

A. H. Habibi, R. E. Hayes, and N. Semagina, *Appl. Catal. A*. 2018, ***556,*** 129-136.

A. H. Habibi, R. E. Hayes, and N. Semagina, *Catal. Sci. Technol.*, 2018, **8**, 798–805.

A. H. Habibi, N. Semagina, and R. E. Hayes, *Ind. Eng. Chem. Res.* 2018, **57**, 8160−8171.

A. J. Forman, J. N. Park, W. Tang, Y. S. Hu, G. D. Stucky and E. W. McFarland, *ChemCatChem,* 2010**, 2**, 1318–1324.

A. Morlang, U. Neuhausen, K. V. Klementiev, F. W. Schütze, G. Miehe, H. Fuess, and E. S. Lox, *Appl. Catal. B*, 2005, **60**, 191–199.

A. P. Wong, E.A. Kyriakidou, T.J. Toops, and J.R. Regalbuto, *Catal. Today,* 2016, **267**, 145–156.

A. S. Pensado and A. A. H. Pádua, *Angew. Chem. Int. Ed.*, 2011, **50**, 8683-8687

A. S. Reddy, H. Y. Jeong, K. Qadir, J. Y. Yun, and J. Y. Park, 18th Int. Conf. Compos. Mater., Jeju Island, South Korea, 2011, pp. 21–26 p. 1-6.

A. Samanta, B. B. Dhar and R. N. Devi, *New J. Chem.,* 2012, **36**, 2625–2629.

A. Van Blaaderen, J. Van Geest and A. Vrij, *J. Colloid Interface Sci.*, 1992, **154**, 481–501.

A. Wheeler, *Catalysis P. H. Emmett, Ed.,*; Reinhold: New York, 1955.

A. Winkler, P. Dimopoulos, R. Hauert, C. Bach, and M. Aguirre, *Appl. Catal. B*, 2008, **841**, 62–169.

A. Yamaguchi and E. Iglesia, *J. Catal.*, 2010, **274**, 52–63.

B. Corain, K. Jerabek, P. Centomo and P. Canton, *Angew. Chem. Int. Ed.,* 2004, **43**, 959-962

B. Liu, R. E. Hayes, M. D. Checkel, M. Zheng and E. Mirosh, *Chem. Eng. Sci.*, 2001, **56**, 2641–2658.

B. P. Bastakoti, Y. Li, N. Miyamoto, N. M. Sanchez-Ballester, H. Abe, J. Ye, P. Srinivasu and Y. Yamauchi, *Chem. Commun.,* 2014, **50**, 9101–9104.

B. Thiébaut, *Platin. Met. Rev.,* 2004, **48**, 62-63

C. A. Muller, M. Maciejewski, R. A. Koeppel, R. Tschan and A. Baiker, *J. Phys Chem,* 1996,

100, 20006–20014.

C. Descorme and D. Duprez, *Appl. Catal. A.*, 2000, **202**, 231–241.

C. F. Cullis and B. M. Willatt, *J. Catal.*, 1983, **83**, 267–285.

C. F. Cullis, T. G. Nevell and D. L. Trimm, *J. Chem. Soc., Faraday Trans.* 1971, **1**, 1406–1412.

C. Graf, D. L. J. Vossen, A. Imhof and A. van Blaaderen, *Langmuir*, 2003, **19**, 6693–6700.

C. L. Pieck, C. R. Vera, E. M. Peirotti and J. C. Yori, *Appl. Catal. A*, 2002, **226**, 281–291.

C. Micheaud, P. Marecot, G. M and Barbier J, *Appl. Catal. A, Gen.*, 1998, **171**, 229–239.

C. R. F. Lund and J. A. Dumesic, *J. Catal.,* 1981, **72**, 21–30.

C. Shao, W. Li, Q. Lin, Q. Huang, and D. Pi, *Energy Technol.,* 2017, **5**, 604–610.

C. Xiao, R. V. Maligal-Ganesh, T. Li, Z. Qi, Z. Guo, K. T. Brashler, S. Goes, X. Li, T. W. Goh, R. E. Winans and W. Huang*, ChemSusChem*, 2013, **6**, 1915–1922.

C. Zhang, Y. Zhou, Y. Zhang, Z. Zhang, Y. Xu and Q. Wang, *Powder Technol.,* 2015, **284**, 387–395.

C.-J. Jia and F. Schüth, *Phys. Chem. Chem. Phys.*, 2011, **13**, 2457-2487

Center for Transportation Research Energy Systems Division, Argonne National Laboratory available at https://www.afdc.energy.gov/pdfs/anl_esd_10-4.pdf, 2010, (last accessed May 2018)

D. Astruc, *Inorg. Chem.*, 2007, **46**, 1884-1894.

D. Ciuparu and L. Pfefferle, *Appl. Catal. A.*, 2001, **209**, 415–428.

D. Ciuparu and L. Pfefferle, *Catal. Today.*, 2002, **77**, 167–179.

D. Ciuparu, F. Bozon-verduraz and L. Pfefferle, *J. Phys, Chem. B*, 2002, **106,** 3434–3442.

D. Ciuparu, M. R. Lyubovsky, E. Altman, L. D. Pfefferle and A. Datye, *Catal. Rev.*, 2002, **44**, 593–649.

D. Ciuparu, N. Katsikis and L. Pfefferle, *Appl. Catal. A.* 2001, **216**, 209–215.

D. Ciuparu, R. Altman and L. Pfefferle, *J. Catal.*, 2001, **203**, 64-74.

D. E. Mears, Tests for Transport Limitations in Experimental Catalytic Reactors. *Ind. Eng. Chem. Process Des. Dev.* **1971**, *10*, 541-547.

D. Gao, S. Wang, C. Zhang, Z. Yuan, and S. Wang, Chin. *J. Catal.,* 2008, **29**, 1221–1225.

D. Pi, W. Z. Li, Q. Z. Lin, Q. F. Huang, H. Q. Hu and C. Y. Shao, *Energy Technol.,* 2016, **4**, 943–949.

D. Roth, P. Gélin, A. Kaddouri, E. Garbowski, M. Primet and E. Tena, *Catal. Today,* 2006, **112**,

134–138.

D. Roth, P. Gélin, M. Primet and E. Tena, *Appl. Catal. A.,* 2000, **203**, 37–45.

D. S. Bae, K.-S. Han and J. H. Adair, *J. Mater. Chem.,* 2002, **12**, 3117–3120.

D. Shen, L. Chen, J. Yang, R. Zhang, Y. Wei, X. Li, W. Li, Z. Sun, H. Zhu, A. M. Abdullah, A. Al-Enizi, A. A. Elzatahry, F. Zhang and D. Zhao, *ACS Appl. Mater. Interfaces,* 2015, **7**, 17450–17459.

D.-S. Bae, K.-S. Han and J. H. Adair, *J. Mater. Chem.*, 2002, **12**, 3117–3120.

Dieselnet Emissions Standards, United States: Cars and Light-Duty Trucks: Tier 3 Introduction, https://www.dieselnet.com/standards/us/ld_t3.php#ftp., 2018, (last accessed May 2018)

Dieselnet Emissions Standards, United States: Heavy-Duty Onroad Engines, https://www.dieselnet.com/standards/us/hd.php., 2018, (last accessed May 2018).

E. Becker, P. Carlsson, H. Grönbeck and M. Skoglundh, *J. Catal.* 2007, **252**, 11–17.

E. Coronado, A. Ribera, J. García-Martínez, N. Linares, L. M. Liz-Marzan, *J. Mater. Chem.,* 2008, **18**, 5682-5688

E. D. Goodman, S. Dai, A. C. Yang, C. J. Wrasman, A. Gallo, S. R. Bare, A. S. Hoffman, T. F. Jaramillo, G. W. Graham, X. Pan, and M. Cargnello, *ACS Catal.,* 2017, **7**, 4372–4380.

E. Genchi, G. and Pipitone, *SAE Int. J. Fuels Lubr.*, 2014, **7**, 1041–1049.

E. J. Opila, N. S. Jacobson, D. L. Myers, and E. H. Copland, *JOM,* 2006, **58**, 22-28.

E. N. Fuller, P. D. Schettler, and J. C. Giddings, *Ind. Eng. Chem*. 1966, **58**, 18-27

E. S. J. Lox and B. H. Engler, *Handbook of Heterogeneous Catalysis*, Volume 4*,* Wiley-VCH, Weinheim, 1997.

F. H. Ribeiro, M. Chow, and R. A. Dalla Betta, *J. Catal.,* 1994, **146**, 537–544.

F. Pinna, 1998, *Catal. Today*, 1998, **41**, 129–137

F. Zaera, *Acc. Chem. Res.*, 2009, **42**, 1152 – 1160.

F. Zaera, *J. Phys. Chem. Lett.*, 2010, **1**, 621 – 627.

G. A. Somorjai and J. Carrazza, *Ind. Eng. Chem. Fundam.*, 1986, **25**, 63–69.

G. A. Somorjai and R. M. Rioux, *Catal. Today*, 2005, **100**, 201–215.

G. A. Somorjai, H. Frei and J. Y. Park, *J. Am. Chem. Soc.*, 2009, **131**, 16589 – 16605.

G. Berhault, M. Bausach, L. Bisson, L. Becerra, C. Thomazeau and D. Uzio, *J. Phys. Chem. C,* 2007, **111**, 5915–5925.

G. Centi, *J. Mol. Catal. A.*, 2001, **173**, 287–312.

G. Ertl, H. Knözinger, F. Schüth and J. Weitkamp, *Handbook of Heterogeneous Catalysis*, Volume 5, 2nd edn., Wiley-VCH, Weinheim, 2008.

G. Groppi, *Catal. Today*, 2003, **77**, 335–346.

G. I. Golodets, *Stud. Surf. Sci. Catal.*, 1983, **15**, 126–150.

G. Lapisardi, L. Urfels, P.Gelin, M. Primet, A. Kaddouri, E. Garbowski, S. Toppi and E. Tena, *Catal. Today* , 2006, **117**, 564–568.

G. Prieto and F. Schüth, *J. Catal.*, 2015, **328**, 59–71.

G. Zhu, J. Han, D. Y. Zemlyanov and F. H. Ribeiro, *J. Am. Chem. Soc.*, 2004, **126**, 9896–9897.

G. Zhu, K. I. Fujimoto, D. Y. Zemlyanov, A. K. Datye and F. H. Ribeiro, *J. Catal.*, 2004, **225**, 170–178.

H. Arai and M. Machida, *Catal. Today*, 1991, **10**, 81–94.

H. Bönnemann and R. M. Richards, *Eur. J. Inorg. Chem.,* 2001, **2001**, 2455-2480

H. Ishizuka, T. Tano, K. Torigoe, K. Esumi and K. Meguro, *Colloids Surf.*, 1992, **63**, 337-340.

H. Liu, H. Yu, C. Xiong and S. Zhou, *RSC Adv*., 2015, **5**, 20238–20247.

H. Liu, K. Tao, C. Xiong and S. Zhou, *Catal. Sci. Technol*., 2015, **5**, 405–414.

H. Nassiri, K. E. Lee, Y. Hu, R. E. Hayes, R. W. J. Scott and N. Semagina, *ChemPhysChem*, 2017, **18**, 238–244.

H. Nassiri, K.-E. Lee, Y. Hu, R. E. Hayes, R. W. J. Scott and N. Semagina, *J. Catal.*, 2017, **352**, 649–656.

H. Nassiri, R. E. Hayes and N. Semagina, *Chem. Eng. Sci.* 2018, **186,** 44-51.

H. Scott Fogler, *Elements of Chemical Reaction Engineering,* 5th edn, Prentice Hall, Kendaville, IN, 2016.

H. Shinjoh, *Catal. Surv. Asia*, 2009, **13**, 184 – 190.

H. W. J. P. Neomagus, G. Saracco, H. F. W. Wessel and G. F. Versteeg, *Chem. Eng. J.*, 2000, **77**, 165–177.

H. Yamamoto and H. Uchida, *Catal. Today*, 1998, **45**, 147–151.

H. Yang, Y. Chong, X. Li, H. Ge, W. Fan and J. Wang, *J. Mater. Chem.,* 2012, **22**, 9069–9076.

H. Yoshida, T. Nakajima, Y. Yazawa and T. Hattori, *Appl. Catal. B*, 2007, **71**, 70–79.

I. Lee, Q. Zhang, J. Ge, Y. Yin and F. Zaera, *Nano Res.*, 2011, **4**, 115–123.

I. Yuranov, L. Kiwi-Minsker and A. Renken, *Appl. Catal., B,* 2003, **43**, 217–227.

J. C. Park, H. J. Lee, J. Y. Kim, K. H. Park and H. Song, *J. Phys. Chem. C,* 2010, **114**, 6381–

6388.

J. C. Park, J. U. Bang, J. Lee, C. H. Ko and H. Song, *J. Mater. Chem.,* 2010, **20**, 1239–1246.

J. C. van Giezen, *The Catalytic Combustion of Methane. Ph.D. Thesis, University Utrecht*; Netherlands, **1997**.

J. Chen, R. Zhang, L. Han, B. Tu and D. Zhao, *Nano Res.,* 2013, **6**, 871–879.

J. F. Le Page, Applied heterogeneous catalysis, TechniP, Paris, 1987.

J. G. Li, C. Y. Tsai and S.-W. Kuo, *RSC Adv*., 2015, **5**, 42798–42807.

J. G. Oh and H. Kim, *Curr. Appl. Phys.,* 2013, **13**, 130–136.

J. H. Sinfelt*, Acc. Chem. Res.,* 1977, **10**, 15–20.

J. J. Barbier and D. Duprez, *Appl. Catal. B*, 1994, **4**, 105–140.

J. J. Willis, A. Gallo, D. Sokaras, H. Aljama, S. H. Nowak, E. D. Goodman, L. Wu, C. J. Tassone, T. F. Jaramillo, F. Abild-pedersen, and M. Cargnello, *ACS Catal.* 2017, **7**, 7810–7821.

J. L. Aluha, G. Pattrick, and E. Van Der Lingen, *Top. Catal.,* 2009, **52**, 1977–1982.

J. Lampert, M. Kazi, and R. Farrauto, *Appl. Catal., B,* 1997, **14**, 211–223.

J. M. Krier, W. D. Michalak, X. Cai, L. Carl, K. Komvopoulos and G. A. Somorjai, *Nano Lett.*, 2015, **15**, 39–44.

J. Martins, N. Batail, S. Silva, S. Rafik-Clement, A. Chaumonnot, D. Uzio, T. S. Nguyen and L. Piccolo, *Appl. Catal., A*, 2015, **504**, 504–508.

J. N. Carstens, S. C. Su and A. T. Bell, *J. Catal.*, 1998, **176**, 136–142.

J. Perez-Ramirez, R. J. Berger, G. Mul, F. Kapteijn, and J. A. Moulijn, *Catal. Today,* 2000, **60**, 93-109

J. S. Bradley and V. G. ed. G. Schmid, *'The Chemistry of Transition Metal Colloids', in: 'Clusters and Colloids: From Theory to Applications'*, Wiley-VCH Verlag GmbH, Weinheim, 1994.

J. Shen and N. Semagina, *ChemCatChem,* 2016, **8**, 2565–2571.

J. T. Wolan, and G. B. Hoflund, *J. Vac. Sci. Technol., A,* 1998, **16**, 3414–3419.

J. Turkevich, P. C. Stevenson and and J. Hillier, *Discuss. Faraday Soc.,* 1951, **11**, 55–75.

J. Xian, Q. Hua, Z. Jiang, Y. Ma and W. Huang, *Langmuir*, 2012, **28**, 6736–6741.

J. Xu, Y. Deng, X. Zhang, Y. Luo, W. Mao, X. Yang, L. Ouyang, P. Tian and Y. Han, *ACS Catal.,* 2014, **4**, 4106–4115.

J. Yang, D. Shen, Y. Wei, W. Li, F. Zhang, B. Kong, S. Zhang, W. Teng, J. Fan, W. Zhang, S. Dou and D. Zhao, *Nano Res.,* 2015, **8**, 2503–2514.

J. Ying, H. Peng, X. Xu, R. Wang, F. Yu, Q. Sun, W. Liu, Z. Gao and X. Wang, *Catal. Sci. Technol.,* 2016, **6**, 5405–5414.

K. An, Q. Zhang, S. Alayoglu, N. Musselwhite, J. Y. Shin and G. A. Somorjai, *Nano Lett.*, 2014, **14**, 4907–4912.

K. Narui, H. Yata, K. Furuta, A. Nishida, Y. Kohtoku, and T. Matsuzaki, *Appl. Catal. A,* 1999, **179**, 165–173.

K. Nomura, K. Noro, Y. Nakamura, Y.Yazawa, H.Yoshida, A. Satsuma and T. Hattori, *Catal. Lett.*, 1998, **53**, 167–169.

K. Otto, *Langmuir*, 1989, **5**, 1369 – 1374.

K. Persson, A. Ersson, A. M. Carrera, J. Jayasuriya, R. Fakhrai, T. Fransson, and S. Järås, *Catal. Today*, 2005, **100**, 479–483.

K. Persson, A. Ersson, K. Jansson, J. L. G. Fierro and S. G. Järås, *J. Catal.*, 2006, **243**, 14–24.

K. Persson, A. Ersson, K. Jansson, N. Iverlund and S. Järås, *J. Catal.*, 2005, **231**, 139–150.

K. Persson, A. Ersson, S. Colussi, A. Trovarelli and S. G. Jaras, *Appl. Catal. B,* 2006, **66**, 175–185.

K. Persson, L. D. Pfefferle, W. Schwartz, A. Ersson and S. G. Järås, *Appl. Catal. B*, 2007, **74**, 242–250.

K. S. N. H. Bonnemann, in *Metal Nanoclusters in Catalysis and Materials Science: The Issue of Size Control*, ed. N. T. B. Corain, G. Schmid, Elsevier B.V., Amsterdam, 2008

K. T. Li, M. H. Hsu and I. Wang, *Catal. Commun*., 2008, **9**, 2257–2260.

K.-I. Fujimoto, F. H. Ribeiro, M. Avalos-Borja and E. Iglesia, *J. Catal.*, 1998, **179**, 431–442.

L. Balogh and D. A. Tomalia, *J. Am. Chem. Soc.,* 1998, **120**, 7355-7356.

L. D. Pfefferle and W. C. Pfefferle, *Catal. Rev. Sci. Eng.*, 1987, **29**, 219–267.

L. F. Zhang, M. Li, T.-Z. Ren, X. Liu and Z.-Y. Yuan, *Int. J. Hydrogen Energy*, 2015, **40**, 2648–2656.

L. K. Yeung and R. M. Crooks, *Nano Lett.*, 2001, **1**, 14-17.

L. Li, S. He, Y. Song, J. Zhao, W. Ji and C.-T. Au, *J. Catal.,* 2012, **288**, 54–64.

L. M. Liz-marzan, M. Giersig and P. Mulvaney, *Langmuir*, 1996, **12**, 4329–4335.

L. Qiu, F. Liu, L. Zhao, W. Yang and J. Yao, *Langmuir*, 2006, **22**, 4480–4482.

L. S. Escandón, D. Niño, E. Díaz, S. Ordóñez and F. V. Díez, *Catal. Commun.*, 2008, **9**, 2291–2296.

L. Tan, X. Wu, D. Chen, H. Liu, X. Meng and F. Tang, *J. Mater. Chem. A,* 2013, **1**, 10382–10388.

L. Van De Beld, M. P. G. Bijl, A. Reinders, B. Van Der Wert and K. R. Westerterp, *Chem. Eng. Sci.*, 1994, **49**, 4361–4373.

L. Wang, J. Shi, Y. Zhu, Q. He, H. Xing, J. Zhou, F. Chen and Y. Chen, *Langmuir*, 2012, **28**, 4920–4925.

L.-K. Chau and H.-T. Chang, *From Bioimaging to Biosensors*, CRC press, New York, 2013.

M. A. Vannice, *Kinetics of Catalytic Reactions*, Springer, New York, 2005.

M. Boşomoiu, G. Bozga and G. Soare, *Rev. Roum. Chim.*, 2008, **53**, 1105–1115.

M. C. Chao, H. P. Lin, C. Y. Mou, B. W. Cheng and C. F. Cheng, *Catal. Today*, 2004, **97**, 81–87.

M. Cargnello, D. Jaén, C. H. Garrido, K. Bakhmutsky, T. Montini, C. Gamez, R. Gorte, and P. Fornasiero, *Science,* 2012, **337**, 713-717.

M. Faraday, *Phil. Trans. Roy. Soc.*, 1857, **147**, 145-181.

M. Kim, S. Lee, K. Kim, D. Shin, H. Kim, and H. Song, *Chem. Commun.* 2014, **50**, 14938–14941.

M. L. Poulton, *Fuel Efficient Car Technology*, Computational Mechanics Publications, Southampton, UK., 1997.

M. Lyubovsky, L. Pfefferle, A. Datye, J. Bravo and T. Nelson, *J. Catal.*, 1999, **187**, 275–284.

M. Seo, S. Kim, D. Lee, H. Eun and K. Lee, *Appl. Catal., A*, 2016, **511**, 87–94.

M. Seo, S. Kim, H. E. Jeong, D. W. Lee and K. Y. Lee, *J. Mol. Catal*. *A: Chem*., 2016, **413**, 1–6.

M. Van Den Bossche and H. Grönbeck, *J. Am. Chem. Soc.*, 2015, **137**, 12035–12044.

N. M. Martin, J. Nilsson, M. Skoglundh, E. C. Adams, X. Wang, P. Velin, G. Smedler, A. Raj, D. Thompsett, H. H. Brongersma, T. Grehl, G. Agostini, O. Mathon, S. Carlson, K. Norén, F. J. Martinez-Casado, Z. Matej, O. Balmes and P.-A. Carlsson, *J. Phys. Chem. C*, 2016, **120**, 28009–28020.

N. M. Martin, M. Van Den Bossche, A. Hellman, H. Grönbeck, C. Hakanoglu, J. Gustafson, S. Blomberg, N. Johansson, Z. Liu, S. Axnanda, J. F. Weaver and E. Lundgren, *ACS Catal.*, 2014, **4**, 3330–3334.

N. S. Jacobson, E. J. Opila, D. L. Myers, and E.H. Copland, *J. Chem. Thermodyn*., 2005, **37**, 1130–1137.

N. Semagina and L. Kiwi Minsker, *Catal. Rev.*, 2009, **51**, 147–217.

N. Toshima and T. Yonezawa, *New J. Chem*., 1998, **22**, 1179-1201

Natural Gas Vehicle Knowledge Base. http://www.iangv.org/, NGV Global. 2018, (last accessed May 2018)

O. Deutschmann, F. Behrendt and J. Warnatz, *Catal. Today*, 1998, **46**, 155–163.

O. Deutschmann, R. Schmidt, F. Behrendt and J. Warnatz, *Proc. Combust. Inst.*, 1996, **26**, 1747–1754.

O. Levenspiel, *Chemical Reaction Engineering: An Introduction to the Design of Chemical Reactors*; Wiley: New York, 1998.

P. Araya, S. Guerrero, J. Robertson and F. J. Gracia, *Appl. Catal. A*, 2005, **283**, 225–233.

P. Castellazzi, G. Groppi and P. Forzatti, *Applied Catal. B*, 2010, **95**, 303–311.

P. Castellazzi, G. Groppi, P. Forzatti, A. Baylet, P. Marécot and D. Duprez, *Catal. Today.*, 2010, **155**, 18–26.

P. F. Skoda, M. F, Astier, and G. M, Pajonk, M, *React. Kinet. Catal. Lett.,* 1995, **55**, 101-110.

P. Gélin and M. Primet, *Appl. Catal. B.*, 2002, **39**, 1–37..

P. Hurtado, S. Ordóñez, H. Sastre and F. V. Diez, *Appl. Catal. B,* 2004, **51**, 229–238.

P. Mars and D. W. van Krevelen, *Chem. Eng. Sci.*, 1954, **3**, 41–59.

P. Migowski and J. Dupont, *Chem. Eur. J*, 2007, **13**, 32-39.

Q. Xu, K. C. Kharas, B. J. Croley, and A. K. Datye*, ChemCatChem*, 2011, **3**, 1004 – 1014.

Q. Zhang, I. Lee, J. Ge, F. Zaera and Y. Yin, *Adv. Funct. Mater.*, 2010, **20**, 2201–2214.

Q. Zhang, T. Zhang, J. Ge and Y. Yin, *Nano Lett*., 2008, **8**, 2867–2871.

R. Abbasi, L. Wu, S. E. Wanke, and R. E. Hayes, *Chem. Eng. Res. Des*., 2012, **90**, 1930–1942.

R. Burch and P. K. Loader, *Appl. Catal. B.,* 1994, **5**, 149–164.

R. Burch, Catal. Today, 1997, **35**, 27–36.

R. Burch, D. J. Crittle and M. J. Hayes, *Catal. Today.*, 1999, **47**, 229–234.

R. Burch, F. J. Urbano and P. K. Loader, *Appl. Catal. A*, 1995, **123**, 173–184.

R. Burch, P. K. Loader and F. J. Urbano, *Catal. Today*, 1996, **27**, 243–248.

R. E. Hayes, *Chem. Eng. Sci.,* 2004, **59**, 4073–4080.

R. E. Hayes, J. P. *Mmbaga, Introduction to chemical reactor analysis,* 2nd Ed., CRC Press,

Taylor and Francis, Boca Raton, 2013.

R. E. Hayes, S. T. Kolaczkowski, P. K. C. Li and S. Awdry, *Chem. Eng. Sci.*, 2001, **56**, 4815–4835.

R. F. Hicks, H. H. Qi, M. L. Young and R. G. Lee, *J. Catal.*, 1990, **122**, 280–294.

R. F. Hicks, H. Qi, M. L. Young and R. G. Lee, *J. Catal.*, 1990, **122**, 295–306.

R. Gholami, and K. J. Smith, *Appl. Catal. B,* 2015, **168–169**, 156–163.

R. Gholami, M. Alyani and K. Smith, *Catalysts*, 2015, **5**, 561–594.

R. I. Nooney, D. Thirunavukkarasu, Y. Chen, R. Josephs and A. E. Ostafin, *Langmuir,* 2003, **19**, 7628–7637.

R. J. Farrauto, M. C. Hobson, T. Kennelly, and E. M. Waterman, *Appl. Catal. A*, 1992, **81**, 227–237.

R. J. Farrauto, *Science*, 2012, **337**, 659–660.

R. K. Sharma, M. Yadav, R. Gaur, Y. Monga and A. Adholeya, *Catal. Sci. Technol.,* 2015, **5**, 2728–2740.

R. Kikuchi, S. Maeda, K. Sasaki, S. Wennerström and K. Eguchi, *Appl. Catal. A*, 2002, **232**, 23–28.

R. L. Oliveira, T. Nijholt, M. Shakeri, P. E. de Jongh, R. J. M. Klein Gebbink and K. P. de Jongh, *Catal. Sci. Technol*., 2016, **6**, 5124–5133.

R. Lamber, N. Jaeger and G. Schulz-Ekloff, *J. Catal.*, 1990, **123**, 285–297.

R. Lanza, S. G. Jaras and P. Canu, *Appl. Catal. A.*, 2007, **325**, 57–67.

R. M. Navarro, B. Pawelec, J. M. Trejo, R. Mariscal, and J. L. G. Fierro, *J. Catal.,* 2000, **189**, 184–194.

R. Mezaki and C. C. Watson, *I&EC Process Des. Dev.*, 1966, **5**, 62–65.

R. S. Miner, S. Namba, and J. Turkevich, *Stud. Surf. Sci., Catal.,* 1981, **7**, 160-172.

R. Strobel, J. Grunwaldt, A. Camenzind, S. E. Pratsinis and A. Baiker, *Catal. Letters*, 2005, **104**, 9–16.

R. van Hardeveld and F. Hartog, *Surf. Sci.*, 1969, **15**, 189–230.

R. Venkatesan, M. H. G. Prechtl, J. D. Scholten, R. P. Pezzi, G. Machado and J. Dupont, *J. Mater. Chem.,* 2011, **21**, 3030-3036.

R. W. J. Scott, O. M. Wilson and R. M. Crooks, *J. Phys. Chem. B.*, 2005, **109**, 692–704.

S. B. Yoon, J. Y. Kim, J. H. Kim, Y. J. Park, K. R. Yoon, S. K. Park and J. S. Yu, *J. Mater.*

Chem., 2007, **17**, 1758-1761.

S. H. Joo, J. Y. Park, C. K. Tsung, Y. Yamada, P. Yang, and G. A. Somorjai, *Nat. Mater.,* 2009, **8**, 126–131.

S. He, Z. Fei, L. Li, B. Sun, X. Feng and W. Ji, *Chin. J. Catal.,* 2013, **34**, 2098–2109.

S. Kang, S. Han, S. Nam, I. Nam, B. Cho, C. Kim and S. Oh, *Top. Catal.*, 2013, **56**, 298–305.

S. Kim, D. W. Lee, K. Y. Lee, and E. A. Cho, *Catal. Lett.,* 2014, **144**, 905–911.

S. Mondal, A. Samanta, B. B. Dhar and R. N. Devi, *Catal. Today*, 2015, **251**, 114–120.

S. Pálfi, W. Lisowski, M. Smutek and S. Černý, *J. Catal.*, 1984, **88**, 300–312.

S. S.-Y. Lee, M. Yamada and M. Miyake, *Sci. Technol. Adv. Mater.*, 2005, **6**, 420-426.

S. Seimanides and M. Stoukides, *J. Catal.*, 1986, **98**, 540–549.

S. Soulé, J. Allouche, J. C. Dupin, and H. Martinez, *Microporous Mesoporous Mater.,* 2013, **171**, 72–77.

S. Specchia, F. Conti and V. Specchia, *Ind. Eng. Chem. Res.*, 2010, **49**, 11101–11111.

S. T. G. Ronald M. Heck, Robert J. Farrauto, *Catalytic Air Pollution Control: Commercial Technology*, John Wiley & Sons, New Jersey, 3rd edn., 2016.

T. Ando, Y. Isobe, D. Sunohara, Y. Daisho and J. Kusaka, *JSAE Rev.*, 2003, **24**, 33–40.

T. Li, J. Moon, A. A. Morrone, J. J. Mecholsk y, D. R. Talham and J. H. Adair, *Langmuir*, 1999, **15**, 4328–4334.

T. R. Baldwin and R. Burch, *Appl. Catal.*, 1990, **66**, 337–358.

T. R. Baldwin, and R. Burch, *Appl. Catal.,* 1990, **66**, 359–381.

T. Teranishi and M. Miyake, *Chem. Mater.,* 1998, **10**, 594–600.

T. V. Choudhary, S. Banerjee and V. R. Choudhary, *Appl. Catal., A*, 2002, **234**, 1–23.

T. W. Hansen, A. T. DeLaRiva, S. R. Challa and A. K. Datye, *Acc. Chem. Res.*, 2013, **46**, 1720 – 1730.

T. Wu, W. Cai, P. Zhang, X. Song and L. Gao, *RSC Adv*., 2013, **3**, 23976–23979.

The International Council on Clean Transportation, Publications, White Paper. Assessment of Heavy-Duty Natural Gas Vehicle Emissions: Implications and Policy Recommendations, https://www.theicct.org/sites/default/files/publications/ICCT_NG-HDV-emissions-assessmnt_20150730.pdf, 2015, (last accsessed May 2010)

The International Council on Clean Transportation, Publications, Briefing, A technical summary of Euro 6/VI vehicle emission standards,

https://www.theicct.org/sites/default/files/publications/ICCT_Euro6-VI_briefing_jun2016.pdf., 2016, (last accsessed May 2010)

U. S. Department of Energy, Energy Efficiency and Renewable Energy, Alternative Fuels Data Center, Fuels and Vehicles, Natural Gas, Natural Gas Vehicle Emissions, https://www.afdc.energy.gov/vehicles/natural_gas_emissions.html., 2018, (last accessed May 2018)

U. S. Department of Energy. Energy Efficiency and Renewable Enrgy, Publications. https://www.afdc.energy.gov/uploads/publication/alternative_fuel_price_report_jan_2018.pdf. 2018, (last accessed May 2018)

U. S. Environmental Protection Agency, New Source Performance Standards and Permitting Requirements, Final Rules. https://www.epa.gov/controlling-air-pollution-oil-and-natural-gas-industry/new-source-performance-standards-and, 2017, (accessed on 21 December 2017).

U. S. Environmental Protection Agency, Summary of the Clean Air Act, 42 U.S.C. 7401 et seq. (1970). https://www.epa.gov/laws-regulations/summary-clean-air-act, 2017, (accessed on 21 December 2017).

U. S. Government. The World Factbook, Central Intelligence Agency. https://www.cia.gov/library/publications/the-world-factbook/geos/xx.html, 2018, (accessed on 20 March 2018).

United States Environmental Protection Agency, Understanding Global Warming Potentials. https://www.epa.gov/ghgemissions/understanding-global-warming-potentials, 2018, (accessed on 20 March 2018).

V. Mazumder and S. Sun, *J. Am. Chem. Soc.*, 2009, **131**, 4588-4589.

V. Sudheeshkumar, A. Shivare and R. W. J. Scott, *Catal. Sci. Technol.,* 2017, **7**, 272–280.

W. Chen, J. R. Davies, D. Ghosh, M. C. Tong, J. P. K. And and S. Chen, *Chem. Mater.*, 2005, **18**, 5253-5259.

W. J. Kuper, M. Blaauw, F. V. Berg and G. H. Graaf, *Catal. Today*, 1999, **47**, 377–389.

W. Juszczyk and Z. Karpiński, *J. Catal*., 1989, **117**, 519–532.

W. Lyons, G. Plisga, M. Lorenz, *Standard handbook of petroleum and natural gas engineering,* 3rd Ed., Elsevier, Oxford, UK, 2016.

W. Qi, J. Ran, R. Wang, X. Du, J. Shi and J. Niu, *RSC Adv.*, 2016, **6**, 109834–109845.

W. R. Schwartz, and L. D. Pfefferle, *J. Phys. Chem. C*, 2012, **116**, 8571–8578.

W. R. Schwartz, D. Ciuparu and L. D. Pfefferle, *J. Phys. Chem. C*, 2012, **116**, 8587–8593.

W. Stöber, A. Fink and E. Bohn, *J. Colloid Interface Sci.*, 1968, **26**, 62–69.

X. Chen, Y. Cheng, C. Yup, J. W. Schwank, and R. W. McCabe, *Appl. Catal. B*, 2015, **163**, 499–509.

X. J. Lin, A. Z. Zhong, Y. B. Sun, X. Zhang, W. G. Song, R. W. Lu, A. M. Cao and L.-J. Wan, *Chem. Commun.,* 2015, **51**, 7482–7485.

Y. Borodko, S. M. Humphrey, T. D. Tilley, H. Frei and G. A. Somorjai, *J. Phys. Chem. C*, 2007, **111**, 6288–6295.

Y. C. Chin and E. Iglesia, *J. Phys. Chem. C ,* 2011, **115**, 17845–17855.

Y. Chin and D. E. Resasco, *J. Catal*, 1999, **14**, 1–39.

Y. Deng and T. G. Nevell, *Catal. Today,* 1999, **47**, 279–286.

Y. H. C. Chin, M. García-Diéguez and E. Iglesia, *J. Phys. Chem. C*, 2016, **120**, 1446–1460.

Y. H. Chin, C. Buda, M. Neurock and E. Iglesia, *J. Am. Chem. Soc.*, 2013, **135**, 15425–15442.

Y. Hu, K. Tao, C. Wu, C. Zhou, H. Yin and S. Zhou, *J. Phys. Chem. C,* 2013, **117**, 8974–8982.

Y. Nagai, T. Hirabayashi, K. Dohmae, N. Takagi, T. Minami, H. Shinjoh and S. Matsumoto, *J. Catal.,* 2006, **242**, 103–109.

Y. Ozawa, Y. Tochihara, A. Watanabe, M. Nagai and S. Omi, *Appl. Catal. A*, 2004, **259**, 1–7.

Y. Wang, A. V. Biradar and T. Asefa, *ChemSusChem,* 2012, **5**, 132–139.

Y. Wang, A. V. Biradar, C. T. Duncan and T. Asefa, J. Mater. Chem., 2010, **20**, 7834–7841.

Y. Wang, J. Liu, P. Wang, C. J. Werth, and T. J. Strathmann, *ACS Catal.,* 2014, **4**, 3551–3559.

Y. Xin, S. Lieb, H. Wang and C. K. Law, *J. Phys. Chem. C*, 2013, **117**, 19499–19507.

Y. Y. Xu, J. Ma, Y. Y. Xu, L. L. Xu, L. L. Xu, H. H. Li and H. H. Li, *RSC Adv.,* 2013, **3**, 851–858.

Y. Zhang, S. Xiang, Y. Zhou, Y. Xu, Z. Zhang, X. Sheng, Q. Wang and C. Zhang, *RSC Adv.*, 2015, **5**, 48187–48193.

Z. Wang, X. Yang, J. Yang, Y. Jiang and N. He, *Anal. Chim. Acta,* 2015, **862**, 53–63

Appendices

Appendix A. The Supporting Information of Chapter 2

Appendix A presents the following:

- Table of reported porosities of the encapsulated nanoparticles prepared using various surfactants/polymers
- Figure A.1. The TEM images of Porous Pd@mSilica nanostructures prepared using CTAB-stabilized Pd NP's reduced by $NaBH_4$.

Table A.1. Reported porosity of the encapsulated structures. The citations refer to the References of Chapter 2 (section 2.5).

	Structure	BET surface area m^2g^{-1}	Pore volume mLg^{-1}	Mean pore diameter nm	Method/Surfactant	Ref.
2003	$Au@SiO_2$	690	0.53	3.14	Hexadecyltrimethylammonium bromide (CTAB)	Nooney[25]
2004	Zr,Ti,Fe@SiO_2	1028-1155	1.17-1.95	2.1-2.4	CTAB, highly acidic	Chao [26]
2008	Au@SiO2	200-300	0.25, 0.27	1.5, 12	Surface-protected etching	Yin [27]
2008	$Pd@SiO_2$	104	-	<4	PVP	Li [13]
2009	Pt@SiO2	440	-	2.3	Tetradecyltrimethyl ammonium bromide (TTAB)	Joo [9]
2010	$Pd@SiO_2$	185	0.5		Igepal CO560	Forman [28]
2010	SiO_2/Pt@SiO_2	113	0.27	13.2	Surface-protected etching	Yin [20]
2010	SiO2/Pd/SiO2	115	0.31	15	Surface-protected Etching	Wang [29]
2010	$Ni@SiO_2$	195	0.38	-	igepal CO-630/C18TMS	Park [30]

2012	$Ni@SiO_2$	117	0.125	3-4	PVP(K30)	Li [21]
2012	SiO_2/Pd/hollowZrO_2	27	0.17	2.3	PVP/(3-Aminopropyl)triethoxysilane (APTES) /Brij30	Wang [31]
2012	AlMgO/SiO_2	456	0.43	3.5	CTAB	Wang[32]
2012	SiO_2/Pd@SiO_2	400	0.23	1.5	PVP/ Dodecyltrimethylammonium chloride (DTAC)	Yang[33]
2013	$Pt@SiO_2$	247	-	2-3	Tetraethyl orthosilicate (TEOS) + Trimethoxy(octadecyl)silane (C18TMS)/CTAB	He [34]
2013	SiO_2/Pt@SiO_2	448-662	0.39-0.55	2.4-2.6	SiO_2/Pt+CTAB, SiO_2	Xiao [35]
2013	$Pd@SiO_2$	171	-	3.2	One pot hydrothermal synthesis	Tan [36]
2013	$Pd@SiO_2$	948	1.6	2.2	TTAB	Hu[17]
2013	$Pd@SiO_2$	401	-	1.1	PVP	Oh [22]
2013	$Pd@SiO_2$	459, 530	1.8, 2.3	2.5	Oleylamine-capped Pd	Xu [37]
2013	$Au@SiO_2$	561	0.524	2.5	CTAB (one pot)	Chen [38]
2013	Ag-Au@SiO_2	1331	-	2.0	CTAB/Galvanic replacement	Soule [16]
2013	Cu-Ni@SiO_2	146	-	-	CTAB	Wu [39]
2014	Mn_3O_4@SiO_2	500-700	-	2-4	CTAB	Xu [40]
2014	SiO_2@Pt@SiO_2	24	-	-	PVP	Zhang [10]
2014	$AuPd@SiO_2$	190-215	-	1.5-3	Thiol-protected	Samanta [41]
2014	$Pd@SiO_2$	323	0.402,0.086	-	PVP	Kim [15]
2014	$Pt@SiO_2$	64	-	30	PS-b-PVP-b-PEO triblock copolymer	Bastakoti [42]

2015	$Pd@SiO_2$	489	1.05	19.4	Block copolymer	Guang-Li [43]
2015	PdONiO@ $mSiO_2$	790	1.1	2.2	TTAB	Liu [44]
2015	Pt@Hollow SiO_2	721	0.33	3.5	Hollow SiO_2 using carbon spheres	Zhang [24]
2015	$Au@SiO_2$	41.5	-	3, 60	PVP+CTAB	Zhang [45]
2015	$Fe_3O_4@SiO_2$ @$mSiO_2$	396	0.54	2.7 and 10.3	Cetyltrimethylammonium chloride solution (CTAC)	Yang [46]
2015	$Pt@SiO_2$	480	-	1.9	CTAB	Wang [47]
2015	Pd@MCM41	935	-	3-3.3	CTAB	Lin [48]
2015	$AgPd@SiO_2$	533	-	1.4	Thiol-protected	Mondal [49]
2015	CeNiO@SiO_2	80-179	0.16-0.43	7.4-11.6	PVP	Zhang [23]
2015	$Pd@SiO_2$	254	0.24	2.9	CTAB	Martins [50]
2015	$Pd@SiO_2$	302-406	1.03	6	CTAC	Shen [51]
2016	$Pd@SiO_2$	383	1.5	8.9	CTAB	Ying [52]
2016	$Pd@SiO_2$	335	0.56	-	PVP	Seo [53]
2017	Au@Silica	70	Micro: 0.0092 Meso:0 .111	9	Mercaptoundecanoic acid (MUA)	Sudheeshkumar [54]
2017	$Pd@SiO_2$	51-70	0.167-0.195	-	PVP during reduction, no porogen	This work
2017	$Pd@mSiO_2$	610-764	0.347-0.403	3.4	PVP during reduction and CTAB during encapsulation	This work

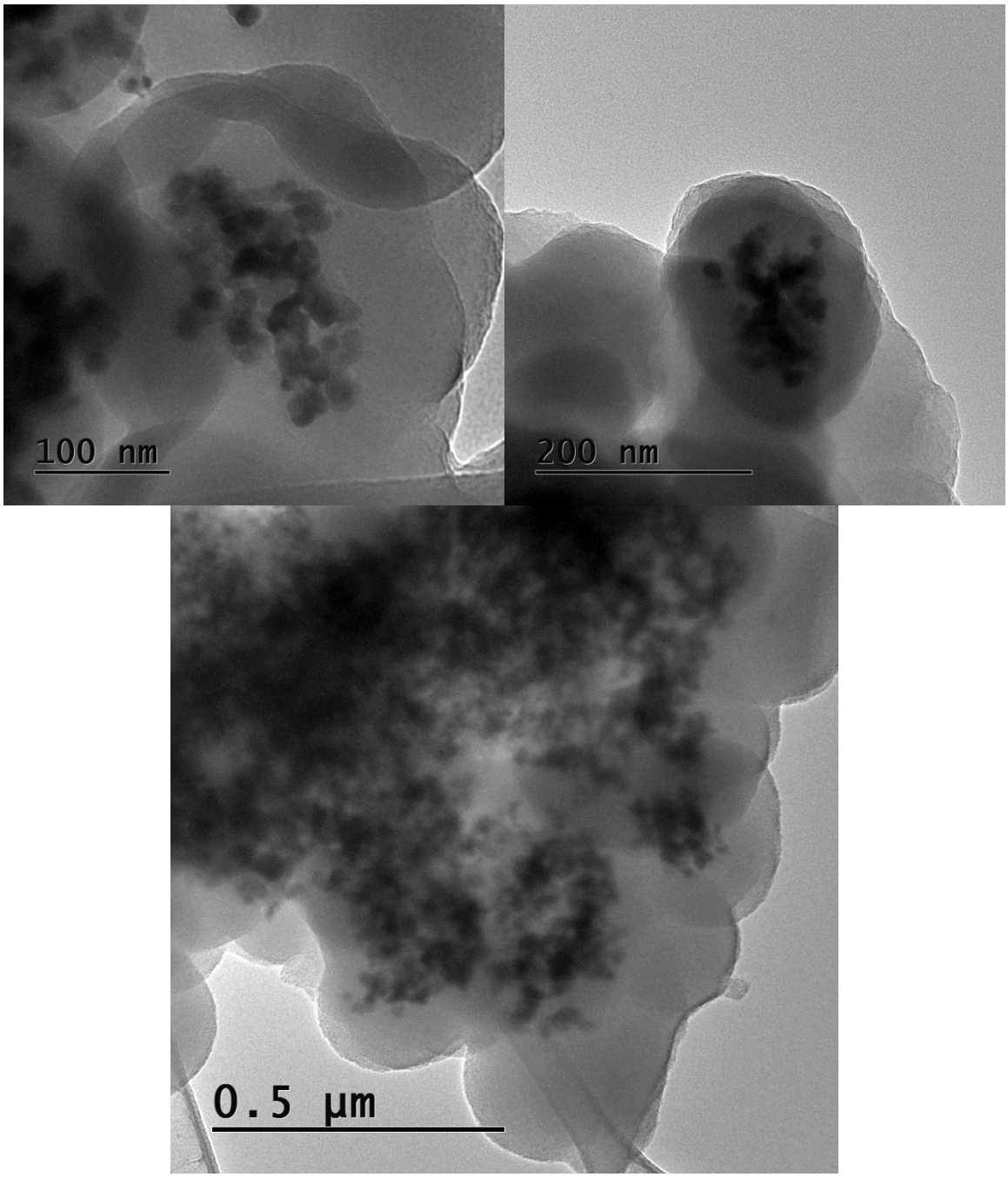

Figure A.1. 5 wt.% Porous Pd@mSiO$_2$ prepared using CTAB-stabilized Pd NP's reduced by NaBH$_4$.

In preparation of these nanostructures (Figure A. 1) the Pd nanoparticles were stabilized using CTAB and the reduction was done using sodiumborohydride. During the encapsulation step, 1 g of CTAB was added as a pore-inducing agent right before Stöber step. Even though the resulting structure was porous, the conversion was extremely low due to agglomeration of the

core NPs as Figure A.1. The probable reason is that at high metal concentrations, the stabilization provided by CTAB was not sufficient to keep the core nanoparticles apart. This synthesis procedure can be compared to the one discussed in Section. 2.1.3.2.

Appendix B. The Supporting information of Chapter 4.

B.1. Calculation of silica shell porosity

The porosity of the shell can be estimated from the data using the parallel pore model, which is valid for a narrow pore size distribution. We note that:

$$d_P = \frac{4\varepsilon}{S_A \rho_S (1-\varepsilon)} \qquad \text{B.1}$$

From Table 1 of the main text, the mean pore diameter of the shell was 3.4 nm, the surface area was 592 m^2/g, and we take the density of the non-porous shell material as 2200 kg/m^3.
Substitute:

$$3.4\times10^{-9}\,\mathrm{m} = \frac{4\varepsilon}{592{,}000\,\frac{\mathrm{m}^2}{\mathrm{kg}}\,2200\,\frac{\mathrm{kg}}{\mathrm{m}^3}(1-\varepsilon)} \qquad \text{B.2}$$

Solving for the porosity gives a value of 52.5%.

B.2. Calculation of the average number of cores in a shell

On average, there are multiple cores per shell. The average number of cores can also be calculated (estimated) from the physical data. The mass percent of PGM in the catalyst calculated from the NAA analysis was 11.19%. The number of cores then depends on the relative densities of the cores and shell. The mass fraction of PGM is given by the formula:

$$X_{PGM} = 0.1119 = \frac{n D_C^3 \rho_C}{n D_C^3 \rho_C + \left(D_S^3 - D_C^3\right)\rho_S (1-\varepsilon)} \qquad \text{B.1}$$

Substitute the numbers:

$$0.1119 = \frac{n 9^3\, 16{,}714}{n 3.4^3\, 16{,}714 + \left(70^3 - n 9^3\right)2200(1-0.525)} \qquad \text{B.1}$$

Solve for n=3.7. On average there should be about 3.7 cores per shell.

B.3. Predicted and experimental ignition curves, Model 1 for dry combustion

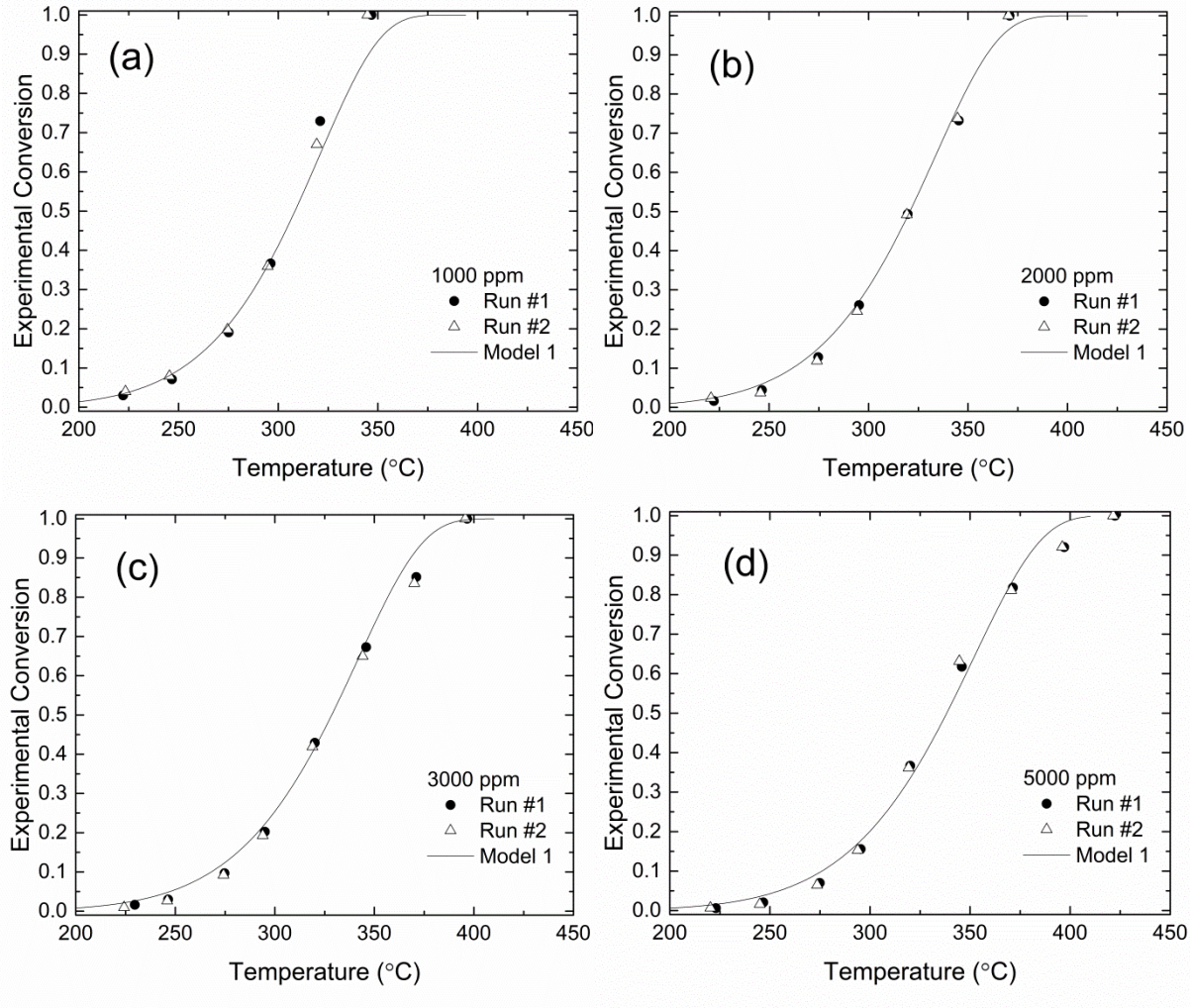

Figure B.1. The predicted ignition curve produced by Model 1 and the experimental points. Reaction in dry conditions, and at an initial CH_4 concentration of a) 1000 ppm, b) 2000 ppm, c) 3000 ppm and d) 5000 ppm.

B.4. Predicted and experimental ignition curves, Model 2 for wet combustion

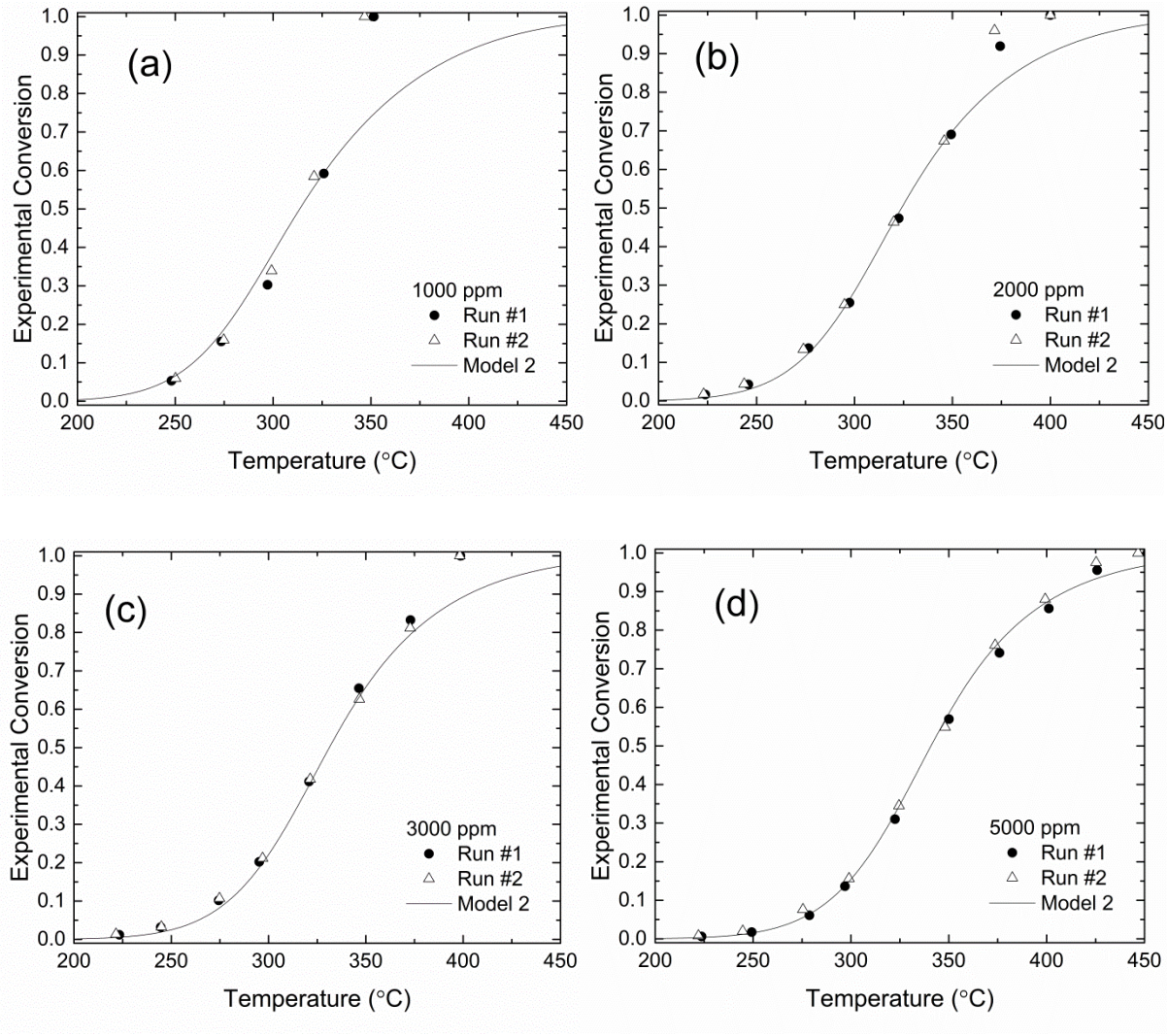

Figure B.2. The predicted ignition curve produced by Model 2 and the experimental points. Reaction in the presence of 5% added H_2O, and at an initial CH_4 concentration of a) 1000 ppm, b) 2000 ppm, c) 3000 ppm and d) 5000 ppm.

Appendix C. Supporting calculations

This section presents the calculations regarding the verification of the following

- Plug flow assumption and absence of axial dispersion
- Absence of the external mass transfer limitations
- Absence of the internal mass transfer limitations
- Absence of the external heat transfer limitations
- Absence of the internal heat transfer limitations
- TOF calculations

C.1. Verification of the plug flow assumption and absence of axial dispersion

Table C.1. Calculations related to the verification of the plug flow assumption and absence of axial dispersion

Catalyst	$Pd@mSiO_2$	$PdPt@SiO_2$	$PdPt@SiO_2$ in wet feed
L_{Bed}	7.00E-03	2.00E-02	2.00E-02
d_p	8.00E-08	7.00E-08	7.00E-08
$d_{reactor}$	0.007747	0.007747	0.007747
Plug flow criterion $\frac{L_{Bed}}{d_p} > 50$ C1	**8.75E+04**	**2.86E+05**	**2.86E+05**
Absence of axial dispersion $\frac{d_{reactor}}{d_p} > 10$ C2	**9.68E+04**	**1.11E+05**	**1.11E+05**

C.2. Verification of the absence of external mass transfer limitations using Mears criterion

Table C.2. Calculations related to the absence of external mass transfer limitations using Mears criterion

Catalyst	$Pd@mSiO_2$	$PdPt@SiO_2$	$PdPt@SiO_2$ (wet feed)
X (conversion) at differential conditions	0.392	0.2229	0.2199
W	2.17E-02	0.1	0.092
T	635.65	626.15	626.15
d_p	8.00E-08	7.00E-08	7.00E-08
Flow rate mL/min (STP)	212	222.9	222.9
Flow rate m^3s^{-1} (at reaction temperature)	8.225E-06	8.52E-06	8.52E-06
ε_{bed}	0.4	0.4	0.4
$d_{reactor}$	0.007747	0.007747	0.007747
Cross sectional area of the reactor tube	4.71E-05	4.71E-05	4.71E-05
Free stream velocity (Flow rate /area (m/s))	0.17458	0.180815	0.180815
Molar methane flow rate F	6.3244E-07	6.32E-07	6.32E-07
L_{Bed}	7.00E-03	2.00E-02	2.00E-02
Reaction Rate			
$(-R_A) = \frac{F_0 X}{W} \quad \frac{\text{mol}}{\text{kg}_{\text{Cat}}\text{s}}$	1.14E-02	1.41E-03	1.51E-03
ν_{CH_4} [C3]	24.42	24.42	24.42
ν_{air} [C3]	20.1	20.1	20.1
Fuller Diffusivity [C3]			
$D_{AB} = \frac{1.013\times10^{-2}T^{1.75}\left(\left(\frac{1}{M_{CH_4}}\right)+\left(\frac{1}{M_{air}}\right)\right)^{0.5}}{P[\left(\sum\nu_{CH_4}\right)^{1/3}+\left(\sum\nu_{air}\right)^{1/3}]^2}$	7.9286E-05	7.72E-05	7.72E-05
$\text{Re} = \frac{U\rho_g d_p}{\mu}$ [C4]	1.00E-04	9.09-05	9.09-05
μ Pa.s [C4]	3.12E-05	3.12E-05	3.12E-05
$\rho_g \frac{\text{kg}}{\text{m}^3}$	0.56	0.56	0.56
$Sc = \frac{\mu}{D_{AB}\rho_g}$ [C5]	0.7027	0.721471	0.721471
$Sh = 2.0 + 0.6\,\text{Re}^{1/2}\,Sc^{1/3}$ [C5]	2.0053	2.00513	2.00513
$k_c = \frac{D_{AB}Sh}{d_p}$ [C5]	1.99E+03	2.21E+03	2.21E+03

ρ_{Cat}	1105	1167	1167
n (Order in Mears formula)	1.00E+00	1.00E+00	1.00E+00
C_{M_0}	7.69E-02	7.42E-02	7.42E-02
$C_M = C_{M_0}(1-X)$	4.68E-02	5.77E-02	5.79E-02
ρ_{Bed}	6.63E+02	7.00E+02	7.00E+02
Mears Number (if < 0.15, mass transfer limitations do not exist) C5 $\frac{-R_A \rho_b Rn}{k_c C_M} < 0.15$	**3.26-09**	**2.71E-10**	**2.89E-10**

C.3. Verification of the absence of internal mass transfer limitations using Weisz-Prater Number

Table C.3. Calculations related to the verification of the absence of internal mass transfer limitations using Weisz-Prater Number.

Catalyst	Pd@mSiO$_2$	PdPt@SiO$_2$	PdPt@SiO$_2$ (wet feed)
d_{pore}	3.40E-09	3.40E-09	3.40E-09
$M_{W\,CH_4}$	1.60E-02	1.60E-02	1.60E-02
$D_K = \frac{d_{pore}}{3}\sqrt{\frac{8RT}{\pi M_W}}$ C6	1.04E-06	1.03E-06	1.03E-06
$D_{pore} = \left(\frac{1}{D_{AB}} + \frac{1}{D_K}\right)^{-1}$ C6	1.026E-06	1.00E-06	1.00E-06
τ	2	2	2
S	695	695	695
$\phi_p = \frac{S\rho_{Cat} d_{pore}}{4}$ C6	0.525	0.525	0.525
Methane concentration $C_M = C_{M_0}(1-X)$	4.68E-02	5.77E-02	5.79E-02
$D_{eff} = \frac{\phi_P D_{pore}}{\tau}$ C6	2.69E-07	2.7E-07	2.7E-07
Weisz-Prater Number C5 $C_{WP} = \frac{-R_A \rho_{Cat} r^2}{D_{eff} C_M} < 0.3$	**1.60E-06**	**1.31E-08**	**1.40E-07**

C.4. Verification of the absence of external heat transfer limitations

Table C.4. Calculations related to the verification of the absence of external heat transfer limitations

Catalyst	$Pd@mSiO_2$	$PdPt@SiO_2$	$PdPt@SiO_2$ in wet feed
$Nu = 2.0 + 0.6\,\mathrm{Re}^{1/2}\,\mathrm{Pr}^{1/3}$ C5	2.0053	2.00503	2.00503
Pr of air at 613 K	0.6811	0.6811	0.6811
k_{air}	0.047	0.047	0.047
$h = \frac{k_{air} Nu}{d_p}$ C5	1.18E+03	1.35E+03	1.35E+03
$\Delta H_{reaction}$ C7	890	890	890
E_A C7	78.2	72.6	72.6
$\Delta T_{ext} = \frac{-R_A(-\Delta H_{reaction})\rho_{bed} r E_A}{h T^2 R_g} < 0.15$ C5	5.33E-12	5.09E-13	5.46E-13

C.5. Verification of the absence of internal heat transfer limitations

Table C.5. Calculations related to the verification of the absence of internal heat transfer limitations

Catalyst	$Pd@mSiO_2$	$PdPt@SiO_2$	$PdPt@SiO_2$ in wet feed
$\beta = \frac{-\Delta H_{reaction} D_{eff} C_M}{k_{eff} T}$ C6	0.0004	0.00051	0.00051
$\Delta T_{max} = \beta T$ C6	0.260	0.319	0.320

C.6. TOF calculations

Table C.6. TOF calculations

Catalyst	Aged PdPt@SiO_2	Aged PdPt/SiO_2	Aged PdPt/Al_2O_3
Chemisorbed CO (μmol/g)	70.145	7.1715	54.419
Metal Dispersion	11.760	1.202	9.123
sample mass in CO chemisorption test	0.031	0.0175	0.017
Pd wt.%	4.205	4.205	4.205
Pt wt .%	6.98	6.98	6.98
Pd content (micromol Pd) $\text{sample mass} \times \frac{\text{mass of Pd}}{\text{100 g of sample}} \times \frac{\text{1 mol Pd}}{\text{106.42 gPd}} \times \frac{\text{1000000 μmol Pd}}{\text{1 mol Pd}}$	12.2491	6.9148	6.7172
Pt content (micromol Pt) $\text{sample mass} \times \frac{\text{mass of Pt}}{\text{100 g of sample}} \times \frac{\text{1 mol Pt}}{\text{195.084 gPt}} \times \frac{\text{1000000 μmol Pt}}{\text{1 mol Pt}}$	11.0916	6.2614	6.0825
Total metal content = μmol Pd + μmol Pt	23.3407	13.17622	12.799
TOTAL chemisorbed CO (μmolCO)	2.1745	0.1255	0.9251
Dispersion (as molCO/mol(Pd+Pt)*100%) $\frac{\text{Chemisorbed CO (μmol)}}{\text{Total metal content (μmol)}} \times 100$	9.3163	0.9525	7.228
mass of Pd in reaction (mg)	4.205	4.205	4.205
mass of Pt in reaction (mg)	6.98	6.98	6.98
mol Pd in reaction $\text{mass Pd mg} \times \frac{\text{1 g}}{\text{1000 mg}} \times \frac{\text{1 mol Pd}}{\text{106.42 gPd}}$	3.951E-05	3.951E-05	3.951E-05
Mol Pt in reaction $\text{mass Pt mg} \times \frac{\text{1 g}}{\text{1000 mg}} \times \frac{\text{1 mol Pt}}{\text{195.084 gPt}}$	3.577E-05	3.577E-05	3.578E-05
Total metal in reaction (mol) Total metal (mol) = Pd (mol) + Pt (mol)	7.529E-05	7.529E-05	7.529E-05
mol surface Pd+Pt in reaction assuming 1:1 CO:metal ratio $\text{dispersion (\%)} \times \frac{\text{mol Pd + mol Pt in raction}}{100}$	7.014E-06	7.171E-07	5.442E-06
F_A (CH_4 molar flowrate $\frac{\text{mol } CH_4}{\text{s}}$)	6.32E-07	6.32E-07	6.32E-07
X	0.0354	0.0126	0.044
T	574.75	622.65	619.55

reference activation energy (J/mol)	72600	72600	72600
T_{ref}	623.15	623.15	623.15
E_A	72600	72600	72600
Turnover rate (in terms of mol CH_4 per mol suface Pd+PT per second) Turnover rate= $\frac{F.X}{\text{mol surface Pd+Pt in raction}}$	0.00319	0.0111	0.005
TOF at the reference temperature (s^{-1}) TOF= Turnover rate $\times \exp\left(\frac{-E_A}{8.314} \times \left(\frac{1}{T_{ref}} - \frac{1}{T}\right)\right)$	**3.06E-03**	**3.31E-03**	**1.63E-03**

C.6. References

C.1. J. F. Le Page, Applied heterogeneous catalysis, TechniP, Paris, 1987.

C.2. J. Perez-Ramirez, R.J. Berger, G. Mul, F. Kapteijn, and J.A. Moulijn, *Catal. Today,* 2000, **60**, 93-109

C.3. E. N. Fuller, P.D. Schettler, and J. C. Giddings, *Ind. Eng. Chem*. 1966, **58**, 18-27

C.4. W. Lyons, G. Plisga, M. Lorenz, *Standard handbook of petroleum and natural gas engineering,* 3rd Ed., Elsevier, Oxford, UK, 2016.

C.5. H. Scott Fogler, *Elements of Chemical Reaction Engineering*, 5th edn, Prentice Hall, Kendaville, IN, 2016.

C.6. R. E. Hayes, J.P. *Mmbaga, Introduction to chemical reactor analysis,* 2nd Ed., CRC Press, Taylor and Francis, Boca Raton, 2013.

C.7. R. Abbasi, L. Wu, S. E. Wanke and R. E. Hayes, *Chem. Eng. Res. Des.*, 2012, **90**, 1930–1942.

Appendix D. Calculations of the PGM loading of a catalytic converter washcoated with PdPt@SiO_2

The loading in a catalytic converter is usually reported as PGM per ft^3 of the catalytic converter (monolith). To calculate the PGM loading of the catalyst, a few assumptions are made.

Assumptions:

The internal structure of a catalytic converter is generally composed of a monolith. The washcoat material accounts for 12% of the total volume of the monolith and has a voidage of 36%. Thus, the volume of the catalyst in 1 ft^3 of the volume of the catalytic converter (monolith) is:

$$1\,\mathrm{ft}^3 \times 0.12 \times (1-0.36) = 0.0768\,\mathrm{ft}^3 = 0.002175\,\mathrm{ft}^3 \qquad \text{C.1}$$

The PGM loading of the catalyst developed in this study (PdPt@SiO_2) is 11.2 wt.% (4.2 wt.% Pd, 7 wt.% Pt).

Assuming an average density of 16175 kg/m^3 and 1400 kg/m^3 for the core (PdPt) and the shell (porous silica) of the catalyst the following apply. A catalyst powder with metal loadings of 1, 5 and 10 wt% PGM on alumina translate into an approximate PGM loading of 90, 450, and 950 g/ft^3 of monolith

$$16175\ \frac{\text{kg PdPt}}{\text{m}^3\text{PdPt}} \times \text{x}\ \frac{\text{m}^3\text{Catalyst}}{\text{m}^3\text{Catalyst}} = 0.112\ \frac{\text{kg PdPt}}{\text{kg Catalyst}} \times \text{y}\ \frac{\text{kg Catalyst}}{\text{m}^3\text{Catalyst}} \qquad \text{C.2}$$

$$1045\ \frac{\text{kg Silica}}{\text{m}^3\text{Silica}} \times (1-\text{x})\ \frac{\text{m}^3\text{Silica}}{\text{m}^3\text{Silica}} = 0.888\ \frac{\text{kg Silica}}{\text{kg Catalyst}} \times \text{y}\ \frac{\text{kg Catalyst}}{\text{m}^3\text{Catalyst}} \qquad \text{C.3}$$

Solving Equations C.2 and C.2 gives the unknowns as

$$\text{x}=0.008\ \frac{\text{m}^3\text{Silica}}{\text{m}^3\text{Silica}},\ \text{y}=1167\ \frac{\text{kg Catalyst}}{\text{m}^3\text{Catalyst}}$$

So, the mass of catalyst in 1 ft^3 of the monolith is

$$0.002174\ \frac{\text{m}^3\text{Catalyst}}{1\ \text{ft}^3\text{monolith}} \times 1167\ \frac{\text{kg Catalyst}}{\text{m}^3\text{Catalyst}} = 2.538\ \frac{\text{kg Catalyst}}{1\ \text{ft}^3\text{monolith}}$$

And thus, the amount of PGM is

$$0.112 \times 2.538 \frac{\text{kg Catalyst}}{1\ \text{ft}^3\text{monolith}} \times 1000 \frac{\text{g Catalyst}}{\text{kg Catalyst}} = 284.2 \frac{\text{g PGM}}{1\ \text{ft}^3\text{monolith}}$$

By comparing this value to the typical PGM of (100 – 200 g/ft^3) it is expected that the catalyst developed here can result in a feasible size of a catalytic converter due to its high PGM loading. For the sake of comparison, similar calculations can be done for alumina-supported catalysts of various loadings. For example, a catalyst powder with metal loadings of 1and 5 wt% PGM on alumina translates into an approximate PGM loading of 90, and 450 g/ft^3 of monolith, respectively. It is also noted that one major concern with increasing the metal loading is the severity of the sintering problem at higher loadings; however, it was proved in this work that the high loading catalysts prepared here were resistant to NP sintering.

Appendix E. MATLAB codes for Kinetic Optimization

This section presents the MATLAB codes used in the kinetic modeling. Several rate equations were tested however only the models that produced reasonable predictions (Model 1 and Model 2) are included here. The codes for dry and wet conditions are similar however need to be saved and run in separate folders.

E.1. MATLAB codes for dry conditions

Contents of the folder for dry conditions:

- model.m: the M-file containing the model equation which allows for switching between two models (Model 1= Kikuchi's rate expression, Model 2= the rate equation proposed in this work)
- x_exp.m is the vector of the experimental conversions for dry conditions.
- Obj. m is the ODE solver that solves Model.m for given k parameters and produces the objective function
- run.m is the optimizer that optimizes the k parameters using patternsearch algorithm
- delta.m is the M-file used to compare the experimental data to the predicted conversion by plotting the results
- lightdry.m is used in the end to plot the light off curves for the optimized values of k
- lightdryxls.m is works in conjunction with lightdry.m and x_exp and saves the light-off curves at various concentrations.

model.m, x_exp.m, obj.m and run. m function together to give the optimized k vector as the *ans* of run.m. This *ans* is used in delta.m to plot the experimental data vs predicted data. The optimized k vector is entered (manually) in the lightdryxls.m to produce the light off curves.

model.m

```
function dxdt = model(t,x,k)

% This code is used to model the DRY conditions.
%A similar code (with different T, Q0, FA0, FB0-and its own x_exp M-file)
%is used for wet conditions. The m-files for wet and dry conditions are to
%be saved and run in separate folders.
%The folder for Dry conditions should contain the following files:
% Model.m, x_exp.m, Obj.m, run.m and delta.m, lightdry.m and lightdryxls.m
%a separate folder with similar files is used for wet conditions.

%Model 1: -rA= k1CA/1+k2CB  Kikuchi's Model
%Model 2: -rA= k1CA/[(k2CB)*(1+k3CA)]- The model Proposed in this work
%Units of rate: mol/gCat.s
% T is the temperature matrix (degree C)
%Model is the model number and functions as a switch between two models
%Q0= total initial volumetric flowrate (m3/s (STP))
%FA0= molar flow rate of CH4 (mol CH4/s)
%FB0= molar flow rate of H2O (mol water/s)
%R= universal gas constant kJ/molK
%Thus, the energies (activation and adsorption) are in kJ
%The catalyst mass (W) which is used in the tspan in the Obj.m is
%in g, thus the rate equation is in mol/gCat.s
%Model. m contains the global variable “Model” and needs to be run before
%running Obj.m, run.m, com.m

%lightdryxls.m saves the lightoff curves in excel by solving lightdry.m
%lightwetxls.m saves the wet lightoff curves in excel by solving lighwet.m
%%%%%%%%%%%%%%%%%%%%%%%%%%%%%%%%%%%%%%%%%%%%%%%%%%%%%%



global Model i
Model = 1;

T= [274.9   295.35  320.05  345.85  371.4   273.6   293.85  319.3   344.6
370.55  274.55  294.75  319.7   345.1   370.9   274.35  294.5   319.3   344.9
370.4   274.75  295 320.05  345.85  274.2   293.9   318.9   344.1   370.05
274.65  295.25  319.7   345.35  274.05  294.25  319.2   344.75  275.15  296.2
321.05  245.45  274.55  294.75  319.3
]+273.15;
Q0=[0.00000357  0.00000357  0.00000357  0.00000357  0.00000357  0.00000357
0.00000357  0.00000357  0.00000357  0.00000357  3.53E-06    3.53E-06
3.53E-06    3.53E-06    3.53E-06    3.53E-06    3.53E-06    3.53E-06
3.53E-06    3.53E-06    0.000003495 0.000003495 0.000003495 0.000003495
0.000003495 0.000003495 0.000003495 0.000003495 0.000003495 3.46E-06
3.46E-06    3.46E-06    3.46E-06    3.46E-06    3.46E-06    3.46E-06
3.46E-06    0.00000342  0.00000342  0.00000342  0.00000342  0.00000342
0.00000342  0.00000342
]; % total flow rate m3/s (STP) descending concentration
FA0=[8.33E-07   8.33E-07    8.33E-07    8.33E-07    8.33E-07    8.33E-07
8.33E-07    8.33E-07    8.33E-07    8.33E-07    6.47E-07    6.47E-07
6.47E-07    6.47E-07    6.47E-07    6.47E-07    6.47E-07    6.47E-07
6.47E-07    6.47E-07    4.99E-07    4.99E-07    4.99E-07    4.99E-07
```

```
4.99E-07    4.99E-07    4.99E-07    4.99E-07    4.99E-07    3.27E-07
3.27E-07    3.27E-07    3.27E-07    3.27E-07    3.27E-07    3.27E-07
3.27E-07    1.64E-07    1.64E-07    1.64E-07    1.64E-07    1.64E-07
1.64E-07    1.64E-07
];% Initial methane molar rate molCH4/s, descending order
FB0=zeros(1, 44); % water  mol/s
R= 8.314E-3; %Kj/molK
%%%%%%%%%%%%%%%%%%%%%%
X=x(1);

           switch Model
          case 1
     Q= Q0(i).*(T(i)/273.15).*(1/2.837);
     k1= (k(1).*exp(-k(2)./(R.*T(i))));
     k2= (k(3).*exp(k(4)./(R.*T(i))));
    dxdt= (k1.*(1-X)./Q)./( ( 1+ (k2.*((FB0(i)+(2*FA0(i).*X))./Q) )));

     case 2
     Q = Q0(i).*(T(i)/273.15).*(1/2.837);
     k1= (k(1).*exp(-k(2)./(R*T(i))));
     k2= (k(3).*exp(k(4)./(R*T(i))));
     dxdt= (k1.*(1-X)./Q)./( ((FB0(i)+(2*FA0(i).*X))./Q) + (k2.*(FA0(i).*(1-
X)./Q).*((FB0(i)+(2*FA0(i).*X))./Q)) );
       otherwise
      error('Model number not found')
           end

  end
```

x_exp.m

```
function u=x_exp(s)
%This file contains the experimental conversion for DRY conditions
%A similar file under the same name (but in a separate folder) exists for WET
%conditions.
A=[7.00444  15.56935    36.67723    61.76741    81.76382    6.45007 15.2747
36.15556    63.15313    81.09573    8.02749 17.38008    38.71781    65.18328
83.16914    7.81314 17.01825    39.0326 65.27764    83.40997    9.69587
20.24149    42.91878    67.2779 9.22619 19.2929 41.88772    65.00714
83.54008    12.83116    26.11926    49.34309    73.2149 11.87066    24.56097
49.2063 73.78462    19.06307    36.65078    72.94871    7.91843 19.79077
35.89204    67
]/100;
u=A(s);
```

Obj.m

```
function obj = Obj(k)

%This m-file calculates the value of the objective function for a given k
%vector. Prior to running this file, the model number needs to be
%entered/saved in the Model.m file
```

```
%%%%%%%%%%%%%%%%%%%%%%%%%
global  Model r i
Model= 1; %Model Number
for i=1:44

tspan=[0 0.092];%0.092g catalyst=92 mg Catalyst
x0= 0;
%x0=[1E-12 1E-12 1E-12 1E-12 1E-12];
[t,x]= ode45(@(t,x)model(t,x,k),tspan,x0);
r(i)=x(end,:); %predicted
end
x_obs =x_exp(1:44);%experimental
obj = sum (( r-x_obs ).^2)/44;
end
```

run.m

```
function [X,FVAL,EXITFLAG,OUTPUT] =  run
%%  This m-file uses the Pattern Search Algorithm to do the optimization.
%Prior to using this file, the desired model number should be entered in
%Model.m, Model. m needs to be saved and run so the global variable "Model"
%is accessible for the Obj.m and run.m.
%The ans of this file is the optimized k vector.
%FVAL is the value of the objective function calculated using the optimized
%k.
%This answer can be saved and plotted by typing delta(ans).
%%%%%%%%%%%%%%%%%%%%%%%%%%%%%%%% %%%%%%%%%%%%%%%%%%%%%%%%%%%%%%%%

tic;
tt = cputime;
objectiveFunction = @Obj; % @scr_opt;
%%
%Bounds
%      1  2  3
% k=[k(1) k(2) k(3) k(4)]
 LB = [1E-3    1E-2   1E-8    0.01];
 UB = [1E+3 150 1E-6 150 ];


%Start with default options
options = psoptimset;
%%compute the  normalized starting points based on opt.par and limits.par
%%
%VAL   =load('opt.par.ini'); %% initial parameter values
%BOUND =load('limits.par');  %% upper and lower bounds file
%[~, n] = size(BOUND);

X0=[17.281810364248777,28.699775294173510,2.5e-07,1.315976061278209e+02]
X0=[44.014037906929445,28.788343335962980,2.500000000000000e-
07,1.316028102982488e+02]
X0=[44.525364998708370,28.846095749925200,2.501017432153440e-
07,1.316008084273576e+02]
%%
%Inequality constraints
```

```
Aineq = [];
Bineq = [];
%Equality Constraints
Aeq = [];
Beq = [];
%ConstraintFunction = @simple_constraint;
%Start with default options
options = psoptimset;
%%Modify some parameters
options = psoptimset(options,'InitialMeshSize' ,500000000000);


options = psoptimset(options,'TolMesh' ,1e-15);
options = psoptimset(options,'TolX'    ,1e-15);
options = psoptimset(options,'TolBind' ,1e-15);
options = psoptimset(options,'TolFun' ,1e-15);
options = psoptimset(options,'MeshRotate' ,'off');
options = psoptimset(options,'PollMethod' ,'GPSPositiveBasis2N');
options = psoptimset(options,'CacheTol' ,1e-20);
options = psoptimset(options,'MeshAccelerator' ,'ON');

options = psoptimset(options,'CompletePoll' ,'ON');
options = psoptimset(options,'PollingOrder' ,'Random');
options = psoptimset(options,'SearchMethod' ,@GPSPositiveBasis2N);
options = psoptimset(options,'CompleteSearch' ,'on');
options = psoptimset(options,'MaxFunEvals' ,8000000000);
options = psoptimset(options,'MaxIter' ,8000000000);
options = psoptimset(options,'Display' ,'iter');
options = psoptimset(options,'UseParallel' ,true);
options = psoptimset(options,'PlotFcns' ,@psplotbestf);

%options = psoptimset(options,'OutputFcns' ,{ { @psoutputhistory } });
%options = psoptimset(options,'PlotFcns' ,{ @plot_lightoff_4NO });
options = psoptimset(options,'Cache' ,'on');
%%Run PATTERNSEARCH
[X,FVAL,EXITFLAG,OUTPUT] =
patternsearch(@Obj,X0,Aineq,Bineq,Aeq,Beq,LB,UB,options);
X
FVAL
```

delta.m

```
function com = delta(k)

%This file gives a comparison the experimental results to the values
%produced by using a given K vector in either of the models (1 or 2).
%The Model is defined as a global parameter and thus prior to using
%delta.m  the model number in Model.m needs to be defined and
%Model.m needs to be saved and run
```

```
global  Model r i
Model= 1; %Model Number

for i=1:44

tspan=[0 0.092];%0.092g catalyst=92 mg Catalyst
x0= 0;
%x0=[1E-12 1E-12 1E-12 1E-12 1E-12];
[t,x]= ode45(@(t,x)model(t,x,k),tspan,x0);
r(i)=x(end,:); %predicted
end
x_obs =x_exp(1:44);%experimental
obj = sum (( r-x_obs ).^2)/44;

figure
scatter (x_obs, r)
hold on
        hline.Color='b';
        hline= refline(1,0);
        precisionT = 4;
        precisionObj=6;
        precisionk=6;
        axis square
        box on
        axis ([0 1 0 1])
        ylabel('Predicted conversion')
        xlabel('experimental ')
        title({['Dry-Model  ',(num2str(Model))]});
        temp=['Dry-',num2str(Model),'.tiff'];
        saveas(gca,temp);
        %%%%%%%%%%%%%
        filename =['Dry Model',num2str(Model),'.xlsx'];
sheet = 1;
xlRange = 'A1';
A = {'Dry Model Number = M'  num2str(Model)};
xlswrite(filename,A,sheet,xlRange)
xlRange = 'A2';
A = {'Experimental Conversion'};
xlswrite(filename,A,sheet,xlRange)

xlRange = 'B2';
A = {'Predicted Conversion'};
xlswrite(filename,A,sheet,xlRange)

xlRange = 'A4';
xlswrite(filename,(x_obs)',sheet,xlRange)
xlRange = 'B4';
xlswrite(filename,r',sheet,xlRange)

xlRange = 'H2';
xlswrite(filename,k,sheet,xlRange)
xlRange = 'H3';
xlswrite(filename,obj,sheet,xlRange)
end
```

lightdry.m

```
function dxdt = lightdry(t,x,k)

%lightdry solves the equation for dry conditions.
% This M-file is used in conjunction with lightdryxls and x_exp.m to plot the
% light off curves at each concentration for DRY conditions.
global   T i

Q0=[0.00000357  0.00000357  0.00000357  0.00000357  0.00000357  0.00000357
0.00000357  0.00000357  0.00000357  0.00000357  3.53E-06    3.53E-06
3.53E-06    3.53E-06    3.53E-06    3.53E-06    3.53E-06    3.53E-06
3.53E-06    3.53E-06    0.000003495 0.000003495 0.000003495 0.000003495
0.000003495 0.000003495 0.000003495 0.000003495 0.000003495 3.46E-06
3.46E-06    3.46E-06    3.46E-06    3.46E-06    3.46E-06    3.46E-06
3.46E-06    0.00000342  0.00000342  0.00000342  0.00000342  0.00000342
0.00000342  0.00000342
]; % total flow rate m3/s (STP) descending concentration
FA0=[8.33E-07   8.33E-07    8.33E-07    8.33E-07    8.33E-07    8.33E-07
8.33E-07    8.33E-07    8.33E-07    8.33E-07    6.47E-07    6.47E-07
6.47E-07    6.47E-07    6.47E-07    6.47E-07    6.47E-07    6.47E-07
6.47E-07    6.47E-07    4.99E-07    4.99E-07    4.99E-07    4.99E-07
4.99E-07    4.99E-07    4.99E-07    4.99E-07    4.99E-07    3.27E-07
3.27E-07    3.27E-07    3.27E-07    3.27E-07    3.27E-07    3.27E-07
3.27E-07    1.64E-07    1.64E-07    1.64E-07    1.64E-07    1.64E-07
1.64E-07    1.64E-07
];% Initial methane molar rate molCH4/s, descending order
FB0=zeros(1, 44); % water  mol/s
R= 8.314E-3; %Kj/molK

%%%%%%%%%%%%%%%%%%%%%%
X=x(1);


     Q= Q0(i).*(T/273.15).*(1/2.837);
     k1= (k(1).*exp(-k(2)./(R.*T)));
     k2= (k(3).*exp(k(4)./(R.*T)));
    dxdt= (k1.*(1-X)./Q)./( ( 1+ (k2.*((FB0(i)+(2*FA0(i).*X))./Q) )));

  end
```

lightdry.xls

```
function obj = lightdryxls(k)

%this m-file saves the lightoff data for dry conditions.
%this m-file needs to be in the same folder as x_exp.m and lightdry.m
%Prior to running this file the lightdry.m should be saved and run
%Model number does not need to be modified (only Model 1 is used for
%plotting the lightoff curves of dry feed).
%The K vector is the optimized k-that was obtained from run.m
```

```
global  T i
%Model Number
Model=1;
k=[44.594740059959630,28.853759758242067,2.505250528938180e-
07,1.315924644074382e+02];
 figure
for CA=1:5
    switch CA
        case 1
            i=1;
        case 2
            i=11;
        case 3
            i=21;
        case 4
            i=31;
        case 5
            i= 41;
    end

m=[200:1:410]+273.15;
for j=1:length(m)
T=m(j);
tspan=[0 0.092];%0.092g catalyst=92 mg Catalyst
x0= 0;
%x0=[1E-12 1E-12 1E-12 1E-12 1E-12];
[t,x]= ode45(@(t,x)lightdry(t,x,k),tspan,x0);
r(j)=x(end,:); %predicte
end
x_obs =x_exp(1:44);%experimental
hold on
plot (m-273.15,r)

filename =['LightoffDry Model-',num2str(Model),'.xlsx'];
sheet = CA;
xlRange = 'A1';
A = {'CA'  num2str(CA)};
xlswrite(filename,A,sheet,xlRange)
xlRange = 'B2';
A = {'Model Conversion'};
xlswrite(filename,A,sheet,xlRange)
xlRange = 'A2';
A = {'Temperature'};
xlswrite(filename,A,sheet,xlRange)

xlRange = 'B4';
xlswrite(filename,r',sheet,xlRange)
xlRange = 'A4';
xlswrite(filename,(m-273.15)',sheet,xlRange)
end
end
```

E.2. MATLAB codes for wet conditions

Contents of the folder for wet conditions:

- model.m: the M-file containing the model equation which allows for switching between two models (Model 1= Kikuchi's rate expression, Model 2= the rate equation proposed in this work)
- x_exp.m is the vector of the experimental conversions for wet conditions.
- Obj. m is the ODE solver that solves Model.m for given k parameters and produces the objective function
- run.m is the optimizer that optimizes the k parameters using patternsearch algorithm
- delta.m is the M-file used to compare the experimental data to the predicted conversion by plotting the results
- lightwet.m is used in the end to plot the light off curves for the optimized values of k
- lightwetxls.m is works in conjunction with lightwet.m and x_exp and saves the light-off curves at various concentrations.

model.m, x_exp.m, obj.m and run. m function together to give the optimized k vector as the *ans* of run.m. This *ans* is used in delta.m to plot the experimental data vs predicted data. The optimized k vector is entered (manually) in the lightwetxls.m to produce the light off curves.

model.m

```
function dxdt = model(t,x,k)

% This code is used to model the WET conditions.
%A similar code (with different T, Q0, FA0, FB0-and its own x_exp M-file)
%is used for dry conditions. The m-files for wet and dry conditions are to
%be saved and run in separate folders.
%The folder for Wet conditions should contain the following files:
% Model.m, x_exp.m, Obj.m, run.m and delta.m, lightwet.m and lightwetxls.m
%a separate folder with similar files is used for dry conditions.

%Model 1: -rA= k1CA/1+k2CB  Kikuchi's Model
%Model 2: -rA= k1CA/[(k2CB)*(1+k3CA)]- The model Proposed in this work
%Units of rate: mol/gCat.s
% T is the temperature matrix (degree C)
%Model is the model number and functions as a switch between two models
%Q0= total initial volumetric flowrate (m3/s (STP))
%FA0= molar flow rate of CH4 (mol CH4/s)
%FB0= molar flow rate of H2O (mol water/s)
%R= universal gas constant kJ/molK
```

```
%Thus, the energies (activation and adsorption) are in kJ
%The catalyst mass (W) which is used in the tspan in the Obj.m is
%in g, thus the rate equation is in mol/gCat.s
%Model. m contains the global variable "Model" and needs to be run before
%running Obj.m, run.m, com.m

%lightdryxls.m saves the lightoff curves in excel by solving lightdry.m
%lightwetxls.m saves the wet lightoff curves in excel by solving lighwet.m
%%%%%%%%%%%%%%%%%%%%%%%%%%%%%%%%%%%%%%%%%%%%%%%%%%%%%%%%%%%%%%%%%%%%%%%
global Model T i
Model = 2;


T= [278.75  296.975 322.55  350.1   375.9   275.45  298.975 324.55  348.1
373.65  276.55  297.45  323 348.75  374.7   273.85  294.5   321.3   346
371.75  274.4   295.25  320.8   346.45  372.95  274.8   296.95  321.4   346.7
372.75  276.55  297.45  322.6   349.35  273.95  294.9   320.05  345.75
273.55  297.2   325.95  274.8   299.2   320.9
]+273.15;

Q0=[3.76E-06    3.76E-06    3.76E-06    3.76E-06    3.76E-06    3.76E-06
3.76E-06    3.76E-06    3.76E-06    3.76E-06    3.72E-06    3.72E-06
3.72E-06    3.72E-06    3.72E-06    3.72E-06    3.72E-06    3.72E-06
3.72E-06    3.72E-06    3.68E-06    3.68E-06    3.68E-06    3.68E-06
3.68E-06    3.68E-06    3.68E-06    3.68E-06    3.68E-06    3.68E-06
3.64E-06    3.64E-06    3.64E-06    3.64E-06    3.64E-06    3.64E-06
3.64E-06    3.64E-06    3.61E-06    3.61E-06    3.61E-06    3.61E-06
3.61E-06    3.61E-06
]; % total flow rate m3/s (STP) descending concentration
FA0=[8.33E-07   8.33E-07    8.33E-07    8.33E-07    8.33E-07    8.33E-07
8.33E-07    8.33E-07    8.33E-07    8.33E-07    6.47E-07    6.47E-07
6.47E-07    6.47E-07    6.47E-07    6.47E-07    6.47E-07    6.47E-07
6.47E-07    6.47E-07    4.99E-07    4.99E-07    4.99E-07    4.99E-07
4.99E-07    4.99E-07    4.99E-07    4.99E-07    4.99E-07    4.99E-07
3.27E-07    3.27E-07    3.27E-07    3.27E-07    3.27E-07    3.27E-07
3.27E-07    3.27E-07    1.64E-07    1.64E-07    1.64E-07    1.64E-07
1.64E-07    1.64E-07
];% Initial methane molar rate molCH4/s, descending order
FB0=[8.35E-06   8.35E-06    8.35E-06    8.35E-06    8.35E-06    8.35E-06
8.35E-06    8.35E-06    8.35E-06    8.35E-06    8.35E-06    8.35E-06
8.35E-06    8.35E-06    8.35E-06    8.35E-06    8.35E-06    8.35E-06
8.35E-06    8.35E-06    8.35E-06    8.35E-06    8.35E-06    8.35E-06
8.35E-06    8.35E-06    8.35E-06    8.35E-06    8.35E-06    8.35E-06
8.35E-06    8.35E-06    8.35E-06    8.35E-06    8.35E-06    8.35E-06
8.35E-06    8.35E-06
]; % water  mol/s
R= 8.314E-3; %Kj/molK
%%%%%%%%%%%%%%%%%%%%%%%%
X=x(1);

          switch Model
         case 1
     Q= Q0(i).*(T(i)/273.15).*(1/2.837);
     k1= (k(1).*exp(-k(2)./(R.*T(i))));
     k2= (k(3).*exp(k(4)./(R.*T(i))));
```

```
    dxdt= (k1.*(1-X)./Q)./( ( 1+ (k2.*((FB0(i)+(2*FA0(i).*X))./Q) )));

        %%%%%%%%%%%%%%%%%%%%%%%%%%%%%%%%%%%%%%%%%%%%%%%%%%%%%%%%


     case 2
     Q = Q0(i).*(T(i)/273.15).*(1/2.837);
     k1= (k(1).*exp(-k(2)./(R*T(i))));
     k2= (k(3).*exp(k(4)./(R*T(i))));
     dxdt= (k1.*(1-X)./Q)./( ((FB0(i)+(2*FA0(i).*X))./Q) + (k2.*(FA0(i).*(1-
X)./Q).*((FB0(i)+(2*FA0(i).*X))./Q)) );
   otherwise
      error('Model number not found')
           end

  end
```

x_exp.m

```
function u=x_exp(s)
%This file contains the experimental conversion for Wet conditions
%A similar file under the same name exists for Dry conditions.

A=[6.09962  13.62963    31.01264    56.94459    74.12045    7.59234 15.62388
34.51307    54.84344    76.12329    9.33192 18.57299    37.76795    60.90982
78.84018    8.4924  17.22135    35.67551    60.17215    78.3675 10.18074
20.23415    41.14048    65.46781    83.25233    10.69902    21.15523
41.76657    62.63764    81.17241    13.70885    25.481  47.33577    69.08
13.38055    24.956  46.36834    67.40202    15.5349 30.25729    59.20051
15.93361    33.90846    58.40389
]/100;

u=A(s);
```

obj.m

```
function obj = Obj(k)
%This m-file calculates the value of the objective function for a given k
%vector. Prior to running this file, the model number needs to be
%entered/saved in the Model.m file
%%%%%%%%%%%%%%%%%%%%%%%%%%
%%%%%%%%%%%%%%%%%%%%%%%%%%
global  Model r i

Model= 2; %Model Number

for i=1:44

tspan=[0 0.092];%0.092g catalyst=92 mg Catalyst
x0= 1E-90;
%x0=[1E-12 1E-12 1E-12 1E-12 1E-12];
```

```
[t,x]= ode45(@(t,x)model(t,x,k),tspan,x0);
r(i)=x(end,:); %predicted
end
x_obs =x_exp(1:44);%experimental
obj = sum (( r-x_obs).^2)/44;
end
```

run.m

```
function [X,FVAL,EXITFLAG,OUTPUT] =  run

%%  This m-file uses the Pattern Search Algorithm to do the optimization.
%Prior to using this file, the desired model number should be entered in
%Model.m, Model. m needs to be saved and run so the global variable "Model"
%is accessible for the Obj.m and run.m.
%The ans of this file is the optimized k vector.
%FVAL is the value of the objective function calculated using the optimized
%k.
%This answer can be saved and plotted by typing delta(ans).
%%%%%%%%%%%%%%%%%%%%%%%%%%%%%%%% %%%%%%%%%%%%%%%%%%%%%%%%%%%%%%%%
tic;
tt = cputime;


objectiveFunction = @Obj; % @scr_opt;
%%
%Bounds
%      1  2  3
% k=[k(1) k(2) k(3) k(4)]
 LB = [1E-4    1E-1   1E-11    1E-1  ];
 UB = [1E-1 150 9E-7 150 ];

%Start with default options
options = psoptimset;
X0=[[0.009999994670930,22.046507046130750,8.349616335123479e-
09,1.032384850656408e+02]]
%%
%Inequality constraints
Aineq = [];
Bineq = [];
%Equality Constraints
Aeq = [];
Beq = [];
%ConstraintFunction = @simple_constraint;
%Start with default options
options = psoptimset;
%%Modify some parameters
options = psoptimset(options,'InitialMeshSize' ,50);


options = psoptimset(options,'TolMesh' ,1e-15);
options = psoptimset(options,'TolX'    ,1e-15);
options = psoptimset(options,'TolBind' ,1e-15);
options = psoptimset(options,'TolFun' ,1e-15);
options = psoptimset(options,'MeshRotate' ,'off');
```

```
options = psoptimset(options,'PollMethod' ,'GPSPositiveBasis2N');
options = psoptimset(options,'CacheTol' ,1e-20);
options = psoptimset(options,'MeshAccelerator' ,'ON');

options = psoptimset(options,'CompletePoll' ,'ON');
options = psoptimset(options,'PollingOrder' ,'Random');
options = psoptimset(options,'SearchMethod' ,@GPSPositiveBasis2N);
options = psoptimset(options,'CompleteSearch' ,'on');
options = psoptimset(options,'MaxFunEvals' ,8000000000);
options = psoptimset(options,'MaxIter' ,8000000000);
options = psoptimset(options,'Display' ,'iter');
options = psoptimset(options,'UseParallel' ,true);
options = psoptimset(options,'PlotFcns' ,@psplotbestf);

%options = psoptimset(options,'OutputFcns' ,{ { @psoutputhistory } });
%options = psoptimset(options,'PlotFcns' ,{ @plot_lightoff_4NO });
options = psoptimset(options,'Cache' ,'on');
%%Run PATTERNSEARCH
[X,FVAL,EXITFLAG,OUTPUT] =
patternsearch(@Obj,X0,Aineq,Bineq,Aeq,Beq,LB,UB,options);
X
FVAL
```

delta.m

```
function com2 = delta(k)

%This file gives a comparison the experimental results to the values
%produced by using a given K vector in either of the models (1 or 2).
%The Model is defined as a global parameter and thus prior to using
%delta.m  the model number in Model.m needs to be defined and
%Model.m needs to be saved and run

global  Model r i
Model= 2; %Model Number

for i=1:44

tspan=[0 0.092];%0.092g catalyst=92 mg Catalyst
x0= 0;

[t,x]= ode45(@(t,x)model(t,x,k),tspan,x0);
r(i)=x(end,:); %predicted
end
x_obs =x_exp(1:44);%experimental
obj = sum (( r-x_obs ).^2)/44;

figure
scatter (x_obs, r)
hold on
        hline.Color='b';
```

```
        hline= refline(1,0);
        precisionT = 4;
        precisionObj=6;
        precisionk=6;
        axis square
        box on
        axis ([0 1 0 1])
        ylabel('Predicted conversion')
        xlabel('experimental ')
        title({['wet-Model  ',(num2str(Model))]});
        temp=['wet-',num2str(Model),'.tiff'];
        saveas(gca,temp);
        %%%%%%%%%%%%%
        filename =['wet Model',num2str(Model),'.xlsx'];
sheet = 1;
xlRange = 'A1';
A = {'wet Model Number = M'  num2str(Model)};
xlswrite(filename,A,sheet,xlRange)
xlRange = 'A2';
A = {'Experimental Conversion'};
xlswrite(filename,A,sheet,xlRange)

xlRange = 'B2';
A = {'Predicted Conversion'};
xlswrite(filename,A,sheet,xlRange)

xlRange = 'A4';
xlswrite(filename,(x_obs)',sheet,xlRange)
xlRange = 'B4';
xlswrite(filename,r',sheet,xlRange)

xlRange = 'H2';
xlswrite(filename,k,sheet,xlRange)
xlRange = 'H3';
xlswrite(filename,obj,sheet,xlRange)
end
```

lightwet.m

```
function dxdt = lightwet(t,x,k)

%lightwet solves the equation for dry conditions.
% This M-file is used in conjunction with lightwetxls and x_exp.m to plot the
% light off curves at each concentration for Wet conditions.

global T i


Q0=[3.76E-06    3.76E-06    3.76E-06    3.76E-06    3.76E-06    3.76E-06
3.76E-06    3.76E-06    3.76E-06    3.76E-06    3.72E-06    3.72E-06
3.72E-06    3.72E-06    3.72E-06    3.72E-06    3.72E-06    3.72E-06
3.72E-06    3.72E-06    3.68E-06    3.68E-06    3.68E-06    3.68E-06
3.68E-06    3.68E-06    3.68E-06    3.68E-06    3.68E-06    3.68E-06
```

```
3.64E-06    3.64E-06    3.64E-06    3.64E-06    3.64E-06    3.64E-06
3.64E-06    3.64E-06    3.61E-06    3.61E-06    3.61E-06    3.61E-06
3.61E-06    3.61E-06
]; % total flow rate m3/s (STP) descending concentration
FA0=[8.33E-07   8.33E-07    8.33E-07    8.33E-07    8.33E-07    8.33E-07
8.33E-07    8.33E-07    8.33E-07    8.33E-07    6.47E-07    6.47E-07
6.47E-07    6.47E-07    6.47E-07    6.47E-07    6.47E-07    6.47E-07
6.47E-07    6.47E-07    4.99E-07    4.99E-07    4.99E-07    4.99E-07
4.99E-07    4.99E-07    4.99E-07    4.99E-07    4.99E-07    4.99E-07
3.27E-07    3.27E-07    3.27E-07    3.27E-07    3.27E-07    3.27E-07
3.27E-07    3.27E-07    1.64E-07    1.64E-07    1.64E-07    1.64E-07
1.64E-07    1.64E-07
];% Initial methane molar rate molCH4/s, descending order
FB0=[8.35E-06   8.35E-06    8.35E-06    8.35E-06    8.35E-06    8.35E-06
8.35E-06    8.35E-06    8.35E-06    8.35E-06    8.35E-06    8.35E-06
8.35E-06    8.35E-06    8.35E-06    8.35E-06    8.35E-06    8.35E-06
8.35E-06    8.35E-06    8.35E-06    8.35E-06    8.35E-06    8.35E-06
8.35E-06    8.35E-06    8.35E-06    8.35E-06    8.35E-06    8.35E-06
8.35E-06    8.35E-06    8.35E-06    8.35E-06    8.35E-06    8.35E-06
8.35E-06    8.35E-06
]; % water  mol/s
R= 8.314E-3; %Kj/molK

%%%%%%%%%%%%%%%%%%%%%%
X=x(1);

  Q = Q0(i).*(T/273.15).*(1/2.837);
     k1= (k(1).*exp(-k(2)./(R*T)));
     k2= (k(3).*exp(k(4)./(R*T)));
     dxdt= (k1.*(1-X)./Q)./( ((FB0(i)+(2*FA0(i).*X))./Q) + (k2.*(FA0(i).*(1-
X)./Q).*((FB0(i)+(2*FA0(i).*X))./Q)) );


  end
```

lightwetxls.m

```
function obj = lightwetxls(k)
global  T i
%this m-file saves the lightoff data for Wet conditions.
%this m-file needs to be in the same folder as x_exp.m and lightdry.m
%Prior to running this file the lightdry.m should be saved and run
%Model number does not need to be modified (only Model 2 is used for
%plotting the lightoff curves of wet feed).
%The K vector is the optimized k-that was obtained from run.m

Model= 2;
k=[0.150048817903749,36.251233330236820,3.330457173127074e-
07,83.590912607770390];
for CA=1:5
    switch CA
        case 1
            i=1;
```

```
        case 2
            i=11;
        case 3
            i=21;
        case 4
            i=31;
        case 5
            i= 41;
    end

m=[200:1:450]+273.15;
for j=1:length(m)
T=m(j);
tspan=[0 0.092];%0.092g catalyst=92 mg Catalyst
x0= 0;

[t,x]= ode45(@(t,x)lightwet(t,x,k),tspan,x0);
r(j)=x(end,:); %predicte
end
x_obs =x_exp(1:44);%experimental
hold on
plot (m-273.15,r)
legend('show')

filename =['Lightoff wet Model-',num2str(Model),'.xlsx'];
sheet = CA;
xlRange = 'A1';
A = {'CA'  num2str(CA)};
xlswrite(filename,A,sheet,xlRange)
xlRange = 'B2';
A = {'Model Conversion'};
xlswrite(filename,A,sheet,xlRange)
xlRange = 'A2';
A = {'Temperature'};
xlswrite(filename,A,sheet,xlRange)

xlRange = 'B4';
xlswrite(filename,r',sheet,xlRange)
xlRange = 'A4';
xlswrite(filename,(m-273.15)',sheet,xlRange)

end
end
```